UNIVERSITÀ DEGLI STUDI DI BARI ALDO MORO

PhD Program in Geosciences
37th Cycle

PhD Thesis

MINERALIZATION OF LONGOBUCCO AND FONTE ARGENTILA (SILA MASSIF, CALABRIA, SOUTHERN ITALY): FROM MINERALOGY TO GENETIC CONTEXT

PhD Candidate:
Antonio Ciccolella

Supervisor:
Prof. Emanuela Schingaro

Co-supervisors:
Dr. Rosa Anna Fregola
Prof. Gennaro Ventruti
Dr. Fabrizio Tursi

To quondam Sergio and Rosa...

To my mother, Angela,

and sister, Noemi

Acknowledgements

My sincere thanks to Professor Schingaro for her support during the most critical moments of this PhD.

I would like to thank my co-supervisors, Dr Fregola and Dr Ventruti, for their contributions.

Special thanks go to Dr Tursi for being an invaluable source of both of scientific insight and personal encouragement throughout this journey.

I am grateful to my collaborators, Professors Vincenzo Festa and Giovanni Ruggieri, for their helpfulness, appreciated support and critical discussions.

A huge thank you goes to my colleagues: Ivana, Gianna, Marina, Filippo, Domenico, Marianna, Maddalena, Umberto, Vito and Alessia, whose company and laughter cheered even the most difficult moments.

I thank my sister Noemi and Dominic for welcoming me into their home in the beautiful English countryside, where I was able to rest and recharge my batteries.

I am grateful to my mother, Angela, for her support and understanding.

I thank Savino and all those who offered me support and laughter.

And to you, Minu: I am honored that you completed your journey with me....

Finally, thank you, Antonio.

Index

Index of figures

Abstract

This study examines, through a multi-scale and multi-methodic approach, the Zn-Pb(-Cu-Fe) mineralization associated with fault zones in the Sila Massif (Calabria, southern Italy), focusing on its paragenetic evolution using samples collected from the historical mining sites of Longobucco (LGB) and Fonte Argentila (FAR). Hosted within Permian–Carboniferous granodiorites of the Sila Batholith, the mineralization exhibits similar mineralogical assemblages from both mining sites and, in addition, shows geochemical features similar to those characteristics of Mississippi Valley Type (MVT) and Sediment-hosted Massive Sulphides (SHMS) systems, despite their vein-like nature in the field. The primary ore mineral, sphalerite, occurs in three distinct generations (Sp1, Sp2, Sp3), reflecting multiple mineralization episodes. The Sp1 is light-colored with relatively low Fe-content, Sp2 is darker and Fe-richer (up to 11.3 wt.%, corresponding to 0.21 mol% FeS), while Sp3 is colorless and with very low Fe-content, and formed through dissolution-precipitation processes. The μ-Raman Spectroscopy evidenced clear dependence on FeS mole fraction in sphalerite through systematic variations in band positions, intensity and area ratios. Based on the trace element signatures, the LGB-FAR sphalerite formed under low-temperature conditions (medians formation temperature of 178–180 °C), as indicated by the GGIMFis geothermometer, by the Ga/In, In/Ge and Zn/Cd ratios, and by single-crystal X-ray diffraction (SCXRD). The reconstructed paragenetic sequence spans four stages. Stage 1 is characterized by the precipitation of sphalerite (Sp1 and Sp2) and quartz (Qz1). Stage 2 is marked by massive precipitation of calcite (Cal), hosting sporadic synchysite crystals (20-60 μm), at LGB and fluorite (Flr) at FAR. Galena and chalcopyrite precipitated during stage 3, while quartz (Qz2) and sphalerite (Sp3) formed in stage 4. The observed geochemical features, as well as the low sulphur fugacity values ($\log_{10} fS_2 = 10^{-17.55}$–$10^{-17.29}$ atm), suggest precipitation from an ore-forming fluid of MVT-SHMS/basinal derivation. This model is also supported by fluid inclusions data that register direct evidence of meteoric to high salinity basinal-type ore-forming fluids trapped within fluorite of the stage-2 (T_h = 72.2–114.6 °C; salinities from 0 to 21.2 wt.% NaCl eq.). Ore-forming fluids later evolved into meteoric to basinal-type with low to moderate salinity (0.5 to 6.1 wt% NaCl eq.), as registered by fluid inclusions trapped within Qz2 of the stage-4, and higher temperature than Flr (T_h = 111.6–163.8 °C), also corroborated by Mg-Li geothermometer (median of 171°C). Rare Earth Element and Yttrium (REY) analyses in Cal and Flr confirm the presence of a diagenetic and basement-derived geochemical signature during their precipitation. These findings suggest that the LGB and FAR mineralization may have formed from fluids of basinal-type derivation, within basement host rocks. The study highlights the importance of fluid mixing and fault-controlled fluid flow in the formation of Zn-Pb deposits in crystalline basement settings, providing a comprehensive model for their paragenetic and geochemical evolution. By comparing our results with those of similar Zn-Pb-deposits, we suggest that the fluids responsible for the peculiar vein-type LGB-FAR mineralization had several characteristics compatible with those of MVT-SHMS deposits, despite an indirect magmatic contribution to the mineralizing fluids cannot be excluded at all.

1. Introduction

The mineralization of Calabria, abandoned and partly forgotten, have been exploited since the Bronze Age, especially for the extraction of Fe, Zn, Pb, Ag, and salts, by various civilizations that inhabited these lands (Cuteri, 1999, 2009, 2012; Saccà et al., 2017; Franco, 2019; Fregola et al., 2023). However, limited economic interest, depletion of ore deposits, and issues related to hydrogeological hazards, which characterize the Calabrian area, have led to the leaving of many mining sites over the centuries and to a decline of interest in the discovery of new ones (Franco, 2003).

This study aims to deepen the knowledge on some Calabrian mineralization, which gathered attention between the 1940s and 1990s due to a potential economic interest (Fregola et al., 2023), through a thorough analytical characterization, including optical microscopy, SEM, EPMA, LA ICP MS, μ-Raman spectroscopy, X-ray diffraction and fluid inclusion analyses. The study areas are located in the northern part of the Sila Massif (Calabria, southern Italy) and comprise: i) the Longobucco (LGB) area, historically known for silver extraction (Lovisato, 1879), and ii) the Fonte Argentila (FAR) area, near the locality of Bonia, where there are indications of Pb mineralization (Cuteri, 2012).

The characterization of the mineralization focused on key minerals (e.g., sphalerite, quartz, fluorite), which are excellent geological indicators for investigating formation conditions and the nature of mineralizing fluids. In particular sphalerite, that is the main ore mineral of both areas, was studied in-depth through chemical, spectroscopic and crystallographic analyses.

Sphalerite is a key ore-forming mineral, typically found in Zn-Pb ore deposits such as Mississippi Valley Type (MVT), Sediment-hosted Massive Sulphides (SHMS), and Volcanic-hosted Massive Sulphides (VHMS) (e.g., Cook et al., 2009; Mudd et al., 2017; Zhao et al., 2023). Due to its ability to incorporate valuable and critical metals (especially Ga, Ge, and In), it holds significant economic importance (Moskalyk, 2003; Alfantazi and Moskalyk, 2003; Höll et al., 2007). Trace elements (e.g., Mn, Fe, Co, Ni, Cu, Ge, Cd, Tl, Pb) in natural sphalerite are valuable geochemical indicators and may also influence its coloration (Cook et al., 2009; Knorsh et al., 2020). These elements help decipher the physical and chemical conditions of the ore-forming environment and the type of ore deposit (Barton & Bethke, 1987; Keith et al., 2014; Frenzel et al., 2016). Typically, sphalerite formed in magmatic-hydrothermal systems preferentially incorporates Mn, Fe, Co, Cu, and In, whereas sphalerite formed in MVT or SHMS deposits is enriched in Ga, Ge, Cd, Tl, and Pb (Cook et al., 2009; Li et al., 2023). Moreover, the texture of sphalerite can serve as a genetic indicator, with colloform banded sphalerite, microcrystalline to fibrous, being typical of many low-temperature systems

(Kelley et al., 2004; Di Benedetto et al., 2005; Pfaff et al., 2011; Belissont et al., 2016; Damian et al., 2020).

In the present study, the sphalerite characterization is combined with chemical and fluid inclusion analyses of gangue minerals (fluorite and quartz) from specific paragenetic stages. Fluid inclusion analysis is a powerful tool for investigating the evolution of mineralized systems, since it can provide direct information on the ore-forming fluids.

Additionally, Raman and crystallographic analyses were conducted on several sphalerite samples to study the effects of cation substitutions by specific elements on the sphalerite vibrational behavior and crystal structure (Zigone et al., 1981; Lepetit et al., 2003; Karbish et al., 2007; Osadchii and Gorbaty, 2010), with the ultimate goal of gaining genetic information.

For the first time in the Longobucco and Fonte Argentila areas, modern analytical techniques have been applied to investigate the ore-forming conditions associated with the paragenetic evolution of the Zn-Pb(-Cu-Fe) mineralization. Our findings were compared to those from other Zn-Pb-type deposits to highlight similarities and differences. Although no direct dating was performed on these deposits, it was possible to extract significant chemical and geochemical information to outline a preliminary evolutionary model of the geological context in which these mineralization likely formed.

Part of the data reported in this PhD thesis has been published in Fregola et al. (2023), regarding historical information on mineralization (i.e., Chapters 2.2-3), and Ciccolella et al. (2024, 2025), for geochemical and fluid inclusions analyses (i.e., Chapters 6.1-7, 6.11, 7.3-6).

2. Overview

2.1. Historical notes on the mining activity at Longobucco (LGB) and Fonte Argentila (FAR) in the Sila Massif

Historically, the district of Longobucco included five main silver-sites of exploitation, in Italian "argentiere" (namely, Longo Bucco, Reynella, Serra Stuppa, Lagonia, Fossi Loco), which constituted the significant silver-bearing district of Calabria (Mazzoleni, 1968). In these areas, the extraction and processing of silver have been known since the Magna Graecia Age (e.g., Cuteri, 2012; Saccà et al., 2017). Information on mine production is scarce and fragmented. The oldest documents directly attesting the presence of mining and maintenance activities in the Longobucco area date back to 1197, 1268, 1496, 1499, 1537, 1539-1540, 1553-56, 1559, 1587-89 (ASdN; Mazzoleni, 1968; Trocino et al., 2008; Adorisio, 2015; Saccà et al., 2017). From these sources, it is evident that the actively operating "argentiere" were those of, Reynella (in the district of Acqua di Radica - Reinella, in Longobucco) and Lagonia (old name for Bonia, in the district of Fonte Argentila). Between 1268 and 1277, the Longobucco deposits produced an annual average of 87 kg of silver, in addition to lead (Cuteri, 2012; Saccà et al., 2017). Silver extraction and mine maintenance were not facilitated by the geology and topography of the areas. Indeed, it is no coincidence that mining activities at some of the "argentiere" in Longobucco had already been suspended due to landslides and the impossibility of recovering the silver vein, as indicated in this 1602 financial report (ASPN) (**Figure 1**):

"*L'Argentera di Longobucco nella Provincia de Calabria Citra è una Montagna di Pietra viva che tiene vene d'Argento et Piombo Critta et Galanza sita appresso detta terra di Longobucco vicino la città di Rossano con grande comodità d'Acqua et legne per il suo lavoro detta Argentera è antiqua […]. In tempo che viveva detto Galeazzo* (Caracciolo) [1537–1551][1] *si scoverse in detta Argentera una vena ricchissima d'Argento et al principio si cominciò a cavare cascò una parte della Montagna che coperse detta vena, et se perdi, di sorte che mai più s'è possuta ritrovare non obstante che l'Affittatori, hanno fatto grossa spesa per cercarla. […] Il lavoro de detta Argentera non si può fare se non li quattro mesi dell'anno d'estate perché il resto dell'anno, sta sempre coverta di neve per l'Altezza de la montagna, et asprezza del loco talché non si può cavare né lavorare. […] non s'è continuato più d'Affittare essendosi visto per esperienza, che non ne risulta Guadagno et ci bisogna molta spesa.*"

[1] Galeazzo Caracciolo was active in the Kingdom of Naples from 1537, the year of his marriage to Vittoria Carafa, duchess of Nocera, to 1551, when he was exiled to Geneva for having accepted the Reformist faith.

“The Argentera of Longobucco in the Province of Northern Calabria is a mountain of massive rock containing veins of silver and lead, with "critta" and "galanza", located near the land of Longobucco, close to the city of Rossano, with abundant availability of water and wood for its works. This Argentera is ancient [...]. During the time when Galeazzo Caracciolo was alive [1537–1551], a very rich vein of silver was discovered in this Argentera, but as extraction began, a part of the mountain collapsed, covering the vein, losing it. Despite the efforts of the tenants, the vein has not been found again. [...] Operative works on this Argentera can only be carried out during four months in the summer, because in the rest of the year it is always covered by snow due to the height of the mountain and its rockiness, making extraction and work impossible. [...] Leasing has not continued because there is no profit and requires significant costs.”

It is likely that the mining site referenced in the report, located in the territory of Longobucco, near the city of Rossano, with ample water availability (possibly Torrente Cino), refers to the area of Lagonia (old name for Bonia, in the Fonte Argentila district), where critta (or gritta), i.e., pure galena, and galanza (or calans), i.e. argentiferous galena, were extracted (Cuteri, 2012).

In 1645, the excavation of a galena vein along the Trionto River produced only 4 parts of Ag per 100 parts of galena (Cuteri, 2012). The mineralization of Longobucco was explored once again from 1723 to 1783, when many tunnels collapsed and were flooded due to a violent earthquake (Arnoni, 1874-1875; Trocino et al., 2008; Saccà et al., 2017). From 1828 to 1832, “1800 cantari" of Pb were mined at the Acqua di Radica site in Longobucco (Lovisato, 1879a). Instead, in the early 19th century, small quantities of Ag-Pb-Sb ± Cu-Fe were extracted (De Beaumont, 1842; Cantarelli, 1844; Arnoni, 1875). Exploitation was finally abandoned in the first half of the 20th century (Saccà et al., 2017).

Nouo ingresso all'extrattion del cannapo.

nouo ingresso al cannapo. L'Ill.mo et Ecc.mo S. vicere con lre spedite a 15 di Gen.o 1560. fa fatta noua imp
sopra li cannauli, che s'extrahono fuora Regno a rag.e di tre scudi q car
dopoi è stata moderata a quindeci car.i per cantaro; et perche di detti a
ci è poca cautela per essere Intrata incerta, perche può essere piu, e m
secondo l'extrattioni, che accadono, per cio nó si pone per intrata fe

Argentera di longobucco.

Argentera di longobucco. L'Argentera di longobucco nella Prou.a di Calab.a Cit.a è una montagna d
Pietra uiua, che tiene vena d'argento, et di piombo, e ricca et Galan
sita appresso detta Tra di longobucco vicino alla Città di Rossano.
gran comodità d'acqua, et legna per il suo lauore, detta argentera
è antiqua, et per il Re Catt.o d'Immortal mem.a fu concessa al q. Ga
leatto Caracciolo in perpetuo, et Infeudo, al quale fu mossa l
per il Regio fisco, a causa, che la concess.ne sua pareua, che contenes
il feudo nominato l'argentera, et che l'intenzione di Sua Catt.a
non era stata di concederli almeno, dal quale si caua l'argen
te fatto sopra cio il procatto Sua Mtà Cattolica determinó, che det
argentera restasse al predetto Galeatto, et a suoi heredi; ma che
quando cuenga sel. donasse reconpensa in un'altro feudo d'I
trata annua di cinquecento ducati d'oro siano tenuti relas
detta argentera alla Regia Corte, et cosi l'hanno tenuta mo[lti] a
finalmente il q. Conte di Biccari figlio del detto Galeatto si è co
tentato pigliarsi la reconpensa di an. ducati cinquecento settan
cinque con.ti Impagamenta fiscali, che li son dati nella prou.a di
et l'argentera è reintegrata alla Reg.a Corte.

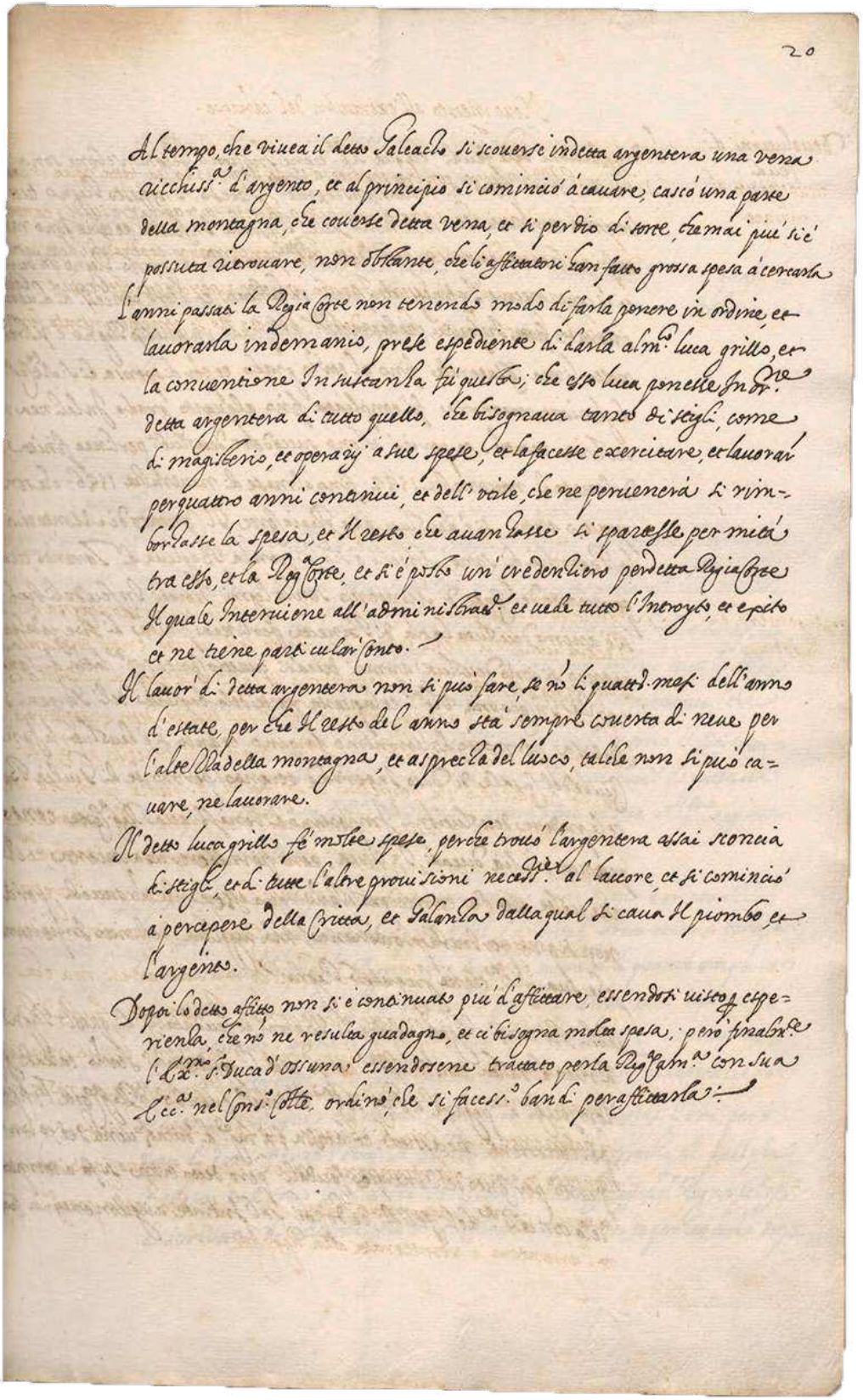

Figure 1 (and previous page). Financial and historical notes about the mining District of Longobucco; archive documents of “Papeles varios sobre el Reino de Nápoles 1590”. Royal Biblioteche of Madrid.

2.2. Relevant polymetallic mineralization in the Longobucco-Corigliano-Rossano area of the Sila Massif

The scientific literature on key mining areas of the Sila Massif is restricted to a few papers and, mainly, dates back to the 19th–20th centuries. Recently, this literature has been reviewed, and three main areas of interest have been highlighted, namely Longobucco-Corigliano-Rossano, San Giovanni in Fiore-Savelli-Cerenzia- Ampollino Lake, and Catanzaro-Tiriolo-Gimigliano, (Fregola et al., 2023, and references therein). Geochemical surveys conducted in these areas recorded positive anomalies for specific elements, among which Mn, Fe, Cu, Zn, As, Sn, Ba, W, Hg, Pb (De Vivo et al. 1981, 1984, 1991, 1998). In particular, the study sites of this thesis, namely Longobucco and Fonte Argentila, fall within the Longobucco-Corigliano-Rossano area (**Figure 2**), which is the richest one based on historical documentary sources (Fregola et al., 2023, and references therein).

Although several reports of ancient mines that were once active in the Longobucco area are mentioned in the older literature (e.g., Paillette, 1842; De Beaumont, 1842), traces of these mines were difficult to find by later investigators (e.g., Vighi, 1953). The Longobucco area (**Figure 2**) was characterized by the presence of argentiferous galena, bournonite, and arsenopyrite, with a higher Ag content in the galena hosted by phyllites compared to that present in granitic rocks (Paillette, 1842). However, nowadays galena samples are rarely found in the Longobucco area. Towards the end of the 19th century, findings of galena samples among landslide debris at Spartari and along the Macrocioli river were reported, but no galena vein was found (Cortese, 1895). Indeed, for the Longobucco area, only Zn-Fe-Sb positive geochemical anomalies were detected by the 20th century surveys, and not Pb and Ag (De Vivo et al., 1991). Some detailed field studies, describing the geology of mineralizations, were performed in the Longobucco area in the late 1940s (Ippolito, 1947a, b, c; Rittmann, 1947; Vighi, 1953). In particular, according to Vighi (1953) the ore bodies at Longobucco are hosted by magmatic rocks (granite, granodiorite, quartz-monzonite, porphyritic dikes, and quartz-monzonitic within granites) and metamorphic rocks (phyllites and marble lenses within phyllites. Multiple fractures and mineralization episodes were recognized, producing the paragenetic sequence: calcite-1 (Cal1) + sphalerite (Sp); quartz (Qz) + pyrite (Py) (± marcasite (Mrc)); Cal2; galena (Gn) + chalcopyrite (Ccp); (secondary) Cal3 (Vighi, 1953). Sphalerite is the most abundant ore-mineral in the entire area (De Vivo et al., 1978), while galena has been found only in traces in small veins filling fractures within Cal2 (Vighi, 1953). Numerous mineralized sites in the Longobucco area are reported in the literature, with similar mineral association: Spagnuolo; San Pietro; Difesella del Trionto; Cozzo Vitalba; Croce della Reghinella (or Reinella), Macchiafarna, Trionto River; La Manna Creek, Macrocioli Creek, Spartari, Mount Cerzito (**Figure 2**) (Fregola et al.,

2023). These Zn-Pb ± Fe-Cu mineralization, in veins within Hercynian granitoids, near the contact with phyllites of the Longobucco Unit, have been classified as pre-Alpine, for which a magmatic-hydrothermal origin was hypothesized (Bonardi et al., 1982). Small occurrences of W-Cu-Zn skarns (with mineral paragenesis: scheelite, garnet, fluorite, edenite, vesuvianite ± amphibole, epidote, scapolite) are also documented in the contact aureole between the Sila batholith and phyllites at Croce Reinella, as well as veins in granitic rocks near the contact with metamorphic rocks, containing scheelite (Omenetto et al., 1988; Croze, 1989; De Vivo et al., 1991).

North of the Longobucco district, other Zn-Pb-Fe mineralization are known, specifically in the Corigliano (namely, Fonte Argentila at Bonia-Baracconi, Patire, Cozzo del Pesco) and Rossano (Cozzo Chinico, Torrente Grammisate) areas (**Figure 2**) (Bonardi et al., 1982; Lorenzoni et al., 1983). Also, at Corigliano and Rossano areas, mineralization occur mainly in veins within Hercynian granitoids near the contact with phyllites, and a magmatic-hydrothermal origin was suggested (Bonardi et al., 1982; Lorenzoni et al., 1983). For the Fonte Argentila site, a higher abundance of galena was reported, associated to minor pyrite in quartz gangue (Cuteri, 2012). Indeed, significant Pb positive geochemical anomalies were detected in this area (De Vivo et al., 1984, 1998). At Cozzo del Pesco site, in the Corigliano area, pyrite is the most abundant ore mineral, with quartz as gangue mineral; minor veins of pyrite and sphalerite are also present within the granodiorites. Aplitic, pegmatitic, and microgranitic dikes are common at this site (CNEN, 1960; De Vivo et al., 1978). Like the Longobucco district, the Rossano area is characterized by the presence of W-Zn-Cu skarn lenses within the contact aureoles of the Sila batholith within phyllites (Omenetto et al., 1988). This finding was confirmed by positive geochemical anomalies of Pb, Zn, Cu, W, and Sn for the Rossano area (De Vivo et al., 1984). Finally, a detailed study on vein-type mineralization in the Rossano area revealed the mineral association: pyrite (including *electrum* within fractures), chalcopyrite, sphalerite, galena, arsenopyrite, as well as pyrrhotite, bismuth-tetrahedrite, native bismuth, Bi-Ag sulfosalt (pavonite), and montroydite (to a lesser extent), in quartz gangue (Benvenuti et al., 1994). For this mineralization, an epithermal origin was suggested by the authors, who determined the ore-forming fluid temperatures <250 °C and salinity of 6.8 to 7.3 wt.% NaCl eq. based on fluid inclusion analysis (Benvenuti et al., 1994).

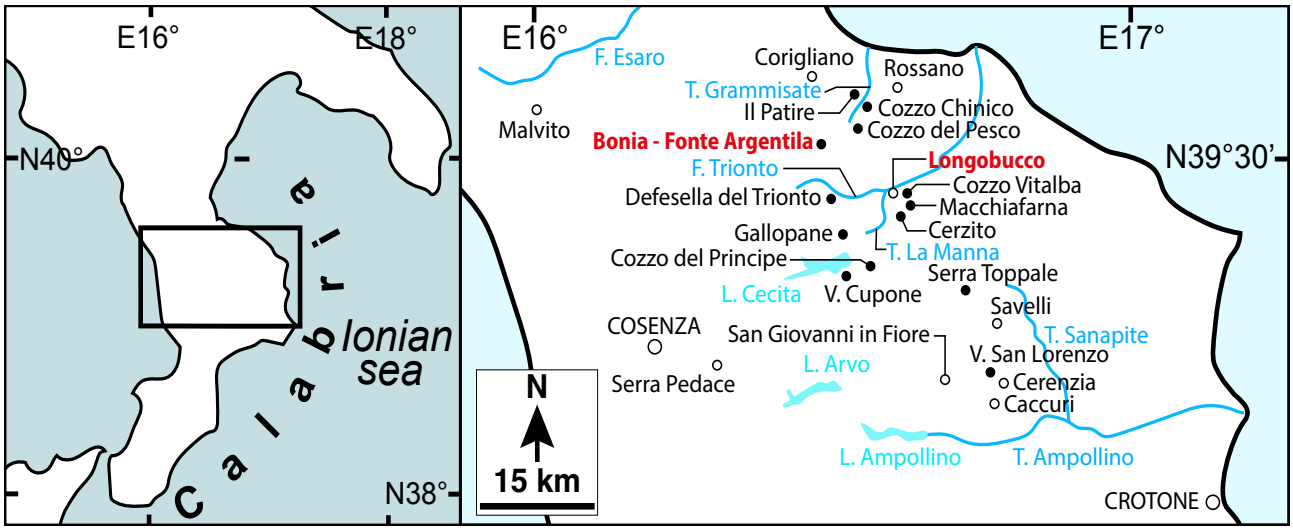

Figure 2. Sketch-map of northern Calabria with toponyms of the areas characterized by mineralization. *The* mineralization sites of this study are highlighted in red.

2.3. Genetic hypothesis of the Sila mineralization

One of the key open questions regarding mineralization in the Sila (and Serre) Massifs is its origin. In earlier literature, a connection between the mineralization and late-Variscan intrusions is strongly emphasized (reviewed in Fregola et al., 2023). While distinct lateral and thermal zonation of mineralization has been observed in the Serre Massif—ranging from high-temperature Mol-Qz to lower-temperature Sp-Gn-Ccp-Qz assemblages (Vighi, 1949)—this pattern has not been clearly documented in the Sila Massif. The spatial association of the Sila mineralization with the Variscan and late-Variscan granite bodies of the batholith led some authors to suggest also a genetic link with them (Vighi, 1953; De Vivo et al., 1978). On the other hand, Bonardi et al. (1982) suggest that part of the mineralization in this region may have formed, or been reworked, during the Alpine orogenic evolution of Calabria. However, the absence of precise geochronological data complicates efforts to address these hypotheses. Another hypothesis posits that the mineralized bodies in the Sila may result from multiple overlapping genetic processes (Bonardi et al., 1982; Lorenzoni et al., 1983).

Among the Sila mineralization, some may be related to ore-deposits found in other European areas, with similar geological settings. Specifically, the main vein-type Zn-Pb-Fe-Cu mineralization in the Longobucco and Rossano areas bears similarities to deposits found in the French Massif Central (Cassard et al., 1993; Marignac and Cuney, 1999; Belisson et al., 2014), the Freiberg District and Harz Mountains in Germany (Alles et al., 2019; Bauer et al., 2019), the Kutná Hora District in the Czech Republic (Pažout et al., 2019), and the Sulcis and Arburese regions in Sardinia (Boni et al., 2002; Naitza et al., 2017; Moroni et al., 2019). These mining regions are characterized by either a

post-Variscan basement, which was also affected by magmatic-hydrothermal events from the Late Carboniferous to the Permian, and by Mesozoic carbonate cover that facilitated later fluid circulations, in some cases continuing into the Holocene (Boni et al., 2009; Alles et al., 2019; Hintzen et al., 2023). The circulation of late low-saline fluids would has been involved in epithermal-type events, with localized presence of sulfosals and native metals (Ag, Au, Bi) (Benvenuti et al., 1994).

2.4. Sphalerite crystal chemistry and mineral chemistry

Zinc sulphide occurs naturally in two distinct polymorphic mineral phases: sphalerite (3C-ZnS, space group F-43m) and wurtzite (2H-ZnS, space group P63mc) (Posfai et al., 1988). The sphalerite structure can be described by a face centered cubic (FCC) lattice with a cubic close-packed (ccp) array of sulphur anions, corresponding to the 3C polytypic stacking sequence (ABCABC). A half of the tetrahedral sites of the sphalerite crystal lattice is occupied by Zn^{2+} cations, with the coordination tetrahedra sharing only their corners (Makovicky, 2006). Wurtzite shows a hexagonal close packed (HCP) array of sulphur anions, represented by the 2H polytypic stacking sequence ABAB (Evans et al., 1959; Fleet, 1977; Makovicky, 2006). A reversible phase transition may occur from sphalerite to wurtzite, accompanied by deformative stacking faults in close-packed planes. This phase transition usually occurs at 1020 °C (at 1 atm), but can be shifted towards lower temperature due to sulfur fugacity conditions and minor/trace elements impurities (Scott and Barnes, 1972; Akizuki, 1981).

Understanding the chemistry of sphalerite and its structure has involved much physico-chemical effort. Among the first geochemical investigations carried out on sphalerite, Stoiber (1940) highlighted the geochemical variability of the mineral, distinguishing between different geological formation settings. Subsequently, Kullerud (1953) and Barton & Toulmin (1966) focused their studies on phase relation and behavior involving the FeS-ZnS-S system at varying temperature (between 580 and 850 °C) and FeS content, obtaining correlations with structural parameters and FeS-content, through X-ray diffraction. Density determination studies (Cabri, 1969) suggested the presence of Fe^{3+} in the interstitial sites of the crystal lattice, corresponding to 1% of the total Fe content. Mössbauer spectroscopy was used to investigate the redox behavior of some metals (e.g., Mn, Fe, Cu, Cd) within the sphalerite and possible Jahn-Teller effects induced by their presence (Manning, 1967; Gerard et al., 1971; Scott, 1971; Di Benedetto et al., 2005a). Scott & Kissin (1973) resumed the FeS-ZnS-S system, studied by Barton & Toulmin (1966), and investigated it at temperatures below 300 °C. Bryndzia et al. (1988) proposed a geobarometer based on the equilibrium between sphalerite and hexagonal pyrrhotite, but Toulmin et al. (1991) revealed some problems both for systems at temperatures below 500° C and for the influence of chalcopyrite within the sphalerite.

Investigations with μ-Raman spectroscopy showed the vibrational effect of the metals (e.g., Mn, Co, Ni, Fe, Zn, Cd) constituting the sphalerite, demonstrating how Fe and Zn predominate in the Raman spectrum of the mineral, with greater sensitivity about Fe content (Zigone et al., 1981; Hope et al., 2001; Osadchii et al., 2010).

Sphalerite, as the primary ore mineral in lead-zinc (Pb-Zn) deposits, not only represents a valuable source for Zn, but it is a host for several metals and trace elements crucial to various high-tech applications (Cook et al., 2009; Ye et al., 2011; Frenzel et al., 2016; Sahlström et al., 2017; Liu et al., 2022; Luo et al., 2022; Cook et al., 2009; Sun et al., 2022;). These elements, particularly Ga, Ge, Cd, In, play central roles as "critical metals" in industries such as aerospace, nuclear energy, information technology, biotechnology and green energy sectors (Li et al., 2010; Werner et al., 2017; Hayes et al., 2018; Summaries, M. C., 2021). Furthermore, the trace elements content of sphalerite provides valuable metallogenic information, underscoring its overall importance (Cook et al., 2009; Frenzel et al., 2016, 2021; Wu et al., 2023).

Due to its simple crystal structure, sphalerite can incorporate significant quantities of minor and trace elements, such as Mn, Fe, Co, Ni, As, Cu, Se, Mo, Ag, Cd, In, Sn, Sb, Hg, Tl, Pb, and Bi. The concentrations of these elements depend on different factors, such as crystallization temperature, pressure, pH, redox potential, fluid chemistry, and mineral assemblages (Cook et al., 2009; Ye et al., 2011; Belissont, 2014; Bonnet et al., 2016; Frenzel et al., 2016; George et al., 2016; Zhuang et al., 2019; Zhu et al., 2021; Luo et al., 2022). These elements can be either incorporated through atomic substitution within the sphalerite crystal lattice or be components of nanometric-sized mineral inclusions in the sphalerite host. However, these features can be challenging to distinguish using conventional detailed analytical methods such as EPMA and LA-ICP-MS (Cook et al., 2009; Pfaff et al., 2011).

While simple substitution mechanisms for Zn^{2+} at tetrahedral sites involving divalent cations are more easily understood (Wright, 2009), heterovalent and coupled substitutions may also occur implying more complex mechanisms. Johan (1988) proposed a general substitution mechanism involving trivalent and tetravalent as well as monovalent and bivalent elements in sphalerite:

$$(x+2y)M^{+} + yM^{2+} + xM^{3+} + yM^{4+} \leftrightarrow (4 - 4y - 2x)Zn^{2+}$$

where M^{+} = Cu, Ag; M^{2+} = Mn, Fe, Co, Zn, Cd, Hg, Pb; M^{3+} = Fe, Ga, Ge, Sb, In, Tl; M^{4+} = Ge, Sn, Mo, W, whereas x and y refer to the atomic proportions of M^{3+} and M^{4+}. The mechanism of direct substitution can be expressed as $Zn^{2+} \leftrightarrow (Fe^{2+}, Cd^{2+})$, but it can also refer to the substitution of anions like $S^{2-} \leftrightarrow Se^{2-}$ (or $3S^{2-} \leftrightarrow 2As^{3-}$+ (vacancy)) (Cook et al., 2009; Belissont et al., 2014). For coupled substitutions, several mechanisms have been proposed, such as: $2Zn^{2+} \leftrightarrow Cu^{+} + In^{3+}$; $2Zn^{2+} \leftrightarrow Cu^{+} + Sb^{3+}$; $3Zn^{2+} \leftrightarrow Ge^{4+} + 2Ag^{+}$; $2Zn^{2+} \leftrightarrow Cu^{+} + Ga^{3+}$; $Sn^{4+} + 2Cu^{+} \leftrightarrow 3Zn^{2+}$; $3Zn^{2+} \leftrightarrow 2Cu^{+} + Ge^{4+}$ and

$2Zn^{2+} \leftrightarrow Ag^{+} + Sb^{3+}$ (Carrillo-Rosúa et al., 2008; Cook et al., 2012; Belissont et al., 2014; Pring et al., 2020; Wei et al., 2019). Instead, for more complex heterovalent substitutions, the following mechanisms have been proposed: $Sb^{3+} + Cu^{+} + Cu^{2+} \leftrightarrow 3Zn^{2+}$; $2Ge^{2+} + Ga^{3+} + 2Cu^{2+} + Cu^{+} \leftrightarrow 6Zn^{2+}$; $3Zn^{2+} \leftrightarrow In^{3+} + Sn^{3+}$ + (vacancy); $2Zn^{2+} \leftrightarrow Ge^{4+}$ + (vacancy); $2(Ag, Cu)^{+} + Sn^{4+} \leftrightarrow 3Zn^{2+}$ (Carrillo-Rosúa et al., 2008; Belissont et al., 2014; Cook et al., 2015; Pring et al., 2020). If minor and trace elements concentrate through substitution in the lattice rather than within mineral inclusions, their distribution through crystal zones, growth-bands, and growth-sectors within sphalerite can vary (Di Benedetto et al., 2005a; Belissont et al., 2014).

The variation in minor and trace element content within sphalerite also strongly depends on the formation environment properties and the types of fluids involved (Cook et al., 2009). In the following, the most common minor and trace elements in sphalerite are described.

Iron is incorporated as Fe^{2+} into the sphalerite lattice over a wide range of geological conditions, correlating both to the sulfur fugacity of the system (Wright and Gale, 2010) and possibly to temperature conditions (Cook, 1996; Frenzel et al., 2016). In natural sphalerite, its content can reach up to 15 wt%, and up to 52 mol% FeS at 700°C (Lepetit et al., 2003). Its content has been widely used as a geo-barometer, related to its presumed dependence on lithostatic pressure of the system (Scott and Barnes, 1971; Scott, 1973; Lusk et al., 1993), but subsequent studies have shown its limited effectiveness (Cook et al., 1994).

Manganese is present as Mn^{2+} and it may range from a few hundred to a few thousand ppm (Cook et al., 2009). The solid solution limit is up to 7 mol% of MnS within sphalerite, but it can reach 50 mol% of MnS within wurtzite (Kaneko et al., 1984). Often, Mn is used as a qualitative indicator of the redox conditions of the system and is influenced by the formation temperature (Kullerud, 1953; Kelley et al., 2004; Frenzel et al., 2016).

Cobalt, like Mn and Fe, can reach high concentrations in sphalerite, namely up to 40 mol% of CoS within ZnS (Cook et al., 2009).

Copper typically does not directly incorporate into sphalerite due to its limited solubility in its structure (Craig, 1973), except for some coupled substitutions (Cook et al., 2009). Indeed, high concentrations of Cu can lead to exsolutions within sphalerite, visible even in reflected light, known as "chalcopyrite disease" (Barton and Bethke, 1987).

Gallium and *germanium* are present in sphalerite from a few tens to thousands ppm (Rambaldi et al., 1986; Höll et al., 2007). Although there is no evidence of direct substitutions with Zn (Moh and Jager, 1979; Möller and Dulski, 1993), their concentration essentially depends on temperature and Fe content, with Ga and Ge preferentially concentrating at low temperatures and low Fe contents

(Rambaldi et al., 1986; Möller, 1987; Cassard et al., 1996; Moskalyk et al., 2003; Frenzel et al., 2016).

Silver in sphalerite does not concentrate beyond a few hundred ppm; often, these concentrations are associated with micrometric- to nanometric-sized mineral inclusions within sphalerite (Chryssoulis and Surges, 1988; Huston et al., 1996; Cook et al., 2009).

Cadmium, after Fe, is the second most abundant element that can be incorporated into the sphalerite structure (up to 7.5 wt%; Cook et al., 2009; Babedi et al., 2019). Some authors have used the Cd/Zn ratio to derive genetic or ore/fluid interaction information (Qian, 1987; Gottesmann and Kampe, 2007; Gottesmann, 2009).

Indium is not a common element in sphalerite, often found associated with Cu substituting for Zn+Fe. In Fe-rich sphalerites, indium concentrates within mineral inclusions (Seifert and Sandmann, 2006; Cook et al., 2009).

Antimony is not commonly found in sphalerite and is not involved in any solid solution with ZnS (Cook et al., 2009).

Tin is present as a limited solid solution of stannite within sphalerite (Oen et al., 1980). Additionally, In-bearing sphalerite shows a tendency to be enriched in Sn (1.8–4.3 wt.%) (Ono et al., 2004).

Mercury is an unusual element in sphalerite. The substitution of Hg for Zn is favoured by low Fe contents (Cook et al., 2009). Significant contents of mercury may occur in sphalerite of epithermal origin, where Hg can reach up to 27 wt% (Grammatikopoulos et al., 2006; Sokol et al., 2021).

Sphalerite is the main source of *thallium* in nature, extracted as a by-product (Nriagu, 1998), although its concentrations do not exceed 355 ppm (Kelley et al., 2004).

Pure colourless ZnS sphalerite is rare in the natural environment, as this mineral often contains various substituting cations within its lattice, from minor to trace element concentrations (Kullerud, 1953). Several correlations between composition and colour are found in literature. Among these, the most established one is that in the system $Zn_{(1-x)}Fe_xS$. The Fe content is so influential that even small amounts of this element may produce shades of yellow and brown in an otherwise colourless sphalerite, while higher Fe contents result in red, dark-brown, or even black colour (Kullerud, 1953; Carrillo-Rosúa et al., 2008; Lockington et al., 2014; Cugerone et al., 2018; Knorsch et al., 2020; Bacik et al., 2023). Several other elements are responsible for the chromatic variety of sphalerite. In detail, Cu and Sn, or Sb and Mn, can determine a brown to reddish colouration of sphalerite (Kelley et al., 2004; Carrillo-Rosúa et al., 2008; Belissont et al., 2016; Knorsh et al., 2020). Moreover, sphalerite colour can also change from colourless to pale yellow and orange due to an increase in its Cd content (Kubo et al., 1992; Bacik et al., 2023). Other elements, such as Ga and Ge, are usually

found in lighter-coloured sphalerite, but do not seem to be responsible for its colour. Significant amounts of Tl may be the cause of the pink colour of sphalerite (Knorsh et al., 2020). Regarding Co, if present in sphalerite, it is responsible for its green colouration, a rare variety often used as gemstone (Rager et al., 1996; Cook et al., 2009; Bacik et al., 2023).

3. Geological setting of the LGB and FAR mineralization

3.1. Geological background of the Sila Massif

The Sila Massif is located in the northern part of the Calabria–Peloritani terrane (Amodio-Morelli et al., 1976; Bonardi et al. 2001), which consists mainly of three tectonic units dominated by basement rocks – the Lower, Intermediate and Upper Complex – stacked during Alpine orogeny.

The Upper Complex (**Figure 3a-c**) comprises continental crust units, with the so-called Sila-Serre Unit (e.g. Festa et al., 2004) at the top, wherein the Zn-Pb(-Fe) mineralization subject of this PhD thesis occurs. In Sila and Serre massifs, this unit consists of tilted blocks of thinned, nearly complete late Variscan continental crust ~23 km-thick, which in turn represents the bedrock of a Mesozoic sedimentary cover (**Figure 3c**). The base of the unit consists of ~6 km-thick upper amphibolite to granulite facies metamorphic rocks (Atzori et al., 1984; Piluso and Morten, 2004; Fornelli et al., 2012; Festa et al., 2024) (e,g, **Figure 3c**), recording Alpine mylonitic reworking at the contact with the underlying or alongside tectonic units (Festa et al., 2016, 2020; Ortolano et al., 2020; Tursi et al., 2021).

The intermediate crust is occupied by a Carboniferous batholith, largely constituted by granodiorites, as well as by tonalites and granites (Ayuso et al., 1994; Langone et al., 2014; Fiannacca et al., 2017) (e.g. **Figure 3c**). Late Variscan high-temperature shear deformation affected the lower and the intermediate crust in the zone straddling the contact between migmatitic paragneisses and foliated granitoids (Festa et al., 2006, 2009).

Phyllites and paragneisses mainly constitute the upper crust rocks (e.g. **Figure 3c**), and record the tectono-metamorphic evolution under greenschist to amphibolite facies conditions, respectively. After peak metamorphism under Barrowian gradient, these rocks were subject to low-pressure contact metamorphism during emplacement of the late Carboniferous batholith, which induced re-equilibration under amphibole-hornfels and amphibolite facies conditions depending on the magma emplacement depth (Angì et al., 2009; Langone et al., 2010; Festa et al., 2013; Tursi et al., 2020).

From late Carboniferous through to early middle Permian, a late magmatic activity occurred, characterized by felsic (microgranite and microgranodiorite) and mafic (microdiorite and microgabbro) dikes, with dikes in the Sila Massif that crosscut the granitoids (Festa et al., 2010) and upper crustal rocks (Romano et al., 2011; Festa et al., 2018).

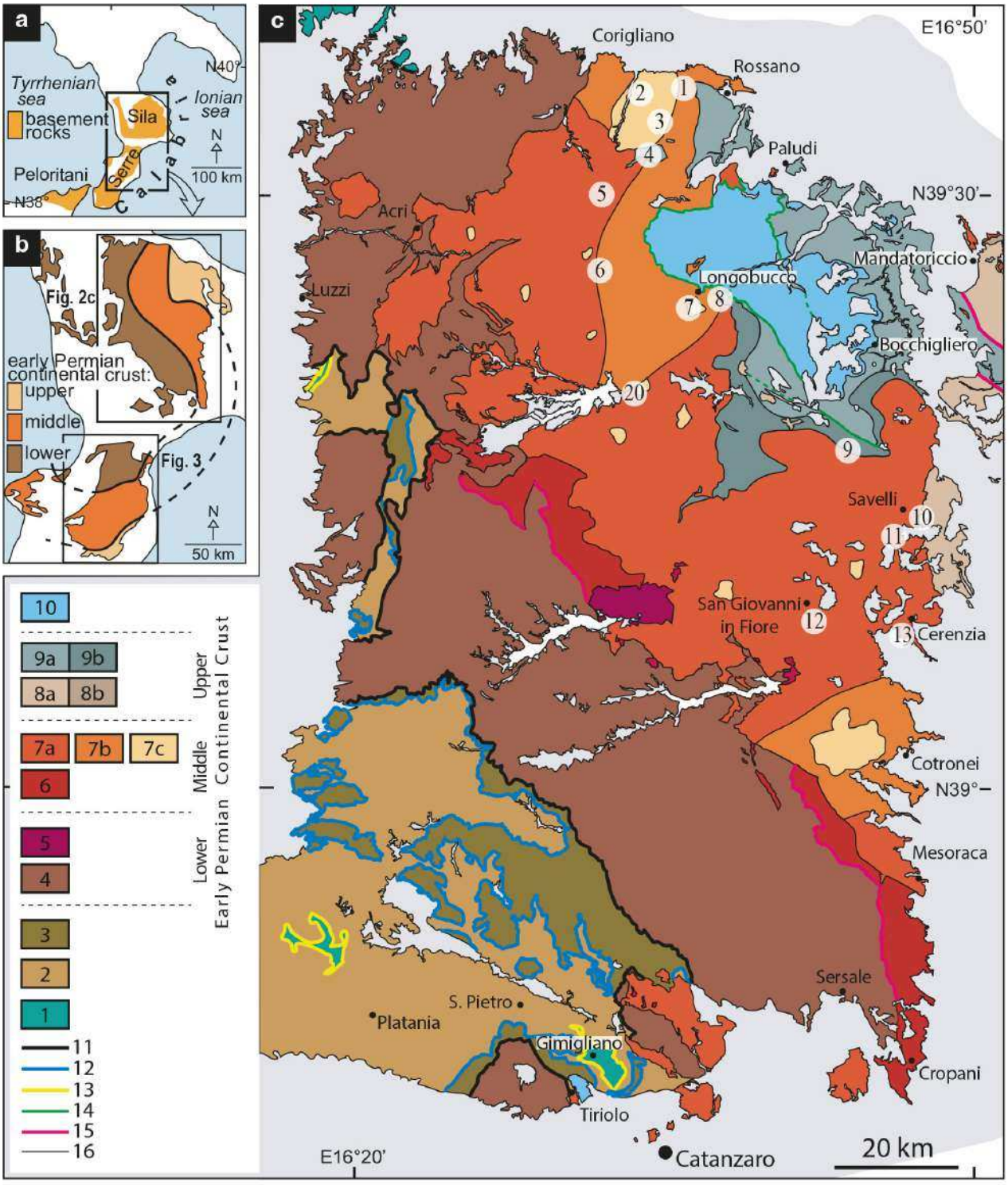

Using Al-in-Hbl geothermobarometry, emplacement of dike magmatism in the Sila Massif was estimated at ~5 km-depth, contextual to crustal thinning and lower crust exhumation in a general transtensional regime (Festa et al., 2010).

According to Santantonio et al. (2016) and Innamorati and Santantonio (2018), Sinemurian–Toarcian tectonics controlled the architecture of the Mesozoic cover, i.e., the Longobucco cover of Vignaroli et al. (2012), deposited in syn-rift environments ranging from fluvial to deep marine, and unconformably resting above the late Variscan basement in the eastern Sila Massif (**Figure 3c**). The siliciclastic and carbonate succession consisting of: red beds (latest Rhaetian?–earliest Hettangian), mixed siliciclastic/carbonate shelf deposits (Hettangian p.p.–lower Sinemurian) and marls with siliciclastic turbidites (Sinemurian p.p.–Toarcian p.p.) (Santantonio et al., 2016). Neptunian dikes of Jurassic sediments penetrating granitoids and phyllites of the bedrock are important evidence of this tectonic evolution, related to the opening of the Neotethys.

The illite crystallinity index, the illitization of kaolinite, and the occurrence of illite layers in illite/smectite mixed ones indicate lithostatic/tectonic loading at depths of at least 4–6 km, at temperatures in the range of 100–160 °C (Perri et al., 2008). In the same area of the Sila Massif, Vignaroli et al. (2012) concluded that the basement rocks, and the Longobucco cover underwent 18–13 Ma crustal shortening, with top-to-the-east kinematics of the thrusts, and exhumation. In this respect, apatite fission-track thermochronology technique were applied to reveal the time and the rates of denudation of the basement, as well as the thermal history of the rocks with cooling across the mean closure temperature of 110 ± 10 °C (Vignaroli et al., 2012).

Figure 3 (previous page). Geological map of the Sila Massif. (a) Sketch map showing the distribution of basement rocks exposed in Southern Italy (modified after Festa et al., 2004). (b) Sketch map of the lower, middle, and upper late-Variscan continental crust exposed in Calabria (modified after Dubois et al., 1971). (c) Geological sketch-map of the Sila Massif area with numbered location of the pertaining mineralization occurrences (modified after Festa et al., 2006; Vignaroli et al., 2012; Cirrincione et al., 2015; Fornelli et al., 2020). 1 – Ophiolite units (e.g., Gimigliano and Diamante-Terranova units). 2 – Fiume Pomo Unit (former Bagni-Fondachelli Unit; dominant phyllites). 3 – Castagna Unit (dominant augen gneisses). Sila-Serre Unit: 4 – former Monte Gariglione and Polia-Copanello units (granulites, gneisses, paragneisses, migmatites); 5, 6, 7a-c – Sila and Serre batholiths (i.e., 5 – norite-diorite; 6 – tonalites; 7a – granodiorite; 7b – Bt-Ms cordierite bearing granodiorite-monzogranite; 7c – Bt-Ms And-Sil-Crd bearing granodiorite-monzogranite, Bt-Ms Sil-And-Crd leucogranite, and small fine-grained granite); 8a – Mandatoriccio/Mammola Unit (dominant schists); 8b – Contact aureole (spotted schists and fels at the expense of the Mandatoriccio/Mammola Unit schists); 9a – Bocchigliero/Stilo-Pazzano Unit (dominant phyllites); 9b – Contact aureole (spotted schists and fels at the expense of the Bocchigliero/Stilo-Pazzano Unit phyllites). 10 – Longobucco/Stilo cover (dominant carbonates). Main Alpine thrust at the base of the: 11 – Sila-Serre Unit; 12 – Castagna Unit; 13 – Fiume Pomo Unit. 14 – Minor Alpine thrust and faults. 15 – Hercynian shear zone. 16 – Lithostratigraphic contact. Numbers 1–13 in the white circles are referred to literature/historical mineralized sites (see Fregola et al., 2023): 1 – Torrente Grammisate; 2 – Santuario del Patire; 3 – Cerasaro-Cozzo Chinico; 4 – Cozzo del Pesco; 5 – Bonia-Fonte Argentila; 6 – Defesella del Trionto; 7 – Reghinella-Macchiafarna; 8 – Torrente La Manna; 9 – Serra Toppale; 10 – Savelli; 11 – Vallone San Lorenzo; 12 – San Giovanni in Fiore; 13 – Cerenzia-Caccuri.

3.2. Basement geochemistry of the Longobucco area

The crystalline basement outcropping in the Longobucco area is characterized by the presence of the Sila Batholith granitoids (Rottura et al., 1990; Caggianelli et al., 2000) and the phyllites of the Bocchigliero Unit, metamorphosed to hornfels in the contact metamorphic aureole (Acquafredda et al., 1994). The granitoids are predominantly composed of granodiorites, with some peraluminous leucogranites (Rottura et al., 1990, 1991; Messina et al., 1991; Acquafredda et al., 1994; Prosser and Caggianelli, 2003), expression of late Variscan (S-type and K-type) and Permian magmatism (A-type) common in the European Variscan Belts (Finger et al., 1997; Wilson et al. 2004). The average SiO_2 content of the granodiorites is 68.92 wt.%, while that of the leucogranites increases up to 73.42 wt.% (Messina et al., 1991; Ayuso et al., 1994). The major and minor element contents in the granodiorites, such as Na_2O (avg. 3.22 wt.%), MgO (avg. 0.97 wt.%), Fe_2O_3 (avg. 3.30 wt.%), K_2O (avg. 3.86 wt.%), and CaO (avg. 1.50 wt.%), are consistent with felsic bodies from other parts of the batholith, and the leucogranites do not deviate significantly from this trend (Messina et al., 1991; Ayuso et al., 1994; Prosser and Caggianelli, 2003). The X-ray fluorescence (XRF) analyses of trace elements in the Longobucco granodiorite show relatively low concentrations of Co (avg. 6.2 ppm), Ni (avg. <15.0 ppm)[2], Cu (avg. <10.0 ppm), Zn (avg. 77.0 ppm), Ga (avg. 19.0 ppm), Ge (avg. 1.4 ppm), As (avg. <5.0 ppm), Ag (avg. <0.5 ppm), In (avg. <0.1 ppm), and Pb (avg. 17.0 ppm), with leucogranites exhibiting even lower values. Only two granodiorite samples show higher Zn-content, ranging from 238 to 265 ppm (Ayuso et al., 1994; Prosser and Caggianelli, 2003). Furthermore, in the late Carboniferous-middle Permian dikes studied by Festa et al. (2010) the Zn content of the magma bodies was not detected. In comparison, phyllites show slightly higher trace element contents of Co (avg. 15.0 ppm), Ni (avg. 35.0 ppm), and Cu (avg. 25.0 ppm), while the concentrations of Zn (avg. 78.0 ppm), Ga (avg. 23.0 ppm), Ge (avg. 1.6 ppm), As (avg. <5.0 ppm), Ag (avg. <0.5 ppm), In (avg. <0.1 ppm), and Pb (avg. 10.0 ppm) are similar to those found in the granitoids (Ayuso et al., 1994; Prosser and Caggianelli, 2003).

[2] values below detection limit are indicate with "<(value)".

4. Fluid Inclusions (FIs)

4.1. FIs in MVT and SHMS ore-deposits

The formation of mineral deposits commonly requires the presence of fluids capable of transporting and depositing metals, and the physical and chemical characteristics of these fluids can vary significantly (Bodnar et al., 2014). Data obtained from the study of fluid inclusions (FIs) have likely contributed more than any other tool to the understanding of the processes involved in the formation of hydrothermal deposits (Roedder, 1967, 1968, 1984). Fluids trapped in microscopic cavities within the host mineral represent a valuable archive of the prevailing physical and chemical conditions occurring during (as well as after) mineral formation, and consequently, of the mineralizing fluids. Fluid inclusions can be primary, if trapped during the crystal growth, or secondary, if trapped later during the healing of fractures formed after the end of crystal growth. Fluid inclusions in many hydrothermal deposits are mainly studied through petrographic microscopes and heating/cooling stages, i.e. through microthermometry (Goldstein and Reynolds, 1994; Roedder, 1984). Microthermometry allows for the measurement of temperatures, such as homogenization temperature (T_h) and ice melting temperature (T_{mi}), providing direct estimates of the minimum values of mineral formation temperatures, as well as of fluid salinities and composition (Roedder and Bodnar, 1980; Roedder, 1984). Although a wide range of methodologies is applied in mineral exploration, results from FIs studies have enabled precise delineation of the temperature and salinity conditions that characterize the formation environment of various types of hydrothermal mineral deposits, among wich MVT and SHMS deposits, whose fluid characteristics are summarized below.

The MVT deposits, characterized by minerals such as sphalerite, galena, and calcite, form in carbonate rocks, typically at low temperatures (Leach et al., 2005). Fluid inclusions in MVT deposits provide T_h data ranging from approximately 75 to 200°C, with salinities of 10–30 wt.% NaCl eq.; such values are similar to those of brines found in modern sedimentary basins (Collins, 1975; Leach et al., 2005). Most fluid inclusions in MVT deposits show high concentrations of Ca and Na (Haynes and Kesler, 1987). In addition to providing information on chemical composition, fluid inclusions also offer insights into the ore formation mechanism. For instance, studies have shown that the mixing of different fluids is a key process in the precipitation of ore minerals in many MVT deposits (Haynes and Kesler, 1987; Leach et al., 1996). Fluid inclusions in these deposits have also been used to estimate the concentrations of metals in the mineralizing fluids, with zinc concentrations up to 575 ppm and lead up to 111 ppm (Carpenter et al., 1974).

In contrast, the SHMS deposits are characterized by stratabound accumulations of Pb and Zn sulfides hosted in fine-grained or clastic sedimentary rocks, where, as with MVT deposits, the hydrothermal fluids show no magmatic contribution (Goodfellow et al., 1993; Leach et al., 2005). Studies of fluid inclusions in SHMS deposits have revealed T_h values ranging from 157 to 335°C and variable salinities of 2.6–18 wt.% NaCl eq. (Gardner and Hutcheon, 1985; Ansdell et al., 1989; Rajabi et al., 2024).

4.2. Previous studies on FIs from the Sila Massif

Previous studies on fluid inclusions in the Sila Massif area were conducted by De Vivo et al. (1991) and Benvenuti et al. (1994), focusing on magmatic quartz from the Variscan batholith and quartz associated with Au-Ag-Bi mineralizations in the Rossano area, respectively. Both works highlight the challenges and limited number of analyzable inclusions, due to their small size (less than 15 μm).

The fluid inclusions in magmatic quartz of the Sila Massif (De Vivo et al., 1991) are mainly liquid-rich two-phase inclusions, with highly variable salinity, and later monophase (liquid) inclusions with low salinity. The T_h range from 50 to 416 °C, while salinities vary from 0 to ~26 wt.% NaCl eq.. The initial melting temperature ranges from -30 to -65 °C; where the values below -50 °C are indicative the presence of Ca^{2+}, Zn^{2+}, and/or Fe^{2+}-bearing fluids (Mylius and Dietz, 1965; Crawford, 1981). This wide range of T_h and salinity values would partly correspond to fluids related to the Variscan magmatic cycle ($T_h > 200$ °C and ~26 wt.% NaCl eq.), whereas the remaining values were attributed to later, more "dynamic" stages in response to the mixing of different fluids, though their precise dating was not possible (De Vivo et al., 1991).

Fluid inclusions studied in quartz from some mineralized veins in the Rossano area (Benvenuti et al., 1994), are primary liquid-rich two-phase inclusions, with T_h values ranging from 135 to 185 °C and T_{mi} values between -4.3 and -4.6 °C, corresponding to salinities of 6.8–7.3 wt.% NaCl eq. However, in many inclusions, metastable ice melting was observed, making salinity estimation difficult (Benvenuti et al., 1994). The association of quartz with arsenopyrite containing Au-Ag would suggest a hydrothermal-epithermal environment for the system, similar to some mineralization found in the French Massif Central (Boiron et al., 1990; Cathelineau et al., 1991).

5. Methods

5.1. Optical Microscopy

A ZEISS Axioscope 5 POL microscope, operating under transmitted and reflected light and equipped with five magnification objective lenses (2.5x, 5x, 10x, 20x, 50x), was used to study thin and thick section samples. The micrographs were carried out with the software AxioCam ERc 5s digital camera on minerals, textures and fluid inclusions.

5.2. Scanning Electron Microscopy (SEM)

A SEM EVO-50 XVP (LEO) (Zeiss, Oberkochen, Germany), equipped with an AZTEC (Oxford Instruments, Abingdon, UK) integrated energy dispersive X-ray Spectroscopy (EDS) microanalysis system with X-Max (80 mm^2) energy dispersive (ED) Silicon drift Oxford detector, equipped with a Super Atmosphere Thin Window ©, was used for preliminary chemical analysis and to acquire Backscattered Electron (BSE), and Variable Pressure Scanning Electron (VPSE) images. Analyses were performed on polished thin sections (samples LGB04b,h, LGB06a-b, FA04, FA11d,f, FA14a, FA17a) of mineralized rocks, covered by carbon coating. Semi-quantitative analyses were obtained using the following operating conditions: 15 kV accelerating potential, 500 pA probe current, about 20 kcps as output count rate on the whole spectrum, counting time 50 s and 8 - 9.5 mm working distance.

5.3. Electron Probe Microanalysis (EPMA)

Major and minor element analyses on sphalerite, galena, chalcopyrite, pyrite, quartz, calcite and REE-F-carbonate, were carried out through EPMA at the CNR IGG of Firenze using a JEOL JXA 8600 microprobe equipped with five wavelength dispersive spectrometers (WDS), each coupled to a different gas-flow proportional counters. An energy-dispersive (EDS) solid-state detector (SDD) has allowed instantaneous acquisition of the emission spectrum and rapid identification of the elements present in the sample. Before the analysis, the samples were uniformly carbon-coated. Analytical conditions include 20 kV accelerating voltage for sulfides and silicates, and 15kV accelerating voltage for carbonates, 20 nA beam current and 30 µm spot size. In total 25 elements

were measured: S, Zn, Ge, Fe, Cu, Cd, Hg, Co, Mn, Pb, Sn, Si, Al, Ca, K, Na, P, Ce, La, Y, Nd, Pm, Sm, Gd, Dy. The heavy REE (Ho, Tm, Er, Yb, Lu) have been excluded due to their low concentration and spectral interference between X-ray emission lines. Calibration was carried out using certified natural and synthetic standard, such as: sphalerite Astimex 42, marcasite Astimex 30, galena Astimex 24 (for sulphides), monazite Astimex 32 (for REE-rich phases), almandine garnet Astimex 2 (for quartz) and calcite Astimex 11 (for carbonates).

5.4. *μ*-Raman Spectroscopy

Unpolarised Raman spectra were collected using a Labram *μ*-Raman spectrometer by Horiba, equipped with an Olympus BX40 confocal microscope, and a Peltier cooled (~200 K) 1024×256 pixels CCD detector. Raman scattering was excited by a He–Ne laser at 633 nm (nominal output power 18 mW).

Raman spectra were collected from sphalerite samples of LGB (LGB04b, LGB04h, LGB06b) and FAR (FA17a) mineralization. Raman spectra have been acquired partly on EPMA spots (avg. of 3-4 spots or specific spots) on 33 *μ*m-thin section and partly on selected fragments from crushed 150 *μ*m-thick sections, with an average composition obtained using three close EPMA spots. The spectral range chosen has been of 50–800 cm^{-1}, with an acquisition time of 3 runs × 60 s, grating 600 gr/mm per each spectral window. A peak fitting procedure has been carried out in the region between 250 and 400 cm^{-1}, after applying a baseline correction, using GRAMS software. The peak fitting procedure has been carried out using pseudo-Voigt function.

Moreover, Raman spectra have been collected on synchysite crystals (thin section, LGB04h) in the range of 50–1400 cm-1, with an acquisition time of 3 runs x 60 s, filter 25%, grating 600 gr/mm per each spectral window. The RRUFF database has been used for the comparison with literature data.

5.5. Powder X-ray diffraction (PXRD)

Two samples of sphalerite (one light- coloured and one dark- coloured sphalerite) have been selected to be investigated by X-ray powder diffraction (XRPD) using a PANalytical Empyrean diffractometer equipped with Cu-Kα radiation (λ=1.5418 Å) and a Real Time Multiple Strip (RTMS) PIXcel3D detector. Analytical conditions were: 40 kV and 40 mA, a scanning step of 0.026 °/s and 2θ range from 20 to 90°. This range covers all the main diffraction peaks of the sphalerite phase.

Instrumental aberrations caused by the parafocusing Bragg-Brentano geometry were diminished by using a 0.125° divergence slit, a 0.25° anti scattering slit, 0.02 rad Soller slits in the incident beam pathway and a 0.02 rad Soller slits and an anti scatter blade (7.5 mm) in the diffracted beam pathway. A Ni filter was mounted in front of the detector to drastically reduce the Kβ radiation. With the same analytical conditions four thin sections have been investigated (two of light, LGB06a-LGB06b, and two of dark, LGB04b-LGB04h, sphalerite). Small regions of the thin sections have been selected using masks (2 or 5 mm) on the incident beam. X-ray diffraction patterns were analyzed by comparing our data with crystallographic data present in the Highscore software.

5.6. Single crystal X-ray diffraction (SCXRD)

A Bruker AXS X8 APEX II automated diffractometer (Bruker 2003), equipped with graphite-monochromatized MoKα X-radiation and a CCD detector has been used. Eleven sphalerite crystal fragments were selected and analysed according to the colour zoning. The intensity data were accurately recorded by a combination of several ω and φ rotation sets with 0.5° scan width. The package SAINT-IRIX (Bruker 2001) was used for data reduction, including intensity integration; the data were corrected for Lorentz, polarization, absorption, background effects and scale variation. The final unit-cell parameters were obtained from the xyz centroids of the measured reflections after integration.

5.7. Laser Ablation-Inductively Coupled Plasma-Mass Spectrometry (LA-ICP-MS)

For sphalerite and chalcopyrite analyses, four polished thick sections from two samples of LGB and two samples of FAR mineralization were selected to be analyzed by LA-ICP-MS. A total of 89 and 16 spot analysis were obtained from sphalerite and chalcopyrite, respectively. Trace element concentrations were measured using a PerkinElmer ELAN DRC-e ICP mass spectrometer combined with a New Wave UP193-FX excimer laser ablation system at the Geological Institute, Bulgarian Academy of Sciences (Sofia, Bulgaria). The ablation was conducted in He medium. In order to maximize sensitivity, the ICP-MS was optimized daily with respect to the oxide production rate of ThO/Th (0.5%). Operating conditions of the laser system include: 6 Hz repletion rate; 35 μm spot size; the homogeneous energy density on sample was 5.8-6.0 l/cm^2 (at 35 μm pit). The nebulizer gas flow rate was 0.76 l/min, whereas auxiliary and make-up gas flows rates were 0.90 and 0.92

l/min. The RF-power was 1500 kV. The analysis time was 120 s (background: 60 s, laser on the sample: 60 s). The acquisition dwell time was set to 20 ms for ^{71}Ga, ^{74}Ge, ^{107}Ag, ^{115}In, ^{118}Sn, ^{185}Re, ^{202}Hg, to 30 ms for ^{197}Au, and to 10 ms for all other elements. The monitored isotopes include: ^{27}Al, ^{34}S, ^{49}Ti, ^{51}V, ^{53}Cr, ^{55}Mn, ^{57}Fe, ^{59}Co, ^{60}Ni, ^{65}Cu, ^{66}Zn, ^{71}Ga, ^{74}Ge, ^{75}As, ^{82}Se, ^{85}Rb, ^{95}Mo, ^{107}Ag, ^{111}Cd, ^{115}In, ^{118}Sn, ^{121}Sb, ^{125}Te, ^{181}Ta, ^{182}W, ^{185}Re, ^{197}Au, ^{202}Hg, ^{203}Tl, ^{208}Pb, ^{209}Bi. Repeated external standardization was conducted by analyzing NIST SRM 610 (glass) and USGS Mass 1 (sulfide) standard. Data reduction was performed by Sills Software (Guillong et al. 2008) using the Zn for sphalerite and Fe for chalcopyrite measured by EPMA. All data below the detection limit were not considered.

For quartz, calcite and fluorite analyses, two polished thick sections from LGB and FAR have been selected to be analyzed at Dipartimento di Scienze, Roma Tre University LA-ICP-MS laboratory using a Teledyne Photon Machine Analyte Excite + ArF (193 nm) excimer laser ablation system coupled to a Thermo-Scientific iCAP RQ (Single Quad). A total of 41, 24 and 15 spots analysis were carried out on quartz, calcite and fluorite, respectively. All analyses were performed at low oxide production rates (232Th.16O/232Th <0.5%). Helium carrier gas stream of ~0.5 and 0.3 l/min are set for the cell and the cup, respectively. A laser spot size of ~85 µm (for standards and unknown samples), with an 8 Hz pulse repetition rate and an energy density of 5-6 J/cm2 was used. The ablation time was set at 60 seconds comprises a background acquisition lasting 15 seconds, succeeded by a sample ablation period of 25 seconds, followed by a 20 second washout phase. The measured masses for fluorite include ^{29}Si, ^{44}Ca, ^{42}Ca, ^{89}Y, ^{93}Nb, ^{139}La, ^{140}Ce, ^{141}Pr, ^{146}Nd, ^{147}Sm, ^{153}Eu, ^{157}Gd, ^{159}Tb, ^{163}Dy, ^{165}Ho, ^{166}Er, ^{159}Tm, ^{172}Yb, ^{175}Lu, ^{181}Ta, ^{238}U. Additional masses including ^{24}Mg, ^{55}Mn, ^{56}Fe, ^{88}Sr, ^{137}Ba, ^{232}Th, ^{178}Hf were measured for calcite. For quartz ^{7}Li, ^{23}Na, ^{24}Mg, ^{27}Al, ^{29}Si, ^{39}K, ^{44}Ca, ^{48}Ti, ^{52}Cr, ^{57}Fe, ^{73}Ge, ^{89}Y, ^{139}La, ^{141}Pr, ^{146}Nd, ^{147}Sm, ^{153}Eu, ^{157}Gd, ^{159}Tb, ^{163}Dy, ^{165}Ho, ^{166}Er, ^{159}Tm, ^{172}Yb, ^{175}Lu, ^{238}U.

Ca and Si are measured for monitoring any possible changes in the matrix of the mineral as well as drift corrections during the measurement. The dwell times are 2-5 ms for the first five masses and 10-15 ms for the rest. Synthetic glass NIST-SRM-612 reference (Jochum et al., 2011) material were used to bracket analyses of unknowns, while NIST-SRM 610 was used for quality control. As for elemental calibration the Iolite software version 4.8.6 (Paton et al., 2011) was used for data reduction and calibrations. both background subtraction and drift corrections are made using a weighted linear factor determined from repeat analysis. The stoichiometric SiO_2 content (99.9 wt.%) of quartz and measured Ca content in calcite and fluorite were used as the internal standard for LA-ICP-MS calibration. All data below the detection limit were not considered

5.8. Fluid Inclusion analyses

Fluid inclusions are small droplets of fluids entrapped within cavities in minerals during crystal growth (P – primary inclusions), or healing fractures formed during (PS - pseudo secondary) or after the end (S – secondary) of crystal growth. They are a powerful tool to get direct information on fluids circulating during or after the mineral formation. A key concept for correctly interpreting fluid inclusion analyses is that of Fluid Inclusion Assemblages (FIAs), introduced by Goldstein & Reynolds (1994). FIAs are groups of inclusions entrapped approximately at the same time during the same geological event, sharing similar textures and physico-chemical characteristics. They are considered representative of a specific genetic event. The application of the FIA concept is of paramount importance to properly reconstruct the sequence of primary and post-trapping events related to the ore forming process. It is essential also for understanding the evolutionary history of fluids in a geologic system, and identifying the occurrence of a mixing process between fluids of different source and composition (Roedder, 1984; Bodnar, 1993).

5.8.1. Petrography of fluid inclusions

A first step in the fluid inclusion studies is given by textural analyses performed on double-polished thick-sections (80-150 μm) using a polarizing optical microscope, to identify the FIs type, their distribution within the crystal and the FIAs to be analyzed by microthermometry. The petrography of fluid inclusions represents a fundamental preliminary study to understand the relationships between different generations of fluid inclusions, connected to various genetic events that affected the crystal from its growth to late-stage processes. Based on the phase relationships at room temperature, fluid inclusions can be classified into: (i) monophase liquid (L) or vapor (V); (ii) biphase liquid-rich (L+V) or vapor-rich (V+L); (iii) multiphase solid (S+L±V), with S < 50%, and multisolid, with S > 50%; (iv) immiscible liquid (L1+L2±V) (Shepherd et al., 1985).

Textural analyses allow the paragenetic classifications of fluid inclusions into: (i) primary (P), trapped during the crystal's growth; (ii) secondary (S), formed later along fractures; (iii) pseudo-secondary (PS), formed along planes or fractures before the end of crystal growth (Roedder, 1984; Shepherd et al., 1985). Fluid inclusions may show crystal-negative shapes (following the crystal symmetry), rounded, irregular or distorted forms, which may indicate deformation or dissolution processes (Bodnar, 1993). After trapping, fluid inclusions may re-equilibrate and undergo a series of processes that may alter their shape, volume, and internal composition (e.g., decrepitation or necking down) (Shepherd et al., 1985; Bodnar, 1993; Goldstein & Reynolds, 1994; Vityk & Bodnar, 1995).

5.8.2. Microthermometry

This analytical method allows to measure the temperature of phase transitions within fluid inclusions, to gain direct information on the physico-chemical conditions (P-T-X) at the time the fluid was trapped. This information is essential for understanding processes such as the formation of mineral deposits or the evolution of hydrothermal systems (Roedder, 1984; Bodnar, 1993; Goldstein & Reynolds, 1994). The homogenization temperatures (T_h°C), and the final melting temperatures of ice (T_{mi}°C) were measured during heating-freezing cycles. Then salinity of the trapped fluids was derived by applying the formula by Bodnar & Vityk (1994).

For this purpose, double polished thick sections (150 μm) were prepared from two samples (FA11 and FA14), for the study of fluid inclusions in fluorite (FA11-Flr-E; FA14-Flr-E; FA14-Flr-F) and quartz (FA14-qz2).

Microthermometry analyses were performed at University of Bari using a Linkam THMSG600 heating-freezing stage (+600 / -196 °C) connected to a Linkam T95-STD temperature controller and mounted on an Olympus BX53P polarizing optical microscope. The latter is equipped with four magnifications (5x, 20x, 50x, 100x) long-working distance objective lenses, a long-working distance condenser lens and a QICAM Fast 1394 QImaging digital camera, connected to a computer for real-time observation and measurement of temperatures through the Linksys32 temperature control software and L320P-DV-NC image capture software. A Linkam standard cooling unit operating with liquid nitrogen-controlled flow and including a liquid nitrogen pump was used to cool the samples. The heating–freezing stage was calibrated using pure H_2O with critical density and mixed H_2O–CO_2 (25 mol% CO_2) synthetic fluid inclusions. Accuracy of measurements was ±0.2°C during freezing and ±0.5°C during heating experiments.

6. Results

6.1. Field observation on LGB and FAR areas

In both sampled localities of LGB and FAR the Carboniferous granodiorite belonging to the Sila batholith (**Figure 4a, b**) is affected by fault zones, which include brittle deformed porphyric sheeted dikes (**Figure 4d-f**). The minor faults composing the network of brittle structures associated to the fault zones are commonly striated, with lineation plunge/dip of 015°/15° at LGB (**Figure 4g**), and of 190°/15° at FAR (**Figure 4h**). The detailed geological mapping revealed the sub-parallelism between the main faults and the porphyric dikes, with general dip-direction/dip of 100/40 and 130/35 in the LGB and FAR, respectively (**Figure 4e, f**). In both localities, the related porphyric dikes tend to arrange along the bottom boundary of the fault zone (**Figure 4c-f**). A thickness up to ~3 m, within a ~6 m-thick fault zone, is reached by the porphyric dike at LGB (**Figure 4e**), whereas a thickness up to ~25 m, within a ~40 m-thick fault zone, is shown by the porphyric dike at FAR (**Figure 4f**). Striated steps observed on minor faults surfaces indicate left- and right-transtensive (dominated by transcurrence) kinematics for the LGB and FAR fault zones, respectively (**Figure 4e-h**). As regards LGB, cm-thick and m-long mineralized veins geometrically follow the upper margin of the fault zone (**Figure 4c, e**), whereas less developed in size veins are scattered within the FAR fault zone (**Figure 4d, f**). As shown in **Figure 4i** and **j**, the mineralized veins are brittle deformed, with the veins in LGB more preserved (**Figure 4i**) than those in FAR, the latter having become fault breccia (**Figure 4j**).

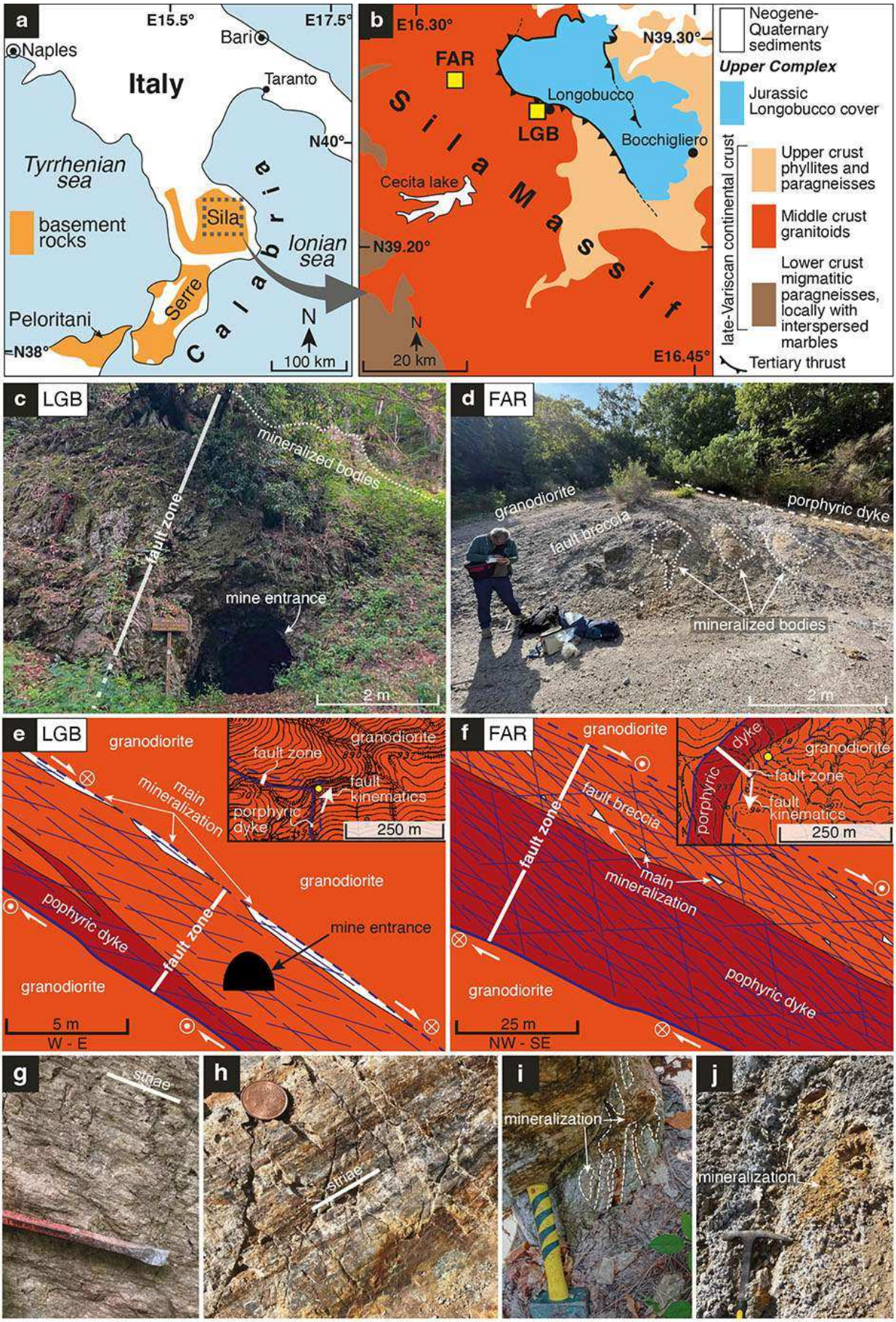
a
E15.5°
E17.5°
Naples
Bari
Italy
Taranto
N40°
Tyrrhenian sea
basement rocks
Sila
Calabrian
Ionian sea
Serre
Peloritani
N38°
N
100 km
b
E16.30°
N39.30°
FAR
Longobucco
LGB
Bocchigliero
Sila Massif
Cecita lake
N39.20°
N
20 km
E16.45°
Neogene-Quaternary sediments
Upper Complex
Jurassic Longobucco cover
late-Variscan continental crust
Upper crust phyllites and paragneisses
Middle crust granitoids
Lower crust migmatitic paragneisses, locally with interspersed marbles
Tertiary thrust
c LGB
mineralized bodies
fault zone
mine entrance
2 m
d FAR
granodiorite
porphyric dyke
fault breccia
mineralized bodies
2 m
e LGB
granodiorite
fault zone
granodiorite
fault kinematics
porphyric dyke
250 m
main mineralization
granodiorite
porphyric dyke
fault zone
mine entrance
granodiorite
5 m
W - E
f FAR
granodiorite
dyke
granodiorite
porphyric
fault zone
fault kinematics
250 m
fault breccia
fault zone
main mineralization
granodiorite
porphyric dyke
25 m
NW - SE
g
striae
h
striae
i
mineralization
j
mineralization

6.2. Sample texture

Mineralized bodies in the LGB and FAR areas consist mainly of sphalerite and galena with variable modal abundances of minor sulphides and gangue minerals (**Figure 5a-i**). At LGB, sphalerite and minor galena are accompanied by quartz and calcite (**Figure 5a-d**). At FAR, instead, the mineralization comprises mainly galena, sphalerite, and chalcopyrite, with gangue quartz and fluorite, and sporadic calcite (**Figure 5e-i**). Although the mineralization develops along fault zones at both sites, at LGB it apparently forms vein-type structures, with lenticular or massive textures of the mineralization (**Figure 5a-d**). On the other hand, at FAR the ore body is strongly brecciated within the damage zone and the reconstruction of the original texture of the mineralization is largely impeded (**Figure 5e-i**), with late cm-thick quartz veins unaffected by brittle deformation (**Figure 5e**). Generally, the host rock is slightly affected by chloritic-sericitic alteration in both sites, which occurs localized next to the mineralized veins (**Figure 5a-c, h**).

Figure 4 (previous page). Sketch map and figures of sampling areas. (a) Sketch map showing the distribution of basement rocks exposed in Southern Italy (modified after Festa et al., 2004). **(b)** Sketch map of a portion of the Sila Massif. **(c)** Areal view of the mine site and outcrop of Longobucco (LGB). **(d)** Areal view (wide angle photo) of the outcrop of Fonte Argentila (FAR). **(e)** Geological sketch map, as inset, and 2D geological sketch model around the mine site in the LGB territory (mine entrance geographic coordinates: 39°26'30.90"N, 16°36'3.19"E); note the fault zone including the porphyritic dike along the bottom margin. **(f)** Geological sketch map, as inset, and 2D geological sketch model around the FAR locality (geographic coordinates of the placeholder in the map: 39°31'27.26"N, 16°31'9.13"E); note the fault zone including the porphyritic dike along the bottom margin. **(g)** Striated fault surface associated to the fault zone outlined in Figure 4e. **(h)** Striated fault surface associated to the fault zone outlined in Figure 4f. **(i)** Brittle deformed mineralized vein in the fault zone outlined in Figure 4e. **(j)** Tectonically brecciated mineralized vein in the fault zone outlined in Figure 4f.

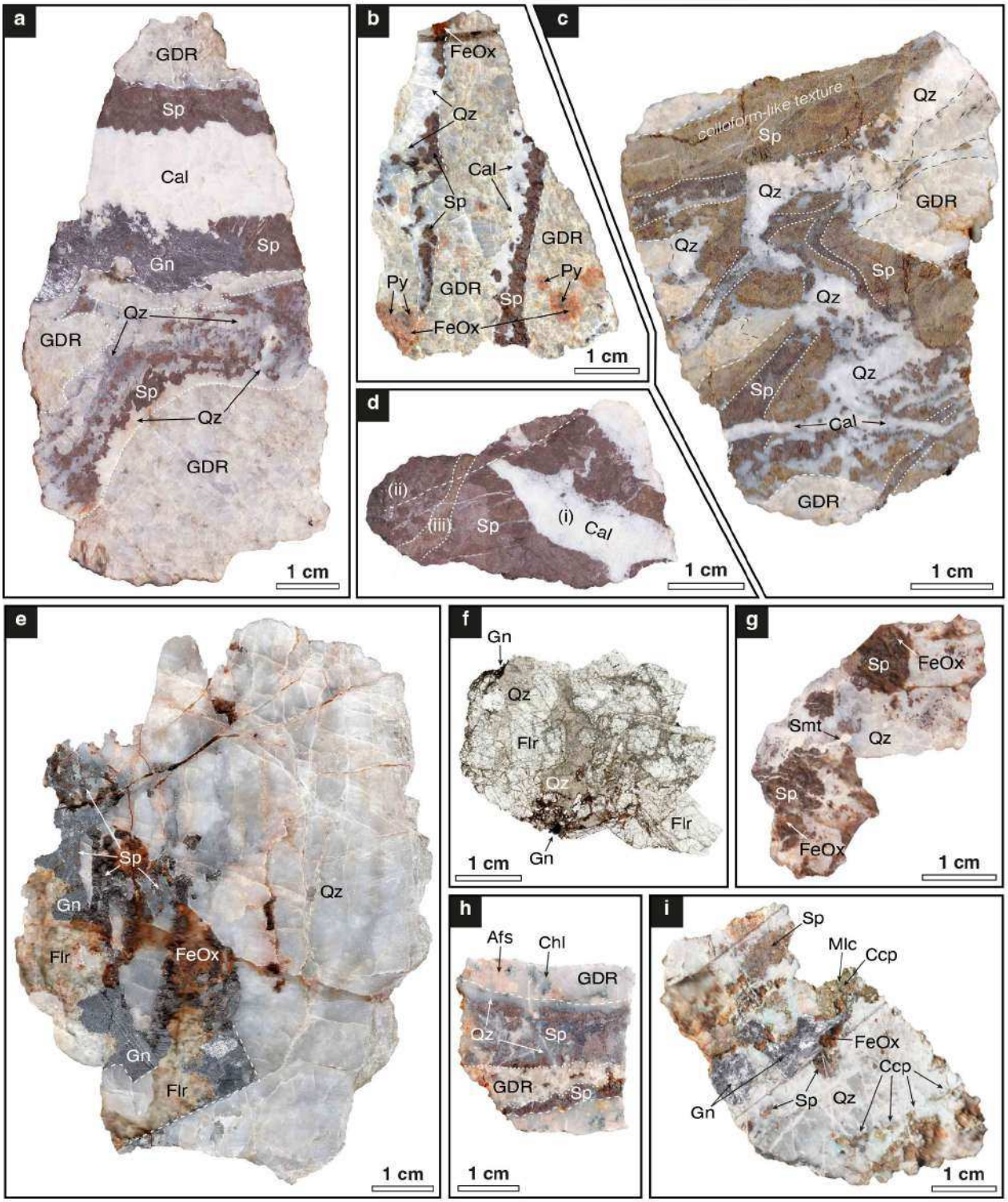
a
GDR
Sp
Cal
Sp
Gn
Qz
GDR
Sp
Qz
GDR
1 cm
b
FeOx
Qz
Cal
Sp
GDR
Py
Py
GDR
Sp
FeOx
1 cm
c
colloform-like texture
Qz
Sp
Qz
GDR
Qz
Sp
Qz
Qz
Sp
Cal
GDR
1 cm
d
(ii)
(iii)
Sp
(i)
Cal
1 cm
e
Sp
Qz
Gn
Flr
FeOx
Gn
Flr
1 cm
f
Gn
Qz
Flr
Qz
Flr
Gn
1 cm
g
Sp
FeOx
Smt
Qz
Sp
FeOx
1 cm
h
Afs
Chl
GDR
Qz
Sp
GDR
Sp
1 cm
i
Sp
Mlc
Ccp
FeOx
Ccp
Gn
Sp
Qz
1 cm

6.3. Ore- and gangue minerals microstructural relationships

The mineralization consist of Sp-Gn(±Py)–Qz-Cal for LGB (**Figure 6a-i**), and Sp-Gn-Ccp(±Py)–Qz-Flr(-Cal) for FAR (**Figure 6j-r**). A schematic representation of the paragenetic sequence for the whole LGB-FAR mineralization is shown in **Figure 7**. Sphalerite is the main ore-mineral in both areas. It occurs in large euhedral to anhedral crystals (0.5–2 cm), showing a distinct colour zoning (**Figure 6a, b, j**). The rhythmic colour bands have thickness from less than 1 μm- to over 1 mm and sometimes follow the crystal's growth directions (**Figure 6b, j**). They span from colourless to reddish and dark brown, passing through yellow–brown colours (**Figure 6a–c, f, g, j, k, o**). A curious aspect, is the presence of optical anomalies (anisotropies) exhibited by sphalerite in the form of lamellae or lenses (**Figure 8a-c**) with birefringence values between 0.002 and 0.008, as previously described by Seal et al. (1985). Three sphalerite growth stages (Sp1-Sp2-Sp3) have been discriminated, each associated to a set of colours. The first-generation sphalerite (Sp1) is subhedral and in some cases shows seemingly colloform texture (**Figure 5c**) and coalescence of several grains into irregular crystal aggregates (**Figure 6a**). The formation of these textures might indicate a relatively high nucleation rate in a relatively supersaturated fluid (Roedder, 1968). The Sp1 is characterized by light colour, ranging from light-yellow to brown (**Figure 6a, j**). The Sp2 has darker colour, ranging from brown to dark-brown, and is subhedral to euhedral, in some cases showing clear tetrahedral crystal habit (**Figure 6**b). Generally, overgrowths of Sp2 are observed along fractures or at the rim of Sp1 (**Figure 6a, b, e**; **Figure 9c-d**), as well as in veins affecting the host granodiorite, associated to Qz1-Cal1 (**Figure 6e, k**).

Figure 5 (previous page). Scan slices of samples collected from the Longobucco (a-d) and Fonte Argentila (e-i) mineralization. **(a)** (sample LGB04h) Sp veins in altered granodiorite. Two associated veins are observable: the larger vein to the top of the sample exhibits massive Sp affected by successive fracturing with Cal precipitation, with Gn that either completely replaces Sp or partially replaces Cal; the smaller vein in the lower part of the sample consists of fine-grained Sp associated with Qz. **(b)** (sample LGB04b) Sub-parallel veins (0.5 cm-thick) made up of Sp, Cal, and Qz in altered granodiorite; the reddish alteration halos are hydroxides around magmatic Py in the granodiorite. **(c)** (sample LGB06b) Superimposed veining events affecting granodiorite. Two sets of veins associated to a first generation of light coloured, apparently colloform Sp1 and a second generation of darker, euhedral Sp2 (highlighted with dashed white lines). A Qz vein crosscutting the two Sp generations is shown, hosting dissolved Sp grains. A late Cal vein crosscut all the previous veins generations in the lower part of the sample. **(d)** (sample LGB04i) Portion of massive Sp crosscut by Cal veins; various stages of superimposed brittle events can be observed: (i) Cal precipitating along fractures affecting massive Sp; (ii) micro-faulting; (iii) micro-brecciation of Sp. **(e)** (sample FA11f) Qz vein with a portion rich in Flr partially replaced by Gn; remnants of Sp overgrown by Gn can still be recognized. **(f)** (sample FA14a) Thick section (150 μm) scan of a vein with greenish Flr; the Flr crystals are fractured and corroded by pervasive Qz; Gn can be also observed. **(g)** (sample FA17a) Portion of a Qz-rich vein with fractured Sp clasts, partially replace by Fe-oxide-hydroxide; late Cal and Smt can be also observed. **(h)** (sample FA11d) Massive Sp veins (0.3–1 cm-thick) in slightly altered granodiorite showing pinkish Afs and completely chloritized Bt; granodiorite between the veins shows a whitish alteration facies. **(i)** (sample FA04) Portion of polymetallic vein with Sp, Gn, and Ccp in a Qz gangue, affected by several fractures; different mineralized sub-parallel layers can be also observed; Mlc formed by alteration of Ccp. Legend: Afs, alkali feldspar; Cal, calcite; Ccp, chalcopyrite; Chl, chlorite; FeOx, Fe-oxide-hydroxide; Flr, fluorite; Gn, galena; GRD, granodiorite; Mlc, malachite; Py, pyrite; Qz, quartz; Smt, smithsonite; Sp, sphalerite.

Locally, Sp1 and Sp2 are partially recrystallized into colourless microcrystalline Sp3, which hosts fragments of the former generation sphalerites (**Figure 6b, c, f, j**; **Figure 9b**). Under reflected light, all generations of sphalerite do not show inclusions or exsolutions of other sulphides. No gangue minerals are observed associated to Sp1 (**Figure 7**). On the other hand, Sp2 is clearly associated with euhedral quartz (Qz1), showing straight grain boundaries (**Figure 6d, e, k**). In the LGB mineralization the Qz1 is also characterized by up to 300 μm-large dark growth bands (**Figure 6d**), missing in the FAR mineralization (**Figure 6k, n**). Py1 and Py2 are accessory sulphides that occur in small, up to 100 µm-sized euhedral crystals, associated to Sp2-Qz1 and Cal1, respectively (**Figure 6i**, **Figure 9a**). The second ore-mineral is Gn, which is particularly abundant in FAR mineralization. It occurs as 0.5–3 cm-sized anhedral crystals (**Figure 6h, m-o**), partially or completely replaces Sp1-Sp2 and isolates comminute Qz-Flr-grains, with sphalerite remnants that can be still observed (**Figure 6h, m, o**). The grain boundary of first-generation calcite (Cal1) with Gn shows corrosion lobes, with Cal1 becoming included in Gn (**Figure 6h**). In addition, apparently euhedral Gn resulting from pseudomorph substitution of euhedral Flr is also observed (**Figure 5e**; **Figure 6n**). In the FAR mineralization, Gn is commonly associated to anhedral μm- to cm-sized Ccp (**Figure 5i**; **Figure 6q, r**). As well as Gn, Ccp grew mainly at the expense of Sp1-Sp2 (**Figure 6p**). The Ccp hosts numerous small inclusions of Py3, which in some cases is associated to Gn (**Figure 6r**), suggesting coeval formation. Pervasive precipitation of fine-grained quartz (Qz2) is observed in all samples from both areas, predominantly at FAR (**Figure 6k, l, n**). The Qz2 in cavities between Flr clasts is euhedral, showing dark growth bands progressively less visible from the microcrystalline edge to the inner part of the cavity (**Figure 6l**). When associated to sulphides, these latter show corrosion lobes, indicating sulphide-Qz2 disequilibrium (**Figure 6d, f, n, o).** The Cal1 occurs as coarse-grained sub-euhedral crystals within fractures affecting Sp1-Sp2 (**Figure 6b, e, h**); this brittle deformation event postdates Sp1 and Sp2 precipitation and is particularly observed in LGB mineralization. Indeed, Cal1 is almost missing in the FAR mineralization, except for some relict grains in fragmented vein of Sp2 and Qz1 (**Figure 6k**). As introduced above, Cal1 is eventually overgrown by Gn (**Figure 6h**). Colourless or pale green Flr is peculiar of the FAR mineralization and occurs as sub-euhedral to euhedral coarse-grained crystals (**Figure 6m**). It is often brecciated in veins consisting of Qz1-Qz2, Gn and Sp1-Sp2 (**Figure 6m, n**), and is overgrown by Gn or corroded by Qz2 (**Figure 6n**). Finally, Cal2 is present in micro-fractures affecting all the previous minerals in both mineralization, with the addition of smithsonite (Smt) and malachite (Mlc) in the FAR (**Figure 6j, q**). Fe-hydroxides locally replaces portions of Sp1-Sp2 (**Figure 6g**).

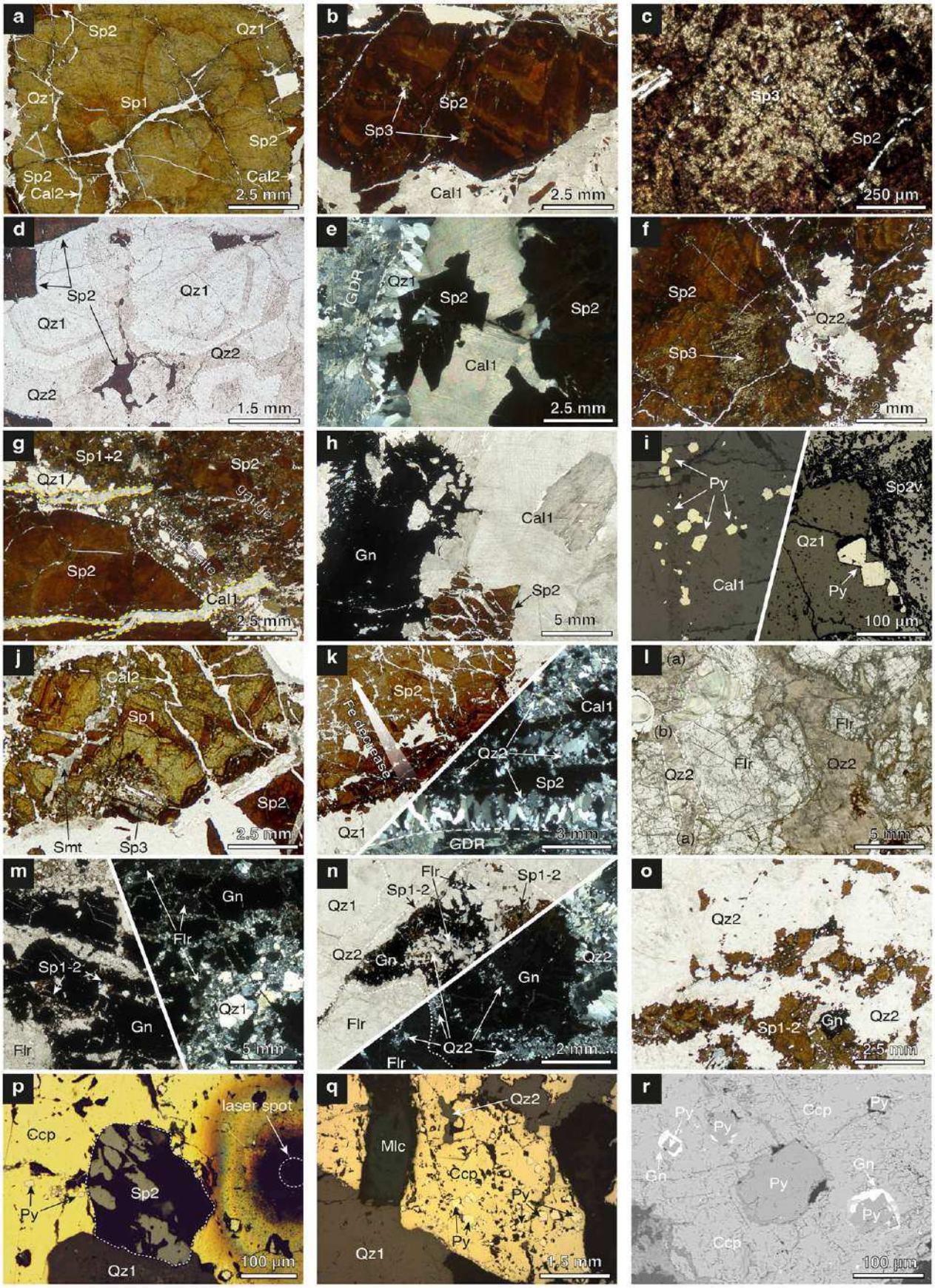
a
Sp2
Qz1
Qz1
Sp1
Sp2
Sp2
Cal2
Cal2
2.5 mm
b
Sp2
Sp3
Cal1
2.5 mm
c
Sp3
Sp2
250 µm
d
Sp2
Qz1
Qz1
Qz2
Qz2
1.5 mm
e
GDR
Qz1
Sp2
Sp2
Cal1
2.5 mm
f
Sp2
Qz2
Sp3
2 mm
g
Sp1+2
Qz1
Sp2
gouge
cataclasite
Sp2
Cal1
2.5 mm
h
Cal1
Gn
Sp2
5 mm
i
Py
Sp2v
Qz1
Cal1
Py
100 µm
j
Cal2
Sp1
Sp2
Smt
Sp3
2.5 mm
k
Sp2
Fe decrease
Cal1
Qz2
Sp2
Qz1
GDR
3 mm
l
(a)
(b)
Flr
Qz2
Flr
Qz2
(a)
5 mm
m
Gn
Flr
Sp1-2
Qz1
Gn
Flr
5 mm
n
Flr
Sp1-2
Sp1-2
Qz1
Qz2
Gn
Qz2
Gn
Flr
Flr
Qz2
2 mm
o
Qz2
Sp1-2
Gn
Qz2
2.5 mm
p
laser spot
Ccp
Sp2
Py
Qz1
100 µm
q
Qz2
Mlc
Ccp
Py
Py
Qz1
1.5 mm
r
Py
Py
Ccp
Py
Gn
Gn
Py
Py
Ccp
100 µm

Figure 6 (previous page). Photomicrographs showing microstructural relationships between ore and gangue minerals from Longobucco (a–i) and Fonte Argentila (j–r) mineralization. **(a)** Light-coloured Sp1; plane polarized light (PPL) thin section scan. **(b)** Dark-coloured Sp2 crosscut by Cal1; PPL thin section scan. **(c)** Colourless Sp3 with irregular texture; PPL micrograph. **(d)** Sp2 with Qz1 exhibiting dark growth bands; PPL thin section scan. **(e)** Sp2-Qz1 vein in granodiorite with Cal1 vein affecting the previous one; cross-polarized light (CPL) thin section scan. **(f)** Qz2 corroding Sp2; colourless Sp3 preferentially forms around or close to corrosion zones; PPL thin section scan. **(g)** Cal1 veins crosscutting Sp affected by a micro-fault (white dotted line); Cal1 crosscut at high angle the fine grained Sp-Qz-rich cataclasite by veins (yellow dashed lines) and pervades the Sp-gauge; PPL thin section scan. **(h)** Fractured Sp2 and filled by Cal1 both overgrown by late Gn; PPL thin section scan. **(i)** Detail of small Py crystals within Qz1 and in Cal1; reflected light (RL) micrograph. **(j)** Fractured sphalerite (Sp1-Sp2-Sp3) with late Cal2 and Smt; PPL thin section scan. **(k)** Qz1-Sp2 vein in granodiorite; PPL thin section scan. **(l)** Brecciated Flr vein partially dissolved by Qz2; PPL thick section scan. **(m)** Qz-Flr-breccia with Gn that replaces Sp; PPL/CPL thin section scan. **(n)** Qz-Flr-vein with Gn that isolates Sp and Flr remnants; Qz2 corrodes Gn-Sp-Flr portions; PPL/CPL thin section scan. **(o)** Remnants of Sp and Gn completely corroded by Qz2; PPL thin section scan. **(p)** Remnant of fractured Sp surrounded by Ccp; RL micrograph. **(q)** Ccp hosting Py; Mlc forms along fractures in Ccp; RL micrograph. **(r)** Py crystals with Gn in Ccp; wavelength-dispersive spectrometry (WDS) image. Legend: Cal, calcite; Ccp, chalcopyrite; FeOx, Fe-oxide-hydroxide; Flr, fluorite; Gn, galena; Mlc, malachite; Py, pyrite; Qz, quartz; Smt, smithsonite; Sp, sphalerite.

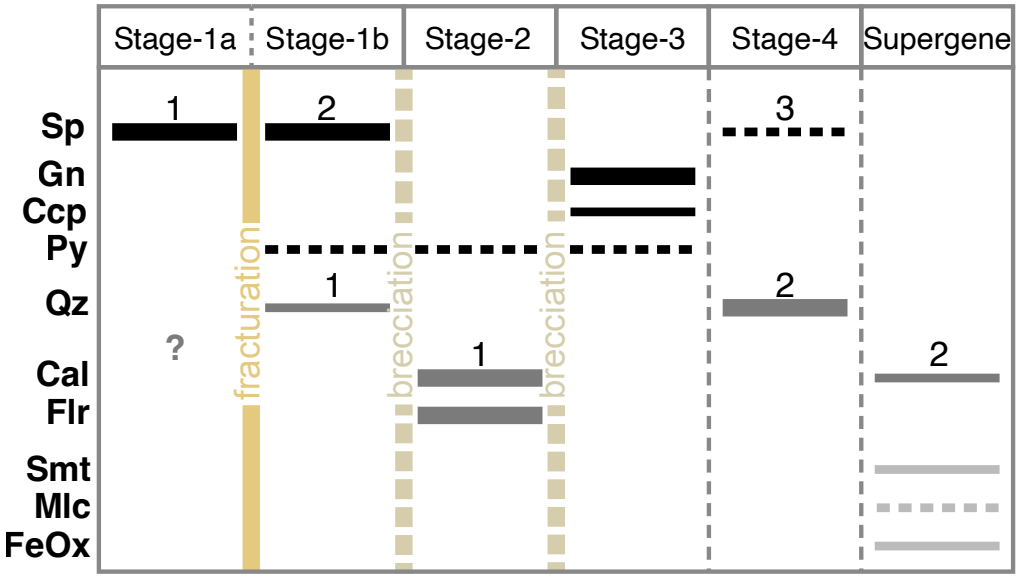

Figure 7. Mineral forming sequence diagram of LGB-FAR mineralization. Legend: main mineral (thick line); secondary mineral (thin line); accessory mineral (dotted line); ore-mineral (black); gangue mineral (dark gray); supergene mineral (light gray). Mineral abbreviations: Cal, calcite; Ccp, chalcopyrite; FeOx, Fe-hydroxide; Flr, fluorite; Gn, galena; Mlc, malachite; Py, pyrite; Qz, quartz; Smt, smithsonite; Sp, sphalerite.

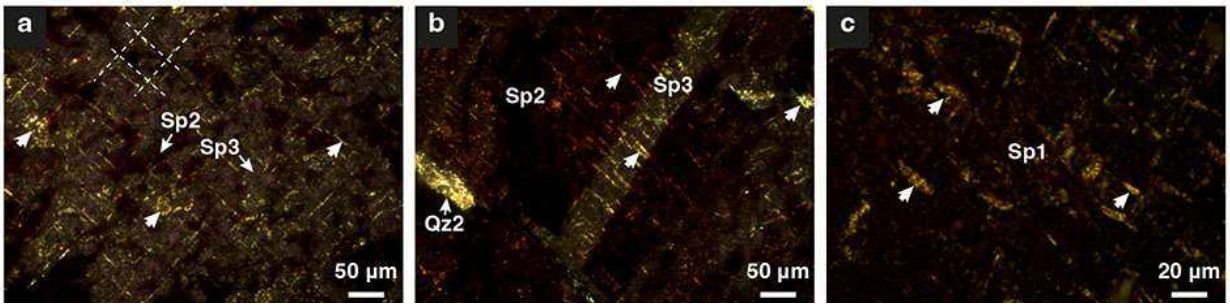

Figure 8. Some examples of optical anisotropy in sphalerite. In the images are shown a gridiron-type **(a)** and *en enchelon* **(b)** textures, with a detail of a gridiron texture **(c)**.

6.4. Sphalerite

6.4.1. Chemistry and chemical zoning

The growth bands and colour zoning observed in sphalerite (Sp) are also associated with chemical zoning of the ore-mineral. EPMA analyses carried out on several zoned crystals of sphalerite show chemical variations in Mn-, Fe-, Co-, Cu-, Cd- and Ge-contents in relation to colour (W–colourless, L–light yellow, Y–yellow, B–brown, R–reddish-brown, D–dark-brown) (**Figure 10a**) and to different generation (Sp1-Sp2-Sp3) (**Figure 10b**; Tables 1a-b) (Tables are present in the Appendix).

The three sphalerite generations are characterized by compositional variations, primarily in Zn and Fe-contents, also observed in BSE and WDS images (**Figure 9a-d**; Tables 1a-b). The light coloured Sp1 is characterized by similar medians (Mdn) Zn content of 63.66 and 64.39 wt.% in both sites, and medians Fe-content of 3.34 wt.% (range 1.57–5.64 wt.%) at LGB and of 2.36 wt.% (range 1.55–7.54 wt.%) at FAR (Tables 1a-b). The Zn-content of the dark-coloured Sp2 is lower than Sp1, showing medians of 59.69 and 58.32 wt.% at LGB and FAR respectively. On the other hand, the Fe-content is higher, with medians of 6.84 wt.% (range 2.88–10.69 wt.%) at LGB and of 7.29 wt.% (range 4.34–11.27 wt.%) at FAR. Amongst LGB-FAR sphalerite generations, the colourless Sp3 has the highest Zn-content, with median of 65.48 wt.%, and the lowest Fe-content (range 0.18–1.36 wt.%; Mdn 0.43 wt.%) (Tables 1a-b).

Cd is the second minor element in sphalerite, with concentrations varying in the range 0.01-0.69 wt% (Mdn of 0.19 wt%) at LGB and 0.01-0.54 wt% (Mdn of 0.18 wt%) at FAR (Tables 1a-b). Contrary to Fe, Cd does not show a correlation between colour and growth bands (**Figure 9a-d**; **Figure 10a**), indeed, through WDS maps it is possible to observe how Cd is concentrated in specific sector zoning (**Figure 9a-d**) within sphalerite.

Unlike the previous cations, Mn, Co, Cu and Ge are present as trace elements and do not show peculiar distribution within sphalerite, (Tables 1a-b). Only Co, like Fe, tend to be concentrated in the darker-coloured sphalerites (**Figure 10a**).

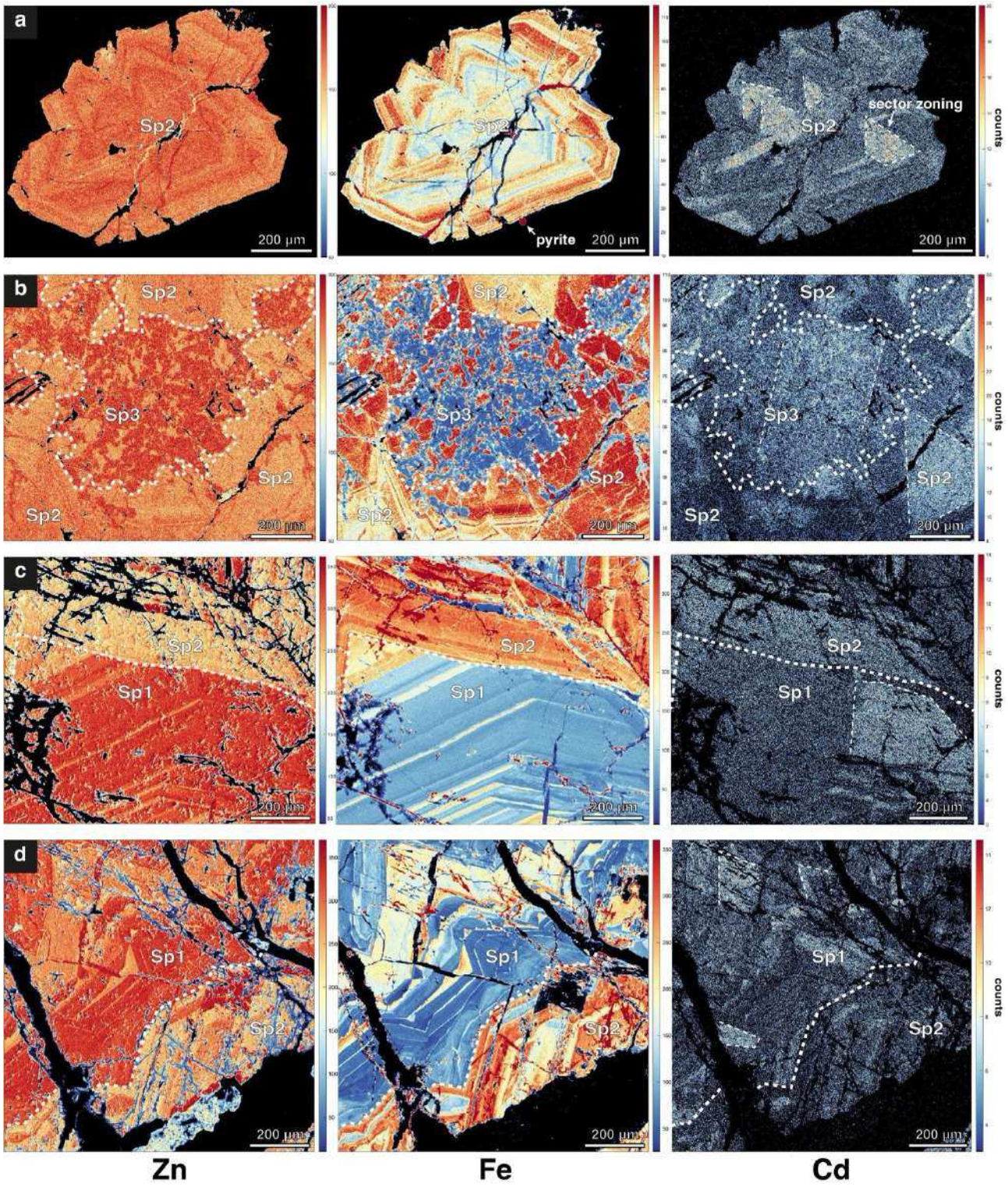

Figure 9. Elemental EPMA maps of sphalerite. EPMA maps elaborated with XmapTools software, showing the distribution of Zn, Fe and Cd in selected part of sphalerite crystals; **(a)** Isolated aggregate of Sp2 with clear Fe-related chemical zoning that follows the mineral growth bands, while Cd is distributed in specific growth sectors; **(b)** Sp2 mineralization corroded by Sp3 with the lowest Fe contents; **(c)** growth discontinuity between Sp1 and Sp2 with Fe-contents in Sp2 higher than Sp1; **(d)** complex growth discontinuity between Sp1 and Sp2.

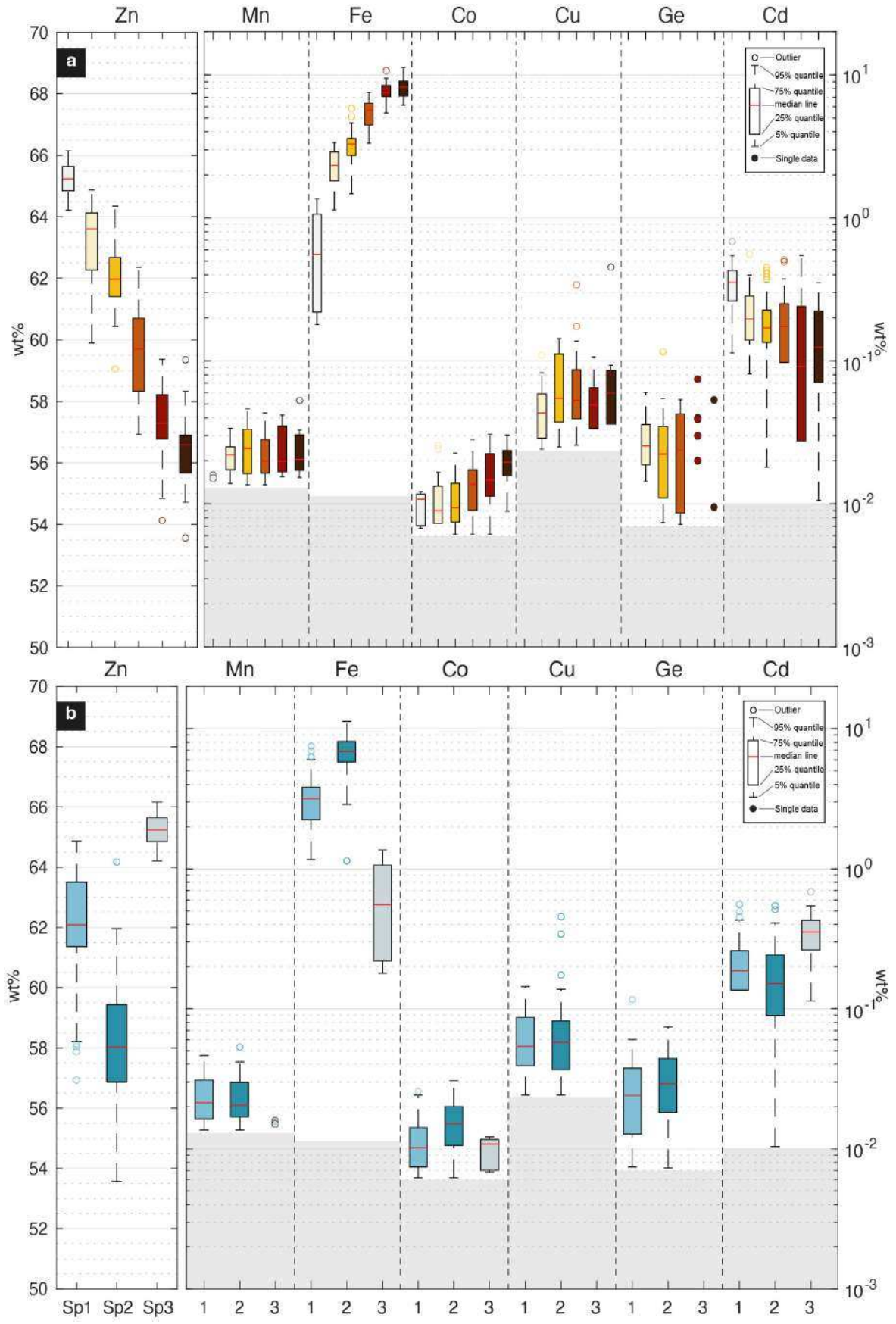

Figure 10. Boxplots of EPMA data of sphalerite. Distribution of major, minor and trace elements in LGB and FAR sphalerite by colour **(a)** and generations **(b)**.

6.4.2. *μ*-Raman

Initially ten Raman spectra from sphalerite samples (n.8 from LGB and n.2 from FAR), were measured alongside specific EPMA spots or on an area associated to an average chemical composition based on 3 to 4 EPMA spots. The measured spectral range, from 50 to 800 cm^{-1}, was truncated to 200–750 cm^{-1} to exclude wavenumbers corresponding to lattice vibrations, as well as TA (transverse acoustic) and LA (longitudinal acoustic) modes (Hope et al., 2001). All spectra exhibit the LO fundamental modes of Fe-S and Zn-S bonds (from 295 to 350 cm^{-1}) (**Figure 11**; Table 2) (Zigone et al. 1981; Hope et al., 2001). In the selected sphalerite samples, having Fe-content ranging from 0.8 to 21.3 mol% FeS, corresponding to colourless up to dark brown sphalerite the expected Raman bands of Fe-rich sphalerite have been found. In particular, the LO mode attributed to Zn-S bond vibrations (347 to 350 cm^{-1}, **Figure 11**; Table 2); the LO mode Y_1 attributed to Fe-S bond vibrations (298 to 296 cm^{-1}, **Figure 11**; Table 2) and LO intermediate modes, Y_2 and Y_3, attributed to metal-S bond, with values of 310 cm^{-1} and 326–331 cm^{-1} (Hope et al., 2001; Karbish et al., 2007; Osadchii and Gorbaty, 2010). In addition, between 601 and 667 cm^{-1}, the composite vibrational modes (TO2, LO+TO, LO2) are found (**Figure 11**), as reported by Hope et al. 2001. A variation of the relative height of the peaks (300 and 350 cm^{-1}) as a function of the Fe-content is apparent.

Accurate peaks parameters (position, height and FWHM, peak area) were obtained by fitting the spectra in the 250–400 cm^{-1} range. The measured spectra were best fitted using up to six bands (299, 305, 311, 331, 339, 350 cm^{-1}) (Table 2). Besides the fundamental modes mentioned, the fitting process revealed two intermediate peaks: one within ranges of 302–309 cm^{-1} and the other within ranges of 336–342 cm^{-1} (**Figure 12**; Table 2), described by Zigone et al. (1981) and Kharbish et al. (2007). The former, clearly visible at high Fe-content (6.16–10.50 wt.%) is probably attributed to low Co-contents in sphalerite, while the latter, visible even from lower Fe-content (1.34–10.50 wt.%), is due to unspecified Fe bonds.

From the fitting results we have obtained that the LO mode position of Zn-S bond vibrations varies from 348 to 353 cm-1, the Y_1 mode of Fe-S bond vibrations varies from 296 to 301 cm^{-1} (**Figure 12**; Table 2). The intermediate LO modes Y_2 and Y_3 exhibit ranges of 309–314 cm^{-1}, and 329–333 cm^{-1}, respectively (**Figure 12**; Table 2). The peak intensity, and respective area (A3) and height (h3), of the LO mode Zn-S decreases when the Fe-content increases, with also increasing intensity (with A1 and h1) of the LO mode Fe-S. The intensities of Y_2 and Y_3 mode substantially do not change.

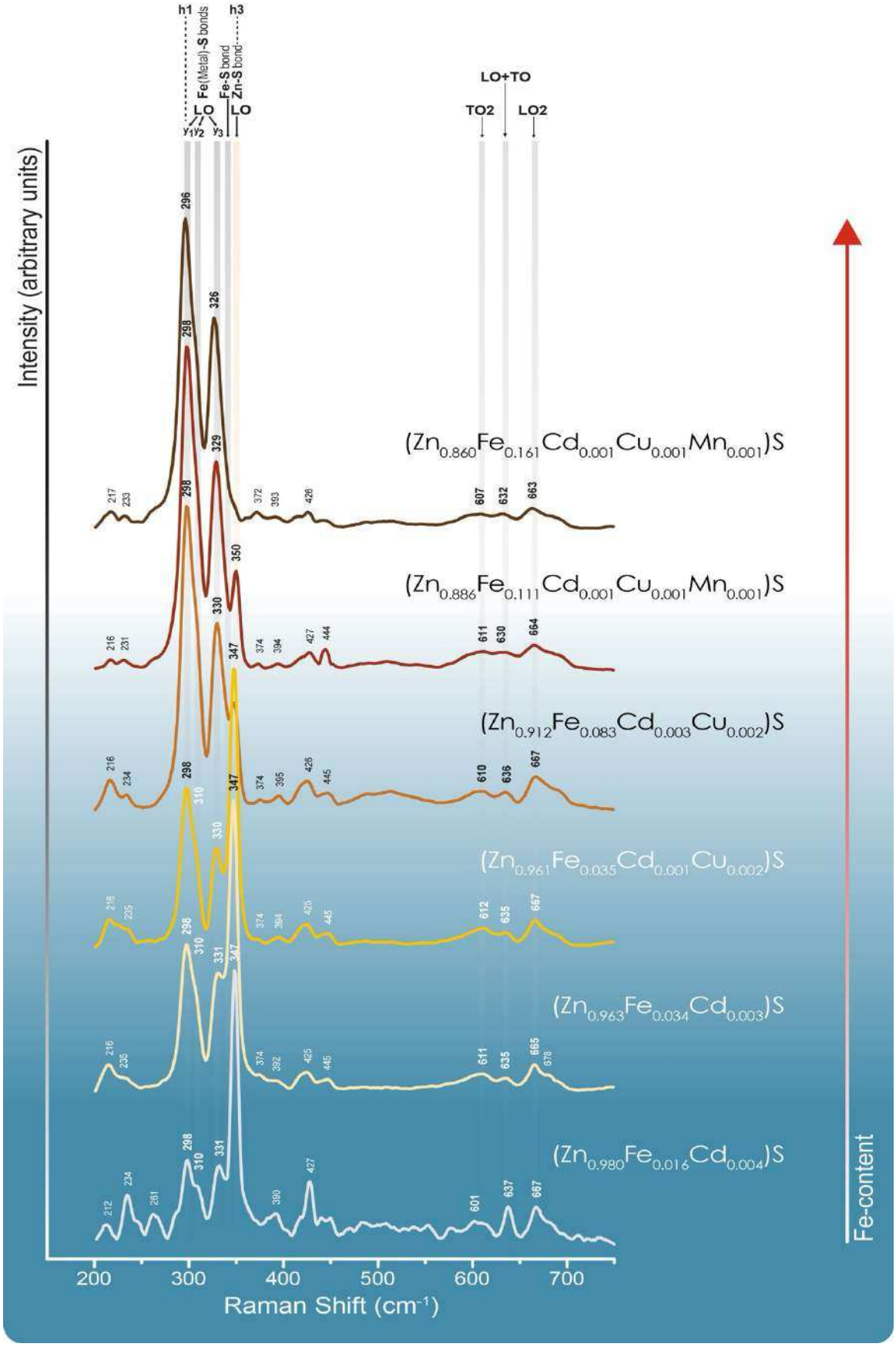

Figure 11. Selected *μ*-Raman spectra associated to colour zoning and chemical composition of sphalerite, related with changes in Raman band intensity.

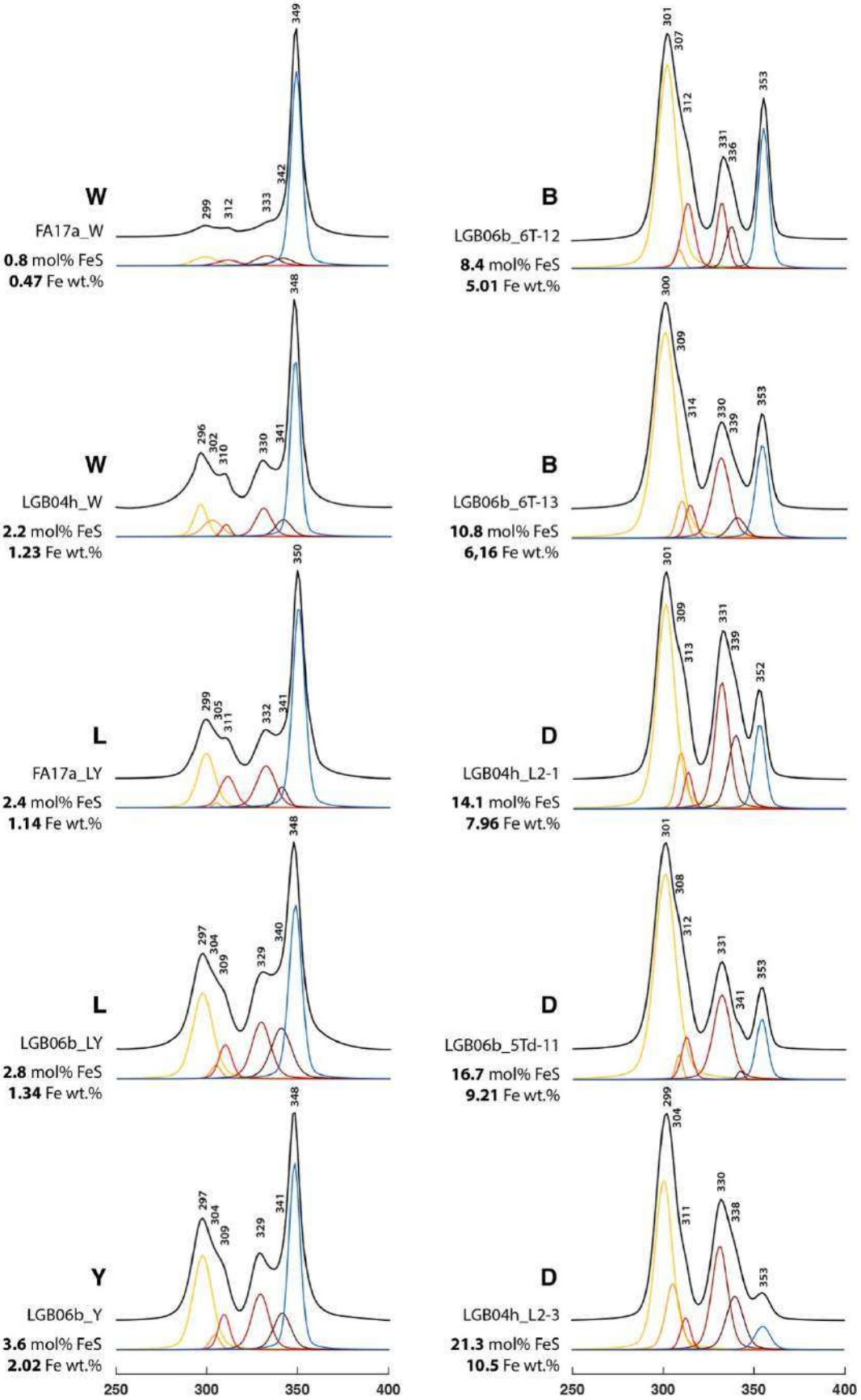

Figure 12. *μ*-Raman spectra of sphalerite obtained after best fitting process.

6.4.3. XRPD

X-ray powder diffraction analyses were performed on two quantities (5 grams each) of natural sphalerite samples selected and ground from section back cuts of macro samples and on four thin/thick sections of the same mineral (Table 3). Specific areas on thin/thick sections corresponding to different sphalerite generations (Sp1-light and Sp2-dark) were measured.

Data treatment and phase identification in the different samples was performed using Highscore software.

Diffraction peaks belonging to the crystalline phase of Fe-sphalerite were identified in all samples. No other ZnS polytype was found. Quartz was identified as a gangue mineral in each sample. Where necessary, a sample displacement correction (z-shift) was applied to some samples using the 2θ 20.86° (d_{100}= 4.2626 Å) quartz peak to obtain an accurate calibration (Table 3). The z-shift corrected 2θ diffraction peak positions agreed with literature data (Mackowsky, 1939; Kullerud, 1953; Skinner, 1961).

Other mineralogical phases belonging to calcite (LGB04h, LGB06a) and K-feldspar (sample LGB04h) were recognized (**Figure 13**).

In addition, the XRD pattern of sample lgb06a_ter shows the appearance of additional diffraction peaks at 2θ 26.65°, 27.19°, 27.43°, 27.50°, 28.29°, 48.54°, and a shoulder at 2θ 47.08°. Some of these additional peaks have been tentatively identified by the Highscore software as being due to the presence of a CdS phase in sphalerite (**Figure 13**). A le Bail refinement was performed to assess the occurrence of such phases. XRD analysis with Le Bail refinement showed that the diffraction peaks at 2θ 26.65°, 28.29°, and at 2θ 47.08° belong to a (Cd-, Fe-rich) sphalerite as attested by the higher value of the cell parameter compared with synthetic sphalerite.

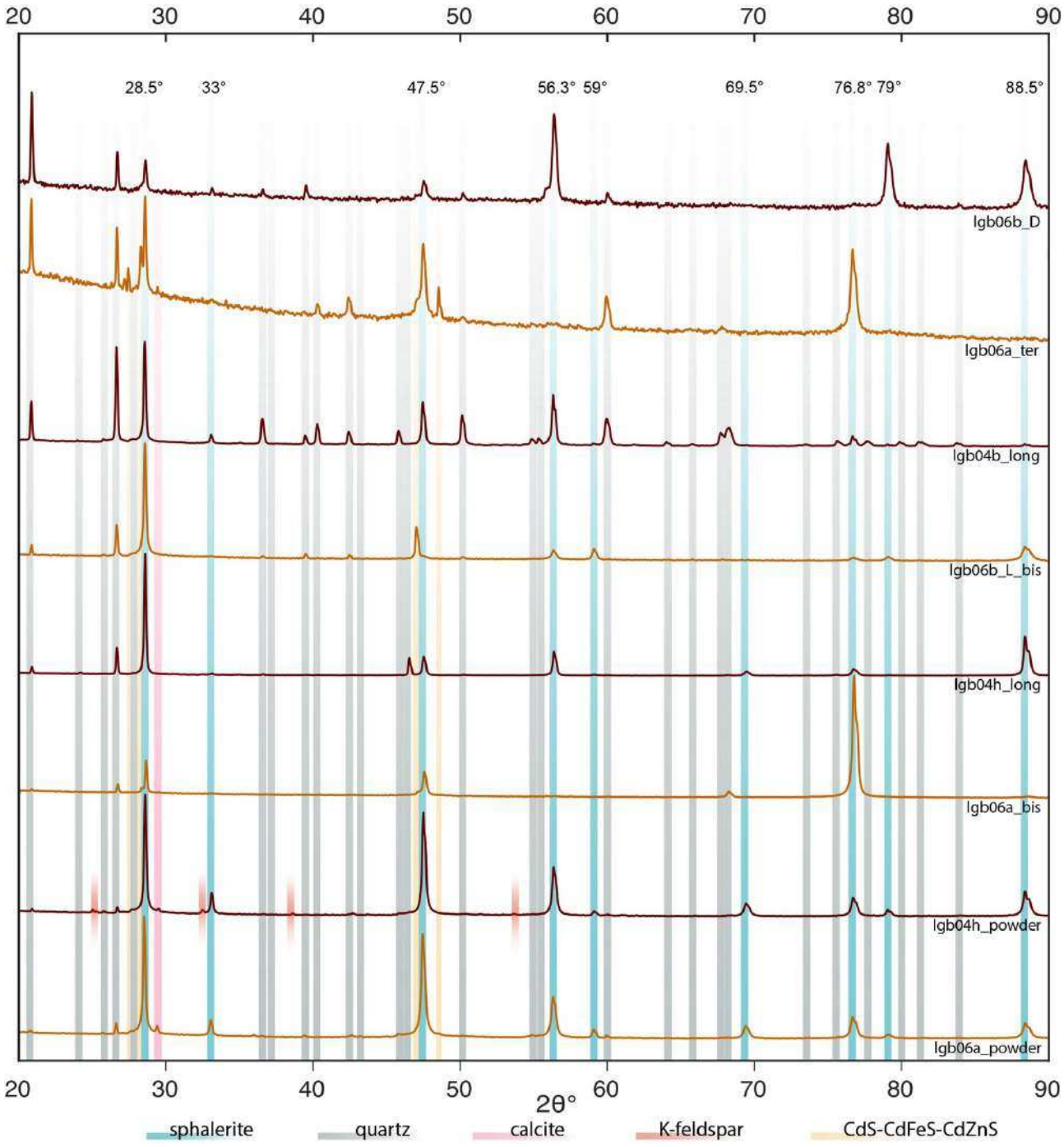

Figure 13. XRPD diffraction patterns of analyzed samples of sphalerite.

6.4.4. SCXRD

Single crystal X-ray diffraction has been performed on 11 sphalerite crystal fragments, selected from a 100 μm-thick section (LGB06b_L), representing five different colour zones of the mineral (L–light yellow; Y–yellow; B–brown; R–reddish brown; D–dark brown). Each fragment has been assigned both a specific chemical composition (SEM analyses on Table 5) and an average chemical composition based on 3 to 4 EPMA spots carried out in areas close to the selected fragments (Table 4). The fragments, initially ~500 μm wide, were further crushed to reach minimum dimensions of 50x100 μm. The primary aim of the SCXRD investigation was to obtain the cell parameters (Å) of each individual sphalerite fragments. and to check for the possible occurrence of polytypes or deviation from perfect cubic symmetry.

The simulated precession diffraction patterns of the all 11 natural sphalerite samples confirm the cubic symmetry but also highlights the poor diffraction quality of the crystals (**Figure 14a-c**). The diffraction peak broadening observed in the precession patterns is indicative of high mosaicity or internal disorder within the analyzed sphalerite.

The obtained cell parameters showed variability both between different colour zones and among samples belonging to the same colour zone, indicating strong chemical inhomogeneity. Among the analyzed samples, the D3 fragment exhibits the smallest refined cubic lattice constant, a = 5.4136 ± 0.0049 Å, while one brown sphalerite fragment (R2) shows the largest, a = 5.4230 ± 0.0046 Å (Table 4). Nevertheless, the average obtained of all cell parameter values, a = 5.4175 Å, in good agreement with reference values for sphalerite (ranging from 5.398 to 5.425 Å) (Kullerud, 1953; Smith, 1955; Skinner, 1961).

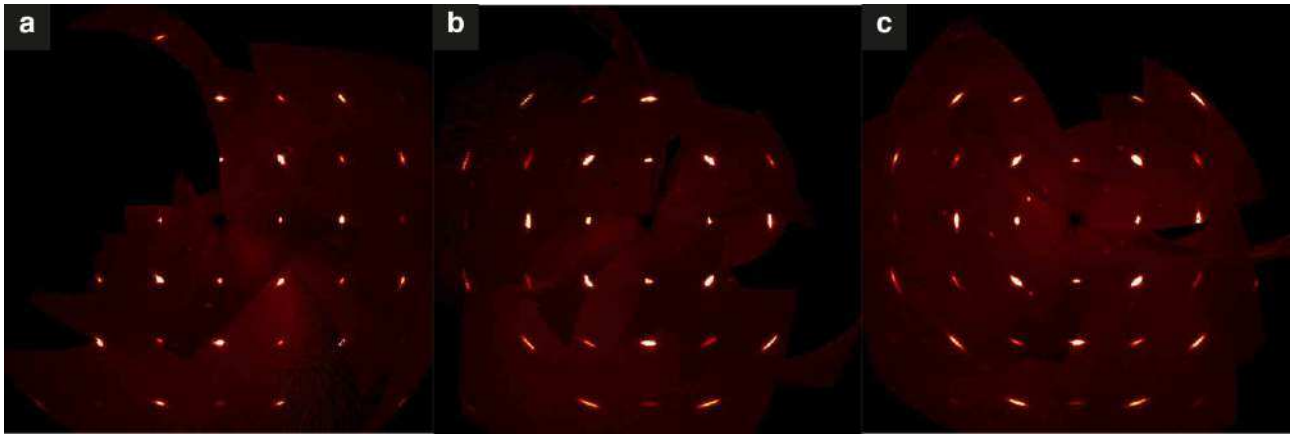

Figure 14. Simulated precession diffraction patterns on selected Y2 sample. (a) 0kl **(b)** h0l **(c)** hk0,

6.4.5. LA-ICP-MS data for Sp1 and Sp2

Among the minor and trace elements measured in sphalerite crystals (**Figure 15**; **Figure 16**; Tables 6a-b), Cd is the most abundant ranging from 1846 to 5329 ppm at LGB and from 1001 to 7589 ppm at FAR, increasing from Sp1 to Sp2. The second most abundant element is Cu, which shows very similar contents in the two mineralization sites, slightly increasing from Sp1 to Sp2 at LGB (**Figure 16**) with more pronounced variations at FAR, from 131.44 to 494.79 ppm median values respectively (**Figure 16**). Regarding the other trace elements, Ga medians of Sp1 and Sp2 are comparable, with higher values at LGB (91,68 ppm for Sp1 and 101.43 ppm for Sp2) than at FAR (33.11 ppm for Sp1 and 42.11 ppm for Sp2) (**Figure 16**). Germanium is particularly present in Sp2 of LGB and FAR (up to 386.01 and 338.79 ppm, respectively) (**Figure 16**; Tables 6a-b). Silver, Sb and Pb show similar distributions and contents, constant from Sp1 to Sp2 at LGB and increasing in Sp2 at FAR (**Figure 16**). Concerning In, it remains almost constant from Sp1 and Sp2 at LGB (Mdn. 0.88 and 0.25 ppm) and decreases in Sp2 at FAR (Mdn. 5.93 and 1.89 ppm) (**Figure 16**). Tin shows the opposite behaviour between the two sites: from Sp1 to Sp2 it decreases at LGB (Mdn. 6.90 and 2.07 ppm) and increases at FAR (Mdn. 1.39 and 15.23 ppm) (**Figure 16**). Finally, Tl occurs in very low concentrations only at LGB (from 0.07 to 0.82 ppm; Mdn. 0.21 ppm) (**Figure 16**; Tables 6a-b).

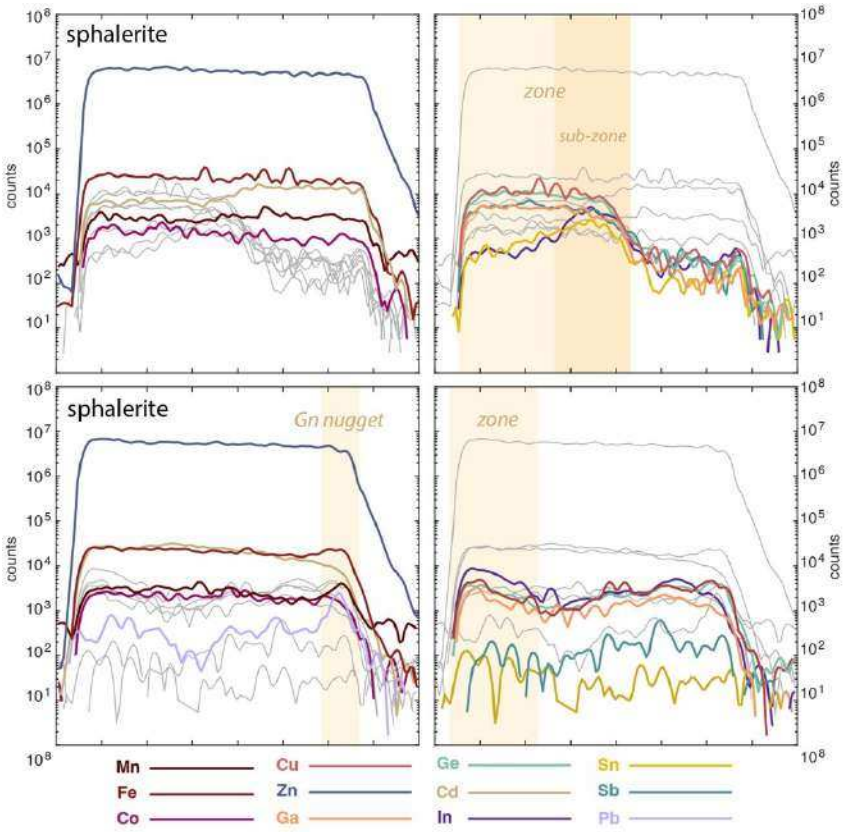

Figure 15. Selected times-resolved LA-ICP-MS profiles of sphalerite crystals. The reported profiles show how the zoned sphalerites can have a variable content in some trace elements within a few microns of thickness affected by the laser beam spot. Although there are no significant differences between major and minor elements (apart from some small Fe-enriched nugget), different chemical zoning can be recognised in the others trace elements.

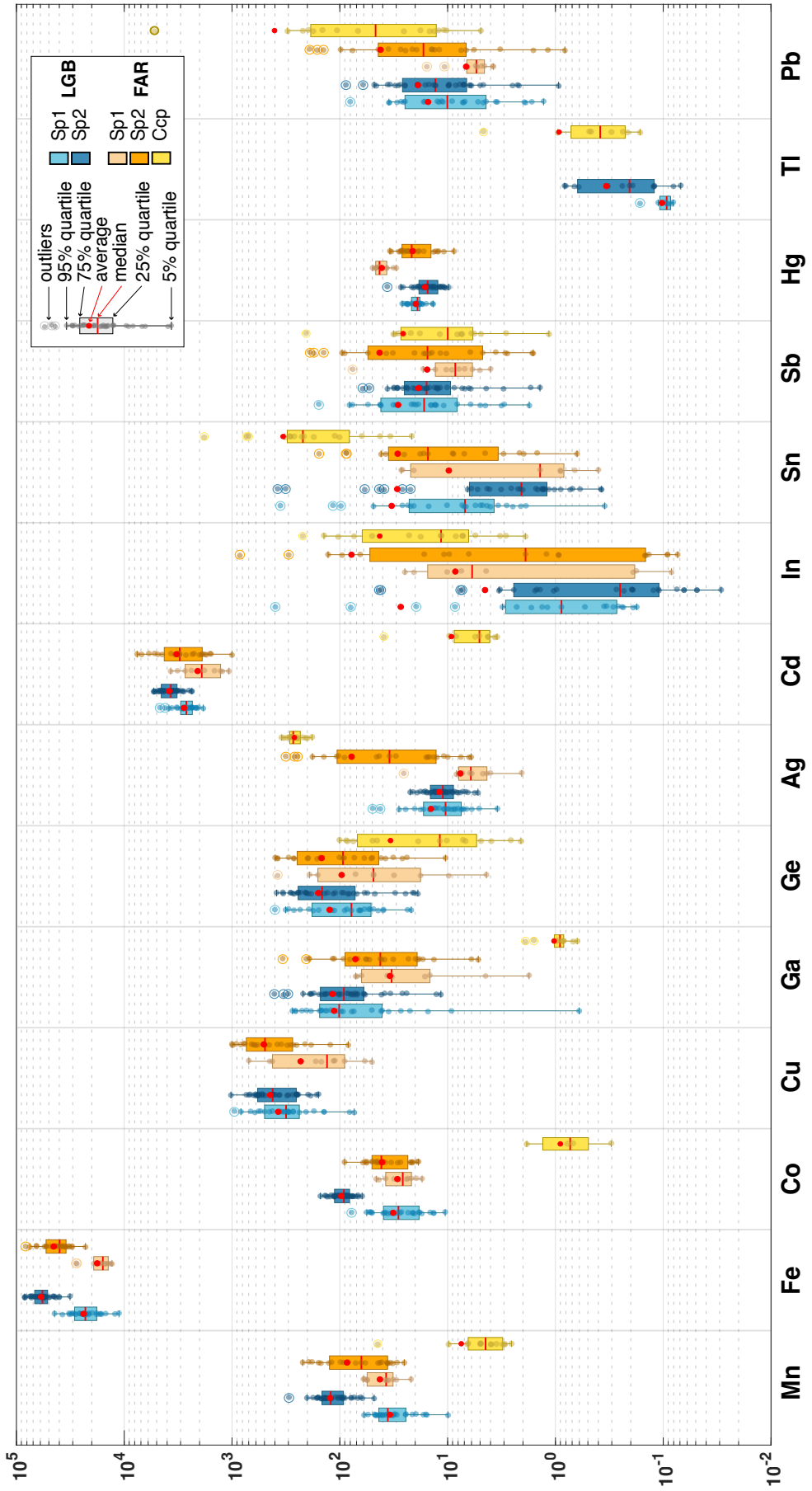

Figure 16. **Boxplots of LA-ICP-MS data of sphalerite crystals**. Trace element distribution (ppm) in LGB and FAR sphalerite of Sp1 and Sp2 generations, and in FAR chalcopyrite, are shown.

6.4.6. GGIMFis geothermometer

Using the Fe- (wt.%), Mn-, Ga-, Ge-, In-contents (ppm) present in the Sp1, Sp2 and partially in Sp3, it has been possible to obtain the formation temperature of the mineral at LGB and FAR through GGIMFis (**G**a-**G**e-**I**n-**M**n-**F**e **i**n **s**phalerite) geothermometer, as proposed by Frenzel et al. (2016), adopting the following formulas:

(1) $PC1^* = \ln [(C_{Ga}^{0.22} \cdot C_{Ge}^{0.22}) / (C_{Fe}^{0.37} \cdot C_{Mn}^{0.20} \cdot C_{In}^{0.11})]$

(2) $T(^{\circ}C) = -(54.4 \pm 7.3) \cdot PC1^* + (208 \pm 10)$

Temperatures obtained in LGB and FAR (Table 7) for Sp1 show a range of 130-206 °C (Mdn of 159 °C) and 110-230 °C (Mdn of 171 °C), respectively (**Figure 17**). Sp2 shows formation temperatures between 150-218 °C (Mdn of 180 °C) at LGB and 148-241 °C (Mdn of 183 °C) at FAR (**Figure 17**). For the formation temperature of Sp3, only a few LA-ICP-MS data available (Table 7), which indicate a median formation temperature of 160 °C.

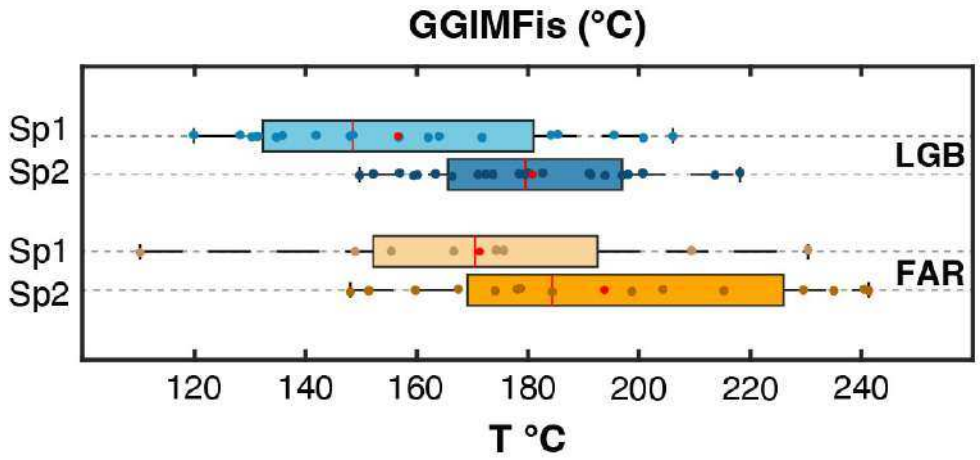

Figure 17. Boxplots indicating GGIMFis temperatures obtained in Sp1 and Sp2. Same average, median, quartile and outlier notations as in the legend of Fig. 16.

6.5. Galena

In reflected light as well as in EDS and WDS images, the LGB and Fonte Argentila galena crystals did not show mineral inclusions, displaying a homogeneous texture (**Figure 6h, 6m, 6n**). The EPMA data confirm this peculiarity, as the galena crystals showed an almost pure composition, with Pb and S medians of 85.83 and 13.02 wt.% at LGB and 86.86 and 13.20 wt.% at FAR (Table 8). The only trace element found in the galena crystals is Sb, with concentrations of 0.03-0.09 wt.% (Mdn of 0.05 wt.%) at LGB and 0.02-0.06 wt.% (Mdn of 0.05 wt.%) at FAR (Table 8).

6.6. Pyrite

SEM and EPMA analyses showed that pyrite crystals occurring within Qz1 and Cal1 (**Figure 6i**), in the LGB area, has nearly pure compositions (Table 9), except for As content (up to 0.85 wt.%; Table 9). In contrast, the pyrite crystals included in chalcopyrite (**Figure 6p-q**), in the FAR area showed concentrations of several minor and trace elements, such as Cu (Mdn of 0.36 wt.%), Ag (Mdn of 0.01 wt.%), Sn (Mdn of 0.01 wt.%) and Au (Mdn of 0.14 wt.%) (Table 9). The notable Au content reaches levels of up to 0.24 wt.% in some pyrite crystals, whereas As exhibits minimal concentrations, with only a few spot analyses indicating an As content of up to 0.07 wt.% (Table 9).

6.7. Chalcopyrite

The EPMA and LA-ICP-MS analyses evidenced that the most abundant trace elements in chalcopyrite are Zn, Ag, and Sn, with concentrations ranging from 127 to 488 ppm, 164 to 313 ppm, and 20 to 1610 ppm, respectively (Tables 10, 11) Their distribution within the crystals is heterogeneous. A single analysis showing anomalously high Zn- and Pb-contents (6218 and 4616 ppm respectively), suggests the presence of micro-inclusions of sphalerite and galena (**Figure 6r**, **Figure 18**). The elements Ge, In, Sb and Pb show intermediate concentrations (**Figure 16**), in line with those of in sphalerite (Table 11). Conversely, Mn, Co, Ga, Cd, Au and Tl show very low concentrations (below 9 ppm; Table 11) and no variation between crystals. The Zn/Cd ratio shows values between 38 and 172.

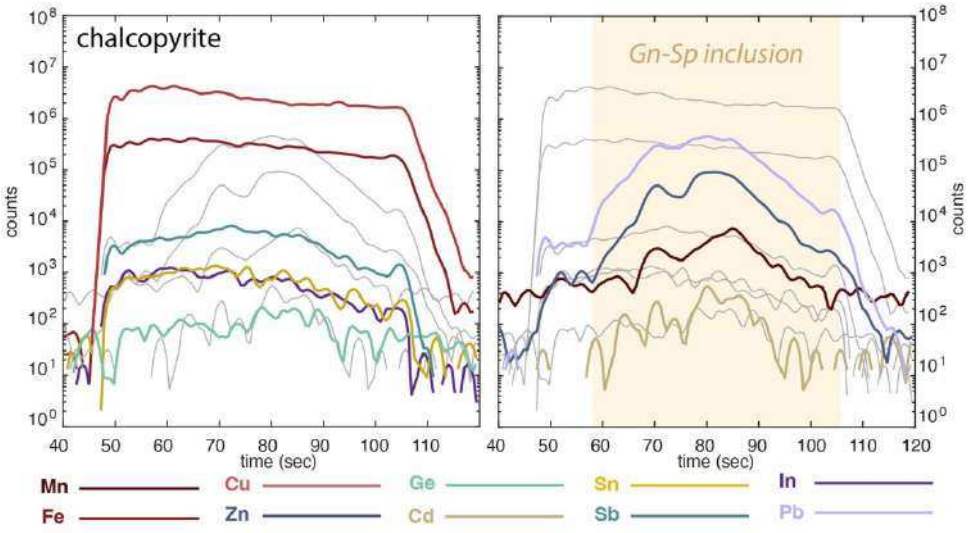

Figure 18. Selected times-resolved LA-ICP-MS profile of chalcopyrite.

6.8. Quartz

Quartz (Qz1-Qz2) found at the LGB and FAR sites can be characterized by the presence of dark growth bands in portions of euhedral quartz crystals (**Figure 6d**). Most of the Qz1 at LGB exhibits a single dark growth band within the crystal, with a thickness ranging from 200 to 250 μm (**Figure 19d**). The cause of these bands is not optically decipherable, although an increase in fluid inclusions smaller than 1 μm can be observed within the dark band (**Figure 19d**). In Qz2 at FAR, instead, fine-grained portions of Qz2, that fill cavities between fluorite crystals (**Figure 6l**), develop quartz crystals with euhedral habit (**Figure 19b, e**) and multiple rhythmic dark bands, ranging in thickness from 50 to 100 μm, in the terminal accretion (**Figure 19b-c**).

The dark bands are not visible in BSE images but can be observed in VPSE images, where they show additional internal zoning with bands characterized by different brightness (**Figure 19a**). EPMA analyses (Table 12) on some banded crystals of Qz1 and Qz2 have highlighted a characteristic chemical composition for minor and trace elements corresponding to the dark bands. In particular, the Al-content increases significantly from light bands (Mdn 0.05 and 0.04 wt.% at LGB and FAR) to dark bands (Mdn 0.15 and 0.29 wt.% at LGB and FAR) (**Figure 19c**), reaching Al-contents of up to 0.39 and 0.73 wt.% at LGB and FAR (Table 12). Unusual cations, such as Na (Mdn 0.03 and 0.02 wt.% at LGB and FAR), K (Mdn 0.03 and 0.02 wt.% at LGB and FAR), and Ca (Mdn 0.03 and 0.03 wt.% at LGB and FAR), also show high concentrations in the dark bands of the quartz (Table 12). Additionally, fine-grained Qz2 at FAR shows elevated medians contents of Na (0.03 wt.%), Al (0.36 wt.%), K (0.04 wt.%), and Ca (0.02 wt.%) (Table 12).

LA-ICP-MS analyses (Table 13) were conducted for the minor and trace elements of fine-grained Qz2 and on banded crystals (**Figure 20**) from the FAR site. The Al-content in banded quartz varies from light bands (Mdn 306 ppm) to dark bands (Mdn 2380 ppm), confirming the EPMA data, with higher contents (Mdn 3170 ppm) in fine-grained quartz (**Figure 20**; Table 13). Trace elements such as Mg (Mdn 38 ppm) and K (Mdn 508 ppm) are concentrated in the dark bands, while Na (Mdn 260 ppm) and Ca (Mdn 940 ppm) are present in the fine-grained portion (**Figure 20**; Table 13). Li-contents are lower in the light bands (2.88–40.30 ppm; Mdn 14.77 ppm), higher in the dark bands (23.70–137 ppm; Mdn 76.60 ppm), and even higher in the fine-grained quartz (141.50–364 ppm; Mdn 233 ppm) (**Figure 20**; Table 13). Ge contents range from 0.64 to 6.67 ppm in banded quartz and from 3.58 to 10 ppm in fine-grained quartz (**Figure 20**; Table 13). Fe contents reach 24.30 ppm in banded quartz and 94.00 ppm in fine-grained quartz, whereas Ti- and Cr-contents are below 2.78 ppm (**Figure 20**; Table 13).

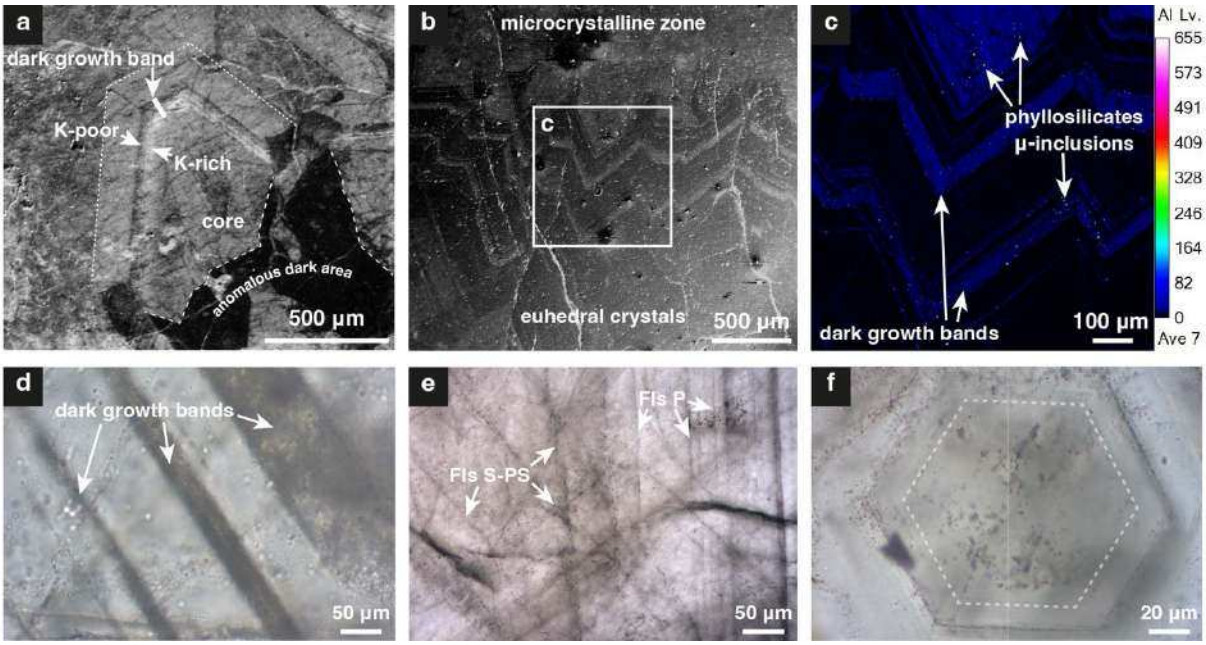

Figure 19. VPSE, WDS and microphotograph images of quartz. VPSE images showing the growth bands of Qz1 **(a)** and Qz2 **(b)** associated with different chemism. **(c)** EPMA X-Ray map showing showing Al concentrations along the dark growth bands of quartz. **(d)** Detail of the dark growth bands. PPL thin section. **(e)** Swarms of sub-micrometric fluid inclusions present in Qz1. PPL thin section. **(f)** Basal section of a Qz2 crystal with primary FIs in the core and along the growth edges of the crystal. PPL thin section.

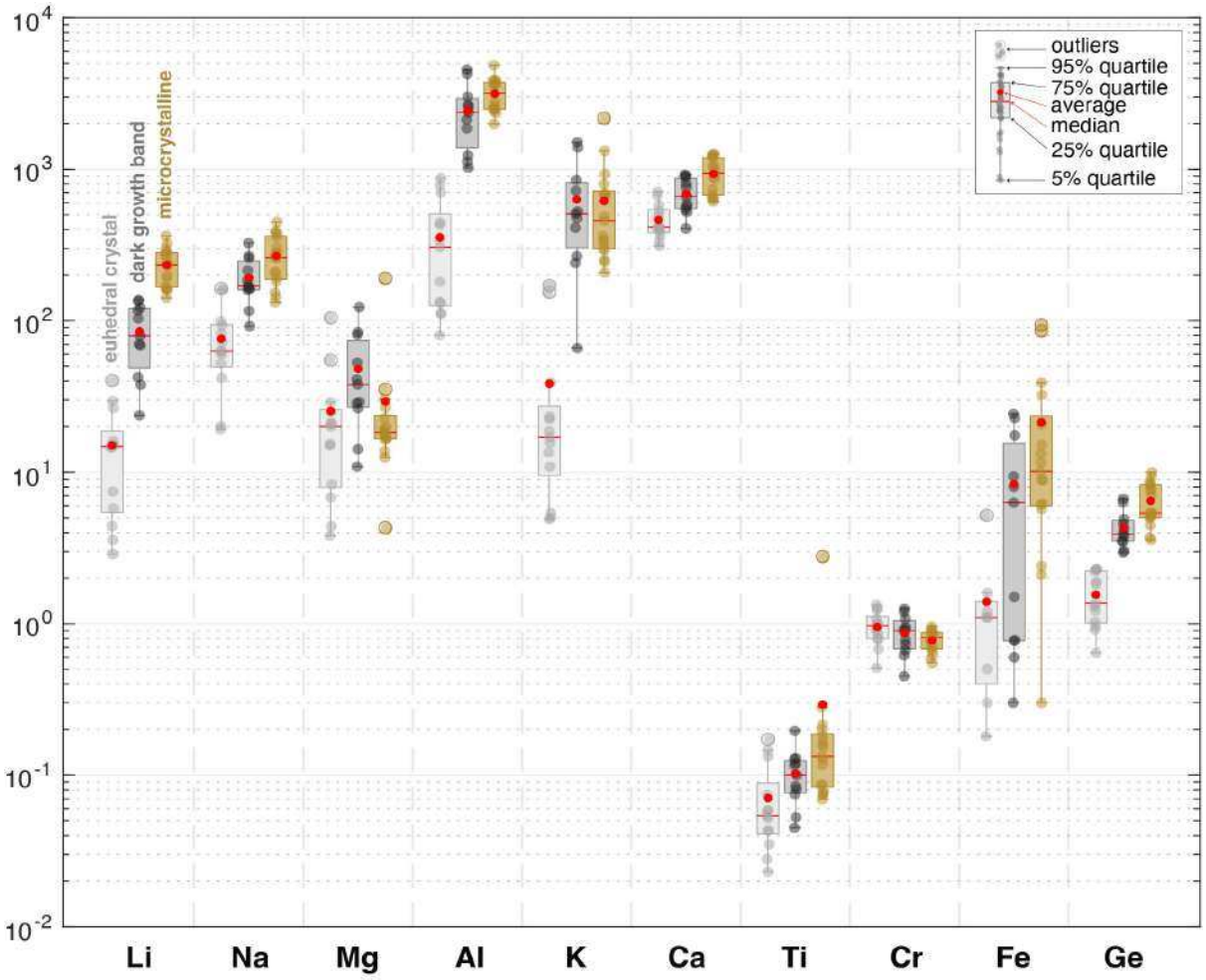

Figure 20. Boxplots of LA-ICP-MS data indicating the distribution of trace elements in Qz2 (ppm).

6.9. Calcite

6.9.1. EPMA and LA-ICP-MS data

As shown in Table 14, EPMA analyses performed on calcite veins (Cal1) from LGB (**Figure 6e, h**) and fragmented Cal1 veins from FAR (**Figure 6k**), have revealed similar compositions in terms of Mg (0.05–0.13 wt.% at LGB; 0.17–0.47 wt.% at FAR), Fe (0.04–0.55 wt.% at LGB; 0.09–0.28 wt.% at FAR) and Mn (0.64–1.54 wt.% at LGB; 0.59–1.38 wt.% at FAR) (Table 14).

LA-ICP-MS analyses were only carried out on calcite veins at LGB; they coinfirmed the EPMA analyses regarding the contents of Mg (9.09–933 ppm; Mdn 157.60 ppm), Fe (44.68–3129 ppm; Mdn 1650.50 ppm) and Mn (1018–12220 ppm; Mdn 7120 ppm) (Table 15a-b).

The X_{Mg}-content in Cal1 shows the same values (0.003) for average and median (**Figure 21b**) (Table 14).

The rare earth elements+Y (REE+Y) present in Cal1 have been divided into light LREE (8.17–884.50 ppm), intermediate MREE (4.30–204.69 ppm), and heavy HREE (1.17–34.94 ppm) (Table 15a). Among the REE+Y, the contents of Y (6.71–310.20 ppm; Mdn 118.70 ppm), La (1.67–190 ppm; Mdn 30.10 ppm), Ce (3.74–418 ppm; Mdn 76.20 ppm) and Nd (2.24–224 ppm; Mdn 44.25 ppm) are the highest. The REE+Y have been normalized according to PAAS (McLennan, 2001) to obtain REE+Y patterns and identify anomalies (**Figure 21a**; Table 16). Cal1 shows slightly negative anomaly for Ce/Ce* (0.27–1.28; Mdn 0.86), positive anomalies for Eu/Eu* (0.82–2.37; Mdn 1.41) and small positive anomaly for Y/Y* (0.87–1.23; Mdn 1.07), with high Y/Ho ratio values ranging from 27.31 to 39.16 (Table 15b).

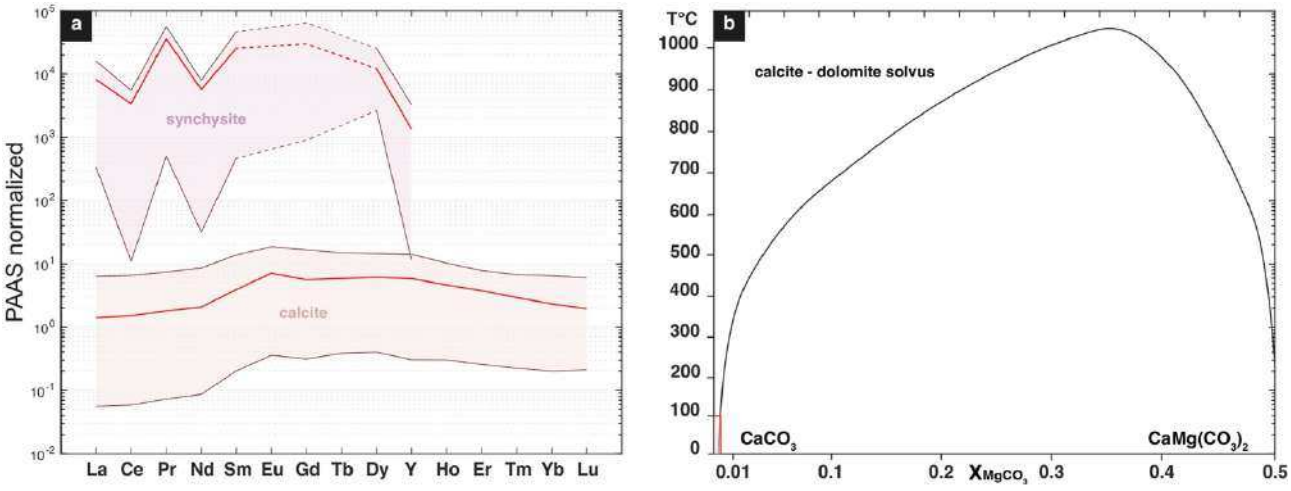

Figure 21. Calcite (and REE-F-carbonate) diagrams. (a) PAAS normalized patterns of carbonates of LGB. **(b)** Calcite-dolomite solvus curve to estimate the temperature formation of Cal1.

6.9.2. REE-F-carbonate

Calcite (Cal1) at LGB contains sporadic REE-F-carbonate crystals (**Figure 22a**). This has not been observed in samples from FAR due to the low presence of Cal1. Being optically "invisible", with a refractive index and colour similar to calcite (**Figure 22b**), the REE-F-carbonate crystals were first identified by BSE images and WDS analyses. They exhibit a crystal habit, from acicular-lamellar to tubular-hexagonal prismatic, with sizes between 20 – 60 μm in length and 2 – 30 μm in width (**Figure 22c-e**), similar to others findings (Mondillo et al., 2015; Uher et al., 2015; Alles et al., 2019). Because of their size, XRD and LA-ICP-MS analyses were not carried out.

EPMA analyses show that these crystals have high contents of Y (0.05–8.89 wt.%; Mdn 3.99 wt.%), La (0.20–9.70 wt.%; Mdn 5.18 wt.%), Ce (0.75–17.56 wt.%; Mdn 12.94 wt.%) and Nd (0.46–8.11 wt.%; Mdn 6.76 wt.%). Meanwhile, Pr, Sm, Gd and Dy are below 4.21 wt.% (Table 16). The values of the La/Ce and La/Nd ratios range between 0.27–0.55 and 0.44–1.45, respectively (Table 16). The results wereb also calculated as oxide, for comparison with REE_2O_3/CaO ratio values of different REE-F-carbonates, confirming that the crystals are compatible with synchysite (**Figure 22f**; Table 16). As for calcite, REE+Y in synchysite have been normalized according to PAAS (McLennan, 2001) (**Figure 21a**).

For further confirmation, Raman spectroscopy has been applied to one of the identified crystals, and the Raman spectrum was compared with a reference spectrum from the RRUFF database (**Figure 22g**). The Raman spectrum of the identified REE-Fcarbonate, showing peak positions at (272, 742, 756, 1083, 1101 cm^{-1}), agrees to the reference spectrum of synchysite and differs from the spectra of other REE-F-carbonates such as parisite and bastnäsite (**Figure 22g**).

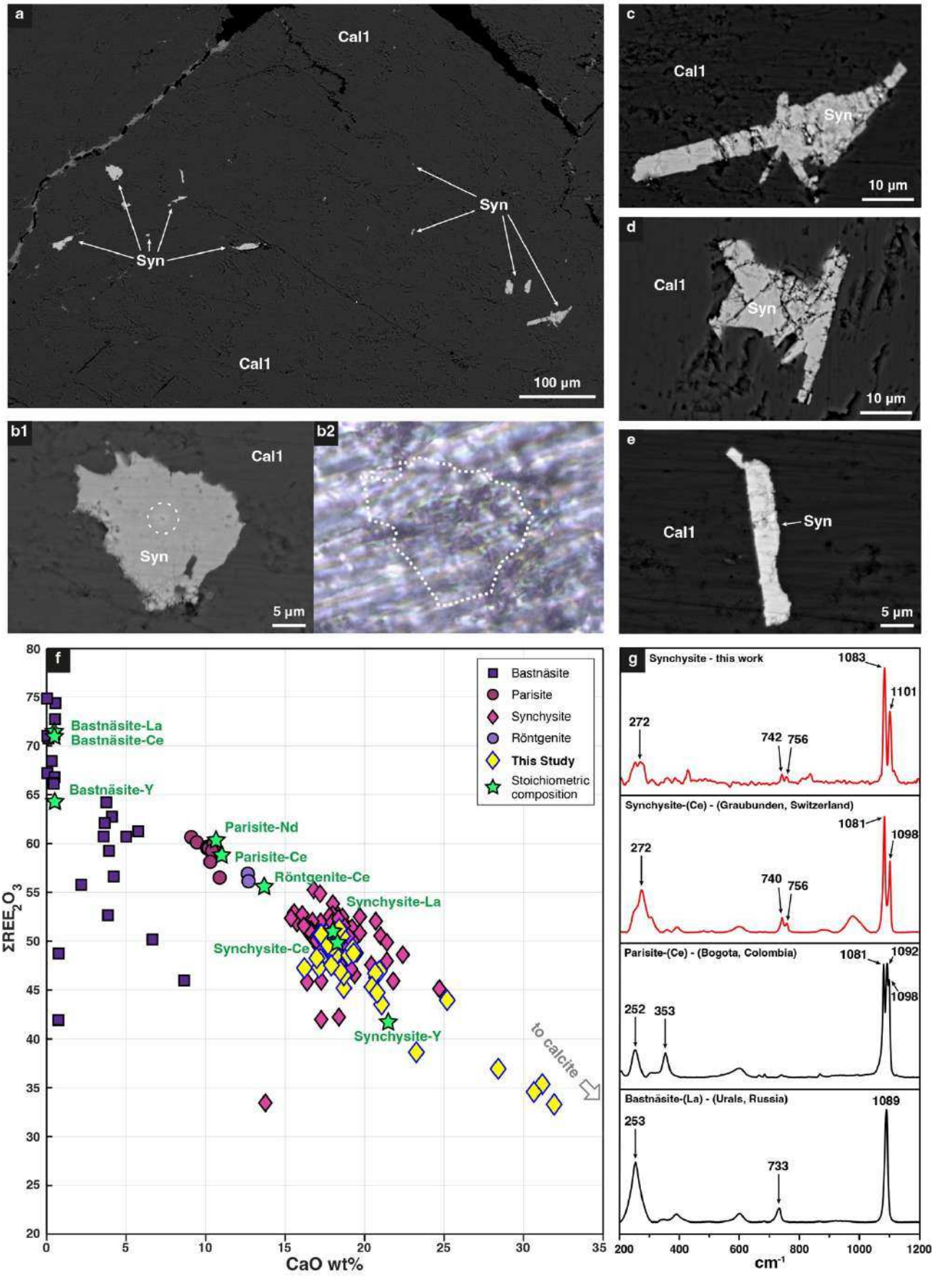
a
Cal1
Syn
Syn
Cal1
100 µm
b1
Cal1
Syn
5 µm
b2
c
Cal1
Syn
10 µm
d
Cal1
Syn
10 µm
e
Cal1
Syn
5 µm
f
Bastnäsite
Parisite
Synchysite
Röntgenite
This Study
Stoichiometric composition
Bastnäsite-La
Bastnäsite-Ce
Bastnäsite-Y
Parisite-Nd
Parisite-Ce
Röntgenite-Ce
Synchysite-La
Synchysite-Ce
Synchysite-Y
to calcite
ΣREE2O3
CaO wt%
g
Synchysite - this work
1083
1101
272
742
756
Synchysite-(Ce) - (Graubunden, Switzerland)
1081
1098
272
740
756
Parisite-(Ce) - (Bogota, Colombia)
1081
1092
1098
252
353
Bastnäsite-(La) - (Urals, Russia)
1089
253
733
cm-1

6.10. Fluorite

LA-ICP-MS analyses performed on fluorite (Flr) veins from FAR (**Figure 6l**) showed a total content of REE + Y trace elements ranging from 18.75 to 502.81 ppm (Table 17a). Specifically, ΣLREE (10.80–291.40 ppm), ΣMREE (3.58–230.79 ppm), and ΣHREE (0.59–32.32 ppm), with Y as the most abundant trace element in fluorite (18.80–481 ppm; Mdn 230 ppm) (Table 17a).

The REE+Y have been normalized according to PAAS (McLennan, 2001) to obtain REE+Y patterns and identify anomalies (**Figure 23a**; Table 17b). Fluorite shows a negative anomaly for Ce/Ce* (0.10–0.81; Mdn 0.46), positive anomalies for Eu/Eu* (1.65–2.82; Mdn 2.16) and Y/Y* (1.34–3.09; Mdn 2.43), with Tb/La and Tb/Ca ratio values of 0.05–0.52 and (0.0–2.0) × 10^{-5}, respectively (**Figure 23b**, Table 17b).

Figure 22 (previous page). REE-F-carbonate descriptive panel. (a) Distribution of the synchysite crystals within Cal1; BSE image. **(b)** Comparison of a synchysite crystal observed in BSE (b1) and through polarized light (PPL) (b2). Decomposition of the mineral can be observed in the center of the crystal after EPMA measuring (dotted circle in b1). **(c)** Aggregates of tabular and acicular crystals. **(d)** Aggregates of tabular crystals, including one in basal section. **(e)** Small isolated tabular crystal. Images (c-e) are BSE. **(f)** REE_2O_3 vs CaO diagram (wt.%) (after Alles et al., 2019) with EPMA data of the synchysite from this study plotted with other fluorocarbonates in the literature [Zaitsev et al., 1998; Forster, 2001; Guastoni et al., 2009; Savko et al., 2011; Augè et al., 2014; Li and Zhou, 2015; Mondillo et al., 2015; Uher et al., 2015; Bernaouda et al., 2017; Broom-Fendley et al., 2017; Schmandt e tal., 2017; Alles et al., 2019; Zeug et al., 2020]. **(g)** Raman spectrum of the synchrisite crystal shown in Figure 22b, compared with reference material from the RRUFF database (highlighting representative Raman peaks), i.e., synchysite-(Ce) (ID: R060971 / 532 nm), parisite-(Ce) (ID: R050308 / 532 nm) and bastnäsite-(La) (ID: R070142 / 532 nm).

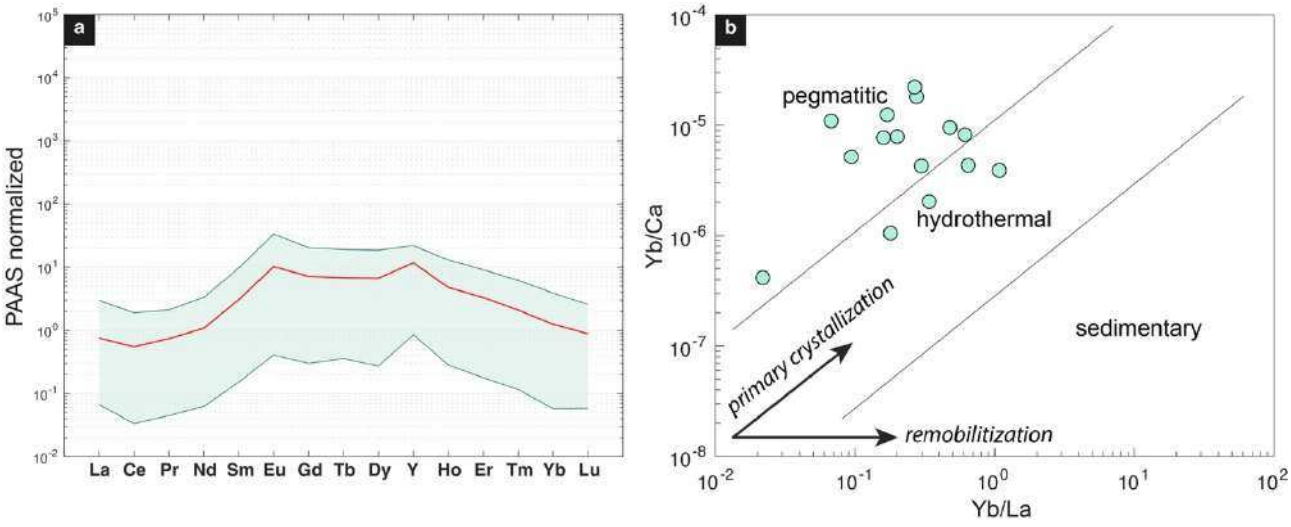

Figure 23. Fluorite diagrams. (a) PAAS normalized patterns of fluorite of FAR. **(b)** Yb/Ca vs Yb/La diagram of fluorite.

6.11. Fluid inclusion analyses

6.11.1. Sphalerite

Petrography of fluid inclusions was studied in sphalerite Sp1 and Sp2 of the LGB06 sample from Longobucco. Sphalerite FIs show ovoid, elongated and rarely negative crystal shapes, with dimensions mostly below size 5 μm, and sporadically up to 20 μm (**Figure 24a-f**). The few larger inclusions (i.e., those up to 20 μm) are often elongated and 3 μm wide (**Figure 24f**). Fluid inclusions in sphalerite FIs are mainly distributed along trails (**Figure 24a**), occasionally in clusters (**Figure 24b**) and are rarely isolate. At room temperature, most fluid inclusions are aqueous two-phase liquid-rich (L+V), even though for inclusions smaller than 3 μm in size, it is impossible to assess the presence of a vapor bubble (**Figure 24a, c-d**). A few two-phase (V+L) vapour-rich (**Figure 24e**) and mono-phase liquid L (**Figure 24c, e**) FIs were also observed. In some cases, elongated monophase liquid L inclusions tend to distribute along the {111} crystal planes (**Figure 24c-d**). They are associated with tens to many hundreds of μm long, and 2–4 μm wide, tubular inclusions, namely "channel-inclusions" (More et al., 1991), that are distributed along the same {111} planes. The latter might be precursor of the abovementioned elongated inclusions, but not yet affected by necking-down (**Figure 24b-d**) (Roedder, 1962; Bodnar, 2003). Unfortunately, fluid inclusions in sphalerite could not be analyzed by microthermometry because they are very small and hidden by the mineral colour.

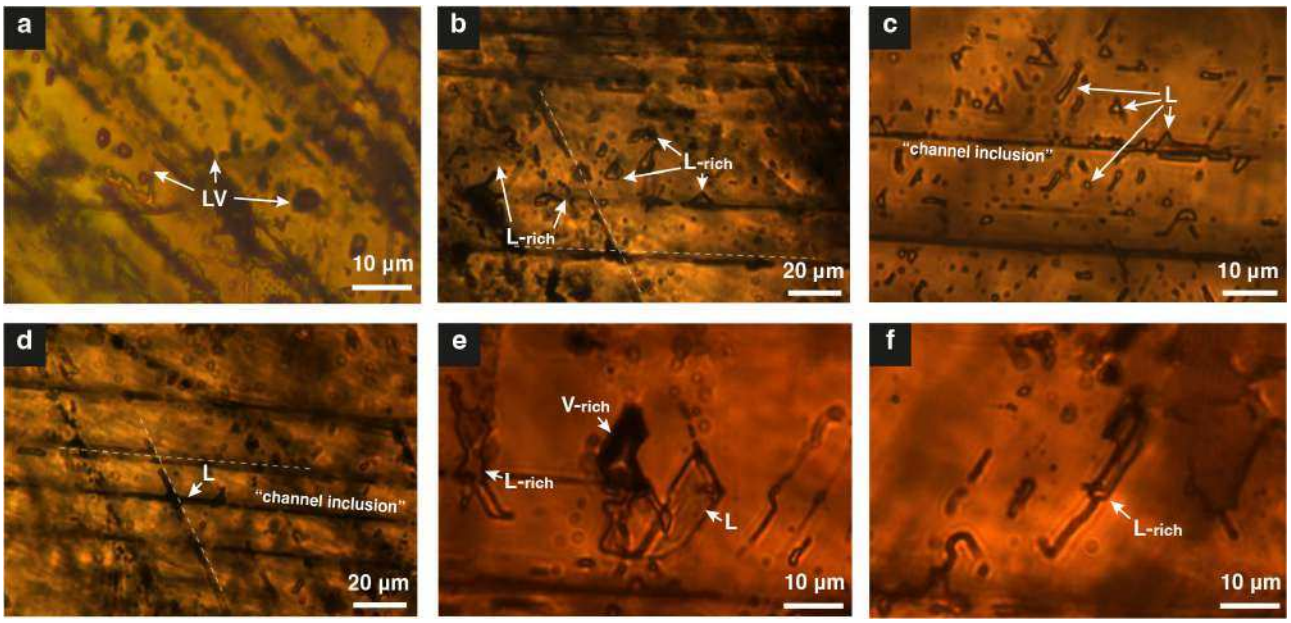

Figure 24. Optical micrographs of fluid inclusions observed in sphalerite. (a) Trail of LV-FIs (magnification 50x). (b) Cluster of L-rich FIs (magnification 50x). (c) "Channel" of monophase-L FIs (magnification 100x). (d) "Channel inclusions" distributed along the {111} crystal planes (magnification 50x). (e) Some "big" FIs in sphalerite (magnification 100x). (f) Elongated L-rich FI (magnification 100x).

6.11.2. Fluorite

Fluid inclusion analyses were performed on three fluorite samples from Fonte Argentila: i) FA11-Flr-E, corresponding to the core of an euhedral crystal from the damage zone; ii) FA14-Flr-E, corresponding to the rim of an euhedral crystal; iii) FA14-Flr-F, a fractured crystal (**Figure 25**; Table 18). For each sample, 3 distinct FIAs were identified by textural analyses, and subsequently analyzed by microthermometry (**Figure 25**; Table 18).

Fluid inclusions in fluorite are abundant and vary in size from 2 to 50 μm (**Figure 25e-i**). Since fluorite crystals are often fractured (**Figure 25b-c**), it is difficult to identify a distribution pattern that correlates with crystal growth. However, where fluorite crystals preserve their habitus (**Figure 25a, d**), primary inclusions were observed along planes and directions of crystal growth (**Figure 25f**). Many pseudo-secondary trails (**Figure 25e-f, i**), cross-cutting the alignments of primary inclusions, were identified (**Figure 25i**). Most inclusions exhibit irregular-angular shapes (**Figure 25i**), although rounded or negative crystal forms are also present (**Figure 25g**).

Fractured fluorite contains higher density of fluid inclusions compared to euhedral fluorite.

At room temperature, two types of fluid inclusions have been distinguished: (i) trails of monophase liquid (L), often with negative crystal shapes (**Figure 25e, f**); (ii) trails of two-phase liquid+vapour (L+V), L-rich inclusions, predominantly with irregular shapes, with no apparent link to growth features (**Figure 25f-i**).

Type (i) inclusions are abundant in fluorite, with sizes ranging from 3 to 10 μm. Upon cooling, a water bubble nucleated in some FIs that were monophase L at room temperature (i.e., FIAs yellow in **Figure 25h**). Type (ii) inclusions are characterized by a volume of the vapour phase between 5 and 10% of the inclusion total volume, and with size usually ≤ 10 μm, sporadically up to 40-50 μm also occur within fluorite (**Figure 25g, i**).

In fluorite, a total number of 67 FIs (belonging to 3 FIAs for each sample) were analysed by microthermometry (Table 18). Due to the predominant small size of FIs in fluorite, microthermometry analyses were carefully performed by making slow heating cycles to measure the homogenization temperatures (T_h) before the cooling cycles to measure the final ice melting temperatures (T_{mi}).

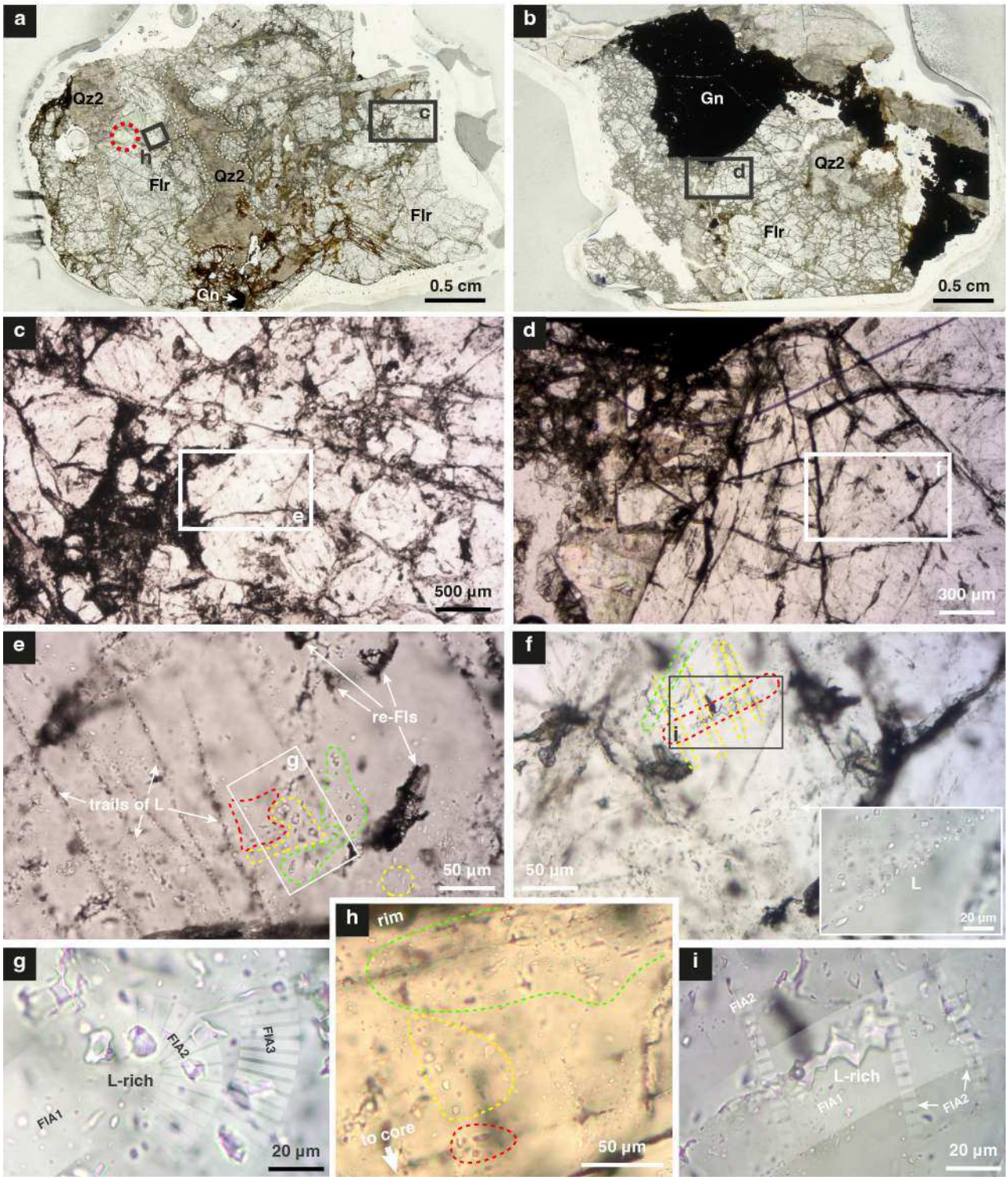

Figure 25. Fluid inclusion analyzed in fluorite. (a) Thick section scan (PPL) of FA14a sample; dashed red circle is the analyzed area for Qz2 (see Figure 26). **(b)** Thick section scan (PPL) of FA11f sample. **(c)** Detail of brecciated fluorite area. **(d)** Detail of less deformed fluorite crystal. **(e)** Areal detail in which it is possible to observe the FIAs analyzed (red-FA14flrE_FIA1; yellow-FA14flrE_FIA2; green-FA14flrE_FIA3); monophase-L inclusion trails are also present. **(f)** Areal detail in which it is possible to observe the FIAs analyzed (red-FA11flrE_FIA1; yellow-FA11flrE_FIA2; green-FA11flrE_FIA3); in detail is shown a monophase-L inclusion trail. **(g)** High magnification images (50x) of analyzed FIAs in FA14a sample. **(h)** Areal detail where it is possible to observe the FIAs analyzed, near the edge of the mineral (red-FA14flrF_FIA1; yellow-FA14flrF _FIA2; green-FA14flrF _FIA3). **(i)** High magnification images (50x) of analyzed FIAs in FA11f sample.

On the contrary, for those inclusions that were monophase liquid at room temperature and where the vapour bubble nucleated upon cooling, only T_{mi} values were measured. In addition, for small FIs with very low salinities, T_{mi} could not be accurately measured because of metastability phenomena, which cause the vapor bubble to disappear upon cooling and suddenly reappear upon heating to temperatures above 0 °C (e.g., for FIA1 and FIA3 of sample FA14-FlrF; Table 18). All this resulted in a limited number of FIs for which both T_h and T_{mi} data were collected, which could be plotted in the T_h vs. salinity graph (**Figure 27**). To get a complete view of all the data collected, the results obtained from the FIAs of all the samples analyzed were reported in cumulative histograms and box-plots of T_h and salinity values (**Figure 27**; **Figure 28a-e**).

For fluorite fluid inclusions, the results fall within the total ranges 72.2-114.6 °C for T_h and 0-21.2 wt% NaCl eq. for salinities. The highest salinity fluids (12.8-21.2 wt% NaCl eq.) are mainly entrapped in FIAs along PS trails (**Figure 25c, f**; **Figure 27**; **Figure 28a-b**; Table 18). Upon cooling, a water bubble nucleated in some FIs, that were monophase at room temperature, along PS trails; salinities of these inclusions are in the 2.6-4.5 wt% NaCl eq. range (**Figure 27**; **Figure 28a, d**; Table 18).

6.11.3. Quartz

Fluid inclusions in quartz are present in both Qz1 and Qz2 (**Figure 19d-f**; **Figure 26c-h**). In both cases, most inclusions do not exceed 6 μm in size and show round, elongated, branched and irregular shapes (**Figure 19d-f**; **Figure 26c-h**).

Within the Qz1 crystals, the inclusions exhibit homogeneous characteristics and dimensions (up to 5 μm) (**Figure 19e**). Primary FIs along crystal growth planes and secondary FIs healing fractures are observed within Qz1 (**Figure 19e-f**). The high density of FIs and their small size make many Qz1 crystals to appear optically opaque in thin section (**Figure 19e**), and "milky" in hand specimens (**Figure 5b-c**, **e**). The prevailing small size of FIs characterizing Qz1 prevents a precise distinction between monophase and two-phase inclusions at room temperature and make them unsuitable for microthermometry analyses.

The Qz2, despite showing widespread microcrystalline portions (**Figure 6l**) similar to chalcedony in old open cavities between fluorite crystals, also forms large euhedral zoned quartz crystals (**Figure 6l**; **Figure 26a-b**). In the microcrystalline Qz2, optical observations of fluid inclusions were hindered. On the contrary, it was possible to observe and analyze fluid inclusions in the Qz2 large euhedral crystals. In general, two types of fluid inclusions have been distinguished within euhedral Qz2 crystals: (i) two-phase, liquid+vapour (L+V), liquid-rich inclusions arranged in clusters, along growth

planes or healed fractures, with sizes up to 10 μm (**Figure 26c-h**); (ii) monophase liquid inclusions along the edges of the euhedral crystals (**Figure 26c**).

Inclusions of the first type are often arranged in clusters within growth zones or along growth bands (i.e., they are primary inclusions (**Figure 26b-g**). Fluid inclusions of the second type are aligned parallel to the edges (close to the rim) of the euhedral Qz2 crystals and they are considered also primary (**Figure 26g**). The absence of a vapor phase in this type of inclusions likely resulted from failure of bubble nucleation due to metastability processes, which usually characterize aqueous fluid inclusions with high fluid density (Roedder, 1984; Goldstein and Reynolds, 1994).

Microthermometric analyses in Qz2 were performed on the primary two-phase FIs spatially associated to six growth zones of an euhedral crystal, occur in clusters within growth zones and aligned within single growth bands, from Fonte Argentila (namely, FA14-qz2; **Figure 26**). A total number of 163 biphasic L-rich fluid inclusions forming 7 FIAs were analysed in the FA14-qz2 sample (**Figure 26**; Table 19).

As for fluorite, due to the small size of fluid inclusions, heating cycles were made before freezing cycles, to avoid producing overpressure inside inclusions which could cause stretching and volume changes of the small FIs. For quartz analyses, only in a few cases (usually in smaller inclusions), fluid inclusions in Qz2 showed the metastability phenomena described for Flr inclusions during ice melting.

For Qz2 fluid inclusions, the results fall within the total ranges 111.6-163.8 °C for T_h and 0.5-6.1 wt% NaCl eq. for salinities (**Figure 27**; **Figure 28a, e**; Table 19). In addition, oscillations in the T_h values are observed from the core to the rim (particularly crossing the growth bands) of the zoned FA14-qz2 crystal (**Figure 26**; **Figure 28a, c**). In some cases, different FIs show distinct mean T_h and T_{mi} values within single bands; an example is shown in figure S3d where four FIAs (4a-d) associated to the same growth band are characterized by relatively different mean T_h and T_{mi} values (**Figure 26c-d**). We also noted that the fifth growth zone is characterized by relatively low T_h mean (122.8°C) (**Figure 28c**; Table 19), whereas within the sixth growth zone close to crystal rim (with mean T_h value of 129.9°C), a cluster (FIA 7) with relatively high mean T_h (145.4°C) is present (**Figure 26c, g**). Finally, mono-phase liquid-only inclusions occur at the edge of the crystal, typical of fluid trapped at low-temperature (< 100°C for inclusions with size < 20 μm, Roedder, 1984).

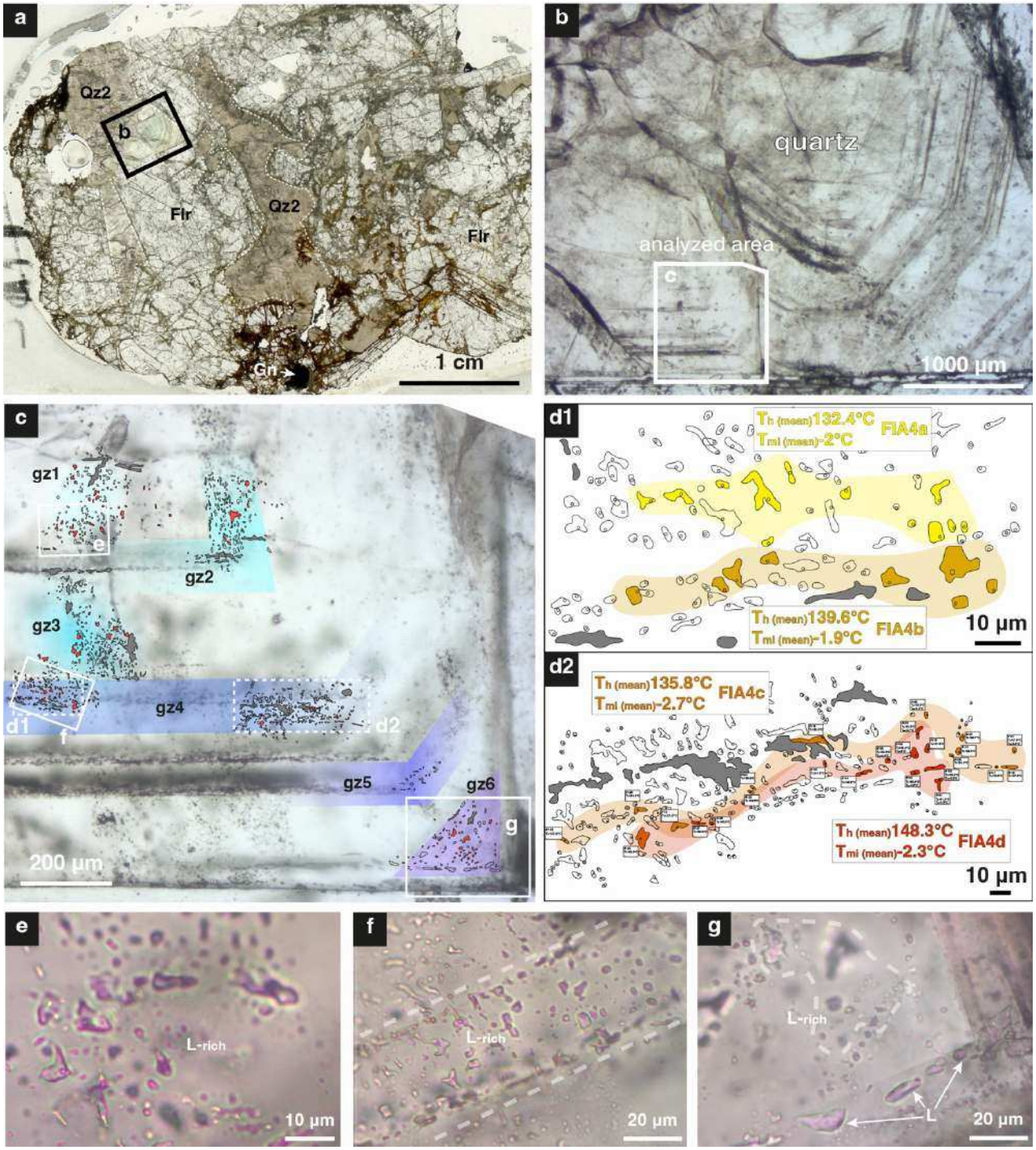

Figure 26. Fluid inclusion analyzed in quartz-2. (a) Thick section scan (PPL) of FA14a sample. **(b)** Detail of euhedral quartz area. **(c)** Detail of inner-to-outer part of the quartz crystal; on the microphotograph are indicated the analyzed growth zones (gz1-6) and reported the fluid inclusion maps. **(d1)** Detailed map of gz4 with FIAs4a-b. **(d2)** Detailed map of gz4 with FIAs4c-d. **(e)** High magnification images (50x) of the gz1 with a detail of the FIA1a. **(f)** High magnification images (50x) of the gz4 with a detail of the FIAs4a-b. **(g)** High magnification images (50x) of the gz6 with a cluster (FIA7) with higher temperature within FIA6; on the edge of the quartz are present monophase-L inclusions.

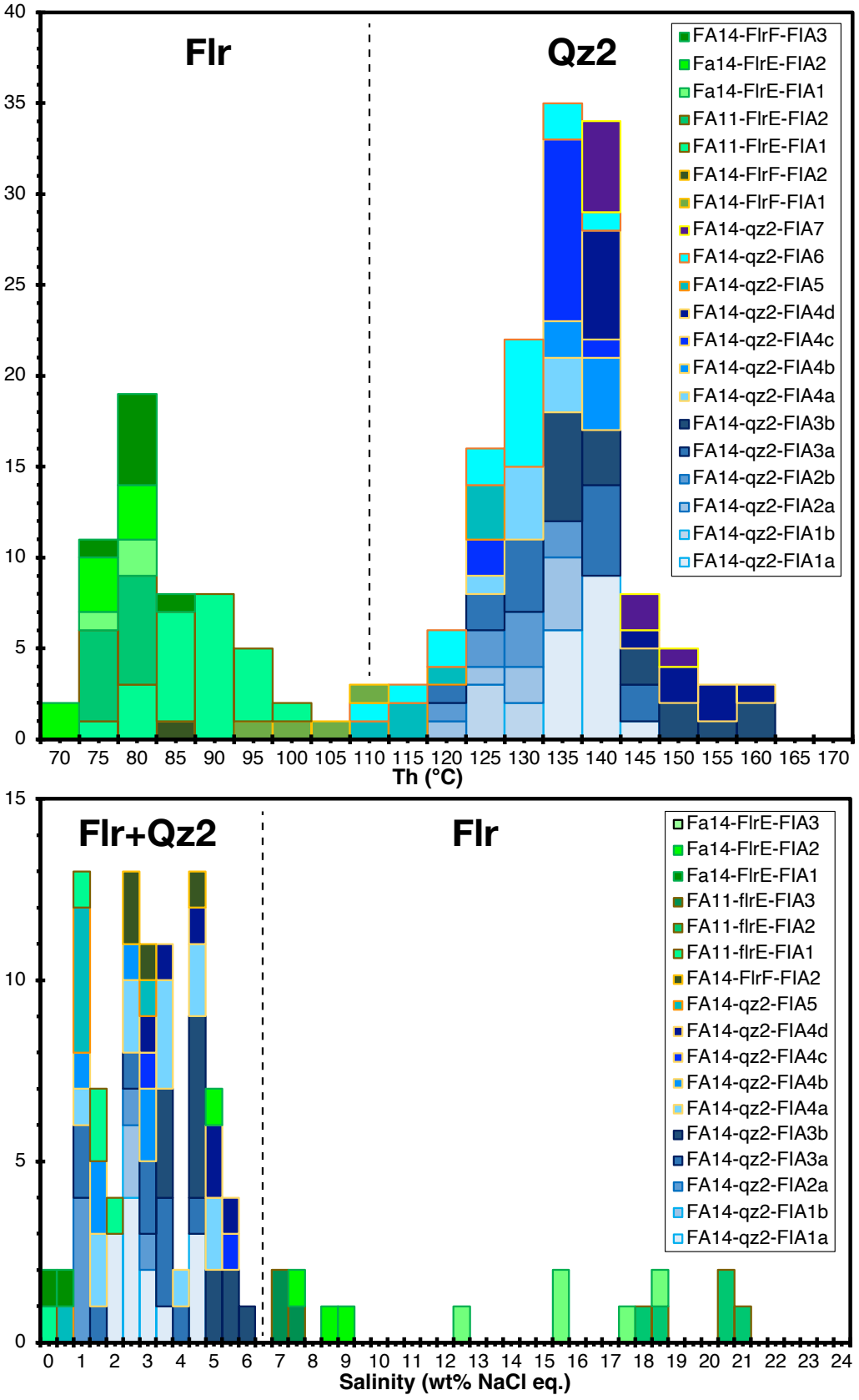

Figure 27. Frequency histograms of homogenization temperature (T_h °C) vs. salinity (wt% NaCl eq.) of fluid inclusions analyzed in fluorite and quartz-2. Histogram of T_h and histograms of salinity vs. n° of measurements.

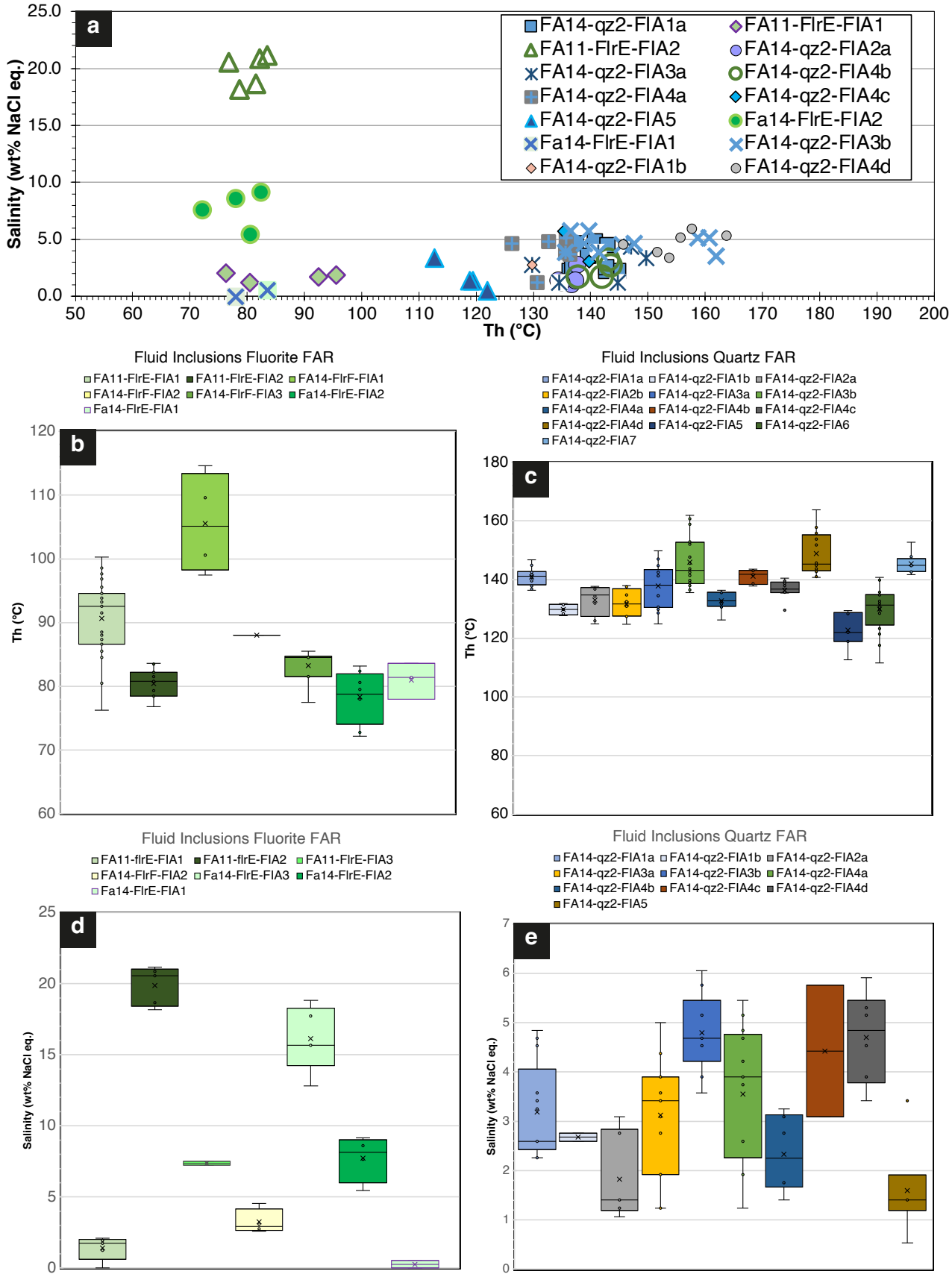

Figure 28. Diagram and boxplots of homogenization temperatures and salinities of Fluid Inclusion Assemblages (FIAs) analysed in fluorite and quartz-2. (a) Scattered diagram with T_h vs. salinity. **(b-e)** Boxplots of T_h and salinity of fluorite and quartz-2 fluid inclusions.

7. Discussions

7.1. Crystal chemical and spectroscopic features of sphalerite

7.1.1. Optical anomalies in sphalerite

Although sphalerite (β-ZnS) is cubic optical anisotropies have been observed in the LGB and FAR sphalerites, classified as gridiron-type (Figure 8a, c) or *en echelon* (Figure 8b) textures (Seal et al., 1985). It is not rare for cubic minerals to show optical anomalies. For instance, Antao et al. (2015) and Schingaro et al. (2016), using XRPD, have found that both Ti-bearing and Ti-free garnets can actually be a mixture of two or more cubic phases with slightly different cell parameters and composition. The consequent structural mismatch causes strain that results in low-to-strong degree of optical anisotropy (birefringence). The occurrence of optical anomalies in sphalerite has been well documented in the literature (Roedder, 1968; Fleet, 1977; Seal et al., 1985; More et al., 1991; Lavrentyev et al., 2006).

Several factors could explain this phenomenon: (i) stacking disorder at nanoscale, with interleaved stacking sequences of sphalerite and wurtzite (Fleet, 1977); (ii) structural defects such as stacking faults and twinning (Seal et al., 1985); (iii) pressure from a deformative (or more) event could induce strain in the cubic crystal lattice, altering the mineral's optical properties (Lavrentyev et al., 2007). The occurrence of multiple substitution involving Fe, Cd and Cu could cause strain of the sphalerite crystal lattice (see also below) leading to optical anisotropy (birefringence). In our samples Fe occurs up to 11.27 wt.% and is associated with locally high concentrations of Cd (up to 0.69 wt.%) and Cu (up to 0.45 wt.%), leading to cell parameters that can be as large as 5.4230 ± 0.0046 Å (Table 4). Furthermore, also the factor (iii) above can be relevant in LGB and FAR sphalerites that might have recorded multiple deformational events, both synchronous and post-paragenetic sequence, likely causing strains at the crystal lattice.

7.1.2. SCXRD and XRPD data

The cell parameters obtained for sphalerite in this study align with those documented in the literature (ranging from 5.398 to 5.425 Å) (Kullerud, 1953; Smith, 1955; Skinner, 1961). Although Fe commonly substitutes in sphalerite, given its ionic radius of 0.63 Å compared to zinc's (Zn^{2+}) 0.60 Å in tetrahedral coordination, the effect of FeS content on sphalerite's cell parameters has been researched extensively. This includes studies on both synthetic and natural samples (refer to

Chareev et al., 2017; Lepetit et al., 2003; Osadchii and Gorbaty, 2010, among others). However, a definitive resolution remains elusive. Most systematic work has focused on synthetic samples. Chareev et al. (2017) identified a parabolic relationship between cell parameters and FeS (mol%) in synthetic sphalerite, whereas Lepetit et al. (2003) and Osadchii and Gorbaty (2010) described this relationship as linear, albeit with varying slopes depending on Fe concentration (see **Figure 29a**).

In natural samples, the situation becomes more complex due to heterogeneous atomic substitutions, such as Fe and Cd replacing Zn (Di Benedetto et al., 2005a, 2005b). Di Benedetto et al. (2005a) used Mössbauer spectroscopy to demonstrate that Fe distribution in natural sphalerite is non-random, even at low Fe concentrations (XFe < 0.06 apfu). Fe^{2+} can exist in three distinct local environments: isolated Fe^{2+}, Fe^{2+}-Fe^{2+} pairs, or Fe^{2+} clusters. The authors caution that, in cases of strong chemical zoning, point analyses like WDS/EPMA or EDS/SEM might not accurately reflect the bulk composition of samples, recommending Atomic Absorption Spectrometry unless a large number of point analyses are conducted. Di Benedetto et al. (2005b) also discuss non-random distributions for other Zn substituents in sphalerite, such as Mn, Cd, Cu, and Hg.

For the samples in this study, comparisons between SEM and EPMA data are presented in Table 4. SEM data were collected on individual sphalerite fragments, while EPMA data refer to matched areas of the zone where the mineral fragments were taken. The imperfect correlation between assigned colour and composition (**Figure 29**) is attributable to the qualitative assignment of colour growth bands on a 100 μm-thick section, which makes the true colour assignment difficult.

Figure 29 illustrates our samples plotted on the diagrams from Lepetit et al. (2003) and Osadchii and Gorbaty (2010), including both SEM (**Figure 29a**) and EPMA (**Figure 29b**) data. The data generally follow a linear trend, clustering near the low-Fe content curves from previous studies, with a slight deviation observed for three fragments (B2, D1, D3) of sphalerite (**Figure 29a-b**). As previously discussed, accurately determining Fe and other metal contents is challenging due to chemical variability within sphalerite crystals, even within individual fragments (50x100 μm).

The cell parameter values may be subject to greater error than usual due to (**Figure 14a**) stacking faults and the presence of multiple nano-domains that may be tilted, rotated, or involve different cell parameters (De Vries et al., 2013). Larger cell parameters relative to observed Fe content suggest the presence of other cations contributing to cell expansion, such as Cd, which has an ionic radius of 0.78 Å (Skinner, 1961). In our samples, Cd content reaches up to 0.89 wt.%, while significant expansions compared to Fe content are anticipated for Cd concentrations exceeding 1 wt.% (**Figure 29d**) (Babedi et al., 2021).

In conclusion, establishing the correlation between Fe content and corresponding cell parameters in natural sphalerites is complex. These minerals not only contain Fe replacing Zn but also involve cations like Mn, Co, Cu, and Cd (Table 1a-b, 6a-b) (Jimenez-Sandoval et al., 2003; Di Benedetto et al., 2005a, 2005b; Buzatu et al., 2013; Babedi et al., 2019, 2021). Di Benedetto et al. (2005b) investigated compositional zoning in natural sphalerite crystals and identified intricate patterns resulting from interactions between Zn and minor/trace element substitutes, as well as among the minor or trace elements themselves. For example, they found homogeneous Cd distribution in Mn-rich sphalerites and oscillatory Fe and Cd distribution in Mn-free samples.

In our case the presence of aggregates of localized CdS phases or exsolutions within the sphalerite may have not been detected during EPMA data collection. However, additional peaks have been found in the XRPD patterns of a couple of samples (**Figure 13**) at the following Bragg positions (2θ) 26.65°, 27.02°, 27.43°, 28.29°, 47.22°, 48.55°. As shown in **Figure 13**, these possible mineral phases present locally in the sphalerite can be referred to: hawleyite (Fm3-m), for peaks 2θ 47.13° and 48.54°; CdFeS phase (F-43m), for peak 2θ 27.44°; CdZnS phase (P-4m2), for peak 2θ 27.43°.

Finally, the cell parameters and the associated Fe-content, were used to estimate sphalerite formation temperatures, using the equation of Chareev et al. (2017) (3), where a (Å) is the cell parameter and x is the mol% FeS.

(3) $T(^{\circ}C) = ((a - (5.4099 \pm 0.0008) - (5.82 \pm 0.36) \cdot 10^{-4} \cdot x - (-4.7 \pm 0.\ 6) \cdot 10^{-6} \cdot x^2) / (4.2 \pm 0.4) \cdot 10^{-5})) + 25$

As shown in **Figure 29c**, some temperature values deviate from the temperature range obtained through GGIMFis (Frenzel et al., 2016) (**Figure 17**), while the remaining data fall within the range of formation temperatures, which according to the diagram of Chareev et al. (2017) describe temperatures of 76 – 250 °C, with SEM Fe-contents, and 82–208 °C, with EPMA Fe-contents (**Figure 29c**; Table 4). The presence of negative data (D1, D3) would be attributed above exposed problems in relating cell parameters with composition in natural sphalerites.

7.2. Evaluation of Fe-content of sphalerite using *μ*-Raman spectra

The measured Raman spectra (**Figure 11**; **Figure 12**) are consistent with those reported in the literature for both synthetic (Osadchii and Gorbaty, 2010) and natural sphalerite (Hope et al., 2001; Kharbish et al., 2007; Buzatu et al., 2013; Bacík et al., 2023). Specifically, in the selected sphalerite samples (Sp1, Sp2, Sp3), an increase in Fe content (from 0.47 to 10.5 wt.%) results in a decrease

in the intensity of the LO Zn-S vibration mode (~350 cm^{-1}) and a corresponding increase in the LO Fe-S vibration modes Y_1, Y_2, Y_3 (~300, ~310, ~330 cm^{-1}) (Hope et al., 2001; Osadchii and Gorbaty, 2010). Additionally, minor shifts in wavenumber (± 3 cm^{-1}) could be linked to the presence of other metals in trace amounts (e.g., Mn^{2+}, Co^{2+}, Cd^{2+}) (Table 2) (Zigone et al., 1981; Jimenez-Sandoval et al., 2003; Kharbish et al., 2007; Buzatu et al., 2013; Dinca et al., 2022), although no specific Raman bands for these elements have been detected. The Cd content (up to 0.54 wt.%) and Mn content (up to 0.07 wt.%) were second only to Fe, yet they were too low to produce distinct bands, as observed by Kharbish et al. (2007) and Jimenez-Sandoval et al. (2003). In the LGB04h spectrum, which pertains to colorless sphalerite with a Cd content of 0.45 wt.%, a shift of the Y1 mode towards the X mode of Cd (296 cm^{-1}) was observed (Babedi et al., 2019) (**Figure 12**; Table 2).

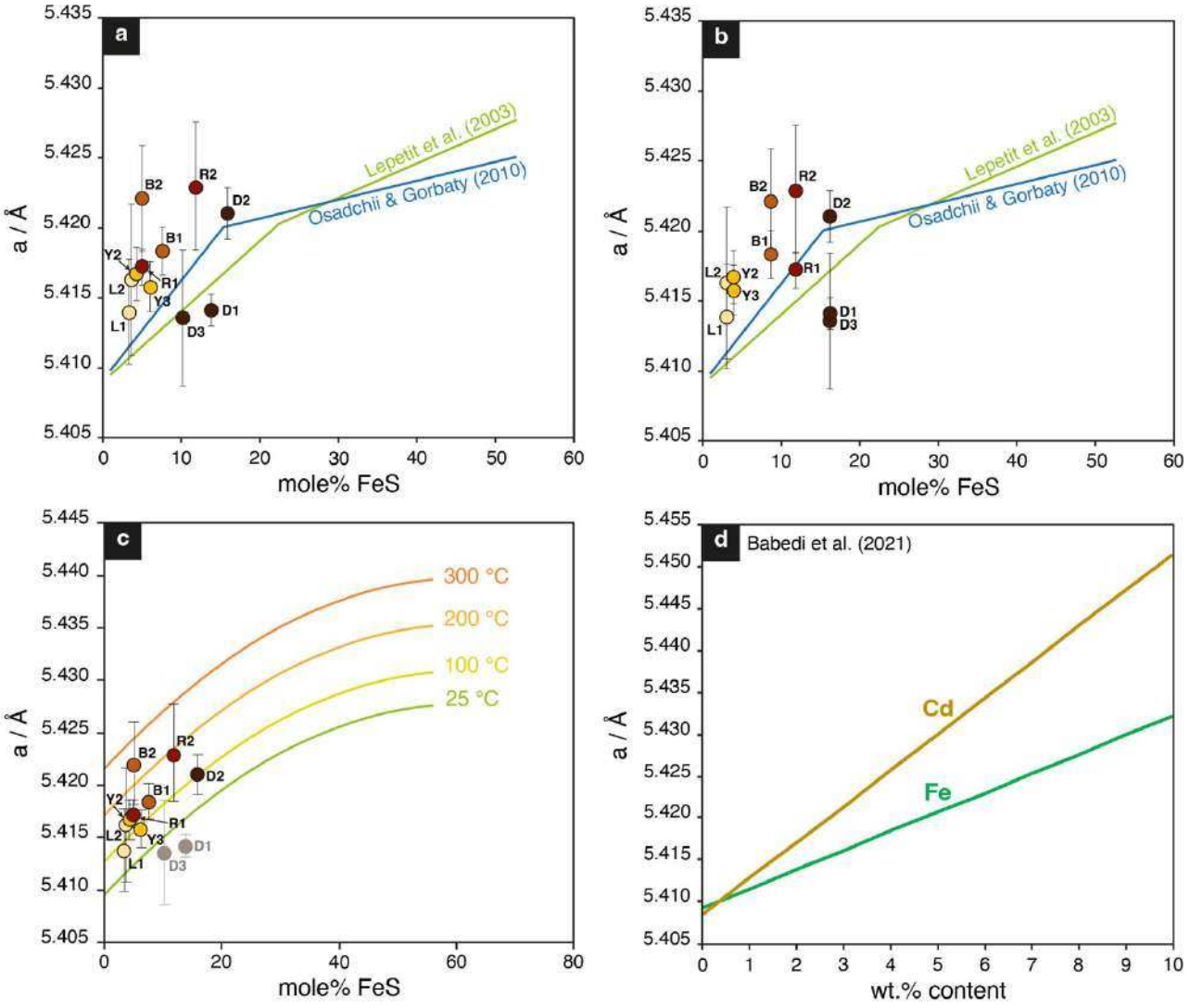

Figure 29. Diagrams of lattice parameter vs chemical composition. (a) Relationship between cell edge and SEM data of mol% FeS of sphalerite compared with literature data obtained from synthetic powder samples (Osadchii and Gorbaty, 2010); **(b)** Same diagram of (a) but with EPMA data of mol% FeS of sphalerite. **(c)** Diagram of lattice parameter-composition dependence at various temperatures (Chareev et al., 2017) (SEM data). Legend: L-light yellow; Y-yellow; B-brown; R-reddish brown; D-dark brown. **(d)** Variation to the unit cell constant as a function of increasing concentration of the respective cation substituents (from Babedi et al., 2021).

Following the fitting procedure for the Raman spectra, as outlined by Osadchii and Gorbaty (2010), the areas (A) and heights (h) of the Raman bands at ~300 cm^{-1} and ~350 cm^{-1}, corresponding to Fe-S (A1-h1) and Zn-S (A3-h3) bonds respectively (Table 2), were used to compare the darta from this study with those existing in literature in relation to Fe content (mol% FeS). The data from this study were plotted on calibration plots from Osadchii and Gorbaty (2010) and Buzatu et al. (2013), which are generally utilized to estimate the Fe-content in Fe-sphalerite. Both the LGB and FAR sphalerite data closely align with the previously described calibration lines (**Figure 30a-b**).

In the A1/A3 versus mol% FeS diagram (**Figure 30a**), sphalerite samples ranging from colorless (W) to brown (B) are positioned close to or on the calibration line, whereas darker sphalerite samples (D) tend to deviate more significantly. Similarly, in the h1/h3 versus mol% FeS diagram (**Figure 30b**), sphalerite samples that are colorless (W) to yellow (Y) align closely with the calibration line, whereas both brown (B) and dark (D) sphalerite exhibit notable deviations. In both diagrams, the regression lines derived from this study, utilizing the A1/A3 ratio (4) and the h1/h3 ratio (5), show only a slight variation in slope compared to those calibrated by Osadchii and Gorbaty (2010), and Buzatu et al. (2013).

(4) $y = 34.738x$ ($R^2 = 0.9814$)

(5) $y = 24.212x$ ($R^2 = 0.9154$)

The agreement of our data with calibration curve from literature is better when band areas ratio is used. The slight deviation observed in the regression data for Fe-rich sphalerites is likely attributed to the challenge of accurately extrapolating the contribution of the Fe-S band during the fitting process. Since the ~350 cm^{-1} band, which is responsible for A3 and h3, it becomes notably weak when Fe contents exceeds 10 wt.% due to interference from other intermediate Raman bands (i.e., ~330 and ~339 cm^{-1}, Fe-S bonds) (**Figure 12**); this complicates the precise measurement of A3 and h3 (Buzatu et al., 2013).

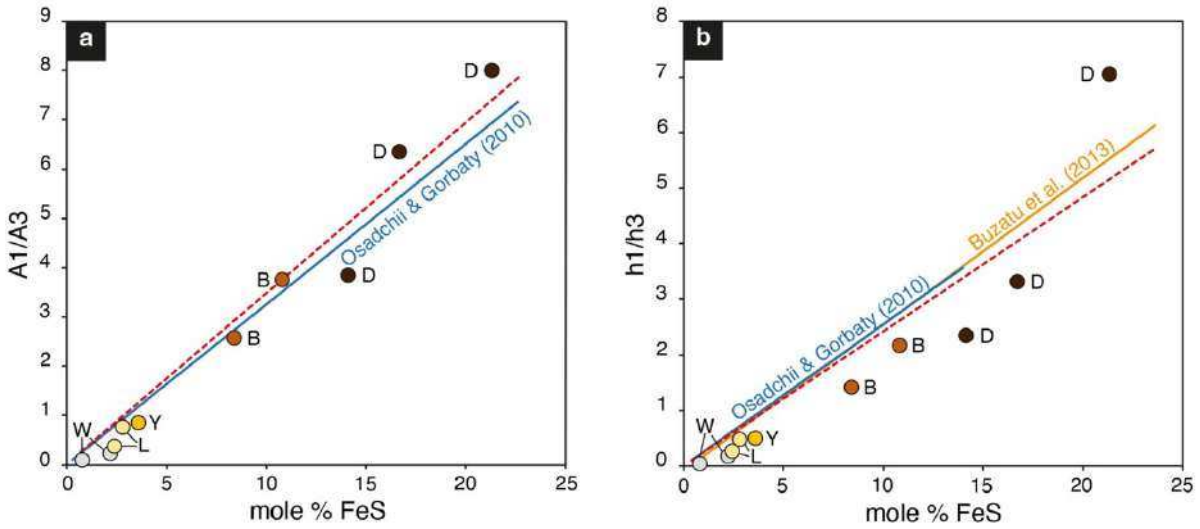

7.3. Minor and trace element distribution in sphalerite

The distribution of minor and trace elements in sphalerite allows conclusions to be drawn about cation substitutions and the presence of growth zones and mineral micro- and nano-inclusions (Cook et al., 2009). The time-resolved LA-ICP-MS compositional profiles obtained on sphalerite (**Figure 15**) evidenced that elements such as Fe, Cd, Mn, and Co are distributed sub-parallel to the Zn-trend, possibly due to cation substitution. On the other hand, elements such as Cu, Ga, Ge, In, Sb, Sn and Pb showed variations across the minerals possibly related to crystal zones or nuggets (Cook et al., 2009) (**Figure 15**). Several studies have investigated how divalent cations (e.g., Mn, Fe, Co, Cd, and Hg) can substitute for Zn in the sphalerite lattice (Di Benedetto et al., 2005a; Cook et al., 2009; Belissont et al., 2014, 2016; George et al., 2016), and the strong negative Zn-Fe correlation (R^2 = 0.971) shown in **Figure 31a**, is indeed predominant. Also, Mn^{2+} (R^2 = 0.764), and to a lesser extent, Co^{2+} (R^2 = 0.654) and Cd^{2+} (R^2 = 0.507) show a negative correlation with Zn (**Figure 31b-d**). Moreover, Hg^{2+} can substitute for Zn^{2+} in the sphalerite structure (Grammatikopoulos et al., 2006; Sokol et al., 2021), but the low positive correlation (R^2 = 0.460) shown in **Figure 31e** suggests competing interactions occurring between other Zn substituents (cfr. Fe-Hg correlation documented in De Benedetto et al., 2005a). In addition, Zn may be involved in heterovalent substitutions with cations like Cu^{+}, Ga^{3+}, Ge^{4+} (**Figure 31**). There is apparently no correlation of Cu with Zn (R^2 = 0.021) or other divalent cations (**Figure 31f**). This also holds for Ga and Ge that do not show any correlation with Zn (R^2 = 0.033 and 0.008, respectively) (**Figure 31g, h**). Missing Cu-Zn and Ge-Zn correlations might be interpreted as due to the presence of Cu-Ge-bearing mineral nano-inclusions within sphalerite or complex cations substitutions (Cugerone et al., 2021; Fougerouse et al., 2023). A strong positive correlation (R^2 = 0.865) of Ge with Cu is observed (**Figure 31i**), showing Ge/Cu ratios close to 0.5. According to Bonnet et al. (2016) these Ge/Cu values could suggest that the $2Cu^{+} + Ge^{4+} \leftrightarrow 3Zn^{2+}$ substitution operated. In addition, Ge seems negatively correlated to Cd in the Sp2 (R^2 = 0.757) (**Figure 31k**). Gallium is not generally correlated with Cu (R^2 = 0.158); a positive correlation of Ga and Cu (R^2 = 0.872) is observed only for the dark brown sphalerite (**Figure 31j**). Our data only partially plot close to the line Ga/Cu = 1 ratio (**Figure 31j**), corresponding to a substitution $Cu^{+} + Ga^{3+} \leftrightarrow 2Zn^{2+}$ (Bonnet et al., 2016). Finally, the incorporation mechanism of Pb in sphalerite remains unclear (Cook et al., 2009; Liu et a., 2022), and the observed correlation with Ag + Sb (R^2 = 0.594) (**Figure 31l**) may indicate the presence of nano-inclusions of galena or sulfosalts within sphalerite.

Figure 30 (previous page). Calibration lines for sphalerite. Relationship between the A1/A3 ratio **(a)** and the h1/h3 ratio **(b)** versus mol% FeS, using the calibration lines from Osadchii and Gorbaty (2010) and Buzatu et al. (2013). The red dashed line corresponds to the line equations obtained from the data in this work. The plotted data on the diagrams refer to sphalerite samples from this work at different Fe-contents. Legend: W-colourless; L-light yellow; Y-yellow; B-brown; D-dark brown.

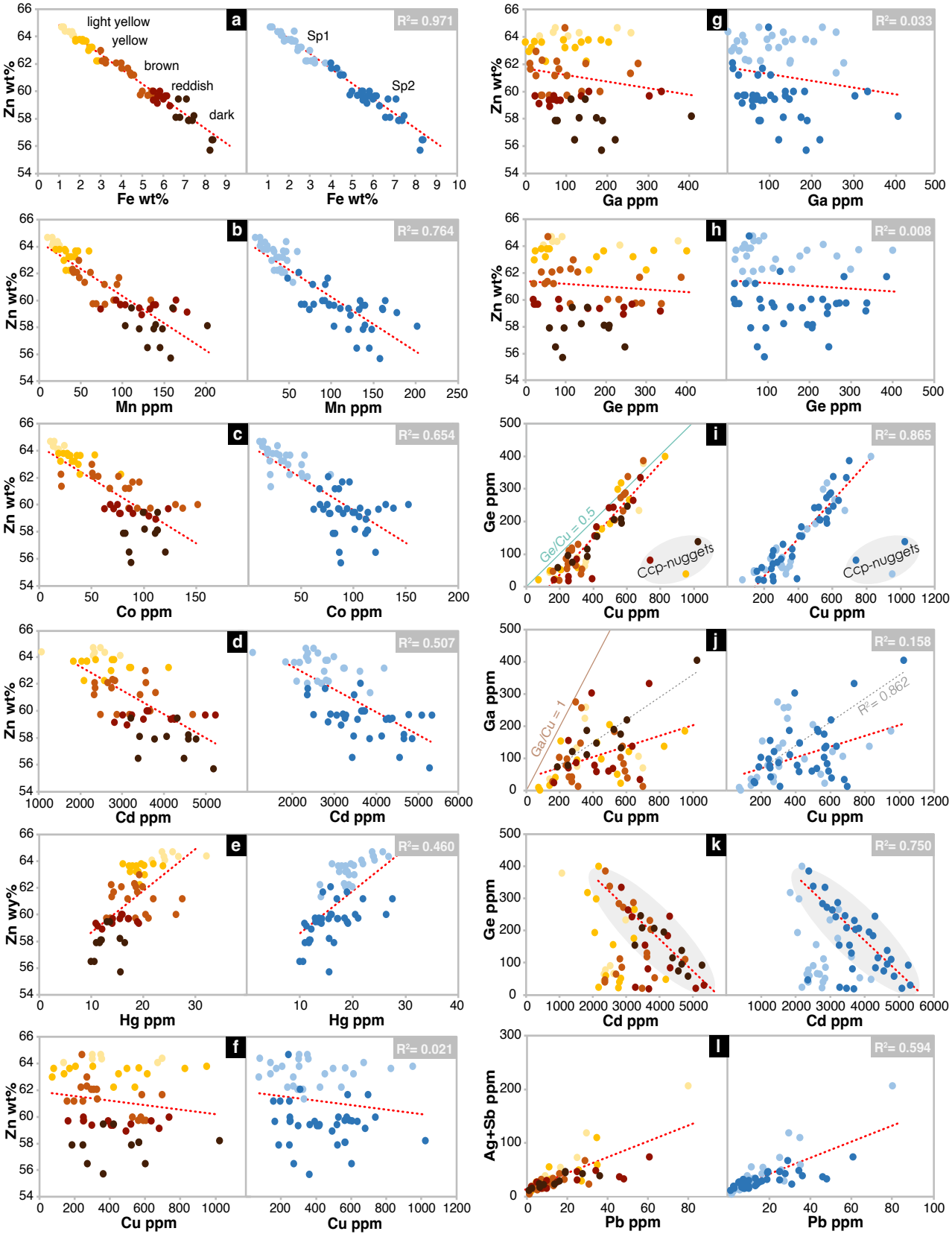

Figure 31. Bivariate diagrams of selected trace elements in sphalerite. The diagrams show the distribution of the data according to the colour (left panel) and generations (right panel) of the sphalerites. The legend is shown in the (a) diagrams.

7.4. Ore-forming conditions

7.4.1. Precipitation of Sp1 and Sp2

The LA-ICP-MS data on Sp1 and Sp2 have also been used to obtain information on the ore-forming conditions, such as temperature, sulphur fugacity (fS_2) and oxidation state (Ye et al., 2011; 2016; Frenzel et al., 2016; 2021). Sphalerite with high Mn-, Fe-, In-, Se-, Te-contents and low Ga/In ratios are often related to high formation temperatures, whereas enrichment in Cd, Ga, Ge, Hg, Tl, and low In/Ge ratios indicate low temperature systems (<200 °C) (Cook et al., 2009; Ye et al., 2016; Hu et al., 2021; Wu et al., 2023). In this study, the Ga/In and In/Ge ratios (Mdn 134.26 and 35.28 at LGB; medians of 0.12 and 0.04 at FAR) indicate low formation temperatures. This is supported by Zn/Cd ratios for LGB and FAR (Mdn 184 and 203, respectively), that are very similar to the Zn/Cd ratios obtained for low temperature MVT-SHMS systems (Wen et al., 2016). Indeed, the minimum formation temperature obtained through the application of the GGIMFis geothermometer (Frenzel et al., 2016) indicate median values of 159 °C for Sp1 and 180 °C for Sp2 at LGB, and 170 °C for Sp1 and 183 °C for Sp2 at FAR (**Figure 17**; Table 7). In addition, formation temperatures (76–250 °C) derived from the ratio of a (Å) to mol% FeS content of sphalerite (Chareev et al., 2017) are close to those obtained from the GGIMFis geothermometer.

Considering the formation temperatures of Sp1 and Sp2 are largely overlapping (**Figure 17**), showing only a slight increase (~20 °C) of the median temperatures in Sp2. The GGIMFis geothermometer is based on the relationships between sphalerite composition and homogenization temperatures (T_h) of fluid inclusions (Frenzel et al., 2016). For our samples, temperatures obtained using the GGIMFis geothermometer cannot be directly compared to the T_h of fluid inclusions, as FIs in sphalerite could not be investigated because of their small size and the poor optical quality of this mineral under transmitted visible light. Therefore, the temperature obtained using this geothermometer must be treated cautiously. Temperature and Fe-contents in sphalerite are good indicators of the chemical-physical conditions in terms of sulphur fugacity (Scott and Barnes, 1971; Frenzel et al., 2021). The mol% FeS in the analysed sphalerite samples ranges from 2 to 15.03 at LGB and from 2.33 to 14.35 at FAR. We have used the FeS-activity in sphalerite to infer the $\log_{10} fS_2$ (Frenzel et al., 2021), considering the temperature obtained by the GGIMFis geothermometer and a reference pressure of 1 bar.

As shown in **Figure 32**, an intermediate sulfidation state is recorded in each mineralization type, with sulfidation state falling close to the boundary with the low-sulfidation field. The $\log_{10} fS_2$ medians for the LGB mineralization are $10^{-17.41}$ atm, whereas it is of $10^{-17.17}$ atm for FAR mineralization (**Figure 32**, Table 2), with no clear fS_2 variations between Sp1 and Sp2 formation stages (Table 7). The

effect of pressure on log10fS_2 calculation is modest, for example considering a pressure of 1000 bars (~4 km depth, assuming crustal density of 2.6 g/cm^3), which takes into account the tectonic/lithostatic loading calculated by Perri et al. (2008), the log10fS_2 are $10^{-17.55}$ atm and $10^{-17.29}$ atm for LGB and FAR mineralization, respectively. The similar values of fS_2 obtained indicate similar sulphur activity in both mineralization sites during Sp1–Sp2 formation (Table 7). Additionally, the T-related $\log_{10}fS_2$ values do not correlate with the rock buffer line or the S-gas buffer line; instead, the LGB–FAR mineralization partially falls within the MVT-SHMS and VHMS fields (**Figure 32**).

A qualitative way to estimate the redox conditions of a system is using the Mn-content in sphalerite (Bernardini et al., 2004; Kelley et al., 2004). Due to its solubility under reducing conditions, Mn is readily incorporated into the crystal lattice of sphalerite (Vaughan & Craig, 1997). Higher Mn-contents correspond to relatively more reducing conditions. Sphalerites from LGB and FAR exhibit relative higher Mn-contents in Sp2 (**Figure 16**; Table 1a-b, 6a-b), indicating relative more reducing conditions during Sp2 precipitation. Noteworthily, the Mn-contents of analysed sphalerites are similar to those measured in sphalerites from other MVT-SHMS deposits (see Wu et al., 2023; and references therein).

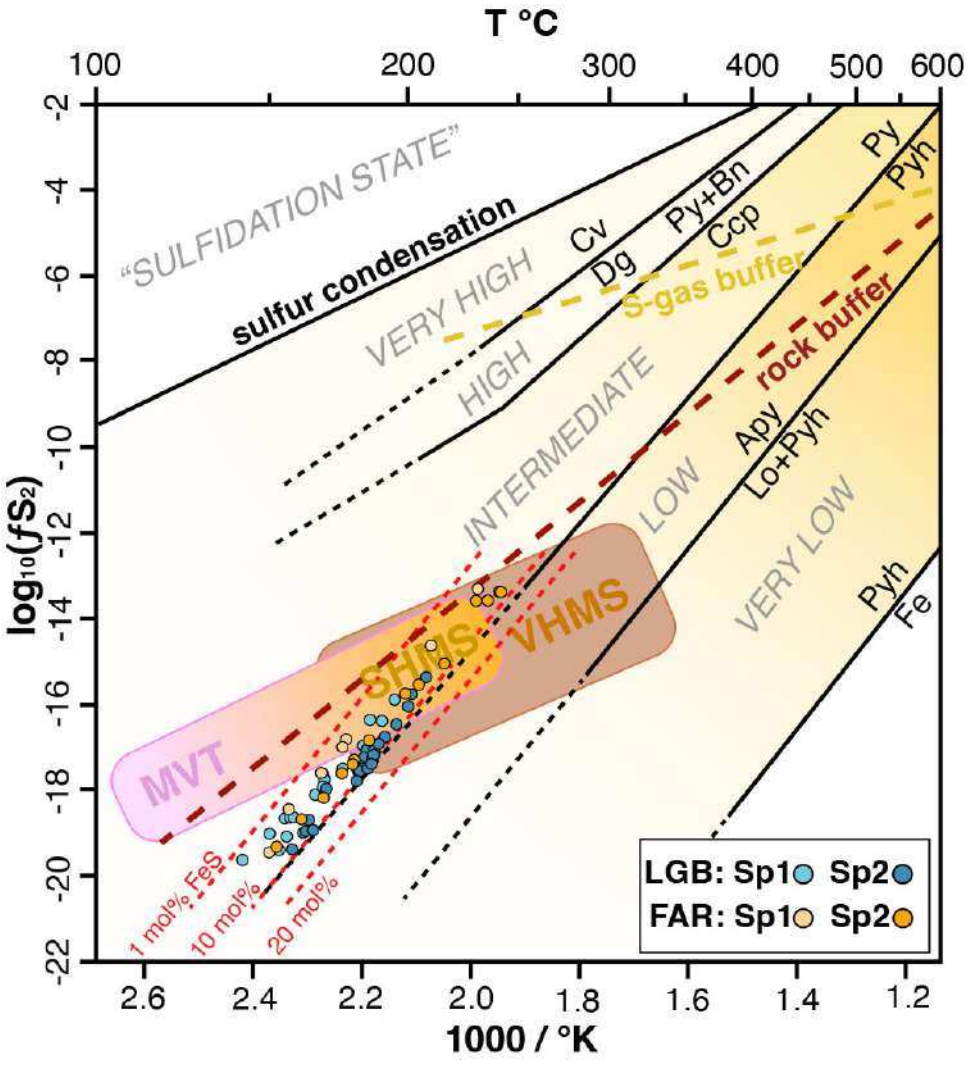

Figure 32. Sulfur fugacity vs inverse temperature plot. The diagram, modified after Frenzel et al. (2022), shows the distribution of the two sphalerite generations from Longobucco and Fonte Argentila mineralization relative to mineral reaction lines (in black), to the sulfur gas (S-gas) and rock buffers of Einaudi et al. (2003), to the isolines describing the variation of mol% FeS in sphalerite according to Frenzel et al. (2022), and to the ore-fields defined by Fontbote et al. (2017).

Mineral abbreviations: Apy, arsenopyrite; Bn, bornite; Ccp, chalcopyrite; Cv, covellite; Dg, digenite; Fe, native iron; Lo, löllingite; Pyh, pyrrhotite; Py, pyrite.

7.4.2. REE+Y as markers of Ca-rich fluids

The REE+Y patterns normalized in carbonates and fluorite are excellent indicators about fluid properties, providing insights into the system's conditions and their origin (magmatic, hydrothermal, or sedimentary) (Bau and Dulski, 1995; Schwinn and Markl, 2005; Mao et al., 2015; Hintzen et al., 2023).

The REE+Y patterns associated with Cal1 (**Figure 21a**) do not show significant fractionation, instead displaying a flat profile similar to that of sedimentary calcite (Bau and Möller, 1993; Göb et al., 2013; Zhao and Jones, 2013), with a slight depletion of LREE compared to HREE, in contrast to more fractionated hydrothermal calcite (Alles et al., 2019). The absence of significant fractionation and anomalies in Ce (Mdn 0.86) and Y (Mdn 1.07) suggests that the transport of REE+Y was facilitated by Cl or HCO_3 ligands, rather than F, which typically promotes transport and subsequent enrichment in Y (Loges et al., 2013). The mild positive anomaly in Eu (Mdn 1.41) could be due to slight fluid interaction with the surrounding granitic rock (Alles et al., 2019). This hypothesis is further supported by the low Mg content (Mdn 157.60 ppm) (Table 14) in Cal1, suggesting a "cold" formation environment with temperatures below 100 °C (Anovitz and Essene, 1987).

The slight depletion in LREE observed in Cal1 might be caused by the presence of synchysite crystals enriched in LREE (**Figure 21a**). Their scattered distribution within Cal1 could indicate a syngenetic formation triggered by the F-content in the system (Alles et al., 2019). In systems with low F-content, the ligand F deposits REE+Y minerals, rather than facilitating their mobility in hydrothermal fluid (Migdisov et al., 2016). In the case of LGB mineralization, the low F-content did not allow the fluorite formation, as occurs in FAR, but promoted the formation of synchysite, which could occur in two formation processes (Alles et al., 2019):

A) $REECl^{2+} + Ca^{2+} + HF + 2HCO_3^- = Ca(REE)(CO_3)_2F + 3H^+ + Cl^-$

B) $REEF^{2+} + Ca^{2+} + 2HCO_3^- = Ca(REE)(CO_3)_2F + 2H^+$

In the case of mineralization at FAR, the F content promotes fluorite formation within the system. The REE+Y pattern displayed by the fluorite is distinctive. The enrichment in MREE compared to LREE and HREE, along with the positive Y anomaly (Mdn 2.43) (**Figure 23a**), indicates prolonged fluid migration from the source (Bau and Dulski, 1995). This characteristic is due to the stability of the $[YF_2]^+$ complex in the hydrothermal fluid, facilitating large-scale transport (Loges et al., 2013). The F-rich hydrothermal source, as indicated by the Tb/Ca and Tb/La ratios (**Figure 23b**; Table 17a), appears to be of igneous origin. This source may also be the origin of the fluid from which synchysite formed. In this case, the “idrothermal-pegmatitic” signal reported in the Yb/Ca vs Yb/La diagram of

the fluorite (**Figure 23b**) could be an indication of the circulation of fluid through the variscan basement, the source for the fluorine-bearing minerals (Hintzen et al., 2023).

The positive Eu anomaly (Mdn 2.16) and the negative Ce anomaly (Mdn 0.46) (**Figure 23a**) indicating a possible oxidizing environment. Since the Eu^{2+}/Eu^{3+} ratio in the upper crust is regulated by temperature and oxygen fugacity (fO_2) (Bau, 1991), temperatures below 200°C, in an oxidizing to mildly reducing environment, favor the incorporation of Eu^{3+} into the fluorite crystal lattice (Möller et al., 1998; Möller, 2000; Schwinn and Markl, 2005), resulting in the observed positive anomaly in our sample. The negative Ce anomaly, due to the Ce^{3+}/Ce^{4+} ratio very sensitive to redox conditions, further suggests relatively less reducing formation conditions (Möller et al., 1998; Möller, 2000; Göb et al., 2013).

7.4.3. Qz2 late silification and Sp3 precipitation

Due to the presence of strong Si-O bonds and the low occurrence of voids in its crystal lattice, quartz is generally unable to incorporate other elements within its structure (Jourdan et al., 2009). Typically, trace elements in pure quartz do not exceed 50 ppm (Fu et al., 2020; Gotze et al., 2021). These elements can enter within crystal lattice through direct substitution of Si^{4+}, such as Al^{3+}, Ge^{4+} and Sb^{3+}, or they can be accommodated within channels of the crystal lattice parallel to the c-axis, as in the case of Li^{+}, Na^{+} and K^{+}, the latter acting as charge compensators (Fu et al., 2020; Gotze et al., 2021).

The pervasive Qz2, particularly present in FAR, exhibits high contents of Li, Na, Mg, Al, K, Ca and Ge (**Figure 20**) (Table 12, 13), characteristic of hydrothermal quartz (Gotze et al., 2004, 2021; Jourdan et al., 2009; Fu et al., 2020). There is no significant difference in the content of these cations between the microcrystalline and euhedral portions (**Figure 33a**), except for the Al-content (Table 12, 13). The epithermal hydrothermal origin of Qz2 is further supported by the Al vs. Ti correlation (**Figure 33b**), which is also used to determine the mineral's crystallization pathway (Müller et al., 2003; Breiter and Müller, 2009; Rusk, 2012; Garate-Olave et al., 2017; Gotze et al., 2021). Additionally, the strong negative correlation between Al-content and pH (Rusk et al., 2008; Müller et al., 2010; Götte, 2018; Ali et al., 2019) suggests that Al-content in Qz2 indicates a fluid with a pH = ~2.5. The Ge content (up to 10 ppm) is also consistent with hydrothermal quartz (Blaukenburg et al., 1994; Gotze et al., 2021).

While the Li-content (up to 364 ppm) in Qz2 is closely correlated with the presence of Al^{3+} (Müller and Koch-Müller, 2003). The high content and availability in the fluid depends on both a hydrothermal source (Fu et al., 2020) and the absence of Li-rich mineral phases during precipitation (Gotze et al.,

2021) (Table 13). Conversely, Na^{+} and K^{+} are distributed either as salts in fluid inclusions or like solid nano-inclusions (K-feldspar or sheet silicates) within the mineral (Gotze et al., 2021), followed by Mg^{2+} and Ca^{2+} (Bottrell et al., 1988). Using the Mg-Li geothermometer (Kharaka and Mariner, 1989; Li et al., 2021) have been obtained formation temperatures of microcrystalline Qz2 (Mdn of 171 °C), light euhedral Qz2 (Mdn of 123 °C) and of dark growth bands (median of 138 °C) (Table 13), indicating a decrease in temperature follows the trend observed in the Al-Ti diagram (**Figure 33b**). In detail, in euhedral quartz the temperature trend (120–174 °C) follows a rhythmic or oscillatory pattern (**Figure 33c**) indicating repetitive thermal pulses, probably due to the recharge of hot fluids in the system (Fall and Bodnar, 2018). Petrographic observations suggest a possible correlation between the presence of pervasive microcrystalline Qz2 with Sp3, as the latter is typically distributed around or near areas affected by silicification alteration (**Figure 6c**).

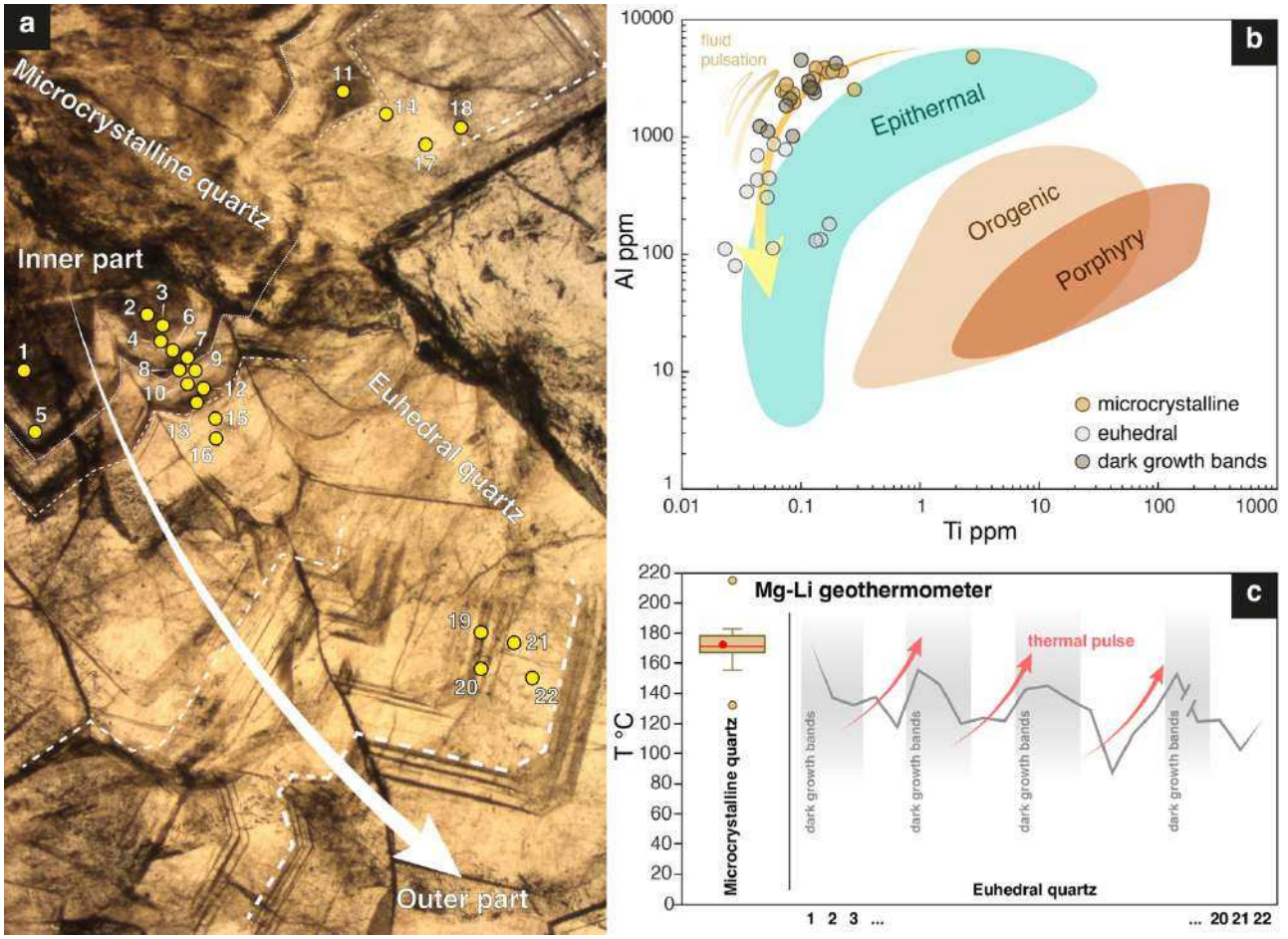

Figure 33. Diagrams of Ti vs Al and temperatures of Qz2. (a) Detail of microphotograph of Qz2 with LA-ICP-MS spots; it is possible to observe better the difference between the microcrystalline Qz2 and the euhedral one. **(b)** Binary discrimination plot of Ti vs. Al contents of the FAR Qz2 (modified after Rusk, 2012) (Data of quartz fields of porphyry, orogenic and epithermal deposits are from Rusk, 2012; Landtwing and Pettke, 2005; Maydagàn et al., 2015; Wertich et al., 2018). **(c)** Mg-Li temperatures of microsrystalline Qz2 compared with euhedral quartz temperatures along the growth direction; thermal pulses recorded from the dark growth bands are observed.

The textures and appearance of Sp3 (**Figure 6c**; **Figure 10b**) suggest the involvement of the acid hydrothermal fluid that caused dissolution-precipitation processes in the earlier Sp1-Sp2 phase (Evans and Tomkins, 2020). Although trace element data for Sp3 is limited due to its small size, the data obtained using the GGIMFis geothermometer (Frenzel et al., 2016) indicate a median temperature of 160 °C (Table 7). This temperature is consistent with those derived from the Li-Mg geothermometer for microcrystalline Qz2, which records similar values, and comparable to the T_h values of FIs measured in Qz2 (see below). Additionally, the colourless appearance of Sp3 suggests relatively less reducing conditions in the system, promoting the release of the Fe^{2+} content, further corroborated by the low Mn-content (Mdn of 18.29 ppm) (Cassard et al., 1993; Bernardini et al., 2004; Kelley et al., 2004).

7.4.4. Nature of ore-forming fluids

Previous research on quartz crystals related to granitoid bodies of the Sila Massif (De Vivo et al., 1991) highlighted fluids with distinct physicochemical properties that influenced the batholith (T_h = 50–416 °C; 0–26 wt.% NaCl eq.). However, the limited number of analyzable fluid inclusions in sphalerite has prevented direct characterization of the mineralizing fluids involved, even though sphalerite is considered an excellent host mineral for studying ore-forming fluids in numerous Zn-Pb deposits (Williams-Jones et al., 2010; Sun et al., 2018; Bauer et al., 2019). Consequently, attention has shifted to the gangue minerals, i.e., fluorite and quartz.

The fluid inclusions found in fluorite (T_h = 72.2–114.6 °C; 0–21.2 wt.% NaCl eq.) (Table 18), which is paragenetically subsequent (stage-2) to the formation of Sp1-Sp2 (stage 1), seem to confirm partially the observations of De Vivo et al. (1991) and provide an information about the process of mixing of at least two distinct fluids (Tornos et al., 1991; Boiron et al., 2010; Fusswinkel et al., 2013; Bodnar et al., 2014; Fall and Bodnar, 2018; Zhao et al., 2023b), both at lower temperature (minimum temperature) in the studied case. This process would also account for the presence of intermediate salinities (5.2–9.1 wt.% NaCl eq.) (**Figure 34**) (Table 18). As shown in **Figure 34**, these fluids would originate from two distinct sources: a more saline basinal fluid and a low-salinity meteoric fluid (Kesler, 2005). The saline basinal (diagenetic) fluid may have traversed the Variscan basement, as suggested by the REE+Y pattern (**Figure 23a**), further enriching itself in salts (e.g., Na, Ca), similar to findings in other Variscan settings in Europe (Munoz et al., 1994; Muchez et al., 2005; Fusswinkel et al., 2013; Moroni et al., 2019). It is also likely, given the paragenetic proximity of the minerals, that a similar fluid was responsible for the precipitation of Sp1-Sp2, since the circulation of saline, Ca-rich fluids through fractures and discontinuities in the Variscan basement, gravity-driven both

vertically and laterally (Gleeson and Yardley, 2002, 2003), promotes the mobilization and transport of metals such as Zn and Pb, as in MVT and SHMS-type deposits (Roedder, 1967; Leach et al., 2005, 2010; Fusswinkel et al., 2013; Bodnar et al., 2014; Zhao et al., 2023b). Although the analyzed fluids in fluorite are representative only of the FAR area, given their proximity and similarity to the LGB mineralization, it is possible that similar fluids played a role in the precipitation of Cal1 (stage-2). The fluids found and analyzed in Qz2, subsequent (stage-4) to Flr (stage-2), show different characteristics, with higher temperatures (minimum temperature) and moderate to low salinities (T_h = 111.6–163.8 °C; 0.5–6.1 wt.% NaCl eq.) (**Figure 34**) (Table 19). The T_h values in Qz2 are mostly higher than those of FIs in Flr, indicating that a relatively hotter fluid circulated after the low-temperature fluid associated with Flr precipitation. These values only partially overlap with those obtained from Flr but fall within the range previously observed in the literature (De Vivo et al., 1991; Benvenuti et al., 1994). In particular, hydrothermal quartz analyzed by Benvenuti et al. (1994) shows characteristics similar to the Qz2 of FAR (T_h = 135–185 °C; 6.8–7.3 wt.% NaCl eq.), although the latter indicates a possible mixing between a meteoric fluid and a more saline fluid (Kesler, 2005), as shown in **Figure 34**, similar to that found in hydrothermal quartz (Fu et al., 2020; Sun et al., 2021).

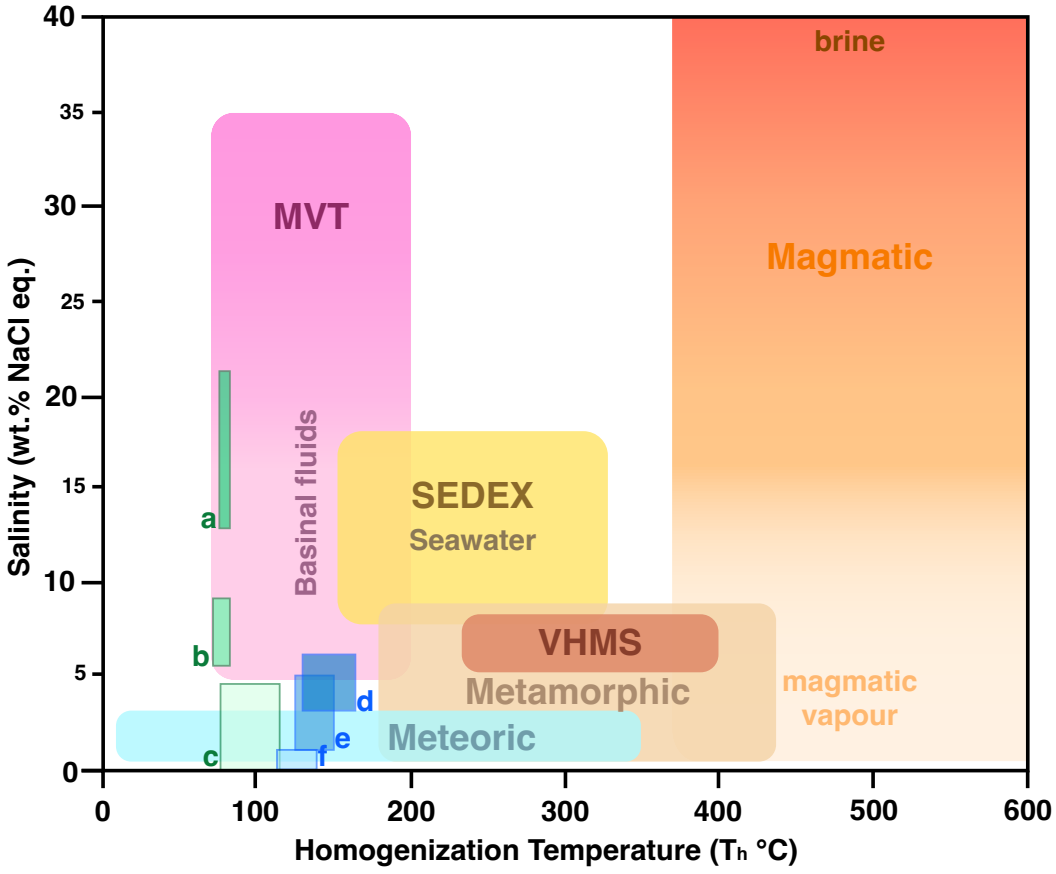

Figure 34. Homogenization temperature vs. salinity ore-forming fluids fields. Homogenization temperature vs. salinity diagram of fluid inclusions, after Kesler (2005). Our data (Tables 18, 19) are plotted in the sub-fields (a-b-c), referred to FIAs of fluorite, and (d-e-f), referred to FIAs of Qz2. In detail: (a) FA11flrE_FIA2, FA14flrE_FIA3; (b) FA11flrE_FIA3, FA14flrE_FIA2; (c) FA11flrE_FIA1, FA14flrE_FIA1, FA14flrF_FIA1-3; (d) FA14qz2_FIAs2a, 4b, 5, 4c; (e) FA14qz2_FIAs1a-b, 3a, 4a; (f) FA14qz2_FIAs3b, 4c-d.

The rhythmicity or oscillation of T_h observed in association with the various FIAs studied along the Qz2 growth bands suggests thermal pulses of the fluid during crystal growth (Fall and Bodnar, 2018). This oscillation was also observed using the Mg-Li geothermometer on quartz (Kharaka and Mariner, 1989; Li et al., 2021) in other inner transects of the same analyzed crystal (**Figure 33c**). The variability in terms of T_h and salinity, observed in the same growth zones, especially in Qz2, suggests the mineral trapped a heterogeneous fluid, with fluid mixing occurring on a small scale (Boiron et al., 2010). Both gangue minerals analyzed contain fluids associated with two different geological contexts, with different mixing trends (**Figure 34**). In particular, the fluids within fluorite are similar to those trapped in other ore and gangue minerals in Jurassic-Cretaceous Pb-Zn deposits of Sardinia, the French Massif Central and Central Europe (Munoz et al., 1994; Boni et al., 2002, 2009; Muchez et al., 2005; Cathelineau et al., 2012; Walter et al., 2016; Bauer et al., 2019; Moroni et al., 2019).

7.5. Paragenetic sequence of the Zn-Pb(-Cu-Fe) mineralization

The microstructural and geochemical results reported and discussed so far allowed the reconstruction of the mineral evolution for the LGB–FAR mineralization, comprising six stages, representing a step forward from Vighi (1953).

Main ore-forming event (stage-1)

During stage-1a, the first massive precipitation of light-coloured sphalerite (Sp1) occurred, probably following the activity of the fault zone affecting the granodiorite (**Figure 35a**). No associated gangue minerals are observed in the samples, even though Vighi (1953) reported the presence of calcite. At this stage sphalerite with relatively low Fe-content (from 1.12 to 4.43 wt.%) precipitated from an ore-forming fluid with GGIMFis medians temperature of 159 and 170 °C. The colour and oscillatory zoning indicate fluctuations in Fe-contents during sphalerite precipitation (cfr. Kelley et al., 2004; Di Benedetto et al., 2005a; Belissont et al., 2016; Wei et al., 2021); these features are also observed in the dark sphalerite (Sp2), that precipitated during the stage-1b. The stage-1b was characterized by precipitation of dark sphalerite (Sp2) and Qz1(and accessory Py1), related to fracturing and partial dissolution of Sp1 (**Figure 35b**). The activity of the fault promoted the circulation of a Fe-bearing fluids, as suggested from precipitation of the Fe-rich Sp2 (up to 11.3 wt.%); additionally, the fluid was enriched in other metals (e.g. Mn, Co, Cu, Ge, Ag, Sb, Pb), and had slightly higher medians temperature (180 and 183 °C) than the previous stage-1a fluid. The higher Mn-content (up to 296 and 194 ppm) also suggests that Sp2 precipitated under relatively more reducing conditions. During Sp2 formation the Fe-content in the fluid decreased, as suggested by decreasing Fe-contents from the core to the edge of some sphalerites (**Figure 6k**). In this case, sphalerite would be a qualitative

marker of the amount of Fe in the fluid. Indeed, the limited occurrence of pyrite during the first stage, suggests a main role played by sphalerite in depleting Fe from the fluid. In both LGB and FAR, the main ore-forming processes occurred in an intermediate sulfidation environment, within pyrite field, near the pyrite-pyrrhotite boundary, with fS_2 values close to MVT, SHMS, and VHMS deposit fields (Fig. 29). Thus, the direct involvement of a hydrothermal-magmatic or epithermal fluid during stage-1 appears improbable, since no pervasive alteration associated to magmatic degassing of the host rock (e.g., phyllic or propylitic) (Burnham & Ohmoto, 1980; Gifkins et al., 2005) promoting Zn-Pb extraction is observed.

Ca-minerals precipitation (stage-2)

Stage-2 is still characterized by brittle fault activity, resulting in the development of breccias and cataclasites involving Sp1-Sp2 and Qz1, with the precipitation of Cal1 at LGB and Flr at FAR in open fractures (**Figure 35c**). The only sulfide present in this phase is accessory Py2 within Cal1. Assuming a relative more oxidising environment than the previous stage (probably a superficial environment), as suggested by the REE+Y pattern and Eu anomaly, the precipitation of Cal1 and Flr occurs under lower temperature conditions (about TX_{Mg}–T_h < 114.6 °C). The presence of Flr and Cal1, with synchysite crystals in the last one, and the wide salinity range in Flr (0–21.2 wt.% NaCl eq.), would suggest a mixing between a basinal and a more superficial fluid of meteoric origin one. The same basinal fluid would have been further enriched in salts and F by crossing the granodioritic host-rock (Fusswinkel et al., 2013).

Secondary sulphides precipitation (stage-3)

This stage is marked by the precipitation of Gn and Ccp, with accessory Py3, replacing Sp1-Sp2, Cal1 and Flr (**Figure 35d**). The precipitation of such sulphides, which again are not associated with gangue minerals, and the absence of sphalerite, would suggest the presence of a different mineralizing fluid. In some cases, the variability of Sp and Gn abundances may be useful to track a chemical zonation of the ore deposit (Zhang et al., 2020), but this is not our case because the two sulphides are paragenetically unrelated. In general, chalcopyrite is not suitable to define accurate formation conditions, since this mineral has not yet been geochemically constrained (George et al., 2016, 2018). The low trace element content in Ccp is typical, whereas a greater variety of trace elements is observed when other base metal sulphides are absent or when formed at high temperature (George et al., 2016). By considering only the trace element content, a low hydrothermal temperature environment might be inferred (Cook et al., 2011; George et al., 2016, 2018), as supported also by the Zn/Cd ratio up to 172.30 (Wen et al., 2016).

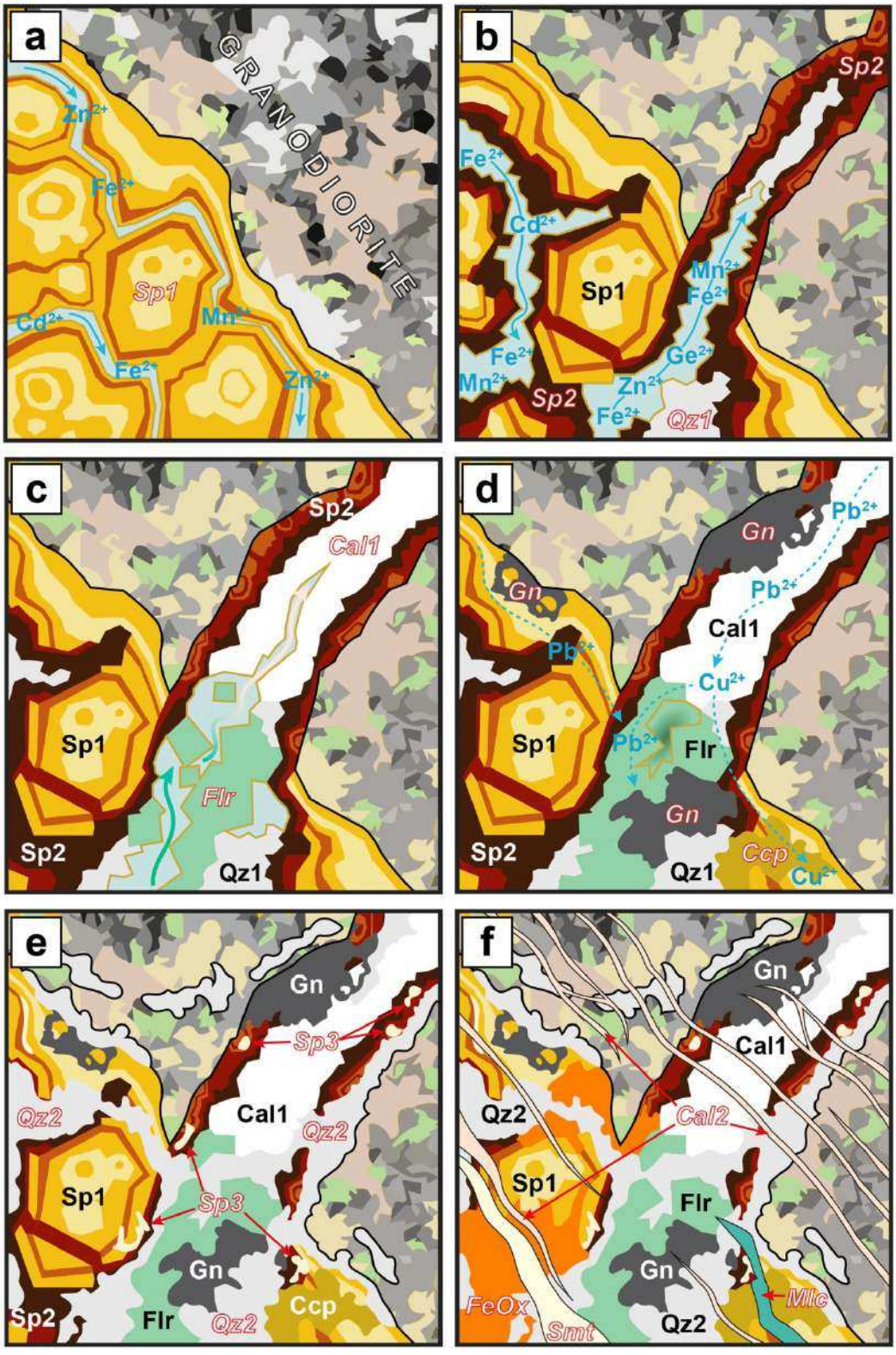

Figure 35 (next page). Paragenetic evolution of LGB-FAR mineralization. Schematic sequence of events that involved LGB-FAR mineralization: stage-1, with the main ore-forming event (a-b); stage-2, with Ca-minerals precipitation (c); stage-3, characterized by secondary sulphides precipitation (d); stage-4, with silification event (e); late supergene alteration (f). Granodiorite is made of: quartz, plagioclase, alkali feldspar and biotite, with the increase of sericite and chlorite (yellowish and greenish colours) during the evolution of the system. Legend: Cal, calcite; Ccp, chalcopyrite; FeOx, Fe-oxide-hydroxide; Flr, fluorite; Gn, galena; Mlc, malachite; Py, pyrite; Qz, quartz; Smt, smithsonite; Sp, sphalerite.

Late stage (stage-4) and supergene alteration

During stage-4 an SiO_2-(Al-, Li-)rich fluid circulated, promoting pervasive, mostly microcrystalline quartz (Qz2) precipitation, typical of silicification process, together with some large euhedral zoned crystals (**Figure 6l; Figure 35e**) (Thyberg et al., 2010; Diamond et al., 2018). Precipitation of microcrystalline quartz occurs at low temperature (T_{Mg-Li} = Mdn of 171 °C), while euhedral quartz precipitates under even lower temperature and moderate to low salinity conditions (T_h = 111.6-163.8 °C; 0.5-6.1 wt% NaCl eq.). A low pH fluid dissolved the former other minerals and promoted the precipitation of Sp3 within Sp1-Sp2, near the areas where Qz2 also precipitated (**Figure 35e**). The low Fe- and Mn-contents in Sp3 suggest that the fluid forming Sp3 and Qz2 was relatively more oxidized than previous ore-forming fluids, facilitating the extraction and the non-repartitioning of these elements from Sp1 and Sp2.

Finally, in the very late oxidizing supergene event, the mineralization is affected by brittle deformation and alteration via meteoric water, with fractures healed by Cal2, smithsonite (Smt) and minor malachite (Mlc), and Fe-hydroxide partially or totally replacing Sp and Ccp (**Figure 35f**).

7.6. Correlation with similar Zn-Pb deposits

As shown in **Figure 32**, during the stage-1 the Zn-Pb mineralization developed under relatively low temperatures (130–218 °C, with medians of 159_{Sp1} and 180_{Sp2} °C, for LGB; 110–241 °C, with medians of 170_{Sp1} and 183_{Sp2} °C, for FAR) and low sulphur fugacity (median values of $10^{-17.55}$ atm for LGB and $10^{-17.0}$ atm for FAR, see Table 7). Particularly, sulphur fugacity values do not arrange along the rock buffer line (**Figure 32**), indicating that the sphalerite precipitated from the fluid did not interact with the granodiorite or porphyric dikes. In addition to temperature and sulphur fugacity, characteristic sphalerite geochemical features, such as Ga/In, In/Ge, and Zn/Cd ratios, indicate formation conditions typical of low-temperature systems like MVT and SHMS deposits (**Figure 32**) (Taylor et al., 1983; Basuki and Spooner, 2002; Leach et al., 2010; Wilkinson, 2013). In figure **Figure 36** we compare the primary features of the LGB-FAR mineralization and those of other world-class Zn-Pb deposits. For comparison we used (i) two deposits classified as MVT, i.e. Tres Marias (Mexico) and Shaojiwan (Guizhou, China) (Saini-Eidukat et al., 2009; Ostendorf et al., 2017; Yang et al., 2022; 2023), (ii) two vein-type deposits, as Saint Salvy (Massif Central, France) and Montevecchio (Sardinia, Italy) (Cassard et al., 1993; Munoz et al., 1994; Bellissont et al., 2014; Moroni et al., 2019), and (iii) two type-deposits from the East Tennessee district (USA) for MVT and the Red Dog deposit for SHMS (Alaska, USA) (Taylor et al., 1983; Kelley et al., 2004; Bonnet et al., 2014) (**Figure 36**).

As shown in **Figure 36**, in contrast to the selected deposits, the LGB-FAR mineralization is not hosted by carbonate or siliciclastic bodies, typical of MVT or SHMS, respectively. Similarly to Saint-Salvy, Shaojiwan, and Montevecchio deposits, the LGB-FAR mineralization is not constrained by the inherited geometries of the host rock, but is distributed along fault zones. Particularly, it occurs within breccias and cataclasites wherein the ore-body is reworked and affected by overprinting fluid-rock interaction events during subsequent brittle deformation stages. The median temperatures of the LGB-FAR mineralization obtained through the GGIMFis geothermometer (Table 2) fall within the range of the estimated formation temperature of the selected deposits (80–200 °C) (**Figure 36**). Indeed, even though the Fe-content is higher than a typical MVT (Bonnet et al., 2014; Li et al., 2023), some MVT deposits, such as Tres Marias (**Figure 36**), show comparable Fe-contents (e.g., 0.2-14 wt%; Saini-Eidukat, 2009). In contrast, Ga- and Ge-contents can be variable, although Ga<Ge, except for Montevecchio. The Cd-content is similar to be that of an MVT or SHMS (**Figure 36**). All these deposits exhibit a mineral assemblage in which sphalerite is often the main ore-mineral. Commonly, LGB and FAR sphalerite is not colloform or fibrous, as typical in MVT or SHMS deposits, but is subeuhedral or euhedral with colour and oscillatory zoning indicating rhythmic pulses of metal-rich fluids (Kelley et al. 2004; Di Benedetto et al., 2005a; Cook et al., 2009; Wei et al., 2021).

Other similarities are observed in terms of ore-forming fluids. The primary fluid inclusions from the Saint-Salvy and Montevecchio sphalerites show similar salinities (14-25.5 wt.% NaCl eq.) (Munoz et al., 1994; Moroni et al., 2019) to some of the salinities observed in the FAR fluorite (12.8-21.2 wt.% NaCl eq.). Given that, as already discussed, fluorite is paragenetically successive to Sp1-Sp2, it is plausible that a similar fluid was involved in their precipitation. Affinities are also found in the respective T_h (minimum temperature). Saint-Salvy shows temperatures (T_h = 80-140 °C) (Munoz et al., 1994) more consistent with those obtained from fluorite at FAR (T_h = 72.2-114.6 °C), while the slightly higher Montevecchio temperatures (T_h = 133-185 °C) (Moroni et al., 2019) overlap with those obtained from Sp1-Sp2 through the GGIMFis geothermometer (medians of 159-183 °C). This puts considerable stress on the affinity between these deposits and those of FAR and LGB (**Figure 36**). Another common aspect between the LGB-FAR and Saint-Salvy mineralization is the presence of a third generation of irregular, colourless and Fe-poorer sphalerite, justified by Cassard et al. (1993) as a response to 'more oxidising' system conditions. The Shaojiwan deposit also shows similar salinities to those previously described, although slightly lower (7-14 wt.% NaCl eq.), but with temperatures consistent with the two previous European deposits (T_h = 120-200 °C) (Yang et al., 2024).

The textural and chemical similarities of the LGB and FAR mineralization with some previously described deposits are further compared with a geochemical signature characterized by elements such as Mn, Fe, Ga, Ge, Cd, In. These elements show that our samples fall within or close to the

typical fields of SHMS and MVT deposits (**Figure 36**; **Figure 37**), while the T_h/salinity values of fluid inclusions in the FAR fluorite fall within the fields of basinal fluids with high to intermediate salinities and of low salinity meteoric fluids (**Figure 34**). Therefore, although the geological-structural context of the LGB-FAR mineralization does not correspond to that of the MVT and SHMS deposits, several compositional characteristics of the sphalerite and indications from both the GGMFis geothermometer and fluid inclusion data suggest similarities between the mineralizing fluids of the LGB-FAR mineralization and those of the SHMS and MVT deposits. However, it should be noted that the nonnegligible Fe contents in Sp1 and especially in Sp2 could suggest a magmatic contribution to the mineralizing fluids, which might be related to an as-yet undefined magmatic source within the two Variscan magmatic cycles of the Sila batholith (Ayuso et al., 1994; Festa et al., 2010; Ortolano et al., 2020). On the other hand, the contents in certain key elements for magmatic contribution, such as Mn and In, are not high. We propose that the Fe-richer fluid responsible for mineralization, is due to interaction with the Variscan basement, which is dominated by granodiorite, leaching some Fe (2.45 wt.%), Mn (0.04 wt.%) and In (<0.1 ppm) already present in it (Prosser and Caggianelli, 2003). In this case, the magmatic contribution would be indirect. This supports the hypothesis that the fluid responsible for the primary mineralization, as well as the subsequent gangue minerals, has a peculiar origin, probably associated to a sedimentary basin. As in the case of Saint-Salvy (Munoz et al., 1994), it is probable that this saline fluid crossed through and permeated the Variscan basement. Subsequently, mixing phenomena involved meteoric fluids. In the end, the fluid did not originate directly from the basement but was influenced by, becoming hybridized. Consequently falling into the category of basement-hosted Pb-Zn deposits (Fusswinkel et al., 2013), which, although located in a crystalline basement, have geochemical features typical of a sedimentary basin environment.

Deposit	Host rock	Ore texture and main minerals	Sphalerite texture	Fe-, Ga-, Ge-, Cd-contents (ppm) in sphalerite	Sphalerite temperature
East-Tenessee (Central USA) *MVT* [1,2]	dolomite and limestone *Carboniferous-Permian*	stratabound paleo karst *Sp-Gn*		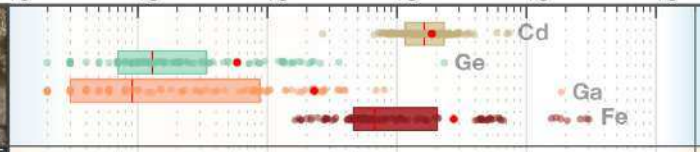	100°-180°C (FI)
Red Dog (Alaska, USA) *SHMS* [3]	black shale and mudstone *Mississipian*	stratabound brecciated *Sp > Py > Gn*		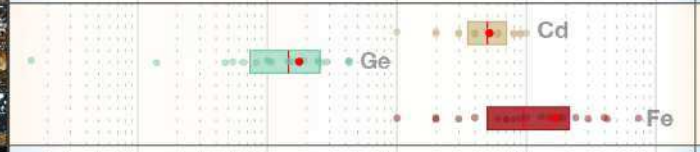	100°-200°C (FI)
Tres Marias (Chihuahua, Mexico) *MVT* [4,5]	limestone *Cretaceous*	massive brecciated *Sp > Gn-Py*	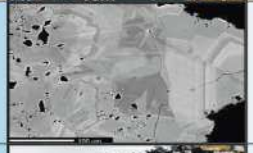	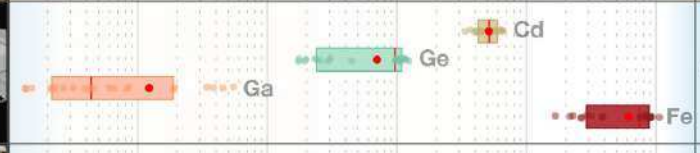	*low temperature*
Shaojiwan (Guizhou, China) *MVT* [6,7]	dolomite and limestone *Devonian-Carboniferous*	massive brecciated *Py > Sp-Gn*			120°-200°C (FI)
Saint-Salvy (Massif Central, France) *vein-type* [8,9,10]	medium-grade schist and meta-carbonate *Cambrian-Silurian*	vein brecciated *Sp > Gn >> Py*	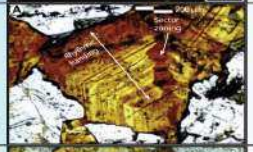		80°-140°C (FI)
Montevecchio (Sardinia, Italy) *vein-type* [11]	low-grade meta-carbonate *Cambrian-Devonian*	vein brecciated *Gn > Sp*		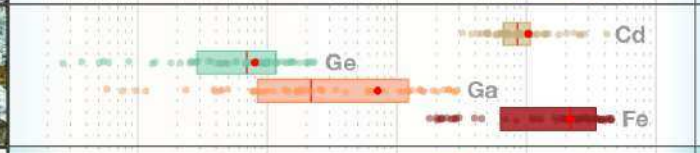	133°-185°C (GGIMFis)
Fonte Argentila (Calabria, Italy) *vein-type* [this study]	granodiorite *Carboniferous*	vein brecciated *Sp > Gn >> Py*		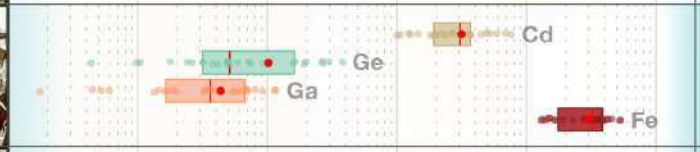	Mdn 170°C (sp1) Mdn 183°C (sp2) (GGIMFis)
Longobucco (Calabria, Italy) *vein-type* [this study]	granodiorite *Carboniferous*	vein brecciated *Sp > Gn >> Py*		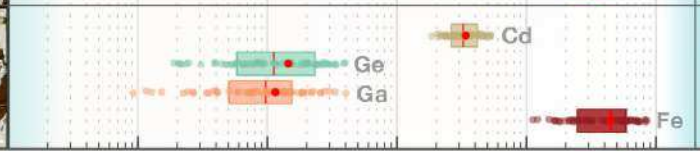	Mdn 159°C (sp1) Mdn 180°C (sp2) (GGIMFis)

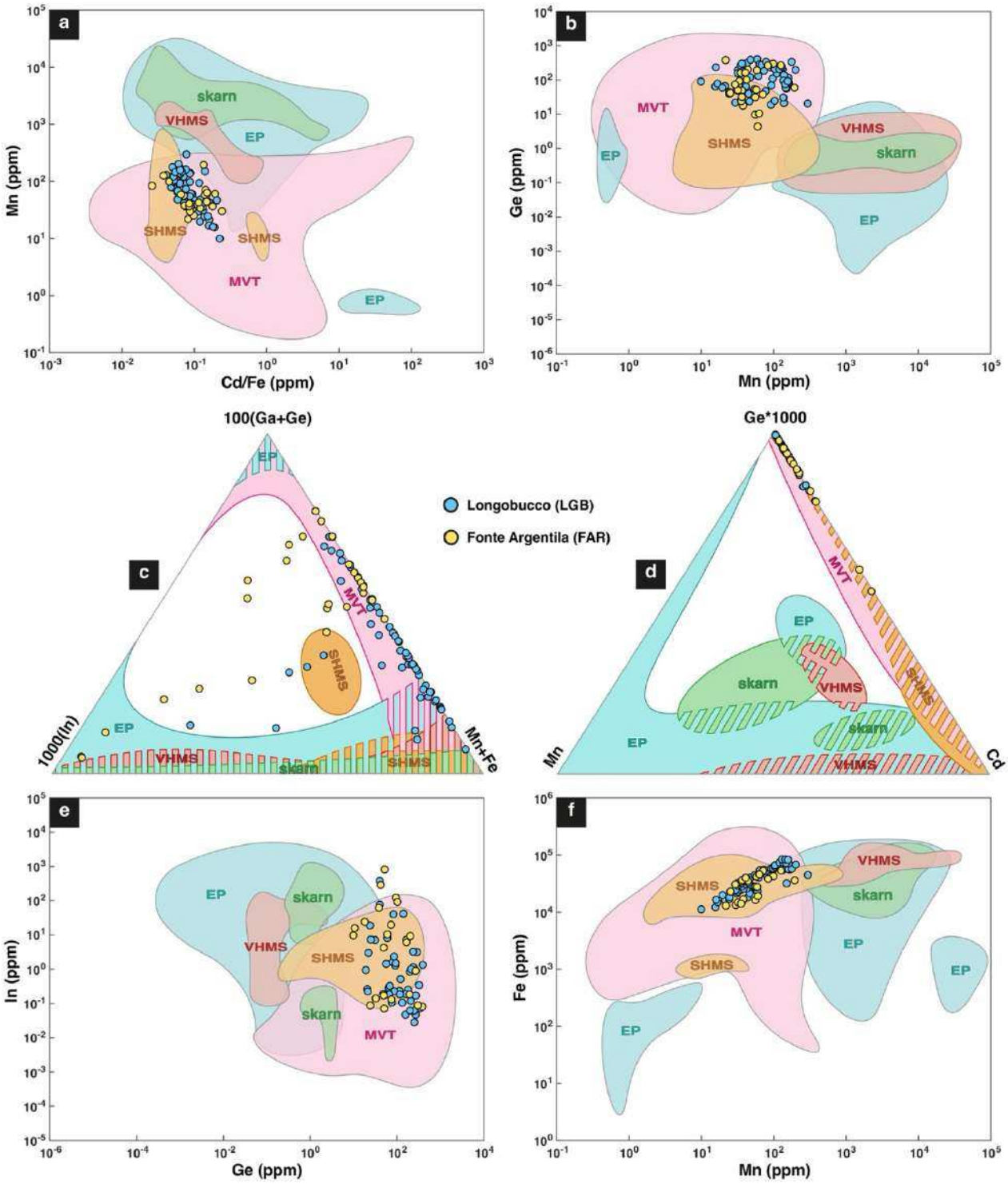

Figure 36 (previous page). Comparative diagram. Synthetic diagram comparing the mineralization of Longobucco and Fonte Argentila, with two typical MVT-SHMS deposits (East-Tenessee, Red Dog) and other deposits (Tres Marias, Shaojiwan, Saint-Salvy, Montevecchio) that have some similarities. References: [1] Taylor et al., 1983; [2] Bonnet et al., 2014; [3] Kelley et al., 2004; [4] Saini-Eidukat et al., 2009; [5] Ostendorf et al, 2017; [6] Yang et al., 2022; [7] 2024; [8] Cassard et al., 1993; [9] Munoz et al., 1994; [10] Bellissont et al., 2014; [11] Moroni et al., 2019.

Figure 37. Geochemical-genetic diagrams for sphalerite. Plots of (a) Cd/Fe vs. Mn, (b) Mn vs. Ge, (e) Ge vs. In, (f) Mn vs. Fe; ternary diagrams of (c) (Mn+Fe)–(100*Ga+Ge)–(1000*In), (d) (Cd)–(1000*Ge)–(Mn) (Modified after Wu et al., 2023). Data of sphalerite fields of MVT, SHMS, skarn, VHMS and epithermal (EP) deposits are from Li et al. (2023).

7.7. Geological and geodynamic considerations

7.7.1. Geological information from minerals

The absence of key mineral dating prevents precise determination of the age of mineralization, limiting the reconstruction of the paragenetic sequence to textural analysis of mineral relationships. According to the literature, such mineralization has historically been associated with post-Variscan events or reworking during the Alpine cycle (Fregola et al., 2023, and references therein).

In this study, calcite and fluorite provide indirect insights into the geodynamic environment of formation. Both minerals are in the middle of the paragenetic sequence and record low temperatures (Cal: T_{XMg} < 100 °C; Flr: T_h = 72.2–114.6 °C) and a wide range of salinity (0–21.2 wt.% NaCl eq.). The salinity range suggests a potential involvement of two distinct fluids (basinal and meteoric), one which, or both, have passed through the crystalline basement, as evidenced by the REE+Y data of fluorite. Additional insights come from fluid inclusions in fluorite, which indicate the circulation of a saline fluid typical of sedimentary basins (12.8–21.2 wt.% NaCl eq.) (**Figure 38a**). These two minerals can be considered as chronological markers of the mineralization. Indeed, considering the geochemical features and formation temperature of fluorite and calcite, a sedimentary cover above the Variscan basement must have already been present, or at least was forming synchronously with respect to their precipitation in the mineralization; with the sedimentary cover possibly in contact with the basement, as observed in the Caloveto area (Santantonio et al., 2016). This suggests that fluorite and calcite formed during a time interval between the Lower Hettangian and Upper Bajocian (~199–167 Ma) in the Jurassic, as justified by the sedimentary sequences in the Longobucco Basin (Santantonio and Teale, 1985; Young et al., 1986; Perri et al., 2008; Santantonio et al., 2016), which at this age would represent a cumulative thickness estimated at ~1 km. Based on the temperatures recorded by these minerals and considering a geothermal gradient typical of a Jurassic rift context (~45 °C/km) (Santantonio and Fabbi, 2020; Innamorati et al., 2018; Kolawole and Evenick, 2023), fluorite would have formed at depth of ~2–3 km, while calcite at ~1 km, possibly near the onset of the Mesozoic cover (**Figure 38a**). This may suggest the percolation of relatively oxidising diagenetic fluids (rich in HCO_3 and Ca) from the cover, which interact with the Variscan basement (rich in F and REE+Ys), with subsequent mixing with meteoric fluids. This fluid circulation would have been favoured by fault activity within extensional system, coinciding with the opening of the Ligurian-Piedmont Ocean and associated basins (Decarlis et al., 2013; Le Breton et al., 2021), in which northern Calabria was involved during the Jurassic, as evidenced by the numerous Toarcian pelagic neptunian dikes affecting both the basement and the Mesozoic sedimentary sequence (Santantonio et al., 2016; Fabbi et al., 2024). In this way, the Cal1-Flr paragenetic association defines a clear

boundary between the main ore-forming process responsible for Sp1 and Sp2, and the later silicification event involving Qz2 (**Figure 38a-c**).

At this point, the main ore-forming process responsible for the genesis of Sp1 and Sp2 can be considered pre-Jurassic or Jurassic. This opens two temporal scenarios for sphalerite formation (**Figure 38b1-2**). In the first scenario, consistent with geochemical data obtained from sphalerite, the formation of the main ore mineral, preceding Cal1 and Flr, occurred between the Rhaetian and Hettangian (~203–196 Ma), during the deposition of the red beds (Monte Paleparto and Torrente Duno Formations) (Bouillin et al., 1988) and the early carbonates (Bocchigliero Formation) (Young et al., 1986; Santantonio et al., 2016). In this context, sphalerite would have formed through the percolation of basinal-type fluids (similar to MVT- or SHMS-type) into the basement, originating from the first sedimentary cover sequences, at temperatures of 160–180 °C, guided by brittle structures. Assuming a Jurassic rift with high geothermal gradient (~40-45 °C/km, from Kolawole and Evenick, 2023), sphalerite would have formed at a depth of ~3–4 km (**Figure 38b1**). Other European Zn(-Pb)-deposits, such as Saint-Salvy and partially the Harz Mountains, show main ore-forming stages in the Jurassic period (~180 Ma) (Beaudoin and Sangster, 1992; Munoz et al., 1994).

In the second scenario, sphalerite formation is placed around 250 Ma, in a "cooled" basement context with a geothermal gradient of ~30 °C/km (Caggianelli et al., 2000), significantly postdating the emplacement of the mafic and felsic dikes in the Sila Massif (295–277 Ma) (Festa et al., 2010), at a depth of ~5–6 km (Caggianelli et al., 2000). In the latter scenario, the geochemical signature of sphalerite could be associated either to a specific vein mineralization or to a sedimentary-derived fluid of unknown origin (**Figure 38b2**).

The event that triggered the precipitation of Qz2 is the least constrained temporally. This event involved the circulation of a fluid postdating Cal1, Flr, Gn, and Ccp, with characteristics typical of a low-temperature hydrothermal to meteoric fluid ($T_{Mg\text{-}Li}$ = 146 °C mdn; T_h = 111.6–163.8 °C; 0.5–6.1 wt.% NaCl eq.; Li-content up to 364 ppm; fluid pH = ~2.5). In this work two possible scenarios in which this event would have occurred (**Figure 38c1-2**) are proposed. In the first scenario, the Qz2 formation could be linked to a very "rapid" thermal anomaly during the latest Jurassic rifting episodes (Innamorati et al., 2018), taking the geothermal gradient temporarily to ~50 °C (Kolawole and Evenick, 2023), which would justify such temperatures for quartz at ~3 km depth, corroborated by the Al/Ti ratio and Li-content; as well for illite in the Torrente Duno Formation, recording a transition to high-diagenetic-anchizonal temperatures (100–160 °C) (Perri et al., 2008) (**Figure 38c1**).

In the second scenario, Qz2 would presumably relate to the Alpine cycle, generating epithermal-like metamorphic fluids (typical of the low-grade metamorphic processes) rich in Cl and SiO_2 (Diamond et al., 2018; Evans et al., 2020). The structural imbrications of basement units in the eastern Sila Massif (east-verging) (Vignaroli et al., 2012), responsible for a crustal thickening and structural

deepening of mineralized sites (estimate of ~4–6 km depth), could be the cause of the thermal anomaly recorded in the Qz2, as well in illite (Perri et al., 2008), while maintaining an orogenic-type geothermal gradient of ~30–35 °C (Diamond et al., 2018). The recorded temperatures are significantly greater than the closure temperature of apatite fission-track in the granodiorite, recording Burdigalian ages (Vignaroli et al., 2012) (**Figure 38c2**).

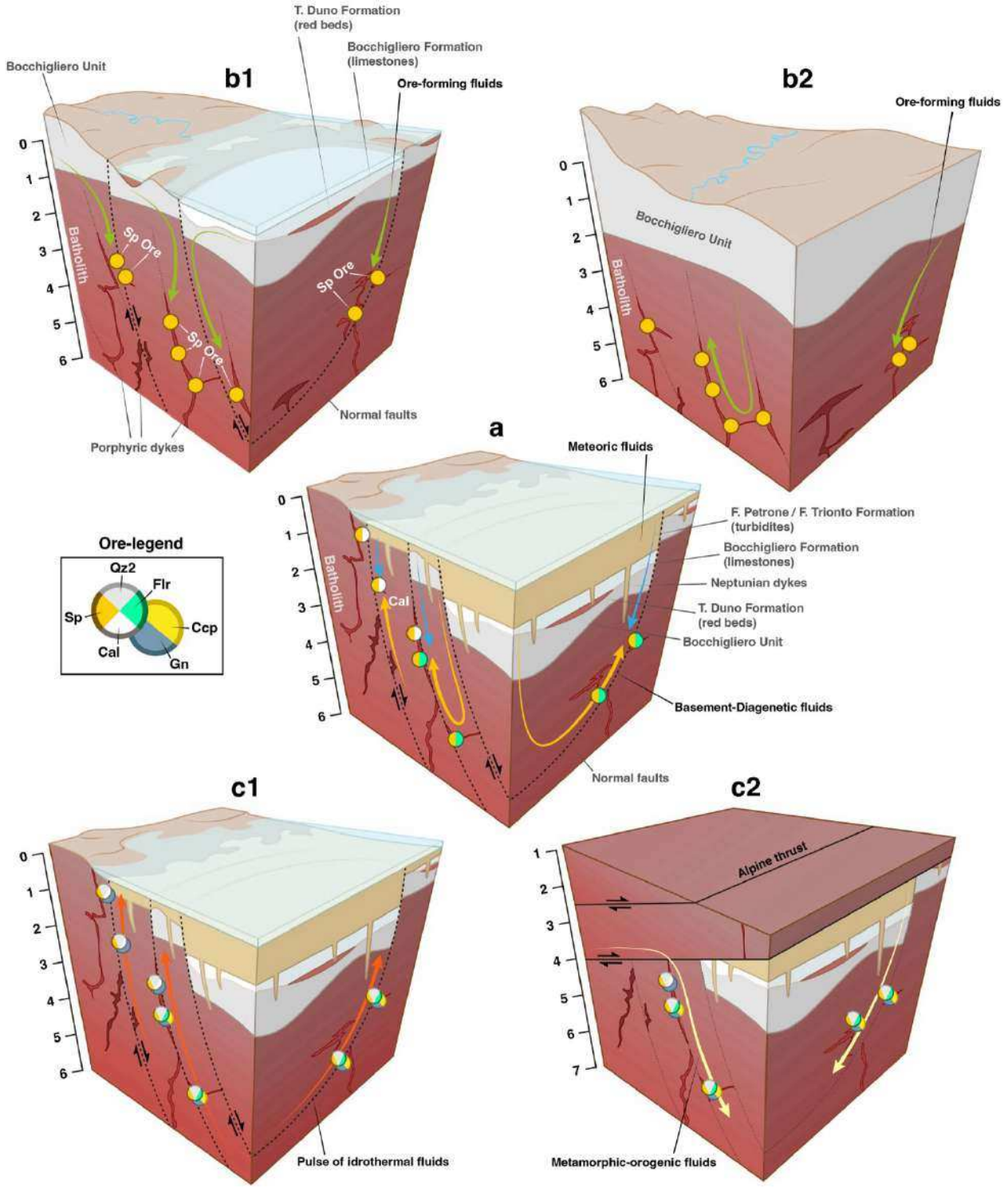

7.7.2. Critical issues on dating

Determining the age of the Zn-Pb mineralization at LGB and FAR and its absolute timing is beyond the scope of this doctoral thesis. This chapter discusses some critical issues for the absolute dating of the key minerals of the studied Zn-Pb mineralization, which are derived from the mineralogical and microchemical analyses performed. Relevant ages must be obtained from some key minerals, Sp1 and Sp2 in this case, to tighten precisely the age of the main ore forming process. Commonly, Rb-Sr dating is used to obtain formation ages of sphalerite (Reesman, 1968), although large uncertainties affect the results, which should be treated accordingly with caution. Previous studies have shown that Rb and Sr may be trapped in voids of the octahedral crystal sites or in lattice defects of sphalerite (Petke and Diamond, 1996); additionally, the presence of micro-inclusions of calcite, Sr-apatite, clays or K-feldspar can affect the results (Brannon et al., 1991; Nakai et al., 1993; Bradley et al., 2004; Saintilan et al., 2015), as well as Sr-rich fluid inclusions (Petke e Diamond, 1996; Saintilan et al., 2015). Potentially, further pitfalls on Rb-Sr dating of sphalerite derive from the mineral microtexture, since colloform or fine-grained sphalerite (pseudo-colloform in our case) can undergo Rb and Sr enrichment, with a high $^{87}Rb/^{86}Sr$ ratio, during rapid precipitation (Lindblom, 1986; Christensen et al., 1996). Concerning the absolute timing of the mineralization, Rb-Sr dating is commonly associated to other isotopic systems (U-Pb, Sm-Nd, Re-Os) of other minerals that are paragenetically related to sphalerite (Chesley et al., 1994; Schneider et al., 2007). In our case, however, the Sp1 and Sp2 of LGB and FAR are not associated with datable minerals. The Py1 crystals associated with Sp2 are too small (maximum size of 100 μm) to be dated using the Re-Os method; similar issues also affect other minerals in the paragenetic sequence, such as calcite and galena. Concerning calcite, Pb-Pb or U-Pb dating is ambiguous, due to the potential abundance of non-radiogenic Pb (~90%) (Roberts et al., 2020) and to post-formation processes that could reopen the system, resetting the Pb signature (Smith et al., 1991; Whitehouse and Russell, 1997; Babinski et al., 1999). A similar situation affects galena, as observed in the Montevecchio mineralization (Ludwig et al., 1989; Boni et al., 1992; Moroni et al., 2019), where Pb may result from mixing of multiple sources, thereby undermining the accurate dating of the mineral.

Figure 38 (previous page). Models of hypothetical geodynamic scenarios. Without geochronological data, geodynamic scenarios were assumed based on the physico-chemical characteristics of the minerals analyzed. Scenario (a), which is better constrained, is related to stage-2, representing a Jurassic rift environment. Scenario (b) is related to the main ore-forming event (stage-1), with sphalerite precipitation occurring either during the Jurassic (b1), or before the development of extensional tectonics (b2). Scenario (c) is related to stages 3-4, assuming an anomalous geothermal gradient due to Jurassic rift (c1), or assuming an orogenic (Alpine) context (c2).

8. Conclusions

Using geochemical, crystallographic, spectroscopic techniques and fluid inclusion analyses, the result of this work detail for the first time the Zn-Pb(-Cu-Fe)-mineralization associated to fault zones affecting the Permian–Carboniferous intrusive bodies exposed in the northern Sila Massif of Calabria, at Longobucco (LGB) and Fonte Argentila (FAR) localities, and highlight the plausible mineralization system. A portion of the data reported in this PhD thesis has been published in Fregola et al. (2023) and Ciccolella et al. (2024, 2025). In summary, in this PhD work it has been demonstrated that:

- Although the LGB and FAR mineralization occur within the ancient Longobucco argentiferous district, no significant silver content was detected in the analysed samples, except for the trace Ag-content in chalcopyrite (164–313 ppm).
- Both LGB and FAR sites can be considered as a single mineralization, exhibiting similar mineral assemblage, textures and chemical characteristics, especially for sphalerite.
- Four paragenetic stages are observed and three generation of sphalerite (Sp1-Sp2-Sp3) can be distinguished in it.
- Sphalerite shows an increase in Fe-content (from ~1.1 to ~8.4 wt.%) from a light pseudo-colloform sphalerite (Sp1) to a darker, sub-euhedral Fe-rich sphalerite (Sp2) (up to 11.27 wt.%). The Sp2 contains the highest amounts of Cu (up to 1023.19 ppm), Ga (up to 338.79), Ge (up to 400.20 ppm), and Cd (up to 7589.09 ppm). Later Sp3 (Fe < 1.36 wt.%) was formed through dissolution-precipitation process of Sp1-Sp2 under less reducing conditions.
- Spectroscopical observation of sphalerite highlight the dependence between Fe-content and intensity variability of the Raman bands in the 300–350 cm^{-1} range.
- XRD data on zoned sphalerite highlight a high disordered structure of the mineral and suggest the localized presence of FeS-CdS-rich sub-micrometric phases.
- The spectroscopic and crystallographic differences observed between our sphalerites and those found in the literature are due to the fact that the literature often uses synthetic samples with a controlled composition, whereas in our natural samples the sphalerites are rich in other metals (e.g., Mn, Co, Cu, Cd) in addition to iron.
- The Zn in sphalerite shows cation substitutions with Fe (R^2 = 0.971), Mn, Co, and partially with Cd. On the other hand, Cu, Ga, and Ge are incorporated into the sphalerite lattice either as mineral nano-inclusions or possibly through $2Cu^{+} + Ge^{4+} \leftrightarrow 3Zn^{2+}$ and/or $Cu^{+} + Ga^{3+} \leftrightarrow 2Zn^{2+}$ heterovalent substitutions.
- The LGB-FAR mineralization formed under low-temperature conditions, similar to MVT or SHMS deposits, with total Sp1-Sp2 median formation temperature of 178–180 °C. Additionally, sulphur

fugacity values ($10^{-17.29}$–$10^{-17.55}$ atm) are close to the MVT and SHMS fields. Moreover, the data do not align on the rock buffer line. Therefore, the data do not record a direct genetic relationship with proximate granodiorite and porphyric dikes, with the ore-forming process that occurred in a relatively cold regime accompanied by brittle deformation.

- Calcite-1 and fluorite describe a cooling of the system under relative more oxidizing conditions. This is confirmed by the presence of fluid inclusions in the fluorite that show T_h = 72.2-114.6 °C and salinities ranging from 0 to 21.2 wt.% NaCl eq., recording a potential mixing between a basinal saline fluid and a meteoric fluid. Moreover, the REE-F-carbonates (synchysite) found in calcite-1 have been described and analyzed for the first time in the Sila Massif.
- Quartz-2 record a late hydrothermal-epithermal event, evidencing the circulation of a SiO_2-rich fluid with low pH (~2.5), high Al- and Li-content (up to 0.73 wt% and up to 364 ppm, respectively), salinity of 0.5-6.1 wt.% NaCl eq., and T_h from 111.6 to 163.8 °C.
- The mineralization of LGB-FAR shows textural, geochemical and fluids similarities with other vein-type deposits (e.g., Saint-Salvy, Montevecchio), as well as with some MVT-type deposits (e.g., Shaojiwan). The geochemistry of LGB-FAR places this mineralization within or near the fields of MVT-SHMS deposits. This suggests that the fluid responsible for the ore formation process is not chemically constrained by the context in which it precipitated, but that a basinal fluid, as shown by high-saline FIs in fluorite, may have circulated through the Permian-Carboniferous 'cold' magmatic bodies, forming a basement-hosted Zn-Pb mineralization. Although data do not suggest a direct genetic relationship with magmatic bodies, a potential magmatic contribution cannot be completely ruled out.
- Although there are no dates for ore and gangue minerals, evidences related to fluids and REE+Y in fluorite imply the formation of this mineral most probably in the Jurassic time, acting as a break-off point between the sphalerite mineralization event first and the possible hydrothermal event later involving galena, chalcopyrite and quartz-2.

References

Acquafredda, P., Lorenzoni, S., & Lorenzoni, E. Z. (1994). Palaeozoic sequences and evolution of the Calabrian-Peloritan Arc (Southern Italy). Terra nova, 6(6), 582-594.

Alfantazi, A. M., & Moskalyk, R. R. (2003). Processing of indium: a review. Minerals Engineering, 16(8), 687-694. https://doi.org/10.1016/S0892-6875(03)00168-7

Ali, A. M., Padmanabhan, E., Mijinyawa, A., & Kwaya, M. Y. (2019). Effect of pH on the stability of quartz in a multi-phase system of kaolinite, hydrous Al (hydr) oxide and quartz. SN Applied Sciences, 1, 1-11.

Alles, J., Ploch, A. M., Schirmer, T., Nolte, N., Liessmann, W., & Lehmann, B. (2019). Rare-earth-element enrichment in post-Variscan polymetallic vein systems of the Harz Mountains, Germany. Mineralium Deposita, 54, 307-328.

Amodio-Morelli, L., Bonardi, G., Colonna, V., Dietrich, D., Giunta, G., Ippolito, F., Liguori, V., Lorenzoni, S., Paglionico, A., Perrone, V., Piccarreta, G., Russo, M., Scandone, P., Zanettin-Lorenzoni, L., & Zuppetta, A. (1976). L'arco Calabro-peloritano nell'Orogene Appeninico-Maghrebide. Memorie della Società Geologia Italiana, 17, 1–60.

Angì, G., Cirrincione, R., Fazio, E., Fiannacca, P., Ortolano, G., & Pezzino, A. (2010). Metamorphic evolution of preserved Hercynian crustal section in the Serre Massif (Calabria–Peloritani Orogen, southern Italy). Lithos, 115(1–4), 237–262. https://doi.org/10.1016/j.lithos.2009.12.008

Anovitz, L. M., & Essene, E. J. (1987). Phase equilibria in the system CaCO3-MgCO3-FeCO3. Journal of Petrology, 28(2), 389-415.

Ansdell, K. M., Nesbitt, B. E., & Longstaffe, F. J. (1989). A fluid inclusion and stable-isotope study of the Tom Ba-Pb-Zn deposit, Yukon Territory, Canada. Economic Geology, 84(4), 841-856.

Arnoni, E. (1875). La Calabria Illustrata. Parte Seconda. Tipografia Municipale Cosenza, Italy. (In Italian).

ASdN – Archivio di Stato di Napoli. Diplomatico 0911-1907, locale 147, armadio XVI, stipo b, Pergamene di Argentera, aa.1496-1553; Regia Camera della Sommaria, Processi antichi, Ordinamento Zeni, b.98, f.12, a.1559; Regia Camera della Sommaria, Segreteria, Partium, Inventario, Vol.202, aa.1539-1540; Repertorio 5 f.241v, aa.1553-1556, Repertorio 6, 72r, Vol.1044, aa.1587-1589 (in italian).

ASPN – Archivio Storico per le Province Napoletane, vol.1, 1876. A cura della Società di Storia Patria. Detken & Rocholl e Giannini Ed, pp.264-265 (in italian).

Atzori, P., Ferla, P., Paglionico, A., Piccarreta, G., & Rottura, A. (1984). Remnants of the Hercynian orogen along the 'Calabrian- Peloritan arc', southern Italy: a review. Journal of the Geological Society, 141(1), 137-145. https://doi.org/10.1144/gsjgs.141.1.0137

Augé, T., Bailly, L., & Wille, G. (2014). An unusual occurrence of synchysite-(Ce) in amygdules from the Esterel volcanic rocks, France: implications for rare-earth element mobility. The Canadian Mineralogist, 52(5), 837-856.

Ayuso, R.A., Messina, A., De Vivo, B., Russo, S., Woodruff, L.G., Sutter, J.F., & Belkin, H.E. (1994). Geochemistry and argon thermochronology of the Variscan Sila Batholith, southern Italy: source rocks and magma evolution. Contributions to Mineralogy and Petrology, 117, 87–109. https://doi.org/10.1007/BF00307732

Babedi, L., Tadie, M., Neethling, P., & Von der Heyden, B. P. (2021). A fundamental assessment of the impacts of cation (Cd, Co, Fe) substitution on the molecular chemistry and surface reactivity of sphalerite. Minerals Engineering, 160, 106695.

Babedi, L., Von Der Heyden, B. P., Neethling, P. H., & Tadie, M. (2019). The effect of Cd-substitution on the Raman vibrational characteristics of sphalerite. Vibrational spectroscopy, 105, 102968.

Babinski, M., Van Schmus, W. R., & Chemale Jr, F. (1999). Pb–Pb dating and Pb isotope geochemistry of Neoproterozoic carbonate rocks from the São Francisco basin, Brazil: implications for the mobility of Pb isotopes during tectonism and metamorphism. Chemical Geology, 160(3), 175-199.

Bačík, P., Fridrichová, J., Rybnikova, O., Štubňa, J., Illášová, Ľ., Škoda, R., Vaculovič, T., Pulišová, Z., and Sečkár, P. (2023). Crystal-Chemical and Spectroscopic Study of Gem Sphalerite from Banská Štiavnica, Slovakia. Minerals, 13(1), 109.

Barton P. B. Jr., Toulmin P., III (1966) Phase relations involving sphalerite in the Fe–Zn–S system. Econ Geol 61: 815–849.

Barton, P. B., & Bethke, P. M. (1987). Chalcopyrite disease in sphalerite; pathology and epidemiology. American Mineralogist, 72(5-6), 451-467.

Basuki, N. I., & Spooner, E. T. C. (2002). A review of fluid inclusion temperatures and salinities in Mississippi Valley-type Zn-Pb deposits: Identifying thresholds for metal transport. Exploration and Mining Geology, 11(1-4), 1-17. https://doi.org/10.2113/11.1-4.1

Bau, M. (1991). Rare-earth element mobility during hydrothermal and metamorphic fluid-rock interaction and the significance of the oxidation state of europium. Chemical geology, 93(3-4), 219-230.

Bau, M., & Dulski, P. (1995). Comparative study of yttrium and rare-earth element behaviours in fluorine-rich hydrothermal fluids. Contributions to Mineralogy and Petrology, 119, 213-223.

Bau, M., & Möller, P. (1993). Rare earth element systematics of the chemically precipitated component in Early Precambrian iron formations and the evolution of the terrestrial atmosphere-hydrosphere-lithosphere system. Geochimica et Cosmochimica Acta, 57(10), 2239-2249.

Bauer, M. E., Burisch, M., Ostendorf, J., Krause, J., Frenzel, M., Seifert, T., & Gutzmer, J. (2019). Trace element geochemistry of sphalerite in contrasting hydrothermal fluid systems of the Freiberg district, Germany:

insights from LA-ICP-MS analysis, near-infrared light microthermometry of sphalerite-hosted fluid inclusions, and sulfur isotope geochemistry. Mineralium Deposita, 54, 237-262.

Beaudoin, G., & Sangster, D. F. (1992). A descriptive model for silver-lead-zinc veins in clastic metasedimentary terranes. Economic Geology, 87(4), 1005-1021.

Belissont, R., Boiron, M. C., Luais, B., & Cathelineau, M. (2014). LA-ICP-MS analyses of minor and trace elements and bulk Ge isotopes in zoned Ge-rich sphalerites from the Noailhac–Saint-Salvy deposit (France): Insights into incorporation mechanisms and ore deposition processes. Geochimica et Cosmochimica Acta, 126, 518-540. https://doi.org/10.1016/j.gca.2013.10.052

Belissont, R., Munoz, M., Boiron, M. C., Luais, B., & Mathon, O. (2016). Distribution and oxidation state of Ge, Cu and Fe in sphalerite by μ-XRF and K-edge μ-XANES: insights into Ge incorporation, partitioning and isotopic fractionation. Geochimica et Cosmochimica Acta, 177, 298-314. https://doi.org/10.1016/j.gca.2016.01.001

Benaouda, R., Devey, C. W., Badra, L., & Ennaciri, A. (2017). Light rare-earth element mineralization in hydrothermal veins related to the Jbel Boho alkaline igneous complex, AntiAtlas/Morocco: The role of fluid-carbonate interactions in the deposition of synchysite-(Ce). Journal of Geochemical Exploration, 177, 28-44.

Benvenuti, M., Morelli, F., Lattanzi, P., Ruggieri, G., & Tanelli, G. (1994). Mineralogy, textures and mineral chemistry of Au-Ag vein mineralization at Rossano, Calabrian-Peloritan Arc (Calabria, Italy). Memorie della Società Geologica Italiana, 48, 723-727.

Bernardini, G. P., Borgheresi, M., Cipriani, C., Di Benedetto, F., & Romanelli, M. (2004). Mn distribution in sphalerite: an EPR study. Physics and chemistry of minerals, 31, 80-84. https://doi.org/10.1007/s00269-003-0374-7

Blankenburg, H. J., Götze, J., & Schulz, H. (1994). Quarzrohstoffe: mit 80 Tabellen. Dt. Verlag für Grundstoffindustrie.

Bodnar, R.J., Vityk, M.O. (1994) Interpretation of microthermometric data for H2O–NaCl fluid inclusions. In: deVivo,B., Frezzotti, M.L. (Eds.), Fluid Inclusions in Minerals, Methods and Applications. Blacksburg, p.117–130.

Bodnar, R. J., Lecumberri-Sanchez, P., Moncada, D., & Steele-MacInnis, M. (2014). 13.5–Fluid inclusions in hydrothermal ore deposits. Treatise on geochemistry, 13, 119-142.

Boiron, M. C., Cathelineau, M., & Richard, A. (2010). Fluid flows and metal deposition near basement/cover unconformity: lessons and analogies from Pb–Zn–F–Ba systems for the understanding of Proterozoic U deposits. Geofluids, 10(1-2), 270-292.

Boiron, M. C., Cathelineau, M., Dubessy, J., and Bastoul, A. M. (1990). Fluids in Hercynian Au veins from the French Variscan belt. Mineralogical Magazine, 54(375), 231-243.

Bonardi, G., Cavazza, W., Perrone, V., & Rossi, S (2001). Calabria-Peloritani terrane and northern Ionian Sea. In Anatomy of an Orogen: The Apennines and Adjacent Mediterranean Basins. Springer, The Netherlands, 287–306. https://doi.org/10.1007/978-94-015-9829-3_17

Bonardi, G., Cello, G., Perrone, V., Tortorici, L., Turco, E., & Zuppetta, A. (1982). The evolution of the northern sector of the Calabria-Peloritani Arc in a semiquantitative palynspastic restoration. Bollettino della Società Geologica Italiana, 101(2), 259-274.

Boni, M., Balassone, G., Fedele, L., & Mondillo, N. (2009). Post-Variscan hydrothermal activity and ore deposits in southern Sardinia (Italy): selected examples from the Iglesiente district and from Gerrei (Silius vein system). Periodico di Mineralogia, 78(3), 19-35.

Boni, M., Iannace, A., Köppel, V., Frueh-Green, G. L., & Hansmann, W. (1992). Late to post-Hercynian hydrothermal activity and mineralization in southwest Sardinia (Italy). Economic Geology, 87(8), 2113-2137.

Boni, M., Muchez, P. H., & Schneider, J. (2002). Permo-Mesozoic multiple fluid flow and ore deposits in Sardinia: a comparison with post-Variscan mineralization of Western Europe. Geological Society, London, Special Publications, 204(1), 199-211.

Bonnet, J. (2014). Distribution et contrôle cristallographique des éléments Ge, Ga et Cd dans les sphalérites des gisements de type Mississippi Valley dans les districts de Central et East Tennessee, USA (Doctoral dissertation, University of Lorraine).

Bonnet, J., Mosser-Ruck, R., Caumon, M. C., Rouer, O., Andre-Mayer, A. S., Cauzid, J., & Peiffert, C. (2016). Trace element distribution (Cu, Ga, Ge, Cd, and Fe) in sphalerite from the Tennessee MVT deposits, USA, by combined EMPA, LA-ICP-MS, Raman spectroscopy, and crystallography. The Canadian Mineralogist, 54(5), 1261-1284. https://doi.org/10.3749/canmin.1500104

Bouillin, J. P., Mouterde, R. E. N. Ê., Olivier, P., & Majesté-Menjoulas, C. (1988). Le Jurassique de Longobucco (Calabre, Italie), a la jonction de la Tethys ligure et de la Tethys maghrebine. Bulletin de la Société géologique de France, 4(1), 93-103.

Bradley, D. C., Leach, D. L., Symons, D., Emsbo, P., Premo, W., Breit, G., & Sangster, D. F. (2004). Reply to Discussion on “Tectonic controls of Mississippi Valley-type lead–zinc mineralization in orogenic forelands” by SE Kesler, JT Christensen, RD Hagni, W. Heijlen, JR Kyle, KC Misra, P. Muchez, and R. van der Voo, Mineralium Deposita. Mineralium Deposita, 39, 515-519.

Brannon, J. C., Podosek, F. A., Viets, J. G., Leach, D. L., Goldhabe, M., & Rowan, E. L. (1991). Strontium isotopic constraints on the origin of ore-forming fluids of the Viburnum Trend, southeast Missouri. Geochimica et Cosmochimica Acta, 55(5), 1407-1419.

Breiter, K., & Muller, A. (2009). Evolution of rare-metal granitic magmas documented by quartz chemistry. European Journal of Mineralogy, 21(2), 335-346.

Broom-Fendley, S., Brady, A. E., Wall, F., Gunn, G., & Dawes, W. (2017). REE minerals at the Songwe Hill carbonatite, Malawi: HREE-enrichment in late-stage apatite. Ore Geology Reviews, 81, 23-41.

Bryndzia, L. T., Scott, S. D., & Spry, P. G. (1988). Sphalerite and hexagonal pyrrhotite geobarometer; experimental calibration and application to the metamorphosed sulfide ores of Broken Hill, Australia. Economic Geology, 83(6), 1193-1204.

Burnham, C. W., & Ohmoto, H. (1980). Late-stage processes of felsic magmatism.

Buzatu, A., Buzgar, N., Damian, G., Vasilache, V., & Apopei, A. I. (2013). The determination of the Fe content in natural sphalerites by means of Raman spectroscopy. Vibrational Spectroscopy, 68, 220-224.

Cabri, L. J. (1969). Density determinations: accuracy and application to sphalerite stoichiometry. American Mineralogist: Journal of Earth and Planetary Materials, 54(3-4), 539-548.

Caggianelli, A., Prosser, G., & Del Moro, A. (2000). Cooling and exhumation history of deep-seated and shallow level, late Hercynian granitoids from Calabria. Geological Journal, 35(1), 33-42.

Cantarelli, F. (1844). De' saggi delle manifatture napolitane nell'anno. Ann. Civ. Regno Due Sicilie 1844, LXVII, 117–169. (In Italian).

Carpenter AB, Trout ML, and Pickett EE (1974) Preliminary report on the origin and chemical evolution of lead and zinc-rich oil field brines in central Mississippi. Economic Geology 69: 1191–1206.

Carrillo Rosúa, F. J., Morales Ruano, S., & Fenoll Hach-Alí, P. (2008). Textural and chemical features of sphalerite from the Palai-Islica deposit (SE Spain): Implications for ore genesis and color.

Cassard D., Chabod J. C., Marcoux E., Bourgine B., Castaing C., Gros Y., Kosakevich A., Moisy M. and Viallefond L. (1993) Mise en place et origine des mine´ralisations du gisement a` Zn, Ge, Ag, (Pb, Cd) de Noailhac – Saint-Salvy (Tarn, France). Chron. Recherche Minie´re 514, 3–37. Bureau de Recherches Géologiques et Minières, RPI 01: rapport de synthèse.

Cathelineau M., Boiron M. C., Poty B. and Marignac C. (1991). Hercynian gold-bearing quartz veins from western Europe: the «shear zone model» revisited. In: (Ladeira E. A., ed.) Brazil Gold'91. A. A. Balkema, Rotterdam, 15- 119.

Cathelineau, M., Boiron, M. C., Fourcade, S., Ruffet, G., Clauer, N., Belcourt, O., ... & Guillocheau, F. (2012). A major Late Jurassic fluid event at the basin/basement unconformity in western France: 40Ar/39Ar and K–Ar dating, fluid chemistry, and related geodynamic context. Chemical Geology, 322, 99-120.

Chareev, D. A., Osadchii, V. O., Shiryaev, A. A., Nekrasov, A. N., Koshelev, A. V., & Osadchii, E. G. (2017). Single-crystal Fe-bearing sphalerite: synthesis, lattice parameter, thermal expansion coefficient and microhardness. Physics and Chemistry of Minerals, 44, 287-296.

Chesley, J. T., Halliday, A. N., Kyser, T. K., & Spry, P. G. (1994). Direct dating of Mississippi Valley-type mineralization; use of Sm-Nd in fluorite. Economic Geology, 89(5), 1192-1199.

Christensen, J. N., Halliday, A. N., & Kesler, S. E. (1996). Rb-Sr dating of sphalerite and the ages of Mississippi-Valley-type Pb-Zn deposits.

Chryssoulis S. L. and Surges L. J. (1988). Behaviour of tetrahedrite in mill circuits of Brunswick mining and Smelting Corporation Ltd.. In Silver Exploration, Mining and Treatment. Inst. Mining Metall, London, pp. 205–216.

Ciccolella, A., Festa, V., Ruggieri, G., Schingaro, E., Tursi, F., Ventruti, G., & Fregola, R. A. (2024). The Zn-Pb (-Cu-Fe) mineralization in the northern Sila Massif (Calabria, southern Italy): Genetic constrains from trace element concentrations in sphalerite (No. EGU24-3657). Copernicus Meetings. https://doi.org/10.5194/egusphere-egu24-3657

Ciccolella, A., Tursi, F., Festa, V., Ruggieri, G., Schingaro, E., Ventruti, G., & Fregola, R. A. (2025). MVT-SHMS signature in basement-hosted Zn-Pb-(Cu-Fe) mineralization in the Sila Massif (Calabria, Italy): Evidence from trace elements and fluid inclusions data. Ore Geology Reviews, Volume 176, 106438, ISSN 0169-1368. https://doi.org/10.1016/j.oregeorev.2024.106438

CNEN (1960). Relazione Sulla Campagna 1960, Internal Report; Gruppo Delta: Bologna, Italy, 1960. (In Italian).

Collins AG (1975). Geochemistry of Oilfield Waters. Amsterdam: Elsevier.

Cook N.J., Etschmann B., Ciobanu C.L., Geraki K., Howard D.L., Williams T., Rae N., Pring A., Chen G., Johannessen B. (2015). Distribution and Substitution Mechanism of Ge in a Ge-(Fe)-Bearing Sphalerite. Minerals. 5(2):117-132. https://doi.org/10.3390/min5020117.

Cook, N. J., Ciobanu, C. L., Brugger, J., Etschmann, B., Howard, D. L., Jonge, M. D. D., Ryan c. and Paterson, D. (2012). Determination of the oxidation state of Cu in substituted Cu-In-Fe-bearing sphalerite via μ-XANES spectroscopy. American Mineralogist, 97(2-3), 476-479.

Cook, N. J., Ciobanu, C. L., Pring, A., Skinner, W., Shimizu, M., Danyushevsky, L., Saini-Eidukat, B., & Melcher, F. (2009). Trace and minor elements in sphalerite: A LA-ICPMS study. Geochimica et Cosmochimica Acta, 73(16), 4761-4791. https://doi.org/10.1016/j.gca.2009.05.045

Cortese, E. (1895). Descrizione Geologica Della Calabria, 2nd ed.; Casa del libro editrice: Roma, Italy, 1983; p. 338. (In Italian).

Craig J. R. (1973). The Cu–Zn–S system. Mineral. Deposita 8, 81– 91.

Crawford, M.L., 1981. Phase equilibria in aqueous fluid inclusions, Mineral. Assoc. Can. Short Course Handb., 6: 75-100.

Croze, V. (1989). Etude du skarn à tungstène de Longobucco (Calabre, Italie) dans son environnement granitique. Pétrographie et géochimie (Doctoral dissertation, Université Pierre et Marie Curie-Paris VI). (in french).

Cugerone, A., Cenki-Tok, B., Chauvet, A., Le Goff, E., Bailly, L., Alard, O., & Allard, M. (2018). Relationships between the occurrence of accessory Ge-minerals and sphalerite in Variscan Pb-Zn deposits of the Bossost anticlinorium, French Pyrenean Axial Zone: Chemistry, microstructures and ore-deposit setting. Ore Geology Reviews, 95, 1-19.

Cugerone, A., Cenki-Tok, B., Munoz, M., Kouzmanov, K., Oliot, E., Motto-Ros, V., & Le Goff, E. (2021). Behavior of critical metals in metamorphosed Pb-Zn ore deposits: example from the Pyrenean Axial Zone. Mineralium Deposita, 56, 685-705. https://doi.org/10.1007/s00126-020-01000-9

Cuteri, F. (1999). Risorse minerarie ed attività metallurgica nella Sila Piccola meridionale e nella Pre-Sila del versante tirrenico: prime osservazioni. (In Italian)

Cuteri, F. A. (2009). La metallurgia di Età medievale in Calabria. Nuovi dati archeologici. In V Congresso Nazionale di Archeologia Medievale (Foggia) (pp. 651-655). (In Italian)

Cuteri, F. A. (2012). Paesaggi minerari in Calabria: l'Argentera di Longobucco (CS). In Proceedings of the "VI Congresso Nazionale di Archeologia Medievale", L'Aquila, Italy (pp. 12-15). (In Italian)

Damian, G., Buzatu, A., Apopei, I.A., Szakács, Z.L., Denuț, Iepure G., & Bârgăoanu D. (2020). Valentinite and collofrom sphalerite in epithermal deposits from Baia Mare area, eastern Carpathians. Minerals, 10, 121; doi:10.3390/min10020121.

De Beaumont, E.; Pelouze, T.J.; Dufrénoy, O.P.M. (1842). Rapport sur un Mémoire de M. Adrien Paillette, ayant pour titre: Étudeshistoriques et géologiques sur le gîtes métallifères des Calabres et du nord de la Sicilie. C. R. Hebd. Acad. Sci., 14, 323–328. (In French).

De Vivo, B., Ayuso, R. A., Belkin, H. E., Lima, A., Messina, A., & Viscardi, A. (1991). Rock chemistry and fluid inclusion studies as exploration tools for ore deposits in the Sila batholith, southern Italy. Journal of Geochemical Exploration, 40(1-3), 291-310.

De Vivo, B., Cavaliere, S., Lima, A., Crisci, G.M. (1981). Active stream sediments multielemental geochemical survey in the Longobucco area (Calabria). Boll. Soc. Geol. Ital., 100, 499–525.

De Vivo, B., Closs, L.G., Lima, A., Marmolino, R., Perrone, V. (1984). Regional geochemical prospecting in Calabria, Southern Italy. J. Geochem. Explor., 21, 291–310.

De Vivo, B., Costabile, S., Lima, A. (1998). Cartografia geochimica della Calabria. Mem. Descr. Carta Geol. Ital., LV, 17–29, (In Italian, English abstract).

De Vries, B., Wahl, U., Ruffenach, S., Briot, O., & Vantomme, A. (2013). Influence of crystal mosaicity on axial channeling effects and lattice site determination of impurities. Applied Physics Letters, 103(17).

Decarlis, A., Dallagiovanna, G., Lualdi, A., Maino, M., & Seno, S. (2013). Stratigraphic evolution in the Ligurian Alps between Variscan heritages and the Alpine Tethys opening: A review. Earth-Science Reviews, 125, 43-68.

Di Benedetto F., Andreozzi G.B., Bernanrdini, G.P., Borgheresi M., Caneschi A., Cipriani C., Gatteschi D., Romanelli M. (2005a) Short-range order of Fe2+ in sphalerite by 57Fe Mössbauer spectroscopy and magnetic susceptibility. Physics and Chemistry of Minerals, 32, 339-348

Di Benedetto, F., Bernardini, G. P., Costagliola, P., Plant, D., & Vaughan, D. J. (2005b). Compositional zoning in sphalerite crystals. American Mineralogist, 90(8-9), 1384-1392. https://doi.org/10.2138/am.2005.1754

Diamond, L. W., Wanner, C., & Waber, H. N. (2018). Penetration depth of meteoric water in orogenic geothermal systems. Geology, 46(12), 1063-1066.

Dinca, G., Apopei, A. I., Szabo, R., & Maftei, A. E. (2022). The Effect of Mn Substitution on Natural Sphalerites by Means of Raman Spectroscopy: A Case Study of the Săcărâmb Au–Ag–Te Ore Deposit, Apuseni Mountains, Romania. Minerals 2022, 12, 885.

Evans, H. T. (1993). Crystal structures of sulfides. Reviews in Mineralogy and Geochemistry, 27(1), 29-65.

Evans, K. A., & Tomkins, A. G. (2020). Metamorphic fluids in orogenic settings. Elements: An International Magazine of Mineralogy, Geochemistry, and Petrology, 16(6), 381-387.

Fabbi, S., Borrelli, M., Innamorati, G., Aldega, L., Daëron, M., Perri, E., & Santantonio, M. (2024). Pervasive calcite veins and cleavage dilation in low-grade metamorphic rocks as a marker of Lower Jurassic rift-basin margins: a signature of microbial colonization. Marine and Petroleum Geology, 107115.

Fall, A., & Bodnar, R. J. (2018). How precisely can the temperature of a fluid event be constrained using fluid inclusions?. Economic Geology, 113(8), 1817-1843.

Festa, V. (2009). C-axis fabrics of quartz-ribbons during high-temperature deformation of syn-tectonic granitoids (Sila Massif, Calabria, Italy). Comptes Rendus Geoscience, 341, 557-567. doi:10.1016/j.crte.2009.06.008

Festa, V., Caggianelli, A., Kruhl, J.H., Liotta, D., Prosser, G., Gueguen, E., & Paglionico, A. (2006). Late-Hercynian shearing during crystallization of granitoid magmas (Sila Massif, southern Italy): Regional implications. Geodinamica Acta, 19, 185–195. https://doi.org/10.3166/ga.19.185-195

Festa, V., Caggianelli, A., Langone, A., & Prosser, G. (2013). Time–space relationships among structural and metamorphic aureoles relatedto granite emplacement: A case study from the Serre Massif (southern Italy). Geological Magazine, 150, 441–454. https://doi.org/10.1017/S0016756812000714

Festa, V., Cicala, M., & Tursi, F. (2020). The Curinga –Girifalco Line in the framework of the tectonic evolution of the remnant Alpine chain in Calabria (southern Italy). International Journal of Earth Sciences, 190, 2583–2598. https://doi.org/10.1007/s00531-020-01918-5

Festa, V., Langone, A., Caggianelli, A., & Rottura, A. (2010). Dike magmatism in the Sila Grande (Calabria, southern Italy): evidence of Pennsylvanian–Early Permian exhumation. Geosphere, 6(5), 549-566. https://doi.org/10.1130/GES00578.1

Festa, V., Messina, A., Paglionico, A., Piccarreta, G., & Rottura, A. (2004). Pre-Triassic history recorded in the Calabria-Peloritani segment of the Alpine chain, southern Italy. An overview. Periodico di Mineralogia, 73(2), 57-71.

Festa, V., Prosser, G., Caggianelli, A., Grande, A., Langone, A., & Mele, D. (2016). Vorticity analysis of the Palmi shear zone mylonites: new insights for the Alpine tectonic evolution of the Calabria–Peloritani terrane (southern Italy). Geological Journal, 51, 670-681. https://doi.org/10.1002/gj.2673

Festa, V., Spiess, R., & Tursi, F. (2024). Garnet coalescence clogs melt extraction channels in migmatite. Lithos, 472-473, 107581. https://doi.org/10.1016/j.lithos.2024.107581

Festa, V., Tursi, F., Caggianelli, A., & Spiess, R. (2018). The tectono-magmatic setting of the Hercynian upper continental crust exposed in Calabria (Italy) as revealed by the 1: 10,000 structural-geological map of the Levadio stream area. Italian Journal of Geosciences, 137(2), 165-174. https://doi.org/10.3301/IJG.2018.03

Fiannacca, P., Williams, I.S., & Cirrincione, R. (2017). Timescales and mechanisms of batholith construction: Constraints from zircon oxygen isotopes and geochronology of the late Variscan Serre Batholith (Calabria, southern Italy). Lithos, 277, 302–314. https://doi.org/10.1016/j.lithos.2016.06.011

Finger, F., Roberts, M. P., Haunschmid, B., Schermaier, A., & Steyrer, H. P. (1997). Variscan granitoids of central Europe: their typology, potential sources and tectonothermal relations. Mineralogy and Petrology, 61(1-4), 67.

Fleet, M. E. (1977). Structural transformations in natural ZnS. American Mineralogist, 62(5-6), 540-546.

Fleischer, M., Rooseboom, E. H., Skinner, Brian (1960) New Mineral Names; New data; Discredited minerals. American Mineralogist, 45 (9-10) 1130-1136

Fornelli, A., Pascazio, A., & Piccarreta G. (2012). Diachronic and different metamorphic evolution in the fossil

Förster, H. J. (2001). Synchysite-(Y)–synchysite-(Ce) solid solutions from Markersbach, Erzgebirge, Germany: REE and Th mobility during high-T alteration of highly fractionated aluminous A-type granites. Mineralogy and Petrology, 72, 259-280.

Fougerouse, D., Cugerone, A., Reddy, S. M., Luo, K., & Motto-Ros, V. (2023). Nanoscale distribution of Ge in Cu-rich sphalerite. Geochimica et Cosmochimica Acta, 346, 223-230. https://doi.org/10.1016/j.gca.2023.02.011

Franco, D. (2003). Il Ferro in Calabria. Kaleidon, Ed.; Reggio: Calabria, Italy; Volume 176. (In Italian)

Franco, D. (2019). Le Reali Fabbriche del Ferro in Calabria. Tra Storia e Archeologia Industriale; Rubbettino Editore: Soveria Mannelli (Catanzaro), Italy; p. 238. (In Italian)

Fregola, R. A., Ciccolella, A., Festa, V., Ruggieri, G., Schingaro, E., Tursi, F., & Ventruti, G. (2023). Review of Polymetallic Mineralization in the Sila and Serre Massifs (Calabria, Southern Italy). Minerals, 13(3), 439. https://doi.org/10.3390/min13030439

Frenzel, M., Hirsch, T., & Gutzmer, J. (2016). Gallium, germanium, indium, and other trace and minor elements in sphalerite as a function of deposit type—A meta-analysis. Ore Geology Reviews, 76, 52-78. https://doi.org/10.1016/j.oregeorev.2015.12.017

Frenzel, M., Voudouris, P., Cook, N. J., Ciobanu, C. L., Gilbert, S., & Wade, B. P. (2021). Evolution of a hydrothermal ore-forming system recorded by sulphide mineral chemistry: a case study from the Plaka Pb–Zn–Ag Deposit, Lavrion, Greece. Mineralium Deposita, 1-22. https://doi.org/10.1007/s00126-021-01067-y

Fu, S., Lan, Q., & Yan, J. (2020). Trace element chemistry of hydrothermal quartz and its genetic significance: A case study from the Xikuangshan and Woxi giant Sb deposits in southern China. Ore Geology Reviews, 126, 103732.

Fusswinkel, T., Wagner, T., Wälle, M., Wenzel, T., Heinrich, C. A., & Markl, G. (2013). Fluid mixing forms basement-hosted Pb-Zn deposits: insight from metal and halogen geochemistry of individual fluid inclusions. Geology, 41(6), 679-682.

Garate-Olave, I., Müller, A., Roda-Robles, E., Gil-Crespo, P. P., & Pesquera, A. (2017). Extreme fractionation in a granite–pegmatite system documented by quartz chemistry: The case study of Tres Arroyos (Central Iberian Zone, Spain). Lithos, 286, 162-174.

Gardner, H. D., & Hutcheon, I. (1985). Geochemistry, mineralogy, and geology of the Jason Pb-Zn deposits, Macmillan pass, Yukon, Canada. Economic Geology, 80(5), 1257-1276.

George, L. L., Cook, N. J., & Ciobanu, C. L. (2016). Partitioning of trace elements in co-crystallized sphalerite–galena–chalcopyrite hydrothermal ores. Ore Geology Reviews, 77, 97-116. https://doi.org/10.1016/j.oregeorev.2016.02.009

Gerard A, Imbert P, Prange H, Varret F, Winterberger M (1971) Fe^{2+} impurities, isolated and in pairs, in ZnS and CdS studied by the Mo¨ ßbauer effect. J Phys Chem Solids 32: 2091–2100.

Gifkins, C. C., Herrmann, W., & Large, R. R. (2005). Altered volcanic rocks: A guide to description and interpretation. University of Tasmania.

Gleeson, S. A., & Yardley, B. W. D. (2002). Extensional veins and Pb-Zn mineralization in basement rocks: The role of penetration of formation brines. Water Science and Technology Library, 40, 189-206.

Gleeson, S. A., & Yardley, B. W. D. (2003). Surface-derived fluids in basement rocks: inferences from palaeo-hydrothermal systems. Journal of Geochemical Exploration, 78, 61-65.

Göb, S., Loges, A., Nolde, N., Bau, M., Jacob, D. E., & Markl, G. (2013). Major and trace element compositions (including REE) of mineral, thermal, mine and surface waters in SW Germany and implications for water–rock interaction. Applied Geochemistry, 33, 127-152.

Goldstein RH and Reynolds TJ (1994). Systematics of fluid inclusions in diagenetic minerals. SEPM Short Course Notes 31: 188.

Goodfellow, W. G. (1993). Geology and genesis of stratiform sediment-hosted (SEDEX) zinc-lead-silver sulphide deposits. Mineral Deposit Modeling., 201-251.

Götte, T. (2018). Trace element composition of authigenic quartz in sandstones and its correlation with fluid–rock interaction during diagenesis.

Gottesmann W. and Kampe A. (2007). Zn/Cd ratios in calcsilicate- hosted sphalerite ores at Tumurtijn-ovoo, Mongolia. Chem. Erde – Geochem. 67, 323–328.

Gottesmann W., Gottesmann B. and Seifert W. (2009). Sphalerite composition and ore genesis at the Tumurtjin-ovoo Fe–Mn–Zn skarn deposit, Mongolia. Neues Jb. Mineral. Abh. 185, 249– 280.

Götze, J., Pan, Y., & Müller, A. (2021). Mineralogy and mineral chemistry of quartz: A review. mineralogical magazine, 85(5), 639-664.

Götze, J., Plötze, M., Graupner, T., Hallbauer, D. K., & Bray, C. J. (2004). Trace element incorporation into quartz: A combined study by ICP-MS, electron spin resonance, cathodoluminescence, capillary ion analysis, and gas chromatography. Geochimica et Cosmochimica Acta, 68(18), 3741-3759.

Grammatikopoulos, T. A., Valeyev, O., & Roth, T. (2006). Compositional variation in Hg-bearing sphalerite from the polymetallic Eskay Creek deposit, British Columbia, Canada. Geochemistry, 66(4), 307-314. https://doi.org/10.1016/j.chemer.2005.11.003

Guastoni, A., Nestola, F., & Giaretta, A. (2009). Mineral chemistry and alteration of rare earth element (REE) carbonates from alkaline pegmatites of Mount Malosa, Malawi. American Mineralogist, 94(8-9), 1216-1222.

Guillong, M., Meier, D. L., Allan, M. M., Heinrich, C. A., & Yardley, B. W. (2008). Appendix A6: SILLS: A MATLAB-based program for the reduction of laser ablation ICP-MS data of homogeneous materials and inclusions. Mineralogical Association of Canada Short Course, 40, 328-333.

Hagni, R. D., Johnson, C. A., & Williams-Jones, A. E. (2005). Geology, petrology, and mineral chemistry of the big zinc deposit, New Brunswick, Canada. Economic Geology, 100(2), 221-250.

Hayes, S. M., & McCullough, E. A. (2018). Critical minerals: A review of elemental trends in comprehensive criticality studies. Resources Policy, 59, 192-199.

Haynes FM and Kesler SE (1987). Chemical evolution of brines during Mississippi Valley-type mineralization: Evidence from East Tennessee and Pine Point. Economic Geology 82: 53–71.

Hintzen, R., Werner, W., Hauck, M., Klemd, R., & Fischer, L. A. (2023). Multistage fluorite mineralization in the southern Black Forest, Germany: evidence from rare earth element (REE) geochemistry. European Journal of Mineralogy, 35(3), 403-426.

Höll, R., Kling, M., & Schroll, E. (2007). Metallogenesis of germanium—A review. Ore Geology Reviews, 30(3-4), 145-180. https://doi.org/10.1016/j.oregeorev.2005.07.034

Hope, G. A., Woods, R., & Munce, C. G. (2001). Raman microprobe mineral identification. Minerals Engineering, 14(12), 1565-1577.

Hu, Y., Wei, C., Ye, L., Huang, Z., Danyushevsky, L., & Wang, H. (2021). LA-ICP-MS sphalerite and galena trace element chemistry and mineralization-style fingerprinting for carbonate-hosted Pb-Zn deposits: Perspective from early Devonian Huodehong deposit in Yunnan, South China. Ore Geology Reviews, 136, 104253. https://doi.org/10.1016/j.oregeorev.2021.104253

Huston D. L., Jablonsky W. and Sie S. H. (1996) The distribution and mineral hosts of silver in Eastern Australian volcanogenic massive sulfide deposits. Can. Mineral. 34, 529–546.

Innamorati, G. & Santantonio, M. (2018). Evidence for extended Hercynian basement and a preserved Jurassic basin-margin tract in Northern Calabria (Southern Italy): The Longobucco Basin. Sedimentary Geology, 376, 147–163. https://doi.org/10.1016/j.sedgeo.2018.08.009

Ippolito, F. (1947a). Il Centro Ricerche Geominerarie dell'IRI (Napoli). Experientia 1947, 3, 124. (In Italian).

Ippolito, F. (1947b). Studi geologici in Calabria. Ric. Sci. E Ricostr. 1947, 17, 54–56. (In Italian).

Ippolito, F. (1947c). Primi risultati di studi geologici eseguiti in Calabria nel 1946. Boll. Soc. Natural. Napoli 1947, LV, 105–107. (In Italian).

Jimenez-Sandoval, S., Lopez-Rivera, A., & Irwin, J. C. (2003). Influence of reduced mass differences on the Raman spectra of ternary mixed compounds: Zn 1− x Fe x S and Zn 1− x Mn x S. Physical Review B, 68(5), 054303.

Joan, Z. (1988). Indium and Germanium in the structure of sphalerite: an example of coupled substitution with copper. - Miner. Petrol. 39: 211-229.

Jourdan, A. L., Vennemann, T. W., Mullis, J., Ramseyer, K., & Spiers, C. J. (2009). Evidence of growth and sector zoning in hydrothermal quartz from Alpine veins. European Journal of Mineralogy, 21(1), 219-231.

Kaneko S., Aoki H., Nonaka I., Imoto F. and Matsumoto K. (1984). Solid solution and phase transformation in the system ZnS–MnS under hydrothermal conditions. J. Electrochem. Soc. 130, 2487–2489.

Keith, M., Haase, K. M., Schwarz-Schampera, U., Klemd, R., Petersen, S., & Bach, W. (2014). Effects of temperature, sulphur, and oxygen fugacity on the composition of sphalerite from submarine hydrothermal vents. Geology, 42(8), 699-702. https://doi.org/10.1130/G35655.1

Kelley, K. D., Leach, D. L., Johnson, C. A., Clark, J. L., Fayek, M., Slack, J. F., Anderson, V. M., Ayuso, R. A., & Ridley, W. I. (2004). Textural, compositional, and sulfur isotope variations of sulfide minerals in the Red Dog Zn-Pb-Ag deposits, Brooks Range, Alaska: Implications for ore formation. Economic Geology, 99(7), 1509-1532. https://doi.org/10.2113/gsecongeo.99.7.1509

Kesler, S. E. (2005). Ore-forming fluids. Elements, 1(1), 13-18.

Keys, J. D., Horwood, J. L., Baleshta, T. M., Cabri, L. J., & Harris, D. C. (1968). Iron-iron interaction in iron-containing zinc sulphide. The Canadian Mineralogist, 9(4), 453-467.

Kharbish, S. (2007). A Raman spectroscopic investigation of Fe-rich sphalerite: effect of Fe-substitution. Physics and Chemistry of Minerals, 34, 551-558.

Knorsch, M., Nadoll, P., & Klemd, R. (2020). Trace elements and textures of hydrothermal sphalerite and pyrite in Upper Permian (Zechstein) carbonates of the North German Basin. Journal of Geochemical Exploration, 209, 106416. https://doi.org/10.1016/j.gexplo.2019.106416

Kolawole, F., & Evenick, J. C. (2023). Global distribution of geothermal gradients in sedimentary basins. Geoscience Frontiers, 14(6), 101685.

Kubo, T., Nakato, T., & Uchida, E. (1992). An experimental study on partitioning of Zn, Fe, Mn and Cd between sphalerite and aqueous chloride solution. Shigen-Chishitsu, 42(235), 301-309.

Kullerud G., (1953) The FeS-ZnS system: A geological thermometer, Norsk Geologisk Tiddskrift, 32, pp. 61-147.

Lanari P, Vidal O, De Andrade V, Dubacq B, Lewin E, Grosch EG, Schwartz S (2014) XMapTools: a MATLAB©-based program for electron microprobe X-ray image processing and geothermobarometry. Comput Geosci 62:227–240. https://doi.org/10.1016/j.cageo.2013.08.010

Lanari, P., Vho, A., Bovay, T., Airaghi, L., & Centrella, S. (2019). Quantitative compositional mapping of mineral phases by electron probe micro-analyser. Geological Society, London, Special Publications, 478(1), 39-63. https://doi.org/10.1144/SP478.4

Landtwing, M. R., & Pettke, T. (2005). Relationships between SEM-cathodoluminescence response and trace-element composition of hydrothermal vein quartz. American Mineralogist, 90(1), 122-131.

Langone, A., Caggianelli, A., Festa, V., & Prosser, G. (2014). Time constraints on the building of the Serre Batholith: Consequences for the thermal evolution of the Hercynian continental crust exposed in Calabria (southern Italy). Journal of Geology, 122, 183–199. https://doi.org/10.1086/675227

Langone, A., Godard, G., Prosser, G., Caggianelli, A., Rottura, A., & Tiepolo, M. (2010). P-T-t path of the Hercynian low-pressure rocks from the Mandatoriccio complex (Sila massif, Calabria, Italy): New insights for crustal evolution. Journal of Metamorphic Geology, 28(2), 137–162. https://doi.org/10.1111/j.1525-1314.2009.00858.x

Lavrentyev, A. A., Gabrelian, B. V., Kulagin, B. B., Nikiforov, I. Y., & Sobolev, V. V. (2007). The influence of pressure on the birefringence in semiconductor compounds ZnS, CuGaS2, and InPS4. physica status solidi (b), 244(1), 315-320.

Le Breton, E., Brune, S., Ustaszewski, K., Zahirovic, S., Seton, M., & Müller, R. D. (2021). Kinematics and extent of the Piemont–Liguria Basin–implications for subduction processes in the Alps. Solid Earth, 12(4), 885-913.

Leach DL, Sangster DF, Kelley KD, et al. (2005) Sediment-hosted lead-zinc deposits; a global perspective. In: Sangster DF (ed.) Carbonate Hosted Lead-Zinc Deposits. Society of Economic Geologists Special Publication 4, pp. 144–170. Littleton, CO: Society of Economic Geologists.

Leach DL, Viets JG, Kozlowski A, and Kibitlewski S (1996) Geology, Geochemistry, and Genesis of the Silesia-Cracow Zinc Lead District, Southern Poland. In: Skinner BJ (ed.) Economic Geology 75th Anniversary Volume 1905–1980. Littleton, CO: Society of Economic Geologists.

Leach, D. L., Taylor, R. D., Fey, D. L., Diehl, S. F., & Saltus, R. W. (2010). A deposit model for Mississippi Valley-type lead-zinc ores (No. 2010-5070-A). US Geological Survey. https://doi.org/10.3133/sir20105070A

Lepetit, P., Bente, K., Doering, T., & Luckhaus, S. (2003). Crystal chemistry of Fe-containing sphalerites. Physics and Chemistry of Minerals, 30, 185-191.

Li, J., Sagoe, G., Wang, X., & Yang, Z. (2021). Assessing the suitability of lithium-related geothermometers for estimating the temperature of felsic rock reservoirs. Geothermics, 89, 101950. https://doi.org/10.1016/j.geothermics.2020.101950

Li, X. F., Zhu, Y. T., & Xu, J. (2020). Indium as a critical mineral: A research progress report. Chin. Sci. Bull, 65(33), 3678-3687.

Li, X. M., Zhang, Y. X., Li, Z. K., Zhao, X. F., Zuo, R. G., Xiao, F., & Zheng, Y. (2023). Discrimination of Pb-Zn deposit types using sphalerite geochemistry: New insights from machine learning algorithm. Geoscience Frontiers, 14(4), 101580. https://doi.org/10.1016/j.gsf.2023.101580

Li, X., & Zhou, M. F. (2015). Multiple stages of hydrothermal REE remobilization recorded in fluorapatite in the Paleoproterozoic Yinachang Fe–Cu–(REE) deposit, Southwest China. Geochimica et Cosmochimica Acta, 166, 53-73.

Lindblom, S. (1986). Textural and fluid inclusion evidence for ore deposition in the Pb-Zn deposit at Laisvall, Sweden. Economic Geology, 81(1), 46-64.

Liu, S., Zhang, Y., Ai, G., Xue, X., Li, H., Shah, S. A., ... & Chen, X. (2022). LA-ICP-MS trace element geochemistry of sphalerite: Metallogenic constraints on the Qingshuitang Pb–Zn deposit in the Qinhang Ore Belt, South China. Ore Geology Reviews, 141, 104659

Lockington, J. A., Cook, N. J., & Ciobanu, C. L. (2014). Trace and minor elements in sphalerite from metamorphosed sulphide deposits. Mineralogy and Petrology, 108, 873-890.

Loges, A., Migdisov, A. A., Wagner, T., Williams-Jones, A. E., & Markl, G. (2013). An experimental study of the aqueous solubility and speciation of Y (III) fluoride at temperatures up to 250 C. Geochimica et Cosmochimica Acta, 123, 403-415.

Lorenzoni, S., Orsi, G., Zanettin Lorenzoni, E. (1983). Metallogenesis in the tectonic units and lithogenetic environments of Calabria (Southern Italy). Mem. Sci. Geol., 35, 411–428.

Lovisato, D. (1879). Cenni geognostici e geologici sulla Calabria settentrionale. Parte II. Boll. R. Com. Geol. Ital., 10, 24–39,108–137. (In Italian)

Ludwig, K. R., Vollmer, R., Turi, B., Simmons, K. R., & Perna, G. (1989). Isotopic constraints on the genesis of base-metal ores in southern and central Sardinia. European Journal of Mineralogy, 1(5), 657-666.

Luo, K., Cugerone, A., Zhou, M. F., Zhou, J. X., Sun, G. T., Xu, J., ... & Lu, M. D. (2022). Germanium enrichment in sphalerite with acicular and euhedral textures: an example from the Zhulingou carbonate-hosted Zn (-Ge) deposit, South China. Mineralium Deposita, 57(8), 1343-1365.

Lusk J., Scott S. D. and Ford C. E. (1993). Phase relations in the Fe–Zn–S system to 5 Kbars and temperatures between 325 and 150 °C. Econ. Geol. 88, 1880–1903.

Manning P. G., (1967) Absorption spectra of Fe(III) in octahedral sites in sphalerite. Can Mineral 9: 57–64.

Manning, P. G. (1968). Optical absorption studies of the mixed-ion (Cu and Al) doping of sphalerite. The Canadian Mineralogist, 9(3), 429-433.

Mao, M., Simandl, G. J., Spence, J., Neetz, M., & Marshall, D. (2015). Trace element composition of fluorite and its potential use as an indicator in mineral exploration. Geological Fieldwork, (2016-1), 181.

Marignac, C., & Cuney, M. (1999). Ore deposits of the French Massif Central: insight into the metallogenesis of the Variscan collision belt. Mineralium Deposita, 34, 472-504.

Maydagàn, L., Franchini, M., Rusk, B., Lentz, D.R., McFarlane, C., Impiccini, A., Ríos, F.J., & Rey, R. (2015). Porphyry to Epithermal Transition in the Altar Cu-(Au-Mo) deposit, argentina, studied by cathodoluminescence, LA-ICP-MS, and fluid inclusion analysis. Econ. Geol. 110, 889–923

Mazzoleni J. (1968). Fonti per la storia della Calabria del Viceregno (1503-1734), Napoli, pp.4-6 (in italian).

Messina, A., Russo, S., Perrone, V., & Giacobbe, A. (1991). Calc-alkaline late Variscan two mica-cordierite-Al-silicate-bearing intrusions of the Sila Batholith (northern sector of the Calabrian-Peloritan Arc-Italy). Bollettino della Società Geologica Italiana, 110(2), 365-389.

Migdisov, A., Williams-Jones, A. E., Brugger, J., & Caporuscio, F. A. (2016). Hydrothermal transport, deposition, and fractionation of the REE: Experimental data and thermodynamic calculations. Chemical Geology, 439, 13-42.

Moeller, P. (2000). Rare earth elements and yttrium as geochemical indicators of the source of mineral and thermal waters. In Hydrogeology of crystalline rocks (pp. 227-246). Dordrecht: Springer Netherlands.

Moh G. H. and Ja¨ger A. (1978). Phasengleichgewichte des Systems Ge–Pb–Zn–S in Relation zu Germanium-Gehalten alpiner Pb– Zn-Lagersta¨tten. Verhandlungen der Geologischen Bundesan- stalt Wien 1978. pp. 437–440.

Möller P. (1987). Correlation of homogenization temperatures of accessory minerals from sphalerite-bearing deposits and Ga/Ge model temperatures. Chem. Geol. 61, 153–159.

Möller, P., Bau, M., Dulski, P., & Lüders, V. (1998, August). REE and yttrium fractionation in fluorite and their bearing on fluorite formation. In Proc 9th Quadr IAGOD Symp (pp. 575-592).

Mondillo, N., Boni, M., Balassone, G., Spoleto, S., Stellato, F., Marino, A., ... & Spratt, J. (2016). Rare earth elements (REE)—Minerals in the Silius fluorite vein system (Sardinia, Italy). Ore Geology Reviews, 74, 211-224.

More, A. P., Vaughan, D. J., & Ashworth, J. R. (1991). Banded sphalerite from the North Pennine orefield. Mineralogical Magazine, 55(380), 409-416.

Moroni, M., Naitza, S., Ruggieri, G., Aquino, A., Costagliola, P., De Giudici, G., ... & Lattanzi, P. (2019). The Pb-Zn-Ag vein system at Montevecchio-Ingurtosu, southwestern Sardinia, Italy: A summary of previous knowledge and new mineralogical, fluid inclusion, and isotopic data. Ore Geology Reviews, 115, 103194. https://doi.org/10.1016/j.oregeorev.2019.103194

Moskalyk, R. R. (2003). Gallium: the backbone of the electronics industry. Minerals Engineering, 16(10), 921-929.

Muchez, P., Heijlen, W., Banks, D., Blundell, D., Boni, M., & Grandia, F. (2005). 7: Extensional tectonics and the timing and formation of basin-hosted deposits in Europe. Ore Geology Reviews, 27(1-4), 241-267.

Mudd G.M., Jowitt S.M., Werner T.T. (2017) The world's lead-zinc mineral resources: Scarcity, data, issues and opportunities. Ore Geology Reviews, 80, 1160-1190

Müller, A., Herrington, R., Armstrong, R., Seltmann, R., Kirwin, D. J., Stenina, N. G., & Kronz, A. (2010). Trace elements and cathodoluminescence of quartz in stockwork veins of Mongolian porphyry-style deposits. Mineralium Deposita, 45, 707-727.

Müller, A., Wiedenbeck, M., Kerkhof, A. M. V. D., Kronz, A., & Simon, K. (2003). Trace elements in quartz-a combined electron microprobe, secondary ion mass spectrometry, laser-ablation ICP-MS, and cathodoluminescence study. European Journal of Mineralogy, 15(4), 747-763.

Munoz, M., Boyce, A. J., Courjault-Rade, P., Fallick, A. E., & Tollon, F. (1994). Multi-stage fluid incursion in the Palaeozoic basement-hosted Saint-Salvy ore deposit (NW Montagne Noire, southern France). Applied geochemistry, 9(6), 609-626. https://doi.org/10.1016/0883-2927(94)90022-1

Mylius, J.L. and Dietz, N., 1965. Solubility of zinc chloride (ZnC12) in water. In: W.F. Linke (Editor), Solubilities of Inorganic and Metal Organic Compounds, 4th ed. Am. Chem. Soc., 2: 892.

Naitza, S., Conte, A. M., Cuccuru, S., Oggiano, G., Secchi, F., & Tecce, F. (2017). A Late Variscan tin province associated to the ilmenite-series granites of the Sardinian Batholith (Italy): The Sn and Mo mineralisation around the Monte Linas ferroan granite. Ore Geology Reviews, 80, 1259-1278.

Nakai, S. I., Halliday, A. N., Kesler, S. E., Jones, H. D., Kyle, J. R., & Lane, T. E. (1993). Rb-Sr dating of sphalerites from Mississippi Valley-type (MVT) ore deposits. Geochimica et Cosmochimica Acta, 57(2), 417-427.

Nriagu J. O. (1998). History, production, and uses of thallium. In Thallium in the Environment (ed. J. O. Nriagu). John Wiley and Sons, Inc., New York, pp. 1–14.

Oen, I. S., Kager, P., & Kieft, C. (1980). Oscillatory zoning of a discontinuous solid-solution series: sphalerite–stannite. American Mineralogist, 65(11-12), 1220-1232.

Omenetto, P., Meggiolaro, V., Spagna, P., Brigo, L., Ferla, P., and Guion, J. L. (1988). Scheelite-bearing metalliferous sequences of the Peloritani Mountains, Northeastern Sicily (with some remarks on Tungsten metallogenesis in the Calabrian-Peloritan Arc). Mineral deposits within the European Community, 179-198.

Ono, S., Hirai, K., Matsueda, H., & Kabashima, T. (2004). Polymetallic mineralization at the Suttsu vein-type deposit, southwestern Hokkaido, Japan. Resource Geology, 54(4), 453-464.

Ortolano, G., Visalli, R., Fazio, E., Fiannacca, P., Godard, G., Pezzino, A., Punturo, R., Sacco, V., & Cirrincione, R. (2020). Tectono-metamorphic evolution of the Calabria continental lower crust: The case of the Sila Piccola Massif. International Journal of Earth Sciences, 109, 1295-1319

Osadchii, E. G., & Gorbaty, Y. E. (2010). Raman spectra and unit cell parameters of sphalerite solid solutions (FexZn1− xS). Geochimica et Cosmochimica Acta, 74(2), 568-573.

Ostendorf, J., Henjes-Kunst, F., Schneider, J., Melcher, F., & Gutzmer, J. (2017). Genesis of the carbonate-hosted Tres Marias Zn-Pb-(Ge) deposit, Mexico: constraints from Rb-Sr sphalerite geochronology and Pb isotopes. Economic Geology, 112(5), 1075-1087. https://doi.org/10.5382/econgeo.2017.4502

Pažout, R., Sejkora, J., & Šrein, V. (2019). Ag-Pb-Sb sulfosalts and Se-rich mineralization of Anthony of Padua Mine near Poličany—Model example of the mineralization of Silver Lodes in the historic Kutná Hora Ag-Pb ore district, Czech Republic. Minerals, 9(7), 430.

Perri, F., Cirrincione, R., Critelli, S., Mazzoleni, P., & Pappalardo, A. (2008). Clay mineral assemblages and sandstone compositions of the Mesozoic Longobucco Group, northeastern Calabria: implications for burial history and diagenetic evolution. International Geology Review, 50(12), 1116-1131.

Petke, T., & Diamond, L. W. (1996). Rb-Sr dating of sphalerite based on fluid inclusion-host mineral isochrons; a clarification of why it works. Economic Geology, 91(5), 951-956.

Pfaff, K., Koenig, A., Wenzel, T., Ridley, I., Hildebrandt, L. H., Leach, D. L., & Markl, G. (2011). Trace and minor element variations and sulphur isotopes in crystalline and colloform ZnS: Incorporation mechanisms and implications for their genesis. Chemical Geology, 286(3-4), 118-134

Piluso, E., & Morten, L. (2004). Hercynian high temperature granulites and migmatites from the Catena Costiera, northern Calabria, southern Italy. Periodico di Mineralogia, 73(2), 159-172

Pring, A., Wade, B., McFadden, A., Lenehan, C. E., & Cook, N. J. (2020). Coupled substitutions of minor and trace elements in co-existing sphalerite and wurtzite. Minerals, 10(2), 147.

Qian X. (1987). Trace elements in galena and sphalerite and their geochemical significance in distinguishing the genetic types of Pb–Zn ore deposits. Chin. J. Geochem. 6, 177–190.

Rager, H., Amthauer, G., Bernroider, M., & Schurmann, K. (1996). Colour, crystal chemistry, and mineral association of a green sphalerite from Steinperf, Dill Syncline, FRG. European Journal of Mineralogy, 8(5), 1191-1198.

Rajabi, A., Mahmoodi, P., Alfonso, P., Canet, C., Colin, A., Azhdari, S., ... & Saeidi, R. (2024). Barite replacement as a key factor in the genesis of sediment-hosted Zn-Pb±Ba and barite-sulfide deposits: Ore fluids and isotope (S and Sr) signatures from sediment-hosted Zn-Pb±Ba deposits of Iran. Minerals, 14(7), 671.

Rambaldi E. R., Rajan R. S., Housley R. M. and Wang D. (1986). Gallium-bearing sphalerite in a metal-sulfide nodule of the Qingzhen (EH3) chondrite. Meteoritics 21, 23–31.

Reesman, R. H. (1968). The Rb-Sr analyses of some sulfide mineralization. Earth and Planetary Science Letters, 5, 23-26.

Rittmann, A. (1947). Il Centro di Studi Silani. Sezione Geomineraria; attività svolta durante l'anno 1947. Ric. Sci. E Ricostr. 1947, 17, 12. (In Italian).

Roberts, N. M., Drost, K., Horstwood, M. S., Condon, D. J., Chew, D., Drake, H., ... & Lee, J. K. (2020). Laser ablation inductively coupled plasma mass spectrometry (LA-ICP-MS) U–Pb carbonate geochronology: strategies, progress, and limitations. Geochronology, 2(1), 33-61.

Roedder, E. (1962). Studies of fluid inclusions; Part 1, Low temperature application of a dual-purpose freezing and heating stage. Economic Geology, 57(7), 1045-1061.

Roedder E (1984). Fluid inclusions. Reviews in Mineralogy 12: 644.

Roedder E and Bodnar RJ (1980). Geologic pressure determinations from fluid inclusion studies. Annual Review of Earth and Planetary Sciences 8: 263–301.

Roedder, E. (1967). Environment of deposition of stratiform (Mississippi Valley-type) ore deposits, from studies of fluid inclusions.

Roedder, E. (1968). The non-colloidal origin of'colloform'textures in sphalerite ores. Economic Geology, 63(5), 451-471.

Roedder, E. (1971). Fluid inclusion studies on the porphyry-type ore deposits at Bingham, Utah, Butte, Montana, and Climax, Colorado. Economic Geology, 66(1), 98-118.

Roedder, E., & Coombs, D. S. (1967). Immiscibility in Granitic Melts, Indicated by Fluid Inclusions in Ejected Granitic Blocks fromAscension Island. Journal of Petrology, 8(3), 417-451.

Romano, V., Cirrincione, R., Fiannacca, P., Lustrino, M., & Tranchina, A. (2011). Late-Hercynian post-collisional dike magmatism in central Calabria (Serre Massif, southern Italy). Periodico Di Mineralogia, 80(3), 489–515

Rottura, A. D. M. A. P. L., Del Moro, A., Pinarelli, L., Petrini, R., Peccerillo, A., Caggianelli, A., ... & Piccarreta, G. (1991). Relationships between intermediate and acidic rocks in orogenic granitoid suites: petrological, geochemical and isotopic (Sr, Nd, Pb) data from Capo Vaticano (southern Calabria, Italy). Chemical Geology, 92(1-3), 153-176.

Rottura, A., Bargossi, G. M., Caironi, V., Del Moro, A., Maccarrone, E., Macera, P., ... & Poli, G. (1990). Petrogenesis of contrasting Hercynian granitoids from the Calabrian Arc, southern Italy. Lithos, 24(2), 97-119.

Rusk, B. (2012). Cathodoluminescent textures and trace elements in hydrothermal quartz. Quartz: Deposits, mineralogy and analytics, 307-329.

Rusk, B. (2012). Cathodoluminescent textures and trace elements in hydrothermal quartz. Quartz: Deposits, mineralogy and analytics, 307-329.

Rusk, B. G., Lowers, H. A., & Reed, M. H. (2008). Trace elements in hydrothermal quartz: Relationships to cathodoluminescent textures and insights into vein formation. Geology, 36(7), 547-550.

Sacca, C., Sacca, D., Nucera, P., & De Fazio, A. (2017). Mineralizzazioni in Calabria Storia e Attualità. (in italian)

Sacca, C., Sacca, D., Nucera, P., & De Fazio, A. (2017). Mineralizzazioni in Calabria Storia e Attualità.

Sahlström, F., Blake, K., Corral, I., & Chang, Z. (2017). Hyperspectral cathodoluminescence study of indium-bearing sphalerite from the Mt Carlton high-sulphidation epithermal deposit, Queensland, Australia. European Journal of Mineralogy, 29(6), 985-993.

Saini-Eidukat, B., Melcher, F., & Lodziak, J. (2009). Zinc–germanium ores of the Tres Marias mine, Chihuahua, Mexico. Mineralium Deposita, 44, 363-370. https://doi.org/10.1007/s00126-008-0222-2

Saintilan, N. J., Schneider, J., Stephens, M. B., Chiaradia, M., Kouzmanov, K., Wälle, M., & Fontboté, L. (2015). A Middle Ordovician age for the Laisvall sandstone-hosted Pb-Zn deposit, Sweden: a response to early Caledonian orogenic activity. Economic Geology, 110(7), 1779-1801.

Santantonio M. & Fabbi S. (2020) - Anatomy and Jurassic evolution of a Hercynian basement high (Caloveto High-Calabria, Southern Italy). Italian Journal of Geosciences, 139(1), 30-53.

Santantonio M. & Teale C. (1987). An example of the use of detrital episodes in elucidating complex basin histories: the Caloveto and Longobucco Groups of NE Calabria, S. Italy. In Marine clastic sedimentology (pp. 62-74). Springer, Dordrecht.

Santantonio, M., Fabbi, S., & Aldega, L. (2016). Mesozoic architecture of a tract of the European–Iberian continental margin: Insights from preserved submarine palaeotopography in the Longobucco Basin (Calabria, Southern Italy). Sedimentary Geology, 331, 94-113

Savko, K. A., & Bazikov, N. S. (2011). Phase equilibria of bastnaesite, allanite, and monazite: Bastnaesite-out isograde in metapelites of the Vorontsovskaya group, Voronezh crystalline massif. Petrology, 19, 445-469.

Schmandt, D. S., Cook, N. J., Ciobanu, C. L., Ehrig, K., Wade, B. P., Gilbert, S., & Kamenetsky, V. S. (2017). Rare earth element fluorocarbonate minerals from the olympic dam Cu-U-Au-Ag deposit, South Australia. Minerals, 7(10), 202.

Schneider, J., Melcher, F., & Brauns, M. (2007). Concordant ages for the giant Kipushi base metal deposit (DR Congo) from direct Rb–Sr and Re–Os dating of sulfides. Mineralium Deposita, 42, 791-797.

Schwinn, G., & Markl, G. (2005). REE systematics in hydrothermal fluorite. Chemical Geology, 216(3-4), 225-248.

Scott S. D. (1973). Experimental calibration of the sphalerite geobarometer. Econ. Geol. 68, 466–474.

Scott S. D. and Barnes H. L. (1971). Sphalerite geothermometry and geobarometry. Econ. Geol. 66, 653–669.

Scott S. D., (1971) Mo¨ ßbauer spectra of synthetic iron-bearing sphalerite. Can Mineral 10: 882–885.

Scott, S. D., & Barnes, H. L. (1972). Sphalerite-wurtzite equilibria and stoichiometry. Geochimica et Cosmochimica Acta, 36(11), 1275-1295

Scott, S. D., & Kissin, S. A. (1973). Sphalerite composition in the Zn-Fe-S system below 300 degrees C. Economic geology, 68(4), 475-479.

Seal, R. R., Cooper, B. J., & Craig, J. R. (1985). Anisotropic sphalerite of the Elmwood-Gordonsville deposits, Tennessee. The Canadian Mineralogist, 23(1), 83-88.

Seifert T. and Sandmann D. (2006). Mineralogy and geochemistry of indium-bearing polymetallic vein-type deposits: implications for host minerals from the Freiberg district, Eastern Erzgebirge, Germany. Ore Geol. Rev. 28, 1–31.

Shepherd, T. J., & Allen, P. M. (1985). Metallogenesis in the Harlech Dome, North Wales: A fluid inclusion interpretation. Mineralium Deposita, 20, 159-168.

Skinner B J (1961) Unit-cell edges of natural and synthetic sphalerites, American Mineralogist, 46, 1399-1411

Smith, F. G. (1955). Structure of zinc sulphide minerals. American Mineralogist, 40 (7-8) 658-675.

Smith, P. E., Farquhar, R. M., & Hancock, R. G. (1991). Direct radiometric age determination of carbonate diagenesis using U-Pb in secondary calcite. Earth and Planetary Science Letters, 105(4), 474-491.

Sokol, E. V., Kokh, S. N., Nekipelova, A. V., Abersteiner, A., Seryotkin, Y. V., Ershov, V. V., ... & Deviatiiarova, A. S. (2021). Ge-Hg-rich sphalerite and Pb, Sb, As, Hg, and Ag sulphide assemblages in mud volcanoes of Sakhalin Island, Russia: An insight into possible origin. Minerals, 11(11), 1186

Stoiber, R. E., (1940). Minor elements in sphalerite. Economic Geology, 35(4), 501-519.

Summaries, M. C. (2021). Mineral commodity summaries. US Geological Survey: Reston, VA, USA, 200.

Sun, Q. F., Wang, K. Y., Geng, J. Z., Liu, W. C., & Lai, C. K. (2022). Age and genesis of the Lamahanshan Ag-Pb-Zn deposit, southern Great Xing'an Range, northeastern China: Constraints from sphalerite Rb-Sr dating, fluid inclusions and HOS-Pb isotopes. Journal of Geochemical Exploration, 237, 107003.

Sun, X. J., Ni, P., Yang, Y. L., Qin, H., Chen, H., Gui, C. J., & Jing, S. (2018). Formation of the Qixiashan Pb–Zn deposit in Middle-Lower Yangtze River Valley, eastern China: Insights from fluid inclusions and in situ LA-ICP-MS sulfur isotope data. Journal of Geochemical Exploration, 192, 45-59.

Sun, Z., Wang, J., Wang, Y., Zhang, Y., & Zhao, L. (2021). Multistage hydrothermal quartz veins record the ore-forming fluid evolution in the Meiling Cu–Zn (Au) deposit, NW China. Ore Geology Reviews, 131, 104002.

Taylor, M., Kesler, S.E., Cloke, P.L., and Kelly, W.C., 1983, Fluid inclusion evidence for fluid mixing, Mascot–Jefferson City zinc district, Tennessee: Economic Geology, v. 78, p. 1425– 1439.

Thyberg, B., Jahren, J., Winje, T., Bjørlykke, K., Faleide, J. I., & Marcussen, Ø. (2010). Quartz cementation in Late Cretaceous mudstones, northern North Sea: Changes in rock properties due to dissolution of smectite and precipitation of micro-quartz crystals. Marine and Petroleum Geology, 27(8), 1752-1764.

Tornos, F., Casquet, C., Locutura, J., & Collado, R. (1991). Fluid inclusion and geochemical evidence for fluid mixing in the genesis of Ba-F (Pb-Zn) lodes of the Spanish Central System. Mineralogical Magazine, 55(379), 225-234.

Toulmin, P., Barton, P. B., & Wiggins, L. B. (1991). Commentary on the sphalerite geobarometer. American Mineralogist, 76(5-6), 1038-1051.

Tursi, F., Acquafredda, P., Festa, V., Fornelli, A., Langone, A., Micheletti, F., & Spiess, R. (2021). What can high-P sheared orthogneisses tell us? An example from the Curinga–Girifalco Line (Calabria, southern Italy). Journal of Metamorphic Geology, 39, 919–944. https://doi.org/10.1111/jmg.12596.

Tursi, F., Spiess, R., Festa, V., & Fregola, R.A. (2020) Hercynian subduction-related processes within the metamorphic continental crust in Calabria (southern Italy). Journal of Metamorphic Geology, 38, 771–793. https://doi.org/10.1111/jmg.12537.

Uher, P., Ondrejka, M., Bačík, P., Broska, I., & Konečný, P. (2015). Britholite, monazite, REE carbonates, and calcite: Products of hydrothermal alteration of allanite and apatite in A-type granite from Stupné, Western Carpathians, Slovakia. Lithos, 236, 212-225.

Vaughan, D. J., & Craig, J.R. (1997). Sulphide ore mineral stabilities, morphologies, and intergrowth textures. In: Barnes HL (ed) Geochemistry of Hydrothermal Ore Deposits. 3rd edition. Wiley Interscience, New York, pp. 367-434.

Vighi, L. (1953). Sulla geologia e sulle mineralizzazioni metallifere della regione di Longobucco in Calabria. Mem. E Note Ist. Geol. Appl. Napoli, 5, 3–61. (In Italian).

Vignaroli, G., Minelli, L., Rossetti, F., Balestrieri, M.L., & Faccenna, C. (2012). Miocene thrusting in the eastern Sila Massif: Implication for the evolution of the Calabria-Peloritani orogenic wedge (southern Italy). Tectonophysics, 538, 105–119. https://doi.org/10.1016/j.tecto.2012.03.011.

Vityk, M. O., & Bodnar, R. J. (1995). Textural evolution of synthetic fluid inclusions in quartz during reequilibration, with applications to tectonic reconstruction. Contributions to Mineralogy and Petrology, 121(3), 309-323.

Walter, B. F., Burisch, M., & Markl, G. (2016). Long-term chemical evolution and modification of continental basement brines–a field study from the Schwarzwald, SW Germany. Geofluids, 16(3), 604-623.

Wang, M., Han, R., Zhou, W., Wu, S., Luo, D., & Song, D. (2023). In situ geochemical and Rb-Sr dating analysis of sphalerite from the Liangyan Pb–Zn deposit in northwestern Guizhou, China: Implication for timing of ore formation. Ore Geology Reviews, 154, 105340.

Wei, C., Ye, L., Huang, Z., Hu, Y., & Wang, H. (2021). In situ trace elements and S isotope systematics for growth zoning in sphalerite from MVT deposits: A case study of Nayongzhi, South China. Mineralogical Magazine, 85(3), 364-378. https://doi.org/10.1180/mgm.2021.29.

Wen, H., Zhu, C., Zhang, Y., Cloquet, C., Fan, H., & Fu, S. (2016). Zn/Cd ratios and cadmium isotope evidence for the classification of lead-zinc deposits. Scientific Reports, 6(1), 25273. https://doi.org/10.1038/srep25273

Werner, T. T., Mudd, G. M., & Jowitt, S. M. (2017). The world's by-product and critical metal resources part III: A global assessment of indium. Ore Geology Reviews, 86, 939-956.

Wertich, V., Leichmann, J., Dosbaba, M., & Götze, J. (2018). Multi-stage evolution of gold-bearing hydrothermal quartz veins at the Mokrsko gold deposit (Czech Republic) based on cathodoluminescence, spectroscopic, and trace elements analyses. Minerals, 8(8), 335.

Whitehouse, M. J., & Russell, J. (1997). Isotope systematics of Precambrian marbles from the Lewisian complex of northwest Scotland: implications for Pb-Pb dating of metamorphosed carbonates. Chemical Geology, 136(3-4), 295-307.

Wilkinson, J. (2013). Sediment-hosted zinc-lead mineralization: processes and perspectives: processes and perspectives.

Williams-Jones, A. E., Samson, I. M., Ault, K. M., Gagnon, J. E., & Fryer, B. J. (2010). The genesis of distal zinc skarns: Evidence from the Mochito deposit, Honduras. Economic Geology, 105(8), 1411-1440.

Wilson, M., Neumann, E. R., Davies, G. R., Timmerman, M. J., Heeremans, M., & Larsen, B. T. (2004). Permo-Carboniferous magmatism and rifting in Europe: introduction. Geological Society, London, Special Publications, 223(1), 1-10.

Wright, K. (2009). The incorporation of cadmium, manganese and ferrous iron in sphalerite: insights from computer simulations. The Canadian Mineralogist, 47(3), 615-623.

Wright, K., & Gale, J. D. (2010). A first principles study of the distribution of iron in sphalerite. Geochimica et Cosmochimica Acta, 74(12), 3514-3520.

Wu, J., Dai, H., Cheng, Y., Xu, S., Nie, Q., Wen, Y., & Lu, P. (2023). LA-ICP-MS Trace Element Geochemistry of Sphalerite and Metallogenic Constraints: A Case Study from Nanmushu Zn–Pb Deposit in the Mayuan District, Shaanxi Province, China. Minerals, 13(6), 793. https://doi.org/10.3390/min13060793.

Yang, Q., Xiong, S. F., & Jiang, S. Y. (2024). Genesis of Pb-Zn deposits in northwestern Guizhou province of China: Constraints from the in situ analyses of fluid inclusions and sulfur isotopes. Ore Geology Reviews, 105842. https://doi.org/10.1016/j.oregeorev.2023.105842.

Yang, Q., Zhang, X. J., Ulrich, T., Zhang, J., & Wang, J. (2022). Trace element compositions of sulfides from Pb-Zn deposits in the Northeast Yunnan and northwest Guizhou Provinces, SW China: Insights from LA-ICP-MS analyses of sphalerite and pyrite. Ore Geology Reviews, 141, 104639. https://doi.org/10.1016/j.oregeorev.2021.104639.

Ye, L., Cook, N. J., Ciobanu, C. L., Yuping, L., Qian, Z., Tiegeng, L., ... & Danyushevskiy, L. (2011). Trace and minor elements in sphalerite from base metal deposits in South China: A LA-ICPMS study. Ore Geology Reviews, 39(4), 188-217. https://doi.org/10.1016/j.oregeorev.2011.03.001.

Ye, L., Li, Z., Hu, Y., Huang, Z., Zhou, J., Fan, H., Danyushevskiy, L., (2016). Trace elements in sulphide from the Tianbaoshan Pb–Zn deposit, Sichuan Province, China: a LA–ICPMS study. Acta Petrol. Sin. 32 (11), 3377–3393 (in Chinese with English abstract).

Young, J. R., Teale, C. T., and Bown, P. R., (1986). Revision of the stratigraphy of the Longobucco Group (Liassic, Southern Italy) based on new data from nannofossils and ammonites: Eclogae Geologicae Helvetica, v. 79, p. 117–135.

Zaitsev, A. N., Wall, F., & Le Bas, M. J. (1998). REE-Sr-Ba minerals from the Khibina carbonatites, Kola Peninsula, Russia: their mineralogy, paragenesis and evolution. Mineralogical Magazine, 62(2), 225-250.

Zeug, M., Nasdala, L., Ende, M., Habler, G., Hauzenberger, C., Chanmuang N, C., ... & Wirth, R. (2021). The parisite–(Ce) enigma: challenges in the identification of fluorcarbonate minerals. Mineralogy and Petrology, 115, 1-19.

Zhao H., Shao Y., Zhang Y., Cao G., Zhao L., Zheng X. (2023a) Big data mining on trace element geochemistry of sphalerite. Journal of Geochemical Exploration 252, 107254. https://doi.org/10.1016/j.gexplo.2023.107254

Zhao, H., & Jones, B. (2013). Distribution and interpretation of rare earth elements and yttrium in Cenozoic dolostones and limestones on Cayman Brac, British West Indies. Sedimentary Geology, 284, 26-38.

Zhao, Z. H., Ni, P., Fan, M. S., Ding, J. Y., Pan, J. Y., Chen, Y. K., Liu Z., and Zhang, Z. (2023b). Multi-stage magmatic fluid recharge and fluid mixing developed the Gongdongchong intermediate-sulfidation type epithermal Pb-Zn deposit, North Huaiyang, China: Constraints from petrography, fluid inclusion and in situ geochemistry studies of sphalerite. *Ore Geology Reviews*, 105719.

Zhu, K. Y., Jiang, S. Y., Su, H. M., & Duan, Z. P. (2021). In situ geochemical analysis of multiple generations of sphalerite from the Weilasituo Sn-Li-Rb-Cu-Zn ore field (Inner Mongolia, northeastern China): Implication for critical metal enrichment and ore-forming process. Ore Geology Reviews, 139, 104473.

Zhuang, L., Song, Y., Liu, Y., Fard, M., & Hou, Z. (2019). Major and trace elements and sulfur isotopes in two stages of sphalerite from the world-class Angouran Zn–Pb deposit, Iran: Implications for mineralization conditions and type. Ore Geology Reviews, 109, 184-200.

Zigone, M., Vandevyver, M., & Talwar, D. N. (1981). Raman scattering and local force variations due to transition-element impurities in zinc-sulfide crystals: Effect of pressure application. Physical Review B, 24(10), 5763.

Appendix

Table 1a. EPMA analyses (wt%) of sphalerite from the Longobucco area (LGB)

colour legend: W (colourless) - L (Light Yellow) - Y (Yellow) - B (Brown) - R (Reddish Brown) - D (Dark Brown)

analysis spot	colour	type	S	Mn	Fe	Co	Cu	Zn	Cd	Total
LGB04h_Line sp1 001	B	sp2	32.54	b.d.l.	4.43	0.02	0.04	60.45	0.17	97.65
LGB04h_Line sp1 002	B	sp2	33.11	0.02	5.73	0.02	b.d.l.	59.69	0.10	98.67
LGB04h_Line sp1 003	R	sp2	31.23	0.03	7.14	0.01	0.04	57.52	0.18	96.16
LGB04h_Line sp1 004	B	sp2	33.16	b.d.l.	6.61	0.02	0.05	58.54	0.13	98.51
LGB04h_Line sp1 005	B	sp2	33.07	0.02	7.52	0.02	0.07	57.64	0.09	98.44
LGB04h_Line sp1 006	Y	sp2	32.54	b.d.l.	5.12	0.01	0.04	60.44	0.10	98.25
LGB04h_Line sp1 007	B	sp2	31.69	b.d.l.	6.08	0.01	0.17	57.67	0.03	95.66
LGB04h_Line sp1 008	R	sp2	34.53	b.d.l.	8.26	0.02	0.08	54.84	0.07	97.80
LGB04h_Line sp1 009	R	sp2	33.09	b.d.l.	8.12	0.03	0.06	56.76	b.d.l.	98.05
LGB04h_Line sp1 010	B	sp2	34.29	b.d.l.	4.40	0.01	b.d.l.	61.20	0.14	100.04
LGB04h_Line sp1 011	D	sp2	33.39	b.d.l.	9.55	0.02	b.d.l.	55.39	0.25	98.60
LGB04h_Line sp1 012	B	sp2	33.10	b.d.l.	6.13	0.02	0.08	59.45	0.12	98.89
LGB04h_Line sp1 013	W	sp3	32.44	b.d.l.	1.07	0.01	b.d.l.	64.70	0.54	98.76
LGB04h_Line sp1 014	W	sp3	33.06	0.02	0.80	0.01	b.d.l.	65.09	0.35	99.33
LGB04h_Line sp2 001	D	sp2	34.84	0.02	6.16	0.01	0.45	56.95	0.24	98.67
LGB04h_Line sp2 001	D	sp2	34.84	0.02	6.16	0.01	0.45	56.95	0.24	98.67
LGB04h_Line sp2 002	B	sp2	32.75	0.02	4.46	0.01	b.d.l.	60.94	0.22	98.40
LGB04h_Line sp2 003	D	sp2	33.74	0.02	10.53	0.02	0.20	53.43	0.00	97.94
LGB04h_Line sp2 005	D	sp2	33.10	0.02	8.58	0.02	0.06	56.49	0.16	98.42
LGB04h_Line sp2 006	D	sp2	33.11	0.02	6.84	0.02	b.d.l.	59.35	0.06	99.39
LGB04h_Line sp2 007	D	sp2	32.35	b.d.l.	9.07	0.02	0.07	55.13	0.01	96.64
LGB04h_Line sp3 001	D	sp2	33.51	0.02	6.62	0.02	0.05	58.33	0.09	98.63
LGB04h_Line sp3 002	R	sp2	35.69	b.d.l.	7.14	0.01	b.d.l.	58.03	0.26	101.14
LGB04h_Line sp3 003	B	sp2	33.18	b.d.l.	5.52	0.01	b.d.l.	60.01	0.15	98.87
LGB04h_Line sp3 004	R	sp2	33.54	0.02	7.08	0.01	b.d.l.	58.22	0.41	99.29
LGB04h_Line sp3 005	B	sp2	33.32	b.d.l.	5.62	0.02	0.05	60.03	0.09	99.13
LGB04h_Line sp3 006	B	sp2	33.42	b.d.l.	4.29	b.d.l.	b.d.l.	61.68	0.17	99.56
LGB04h_Line sp3 007	B	sp2	32.24	b.d.l.	6.34	0.02	0.03	58.53	0.07	97.23
LGB04h_Line sp4 001	R	sp2	34.70	0.02	10.69	0.01	0.11	54.13	0.07	99.72
LGB04h_Line sp4 002	B	sp2	33.32	b.d.l.	5.39	0.01	b.d.l.	59.73	0.34	98.79
LGB04h_Line sp4 003	W	sp3	32.92	b.d.l.	1.05	0.01	b.d.l.	64.37	0.69	99.04
LGB04h_Line sp4 005	W	sp3	36.12	b.d.l.	1.23	0.01	b.d.l.	64.21	0.47	102.04
LGB04h_Line sp4 006	R	sp2	33.32	b.d.l.	7.01	0.02	b.d.l.	57.81	0.32	98.48
LGB04h_Line sp4 007	R	sp2	32.74	0.04	8.86	0.01	0.03	55.39	0.08	97.15
LGB04h_Line sp4 008	R	sp2	33.54	0.02	9.23	0.01	b.d.l.	55.72	0.29	98.80
LGB04h_Line sp4 009	B	sp2	33.37	0.01	7.15	0.01	b.d.l.	57.90	0.34	98.78
LGB04h_Line sp4 010	B	sp2	33.24	0.02	7.32	0.01	b.d.l.	57.64	0.36	98.59
LGB06a-1La-1T 001	Y	sp1	32.65	b.d.l.	3.47	b.d.l.	b.d.l.	61.14	0.12	97.38
LGB06a-1La-1T 002	Y	sp1	32.90	b.d.l.	3.48	0.01	b.d.l.	62.09	0.13	98.61
LGB06a-1La-1T 003	Y	sp1	32.76	b.d.l.	3.23	0.01	b.d.l.	62.00	0.45	98.45
LGB06a-1La-1T 004	L	sp1	32.95	b.d.l.	2.50	0.01	b.d.l.	62.73	0.23	98.42
LGB06a-1La-1T 005	Y	sp1	32.93	0.02	4.09	0.01	b.d.l.	61.03	0.41	98.48
LGB06a-1La-1T 006	Y	sp1	32.73	b.d.l.	3.23	0.01	0.05	62.28	0.15	98.45
LGB06a-1La-1T 007	Y	sp1	32.36	b.d.l.	3.18	b.d.l.	b.d.l.	62.12	0.14	97.80
LGB06a-1La-1T 008	L	sp1	32.69	b.d.l.	2.89	b.d.l.	b.d.l.	62.26	0.56	98.40
LGB06a-1La-1T 010	Y	sp1	32.94	0.01	3.84	0.01	0.03	61.47	0.14	98.45
LGB06a-1La-1T 011	Y	sp1	32.71	0.05	4.61	b.d.l.	b.d.l.	60.45	0.32	98.14
LGB06a-1La-1T 012	Y	sp1	32.86	b.d.l.	4.27	0.01	b.d.l.	61.01	0.20	98.34
LGB06a-1La-2.1	R	sp2	33.06	0.02	9.44	0.02	0.04	55.42	0.10	98.10
LGB06a-1La-2.3	L	sp1	32.79	b.d.l.	3.23	b.d.l.	b.d.l.	61.90	0.55	98.47
LGB06a-1La-2.4	Y	sp1	32.76	b.d.l.	3.46	b.d.l.	b.d.l.	61.77	0.18	98.17
LGB06a-1La-2.5	R	sp2	33.23	0.02	8.38	0.03	0.06	56.59	0.06	98.37
LGB06a-1La-2.6	R	sp2	33.09	0.02	6.88	0.03	b.d.l.	58.06	0.22	98.29
LGB06a-1La-2.7	B	sp2	32.90	b.d.l.	7.26	0.01	0.14	57.21	0.20	97.72
LGB06a-1La-2.8	B	sp2	32.40	b.d.l.	6.73	0.03	0.04	58.10	0.14	97.44
LGB06a-1La-2T 001	Y	sp1	32.97	0.02	3.44	0.01	b.d.l.	61.57	0.19	98.21
LGB06a-1La-2T 002	Y	sp1	32.80	b.d.l.	3.67	0.01	b.d.l.	61.70	0.25	98.43
LGB06a-1La-2T 003	Y	sp1	33.15	0.01	3.48	b.d.l.	b.d.l.	61.38	0.26	98.29
LGB06a-1La-2T 004	L	sp1	32.57	0.02	2.49	0.01	0.06	62.68	0.20	98.03
LGB06a-1La-2T 006	L	sp1	32.77	b.d.l.	3.10	0.01	0.06	61.91	0.22	98.06
LGB06a-1La-2T 007	Y	sp1	32.67	b.d.l.	3.06	0.02	b.d.l.	62.36	0.15	98.27
LGB06a-1La-2T 008	L	sp1	32.73	b.d.l.	3.14	b.d.l.	0.03	62.09	0.18	98.16
LGB06a-1La-2T 009	B	sp1	32.97	b.d.l.	5.64	0.00	0.04	59.39	0.20	98.24
LGB06a-1La-2T 010	Y	sp1	32.82	0.03	3.86	0.01	0.05	60.79	0.19	97.76
LGB06a-1La-3Ta 001	Y	sp1	32.86	b.d.l.	3.25	b.d.l.	b.d.l.	62.15	0.22	98.48
LGB06a-1La-3Ta 002	L	sp1	32.49	b.d.l.	1.57	b.d.l.	b.d.l.	63.83	0.28	98.17
LGB06a-1La-3Ta 003	Y	sp1	32.80	0.02	3.56	0.01	b.d.l.	61.77	0.25	98.40
LGB06a-1La-3Ta 004	B	sp1	32.70	b.d.l.	4.52	0.02	0.08	60.63	0.32	98.26
LGB06a-1La-3Ta 005	B	sp1	32.45	b.d.l.	4.14	0.02	0.10	60.98	0.17	97.86
LGB06a-1La-3Ta 006	Y	sp1	32.17	b.d.l.	3.07	0.01	0.09	62.05	0.07	97.46

Table 1a. EPMA analyses (wt%) of sphalerite from the Longobucco area (LGB) **(continue)**

colour legend: W (colourless) - L (Light Yellow) - Y (Yellow) - B (Brown) - R (Reddish Brown) - D (Dark Brown)

analysis spot	colour	type	S	Mn	Fe	Co	Cu	Zn	Cd	Total
LGB06a-1La-3Ta 007	Y	sp1	31.39	b.d.l.	2.68	0.01	0.12	61.61	0.15	95.96
LGB06a-1La-3Tb 001	Y	sp1	32.92	b.d.l.	3.31	b.d.l.	b.d.l.	62.10	0.15	98.48
LGB06a-1La-3Tb 002	Y	sp1	32.46	b.d.l.	2.23	b.d.l.	0.06	63.24	0.16	98.15
LGB06a-1La-3Tb 004	Y	sp1	32.72	b.d.l.	3.03	b.d.l.	0.04	62.36	0.17	98.33
LGB06a-1La-3Tb 005	Y	sp1	32.91	b.d.l.	3.49	0.01	0.05	62.00	0.21	98.67
LGB06a-1La-3Tb 006	Y	sp1	32.85	b.d.l.	3.61	b.d.l.	b.d.l.	61.89	0.21	98.56
LGB06a-1La-3Tb 007	Y	sp1	33.33	0.03	3.14	0.01	b.d.l.	61.68	0.43	98.62
LGB06a-1La-3Tb 008	Y	sp1	32.87	b.d.l.	4.06	0.01	b.d.l.	61.12	0.37	98.43
LGB06a-1La-3Tb 009	B	sp2	32.82	0.03	6.30	0.02	b.d.l.	58.77	0.25	98.19
LGB06a-1La-3Tb 010	Y	sp2	31.50	b.d.l.	2.88	0.02	b.d.l.	61.23	0.07	95.70
LGB06a-1La-4Ta 002	L	sp1	32.60	b.d.l.	2.66	0.01	0.03	61.82	0.34	97.46
LGB06a-1La-4Ta 003	L	sp1	32.63	b.d.l.	2.63	0.02	b.d.l.	62.37	0.30	97.95
LGB06a-1La-4Ta 004	L	sp1	32.69	b.d.l.	2.92	0.01	b.d.l.	62.46	0.23	98.31
LGB06a-1La-4Ta 005	Y	sp1	32.73	b.d.l.	3.28	b.d.l.	b.d.l.	62.10	0.15	98.26
LGB06a-1La-4Ta 006	L	sp1	32.69	b.d.l.	3.09	0.03	b.d.l.	62.22	0.11	98.14
LGB06a-1La-4Ta 007	Y	sp1	32.91	0.02	3.29	0.02	0.05	62.55	0.14	98.97
LGB06a-1La-4Ta 008	Y	sp1	32.87	0.02	3.49	b.d.l.	b.d.l.	61.67	0.17	98.22
LGB06a-1La-4Ta 009	B	sp1	33.01	0.02	3.81	b.d.l.	0.06	61.44	0.22	98.56
LGB06a-1La-4Ta 010	B	sp1	32.79	0.02	4.66	0.01	b.d.l.	60.36	0.37	98.21
LGB06a-1La-4Tb 001	B	sp1	33.05	b.d.l.	4.24	0.02	b.d.l.	60.86	0.22	98.39
LGB06a-1La-4Tb 002	B	sp1	32.88	0.02	3.91	0.01	0.05	61.16	0.12	98.15
LGB06a-1La-4Tb 003	Y	sp1	33.04	b.d.l.	3.37	0.01	0.06	61.81	0.17	98.45
LGB06a-1La-4Tb 004	Y	sp1	32.85	0.02	3.54	0.01	0.03	60.83	0.22	97.49
LGB06a-1La-4Tb 005	Y	sp1	32.82	b.d.l.	3.56	b.d.l.	b.d.l.	61.54	0.18	98.10
LGB06a-1La-4Tb 006	L	sp1	32.79	b.d.l.	3.26	b.d.l.	0.04	61.96	0.18	98.23
LGB06a-1Lb-4Tb 007	L	sp1	32.64	b.d.l.	2.98	0.01	b.d.l.	61.96	0.18	97.77
LGB06a-1Lb-4Tb 008	B	sp2	33.02	b.d.l.	4.57	0.01	0.34	57.51	0.11	95.56
LGB06a-1Lb-5Ta 001	L	sp1	32.98	b.d.l.	1.90	0.01	b.d.l.	63.78	0.28	98.95
LGB06a-1Lb-5Ta 002	L	sp1	32.92	b.d.l.	1.98	b.d.l.	b.d.l.	63.80	0.30	99.00
LGB06a-1Lb-5Ta 003	L	sp1	32.96	b.d.l.	1.88	b.d.l.	b.d.l.	63.71	0.31	98.86
LGB06a-1Lb-5Ta 004	L	sp1	32.73	b.d.l.	2.06	0.01	b.d.l.	63.66	0.33	98.79
LGB06a-1Lb-5Ta 005	L	sp1	33.15	b.d.l.	1.91	b.d.l.	b.d.l.	63.56	0.27	98.89
LGB06a-1Lb-5Ta 006	L	sp1	32.53	0.02	1.69	b.d.l.	0.08	63.61	0.28	98.22
LGB06a-1Lb-5Ta 007	L	sp1	32.82	0.02	1.85	0.01	0.06	64.09	0.17	99.02
LGB06a-1Lb-5Ta 008	Y	sp1	32.80	b.d.l.	1.47	b.d.l.	0.09	64.30	0.11	98.77
LGB06a-1Lb-5Tb 001	Y	sp1	33.02	b.d.l.	1.94	0.01	0.12	63.83	0.22	99.14
LGB06a-1Lb-5Tb 003	Y	sp1	32.78	b.d.l.	1.62	b.d.l.	0.13	64.16	0.13	98.82
LGB06a-1Lb-5Tb 004	Y	sp1	32.90	b.d.l.	1.83	b.d.l.	0.13	62.79	0.14	97.79
LGB06a-1Lb-5Tb 005	Y	sp1	32.81	b.d.l.	1.52	b.d.l.	0.12	64.35	0.13	98.94
LGB06a-1Lb-5Tb 006	Y	sp1	32.92	b.d.l.	2.02	b.d.l.	0.04	63.68	0.20	98.86
LGB06a-1Lb-5Tb 007	L	sp1	32.92	b.d.l.	1.87	0.02	b.d.l.	63.68	0.40	98.89
LGB06a-1Lb-5Tb 008	Y	sp1	32.88	b.d.l.	2.35	b.d.l.	0.14	63.23	0.13	98.74
LGB06a-1Lb-5Tb 009	R	sp1	32.66	b.d.l.	5.43	b.d.l.	b.d.l.	59.37	0.42	97.88
LGB06a-1Lb-5Tb 010	B	sp1	32.92	b.d.l.	3.74	0.01	0.09	61.69	0.25	98.70
LGB06a-1Lb-5Tc 001	Y	sp1	33.14	0.02	3.50	0.01	b.d.l.	62.09	0.25	99.01
LGB06a-1Lb-5Tc 002	Y	sp1	32.98	b.d.l.	3.37	0.01	0.03	62.24	0.24	98.87
LGB06a-1Lb-5Tc 003	L	sp1	32.64	b.d.l.	2.87	b.d.l.	b.d.l.	59.90	0.20	95.61
LGB06a-1Lb-5Tc 004	L	sp1	32.68	0.02	3.35	b.d.l.	0.03	62.32	0.14	98.54
LGB06a-1Lb-5Tc 005	Y	sp1	32.09	b.d.l.	3.91	0.01	0.03	61.37	0.22	97.63
LGB06a-1Lb-5Tc 007	Y	sp1	33.31	0.03	4.18	b.d.l.	0.04	61.36	0.21	99.13
LGB06a-1Lb-5Tc 008	Y	sp1	32.32	0.03	4.13	0.01	b.d.l.	60.74	0.39	97.62
LGB06a-1Lb-5Tc 009	L	sp1	32.71	b.d.l.	1.16	0.01	b.d.l.	64.70	0.29	98.87
LGB06a-1Lb-5Tc 010	L	sp1	32.78	b.d.l.	2.67	b.d.l.	b.d.l.	62.98	0.15	98.58
LGB06a-1Lb-5Td 001	L	sp1	30.89	b.d.l.	3.37	0.01	b.d.l.	61.78	0.21	96.25
LGB06a-1Lb-5Td 002	L	sp1	31.87	b.d.l.	2.41	0.01	0.11	62.66	0.11	97.17
LGB06a-1Lb-5Td 003	L	sp1	32.90	0.02	3.34	0.01	0.02	62.08	0.13	98.49
LGB06a-1Lb-5Td 005	R	sp2	33.34	b.d.l.	6.42	0.03	b.d.l.	58.94	0.06	98.79
LGB06a-1Lb-5Td 006	D	sp2	33.28	b.d.l.	8.44	0.03	0.04	55.67	0.15	97.60
LGB06a-1Lb-5Td 007	B	sp2	33.08	0.02	5.87	0.01	0.10	59.41	0.18	98.67
LGB06a-1Lb-5Td 008	B	sp2	32.74	b.d.l.	5.09	0.01	b.d.l.	59.74	0.51	98.09
LGB06a-1Lb-5Td 009	Y	sp2	32.90	0.01	4.08	b.d.l.	b.d.l.	61.62	0.14	98.75
LGB06a-1Lb-5Td 010	R	sp2	31.80	0.04	6.19	0.03	0.05	58.34	0.10	96.54
LGB06a-1Lb-5Td 011	D	sp2	30.74	0.07	9.21	0.02	0.03	54.84	0.14	95.05
LGB06a-1Lb-5Td 012	Y	sp2	34.41	0.03	3.87	0.01	b.d.l.	61.53	0.09	99.94
LGB06a-1Lb-6T 001	D	sp2	32.78	0.02	6.99	0.02	b.d.l.	56.78	0.10	96.68
LGB06a-1Lb-6T 002	D	sp2	33.03	b.d.l.	7.13	0.02	0.09	57.55	0.04	97.86
LGB06a-1Lb-6T 003	B	sp2	33.07	0.03	4.27	0.01	b.d.l.	60.98	0.27	98.63
LGB06a-1Lb-6T 005	Y	sp2	32.93	0.04	3.40	0.01	b.d.l.	61.36	0.35	98.09
LGB06a-1Lb-6T 006	R	sp2	33.14	b.d.l.	5.60	0.01	0.06	59.15	0.11	98.06
LGB06a-1Lb-6T 007	L	sp2	33.15	0.03	1.14	b.d.l.	b.d.l.	64.18	0.19	98.69

Table 1a. EPMA analyses (wt%) of sphalerite from the Longobucco area (LGB) **(continue)**

colour legend: W (colourless) - L (Light Yellow) - Y (Yellow) - B (Brown) - R (Reddish Brown) - D (Dark Brown)

analysis spot	colour	type	S	Mn	Fe	Co	Cu	Zn	Cd	Total
LGB06a-1Lb-6T 008	R	sp2	32.63	0.02	6.14	0.02	0.07	57.20	0.19	96.26
LGB06a-1Lb-6T 009	B	sp2	33.18	b.d.l.	6.52	0.02	0.08	58.11	0.13	98.05
LGB06a-1Lb-6T 011	B	sp2	33.00	0.02	6.30	0.02	0.03	57.98	0.31	97.66
LGB06a-1Lb-6T 012	B	sp2	32.92	b.d.l.	5.01	b.d.l.	b.d.l.	59.72	0.25	97.90
LGB06a-1Lb-6T 013	B	sp2	33.07	0.02	7.96	0.02	b.d.l.	56.39	0.35	97.82
LGB06a-1Lb-6T 014	B	sp2	31.70	b.d.l.	6.88	0.01	b.d.l.	57.66	0.26	96.50
LGB06a-1Lb-6T 015	D	sp2	33.09	0.03	7.59	0.03	0.04	56.75	0.21	97.74

n° of analyses		S	Mn	Fe	Co	Cu	Zn	Cd
147	min	30.74	0.01	0.80	0.00	0.02	53.43	0.00
	max	36.12	0.07	10.69	0.03	0.45	65.09	0.69
	average	32.92	0.02	4.51	0.01	0.08	60.54	0.21
	median	32.90	0.02	3.86	0.01	0.06	61.36	0.19
	st.dev	0.68	0.01	2.24	0.01	0.08	2.60	0.12

	D.L.	S	Mn	Fe	Co	Cu	Zn	Cd
	average	0.01	0.01	0.01	0.01	0.02	0.01	0.01

b.d.l. below detection limit

Table 1b. EPMA analysis (wt%) of sphalerite from the Fonte Argentila area (FAR)

colour legend: W (colourless) - L (Light Yellow) - Y (Yellow) - B (Brown) - R (Reddish Brown) - D (Dark Brown)

analysis spots	colour	type	S	Mn	Fe	Co	Cu	Zn	Cd	Total
FA04_sp1 L 002	B	sp1	30.85	b.d.l.	6.20	0.02	b.d.l.	58.13	0.49	95.69
FA04_sp1 L 004	Y	sp1	32.33	b.d.l.	2.43	b.d.l.	b.d.l.	61.71	0.15	96.62
FA04_sp1 L 005	B	sp1	33.24	b.d.l.	3.82	b.d.l.	b.d.l.	62.03	0.11	99.20
FA04_sp1 L 006	Y	sp1	31.50	b.d.l.	2.24	b.d.l.	b.d.l.	62.72	0.23	96.69
FA04_sp1 L 007	B	sp1	32.28	b.d.l.	4.24	0.01	0.04	60.42	0.18	97.18
FA04_sp1 L 008	B	sp1	33.02	b.d.l.	4.52	b.d.l.	0.04	61.16	0.24	98.98
FA04_sp1 L 009	B	sp1	34.53	b.d.l.	4.41	b.d.l.	b.d.l.	60.29	0.29	99.52
FA11d_L1 sp 001	R	sp2	33.51	0.02	8.26	0.02	0.02	56.88	b.d.l.	98.71
FA11d_L1 sp 003	D	sp2	33.61	b.d.l.	8.01	0.02	b.d.l.	56.86	b.d.l.	98.51
FA11d_L1 sp 004	B	sp2	33.22	0.02	5.62	0.01	b.d.l.	60.23	b.d.l.	99.10
FA11d_L1 sp 005	B	sp2	33.07	0.03	5.76	0.01	0.03	59.23	0.02	98.15
FA11d_L1 sp 006	B	sp2	33.16	0.02	6.49	b.d.l.	0.10	58.97	b.d.l.	98.74
FA11d_L1 sp 007	D	sp2	33.44	0.03	9.17	0.02	0.08	56.23	b.d.l.	98.97
FA11d_L1 sp 008	D	sp2	33.52	b.d.l.	8.45	0.01	0.03	56.90	b.d.l.	98.91
FA11d_L1 sp 009	D	sp2	33.41	b.d.l.	8.53	0.01	0.00	56.68	b.d.l.	98.63
FA11d_L1 sp 010	R	sp2	32.91	b.d.l.	7.31	0.01	0.06	57.90	0.04	98.22
FA11d_L2 sp 001	Y	sp1	33.36	0.03	5.84	0.01	b.d.l.	59.05	0.04	98.33
FA11d_L2 sp 002	B	sp1	33.13	0.04	6.94	0.02	b.d.l.	57.87	b.d.l.	97.99
FA11d_L2 sp 003	Y	sp1	32.82	0.01	2.01	b.d.l.	b.d.l.	63.33	0.19	98.37
FA11d_L2 sp 004	Y	sp1	33.13	0.04	2.22	b.d.l.	b.d.l.	61.97	0.26	97.62
FA11d_L2 sp 005	B	sp1	33.54	0.03	7.48	0.02	b.d.l.	56.93	b.d.l.	98.00
FA11d_L2 sp 006	B	sp1	33.32	0.01	6.35	0.01	b.d.l.	58.04	0.01	97.75
FA11d_L3 sp 001	D	sp2	33.64	0.05	11.27	0.03	0.07	53.56	b.d.l.	98.62
FA11d_L3 sp 003	B	sp2	33.13	b.d.l.	4.34	0.01	b.d.l.	61.96	b.d.l.	99.44
FA11d_L3 sp 004	D	sp2	33.30	b.d.l.	9.12	0.03	b.d.l.	56.31	0.09	98.84
FA11d_L3 sp 005	D	sp2	32.61	0.03	8.06	0.02	0.09	54.71	b.d.l.	95.53
FA11d_L3 sp 006	R	sp2	32.80	0.04	8.00	0.02	0.04	56.98	0.09	97.96
FA17a_L1 001	L	sp1	31.78	0.02	1.77	b.d.l.	b.d.l.	62.37	0.18	96.13
FA17a_L1 002	R	sp2	33.67	b.d.l.	8.75	0.01	b.d.l.	57.14	b.d.l.	99.57
FA17a_L1 003	L	sp1	32.81	b.d.l.	2.13	b.d.l.	b.d.l.	64.19	0.18	99.31
FA17a_L1 004	Y	sp1	32.12	0.03	2.39	b.d.l.	b.d.l.	63.27	0.30	98.10
FA17a_L1 005	Y	sp1	32.92	b.d.l.	2.40	0.01	b.d.l.	63.70	0.36	99.38
FA17a_L1 006	L	sp1	33.13	b.d.l.	1.55	b.d.l.	b.d.l.	64.53	0.18	99.39
FA17a_L1 007	L	sp1	32.80	b.d.l.	1.59	b.d.l.	b.d.l.	64.87	0.13	99.39
FA17a_L1 008	W	sp3	32.79	b.d.l.	1.36	b.d.l.	b.d.l.	65.00	0.11	99.26
FA17a_L1 009	R	sp2	33.08	b.d.l.	7.29	b.d.l.	0.05	58.80	b.d.l.	99.22
FA17a_L1 010	L	sp1	32.94	b.d.l.	2.33	b.d.l.	b.d.l.	64.26	0.12	99.65
FA17a_L1 011	Y	sp1	32.98	0.02	3.16	b.d.l.	b.d.l.	62.95	0.17	99.28
FA17a_L1 012	B	sp1	33.16	0.02	5.33	0.01	b.d.l.	60.64	0.09	99.25
FA17a_L1 013	R	sp1	33.06	b.d.l.	7.54	0.01	0.04	58.21	b.d.l.	98.86
FA17a_L1 016	B	sp1	32.95	0.04	6.04	0.01	0.05	59.65	0.04	98.78
FA17a_L1 017	Y	sp1	33.02	0.02	2.92	0.01	0.07	63.54	0.10	99.67
FA17a_L1 018	L	sp1	32.80	0.02	1.69	b.d.l.	b.d.l.	64.69	0.08	99.28
FA17a_L1 019	Y	sp1	33.14	b.d.l.	2.29	b.d.l.	0.03	64.03	0.13	99.61
FA17a_L1 020	L	sp1	33.07	b.d.l.	1.82	0.01	b.d.l.	64.50	0.12	99.52
FA17a_L2 002	L	sp1	32.98	b.d.l.	1.48	0.01	b.d.l.	64.72	0.09	99.28
FA17a_L2 003	L	sp1	31.73	0.01	1.17	b.d.l.	b.d.l.	64.15	0.13	97.20
FA17a_L2 005	W	sp3	32.96	b.d.l.	0.63	b.d.l.	b.d.l.	65.54	0.19	99.32
FA17a_L2 006	W	sp3	32.48	b.d.l.	0.22	b.d.l.	b.d.l.	65.74	0.24	98.67
FA17a_L2 007	W	sp3	32.52	b.d.l.	0.48	0.01	b.d.l.	65.32	0.37	98.69
FA17a_L2 008	W	sp3	32.42	b.d.l.	0.45	b.d.l.	b.d.l.	65.16	0.36	98.38
FA17a_L2 009	W	sp3	32.50	0.02	0.18	b.d.l.	b.d.l.	66.15	0.29	99.13
FA17a_L2 010	W	sp3	31.71	b.d.l.	0.21	b.d.l.	b.d.l.	65.41	0.31	97.64
FA17a_L2 011	Y	sp1	32.38	0.03	1.74	0.01	b.d.l.	64.17	0.40	98.73
FA17a_L2 012	W	sp3	32.37	b.d.l.	0.22	b.d.l.	b.d.l.	66.06	0.39	99.04
FA17a_L2 014	R	sp2	33.36	b.d.l.	8.16	0.01	0.07	57.29	b.d.l.	98.89
FA17a_L2 015	R	sp2	32.99	0.04	8.36	0.02	b.d.l.	56.96	b.d.l.	98.37
FA17a_L3 001	R	sp2	32.59	b.d.l.	7.15	0.01	0.11	58.32	0.37	98.55
FA17a_L3 004	R	sp2	33.11	b.d.l.	7.23	0.02	0.08	57.45	0.23	98.13
FA17a_L3 005	R	sp2	32.88	b.d.l.	8.61	0.01	0.03	56.79	0.54	98.87
FA17a_L3 006	B	sp2	33.02	b.d.l.	6.23	0.01	0.06	59.41	0.21	98.95
FA17a_L3 007	B	sp2	31.32	b.d.l.	5.83	0.01	0.03	59.30	0.23	96.72
FA17a_L3 008	B	sp2	32.70	b.d.l.	5.88	0.02	b.d.l.	59.76	0.19	98.55
FA17a_L3 009	B	sp2	32.45	b.d.l.	6.33	0.01	0.05	58.79	0.19	97.82
FA17a_L3 010	B	sp2	32.75	b.d.l.	5.87	0.02	b.d.l.	59.86	0.22	98.71
FA17a_L4 001	Y	sp1	32.31	b.d.l.	2.78	b.d.l.	b.d.l.	63.50	0.02	98.61
FA17a_L4 002	B	sp1	33.03	b.d.l.	3.33	b.d.l.	b.d.l.	62.36	0.26	98.98
FA17a_L4 003	L	sp1	33.02	0.03	1.83	0.01	b.d.l.	64.39	0.10	99.38
FA17a_L4 004	B	sp1	33.01	0.02	5.12	0.01	b.d.l.	60.77	b.d.l.	98.93
FA17a_L4 005	L	sp1	33.12	b.d.l.	2.36	b.d.l.	b.d.l.	63.90	0.14	99.52

Table 1b. EPMA analysis (wt%) of sphalerite from the Fonte Argentila area (FAR) **(continue)**

colour legend: W (colourless) - L (Light Yellow) - Y (Yellow) - B (Brown) - R (Reddish Brown) - D (Dark Brown)

analysis spots	colour	type	S	Mn	Fe	Co	Cu	Zn	Cd	Total
FA17a_L4 006	B	sp2	33.37	0.02	7.36	0.01	b.d.l.	58.57	0.12	99.45
FA17a_L4 007	R	sp2	33.70	0.02	8.74	0.01	0.06	56.85	0.07	99.45
FA17a_L4 010	Y	sp1	32.48	b.d.l.	2.73	b.d.l.	b.d.l.	62.83	0.11	98.15

n° of analyses		S	Mn	Fe	Co	Cu	Zn	Cd
73	min	30.85	0.01	0.18	0.01	0.00	53.56	0.01
	max	34.53	0.05	11.27	0.03	0.11	66.15	0.54
	average	32.87	0.03	4.66	0.01	0.05	60.86	0.19
	median	32.99	0.02	4.52	0.01	0.05	60.64	0.18
	sigma	0.59	0.01	2.91	0.01	0.03	3.28	0.12

	D.L.	S	Mn	Fe	Co	Cu	Zn	Cd
	average	0.01	0.01	0.01	0.01	0.02	0.01	0.01

b.d.l. below detection limit

Table 2a. μ-Raman data of selected sphalerite samples

sample	spot or area	colour	EPMA data				Raman bands (cm^{-1})					
			Fe wt.%	mol% FeS	Cd wt.%	mol% CdS	Y_1		Y_2	Y_3		LO (Zn)
LGB04h	area	W	0.94	1.44	0.45	0.69	*296*[1,2,3]	***302***[1]	*310*[1,3]	*330*[1,3]	***341***[1,3]	**348**[1,2,3]
FA17a	area	W	0.47	0.71	0.28	0.43	*299*[1,2,3]	–	*312*[1,3]	*333*[1,3]	***342***[1,3]	**349**[1,2,3]
LGB06b	area	L	1.92	3.01	0.30	0.47	297[1,2,3]	***304***[1]	*309*[1,3]	329[1,3]	***340***[1,3]	**348**[1,2,3]
FA17a	area	L	1.34	2.06	0.11	0.17	299[1,2,3]	***305***[1]	*311*[1,3]	332[1,3]	***341***[1,3]	**350**[1,2,3]
LGB06b	area	Y	2.02	3.18	0.16	0.26	297[1,2,3]	***304***[1]	309[1,3]	329[1,3]	***341***[1,3]	**348**[1,2,3]
LGB06b_6T_12	6T-12	B	5.01	8.39	0.25	0.42	**301**[1,2,3]	***307***[1]	312[1,3]	331[1,3]	***336***[1,3]	**353**[1,2,3]
LGB06b_6T_13	6T-13	B	7.96	14.12	0.35	0.62	**300**[1,2,3]	***309***[1]	314[1,3]	330[1,3]	***339***[1,3]	353[1,2,3]
LGB04h_L2_1	L2-01	D	6.16	10.82	0.24	0.41	**301**[1,2,3]	***309***[1]	*313*[1,3]	**331**[1,3]	***339***[1,3]	352[1,2,3]
LGB04h_L2_3	L2-03	D	9.21	16.79	0.14	0.25	**301**[1,2,3]	***308***[1]	*312*[1,3]	331[1,3]	***341***[1,3]	353[1,2,3]
LGB06b_5Td_11	5Td-11	D	10.53	21.30	0.00	0.00	**301**[1,2,3]	***308***[1]	*312*[1,3]	331[1,3]	***341***[1,3]	353[1,2,3]

legend: **vs** - very strong; **s** - strong; m - medium; *w* - weak; *sh* - shoulder
[1] Zigone et al., 1981; [2] Hope et al., 2001; [3] Karbish et al., 2007

Table 2b. μ-Raman data of areas and heights ratios after best fitting process of selected sphalerite samples

sample	spot or area	colour	300 cm^{-1} A1	350 cm^{-1} A3	A1/A3	300 cm^{-1} h1	350 cm^{-1} h3	h1/h3	Fe wt%	mol% FeS
LGB04h	area	W	3829	16354	0.23	400	2266	0.18	1.23	2.2
FA17a	area	W	6137	68219	0.09	352.00	8114.00	0.04	0.47	0.8
LGB06b	area	L	102974	133762	0.77	6693	13776	0.49	1.14	2.8
FA17a	area	L	19923	53314	0.37	1520	5700	0.27	1.34	2.4
LGB06b	area	Y	132939	156397	0.85	9200	18600	0.49	2.02	3.6
LGB06b_6T_12	6T-12	B	23427	9115	2.57	1630	1150	1.42	5.01	8.4
LGB06b_6T_13	6T-13	B	29762	7923	3.76	1780	820	2.17	6.16	10.8
LGB04h_L2_1	L2-01	D	2864	745	3.84	208	88	2.36	7.96	14.1
LGB04h_L2_3	L2-03	D	6076	956	6.36	375	113	3.32	9.21	16.7
LGB06b_5Td_11	5Td-11	D	6700	837	8.00	508	72	7.06	10.53	21.3

Table 3. XRPD acquisition setting of sphalerite samples

	THICK AND THIN SECTIONS						POWDERS	
Sample	LGB06a_bis thin section 30 micron	LGB04h_long thick section 100 micron	LGB06a_ter thin section 30 micron	LGB06b_L thin section 30 micron	LGB04b_long thick section 150 micron	LGB06b_D thin section 30 micron	LGB06a powder	LGB04h powder
Type	Sp1-light	Sp2-dark	Sp1-light	Sp1-light	Sp2-dark	Sp2-dark	Sp1-light	Sp2-dark
Acquisition	3 hours	3 hours	5 hours	5 hours	5 hours	5 hours	3 hours	3 hours
Mask	5x1 mm	5x1 mm	2x1 mm	2x1 mm	2x1 mm	2x1 mm	5x1 mm	5x1 mm

Table 4. Single crystal X-ray diffraction and EPMA data of selected sphalerite fragments

sample	L1	L2	Y2	Y3	B1	B2	R1	R2	D1	D2	D3
Space group	F-43m										
a (Å)	5.4139	5.4163	5.4168	5.4158	5.4184	5.4221	5.4173	5.4230	5.4142	5.4211	5.4136
sd (Å)	0.0039	0.0054	0.0019	0.0018	0.0017	0.0041	0.0013	0.0046	0.0011	0.0019	0.0049
Cell volume (Å^3)	158.680	158.890	158.936	158.856	159.076	159.410	158.979	159.486	158.713	159.443	158.653
sd (Å)	0.350	0.474	0.163	0.162	0.152	0.360	0.117	0.409	0.100	0.172	0.432
type	Sp1-light		Sp1-light		Sp1-light		Sp2-dark		Sp2-dark		

Fe wt.% (SEM)	2.110	2.340	2.700	3.610	4.640	3.080	3.070	7.030	7.750	*8.825*	6.110
mol% FeS	*3.3*	*3.6*	*3.6*	*6.0*	*7.5*	*4.9*	*4.9*	*11.8*	*13.7*	*15.8*	*10.1*

Fe wt.% (EPMA)	1.140		2.020		4.685		6.420		8.825		
mol% FeS	*2.8*		*3.6*		*8.3*		*11.5*		*15.8*		

Temperature obtained from Chareev et al. 2017 using SEM data

sample	L1	L2	Y2	Y3	B1	B2	R1	R2	D1	D2	D3
T°C	76	129	133	86	130	250	136	189	-41	101	-15

Temperature obtained from Chareev et al. 2017 using EPMA data

sample	L1	L2	Y2	Y3	B1	B2	R1	R2	D1	D2	D3
T°C	82	139	141	117	120	208	57	192	-64	101	-78

Table 5. SEM analyses (wt.%) on fragments of Longobucco (LGB) sphalerite

colour legend: L (Light Yellow) - Y (Yellow) - B (Brown) - R (Reddish Brown) - D (Dark Brown)

fragment	analyses spots	S	Fe	Zn	Cd
L1	1	32.97	2.25	64.34	0.44
	2	32.84	2.18	64.66	0.32
	3	32.90	1.93	64.85	0.32
	whole	33.05	2.08	64.41	0.46
	2σ	*0.07*	*0.06*	*0.09*	*0.06*
	average	32.94	2.11	64.57	0.39
L2	1	32.80	2.57	63.79	0.84
	2	32.86	2.26	64.42	0.46
	3	32.94	2.19	64.56	0.30
	whole	32.90	2.35	64.21	0.54
	2σ	*0.07*	*0.06*	*0.09*	*0.06*
	average	26.31	2.34	64.25	0.54
Y1	1	32.93	2.43	64.32	0.32
	2	32.93	2.29	64.39	0.39
	3	33.12	4.34	62.33	0.21
	whole	33.41	2.48	63.72	0.39
	2σ	*0.07*	*0.06*	*0.09*	*0.06*
	average	26.49	2.89	63.69	0.33
Y2	1	32.77	2.52	64.34	0.37
	2	32.74	2.85	64.08	0.32
	3	32.86	2.88	63.98	0.29
	whole	32.92	2.64	64.10	0.33
	2σ	*0.07*	*0.06*	*0.09*	*0.06*
	average	26.27	2.72	64.13	0.33
Y3	1	36.02	3.59	60.05	0.34
	2	35.84	3.62	60.18	0.36
	3	35.79	3.67	60.22	0.31
	whole	36.57	3.57	59.49	0.37
	2σ	*0.10*	*0.09*	*0.12*	*0.08*
	average	28.86	3.61	59.99	0.35
B1	1	33.17	5.03	60.92	0.89
	2	33.08	4.48	61.98	0.47
	3	33.25	4.47	61.88	0.40
	whole	33.24	4.58	61.60	0.58
	2σ	*0.08*	*0.07*	*0.09*	*0.06*
	average	26.56	4.64	61.60	0.59
B2	1	32.95	3.59	63.08	0.38
	2	33.18	3.15	63.43	0.23
	3	33.17	2.60	63.94	0.28
	whole	33.24	3.01	63.37	0.39
	2σ	*0.07*	*0.06*	*0.09*	*0.06*
	average	26.52	3.09	63.46	0.32
R1	1	33.99	3.23	62.58	0.19
	2	34.04	2.93	63.03	0.00
	3	33.82	2.98	62.94	0.26
	whole	33.88	3.13	62.80	0.19
	2σ	*0.08*	*0.07*	*0.09*	*0.06*
	average	27.16	3.07	62.84	0.16

Table 5. SEM analyses (wt.%) on fragments of Longobucco (LGB) sphalerite **(continued)**

colour legend: L (Light Yellow) - Y (Yellow) - B (Brown) - R (Reddish Brown) - D (Dark Brown)

fragment	analyses spots	S	Fe	Zn	Cd
R2	1	33.12	6.9	59.53	0.45
	2	32.96	6.83	59.77	0.44
	3	32.95	5.95	60.74	0.36
	whole	32.63	8.43	58.48	0.46
	2σ	*0.08*	*0.08*	*0.09*	*0.06*
	average	26.35	7.03	59.63	0.43
D1	1	35.19	8.03	56.39	0.39
	2	35.01	7.22	57.35	0.42
	3	34.72	7.88	56.96	0.44
	whole	35.45	7.85	56.27	0.43
	2σ	*0.10*	*0.10*	*0.12*	*0.07*
	average	28.09	7.75	56.74	0.42
D3	1	32.9	5.72	61.12	0.25
	2	32.94	6.46	60.23	0.37
	3	32.87	6.15	60.57	0.42
	whole	32.96	6.09	60.59	0.35
	2σ	*0.08*	*0.08*	*0.09*	*0.06*
	average	26.35	6.11	60.63	0.35

Table 6a. LA-ICP-MS analysis (ppm) of sphalerite from the Longobucco area (LGB)

colour legend: L (Light Yellow) - Y (Yellow) - B (Brown) - R (Reddish Brown) - D (Dark Brown) (standard by EPMA Zn-content)

														standard					
Laser spots	colour	type	Al	S wt%	Mn	Fe wt%	Co	Cu	Zn wt%	Ga	Ge	Ag	Cd	In	Sn	Sb	Hg	Tl	Pb	Bi
LGB06c, sph, p.15	L	Sp1	b.d.l.	31.95	9.92	1.12	14.51	302.98	64.70	74.17	90.17	24.52	2513.14	1.33	22.04	30.04	25.35	b.d.l.	16.69	0.25
LGB06c, sph, p.14	L	Sp1	b.d.l.	32.50	15.62	1.22	10.53	350.09	64.70	224.80	64.17	20.22	2328.40	0.29	3.40	18.70	23.33	b.d.l.	9.09	b.d.l.
LGB06c, sph, p.16	L	Sp1	b.d.l.	33.64	21.31	1.63	13.45	300.32	64.35	132.08	66.63	17.87	2619.08	0.34	4.31	54.80	26.39	b.d.l.	24.85	0.25
LGB06c, sph, p.2	L	Sp1	b.d.l.	32.22	16.78	1.49	13.51	355.97	64.35	258.01	78.06	42.22	2370.32	1.67	5.52	76.38	23.65	b.d.l.	29.44	0.26
LGB06c, sph, p.1	L	Sp1	b.d.l.	31.74	15.93	1.65	17.39	671.55	64.09	105.18	233.71	49.68	2989.69	1.19	26.28	156.76	23.85	b.d.l.	80.16	0.15
LGB06c, sph, p.3	L	Sp1	b.d.l.	32.58	24.40	1.70	18.40	139.79	64.09	35.27	44.15	11.98	2335.08	b.d.l.	2.49	21.65	21.36	b.d.l.	12.04	0.11
LGB06c, sph, p.5	Y	Sp1	b.d.l.	33.09	30.90	2.13	23.28	206.06	63.80	153.97	52.26	10.80	2843.64	b.d.l.	2.10	20.66	19.39	b.d.l.	11.35	b.d.l.
LGB06c, sph, p.6	Y	Sp1	b.d.l.	33.64	24.53	1.81	18.28	950.85	63.80	185.15	39.42	16.74	2795.34	396.74	355.87	42.15	15.83	b.d.l.	35.01	0.22
LGB06c, sph, p.9	Y	Sp1	b.d.l.	32.40	19.70	1.99	26.91	304.94	63.80	93.61	59.09	8.01	2389.85	8.54	97.74	12.75	21.63	b.d.l.	7.24	0.14
LGB06c, sph, p.35	Y	Sp1	b.d.l.	29.74	43.45	1.80	53.10	566.41	63.68	22.37	318.14	12.84	1846.25	0.35	7.33	13.09	19.93	0.16	6.93	0.18
LGB06c, sph, p.42	Y	Sp1	b.d.l.	29.93	46.66	2.27	27.61	81.31	63.66	0.60	b.d.l.	9.80	4664.06	2.29	2.83	2.99	23.51	0.11	1.89	b.d.l.
LGB06c, sph, p.39	Y	Sp1	b.d.l.	31.19	59.58	2.32	36.05	826.42	63.66	136.57	400.20	13.26	2177.16	b.d.l.	1.88	41.65	18.39	b.d.l.	11.04	0.62
LGB06c, sph, p.38	Y	Sp1	b.d.l.	30.32	32.07	2.27	29.59	499.12	63.66	203.98	194.08	9.22	2049.33	0.88	15.00	10.88	17.71	0.08	4.40	0.21
LGB06c, sph, p.34	Y	Sp1	4.00	29.90	46.49	2.14	39.40	173.82	63.66	40.48	23.55	14.70	2177.08	19.57	48.77	14.33	17.09	b.d.l.	27.04	0.88
LGB06c, sph, p.40	Y	Sp1	b.d.l.	30.44	35.27	2.47	31.31	613.07	63.23	121.49	266.44	7.07	3249.88	0.18	4.74	19.72	18.42	b.d.l.	4.67	0.43
LGB06c, sph, p.37	Y	Sp1	b.d.l.	29.99	42.81	2.60	33.64	140.45	63.23	15.23	48.81	6.67	4182.59	b.d.l.	0.35	3.16	18.78	0.09	1.94	0.12
LGB06c, sph, p.33	Y	Sp1	2.79	28.79	38.10	2.58	20.28	450.56	63.23	97.67	176.63	7.28	3223.99	0.26	23.42	42.18	17.27	b.d.l.	25.57	1.34
LGB06c, sph, p.4	Y	Sp1	b.d.l.	32.19	29.65	2.43	37.52	73.52	62.98	9.23	21.76	8.76	2764.30	3.10	7.04	6.12	19.99	b.d.l.	3.47	b.d.l.
LGB06c, sph, p.10	Y	Sp1	b.d.l.	31.79	36.52	2.81	77.89	543.83	62.24	50.51	299.24	5.10	2103.72	b.d.l.	b.d.l.	4.47	18.36	b.d.l.	1.66	b.d.l.
LGB06c, sph, p.13	Y	Sp1	b.d.l.	31.35	32.12	2.89	38.91	422.39	62.24	148.92	157.11	28.29	2599.77	b.d.l.	b.d.l.	81.35	19.04	0.08	34.73	0.66
LGB04h, sph, p.53	B	Sp2	343.21	32.31	150.46	3.18	134.31	242.54	64.70	97.23	55.54	10.36	4503.24	1.49	22.14	29.26	36.32	0.33	87.79	0.20
LGB06c, sph, p.36	B	Sp1	b.d.l.	30.07	47.74	3.00	50.37	271.79	62.98	27.17	118.74	10.14	3613.60	0.53	4.96	14.16	19.03	b.d.l.	12.45	0.26
LGB06c, sph, p.41	B	Sp1	b.d.l.	31.29	39.95	3.21	50.60	271.03	62.32	41.28	112.41	5.97	2809.47	0.24	4.01	8.15	18.10	0.10	3.57	0.15
LGB06c, sph, p.8	B	Sp1	b.d.l.	33.00	40.12	3.08	20.99	237.44	62.24	77.57	85.94	8.50	2863.90	0.23	10.13	13.11	13.64	b.d.l.	7.12	b.d.l.
LGB06c, sph, p.11	B	Sp1	2.91	31.78	45.07	3.25	51.69	326.00	62.09	147.68	39.50	7.48	2364.22	79.23	115.96	4.98	19.67	b.d.l.	5.23	b.d.l.
LGB06c, sph, p.12	B	Sp1	170.93	31.67	41.43	3.75	56.26	295.18	62.09	275.33	64.97	3.46	2689.55	0.19	20.62	1.75	18.39	b.d.l.	1.29	0.07
LGB06c, sph, p.25	B	Sp2	b.d.l.	31.04	61.65	4.00	75.71	309.10	62.09	11.55	130.17	5.61	3621.82	0.11	0.69	14.76	15.58	b.d.l.	13.08	b.d.l.
LGB06c, sph, p.21	B	Sp2	25.80	29.62	95.56	4.30	89.06	582.09	61.69	82.67	283.31	9.85	2785.78	3.26	6.03	24.35	18.64	0.19	12.91	b.d.l.
LGB06c, sph, p.30	B	Sp2	b.d.l.	30.65	48.10	4.02	95.77	697.37	61.69	12.73	386.01	13.02	2374.74	1.39	2.01	12.19	14.16	b.d.l.	6.19	0.34
LGB06c, sph, p.7	B	Sp1	b.d.l.	33.67	54.71	4.43	21.16	331.12	61.36	256.95	53.86	10.78	3855.37	b.d.l.	6.77	31.91	13.80	0.09	16.24	0.43
LGB04h, sph, p.49	B	Sp2	48.01	33.37	93.13	4.46	85.86	249.44	61.20	72.29	69.57	13.88	5222.97	b.d.l.	4.29	53.48	21.62	b.d.l.	28.80	b.d.l.
LGB04h, sph, p.65	B	Sp2	80.87	33.10	296.28	4.46	67.39	197.09	61.20	101.86	20.44	5.23	3476.79	0.27	2.57	18.10	27.18	b.d.l.	30.73	b.d.l.
LGB04h, sph, p.66	B	Sp2	b.d.l.	33.43	78.06	4.59	82.20	157.81	61.20	26.32	47.24	8.72	2355.68	0.20	b.d.l.	6.92	16.77	b.d.l.	7.73	b.d.l.
LGB04h, sph, p.56	B	Sp2	49.26	33.10	89.58	5.00	130.37	575.99	60.01	137.46	231.95	19.12	3710.16	3.34	43.07	13.22	25.96	b.d.l.	7.07	b.d.l.
LGB04h, sph, p.57	B	Sp2	168.23	35.11	134.10	5.45	151.57	528.73	60.01	183.02	203.98	17.89	3731.26	0.12	2.12	10.12	20.18	b.d.l.	7.07	b.d.l.
LGB06c, sph, p.24	B	Sp2	b.d.l.	33.05	64.14	5.44	106.13	590.75	59.74	59.37	287.74	7.20	3214.89	b.d.l.	b.d.l.	12.59	13.46	b.d.l.	9.66	0.72
LGB06c, sph, p.32	B	Sp2	b.d.l.	30.45	68.30	4.91	137.28	563.74	59.74	102.35	272.64	13.12	2913.50	b.d.l.	1.15	6.10	12.71	b.d.l.	2.18	0.14
LGB04h, sph, p.51	B	Sp2	b.d.l.	32.86	97.43	5.45	85.55	253.93	59.73	41.13	110.37	14.25	4771.88	b.d.l.	1.31	17.33	20.77	b.d.l.	18.59	b.d.l.
LGB04h, sph, p.52	B	Sp2	19.68	31.14	78.94	5.27	93.66	605.85	59.73	38.43	337.77	13.27	2507.11	0.07	1.52	12.55	18.24	0.12	4.67	b.d.l.
LGB04h, sph, p.63	R	Sp2	b.d.l.	33.00	164.09	5.54	67.91	737.25	60.01	332.63	81.53	22.25	3647.29	41.61	318.47	25.98	15.81	0.12	34.30	b.d.l.
LGB04h, sph, p.64	R	Sp2	b.d.l.	32.67	92.14	5.83	74.94	252.30	60.01	155.66	18.88	8.01	3684.74	0.98	6.53	7.34	15.57	b.d.l.	7.16	b.d.l.
LGB04h, sph, p.58	R	Sp2	b.d.l.	34.29	97.29	5.86	123.23	636.08	59.69	136.86	264.74	20.92	3058.54	0.05	2.23	6.35	15.28	b.d.l.	4.99	b.d.l.
LGB04h, sph, p.59	R	Sp2	b.d.l.	32.81	139.71	5.75	70.97	164.68	59.69	24.04	21.06	9.08	5078.78	0.23	1.31	23.49	16.98	0.21	47.97	0.10
LGB04h, sph, p.60	R	Sp2	b.d.l.	30.06	136.77	6.11	62.12	251.28	59.69	69.40	30.70	12.91	5329.22	7.35	58.77	61.36	16.85	b.d.l.	60.89	0.24

Table 6a. LA-ICP-MS analysis (ppm) of sphalerite from the Longobucco area (LGB) **(continue)**

LGB04h, sph, p.61	R	Sp2	b.d.l.	32.97	103.40	6.18	86.40	392.64	59.69	302.21	24.56	16.77	3277.20	7.60	38.79	1.70	13.98	b.d.l.	2.25	b.d.l.
LGB04h, sph, p.50	R	Sp2	2.03	31.41	120.26	6.01	100.75	520.00	59.45	68.63	244.20	16.17	4296.57	0.06	0.59	20.95	18.66	0.24	45.90	0.18
LGB06c, sph, p.22	R	Sp2	b.d.l.	30.17	132.79	5.64	89.78	407.29	59.37	77.70	155.30	11.00	3558.26	0.19	3.19	16.23	18.88	0.61	14.91	0.51
LGB06c, sph, p.23	R	Sp2	b.d.l.	32.06	161.00	5.62	76.49	299.85	59.37	86.14	84.51	6.83	4320.33	2.44	5.27	23.75	13.88	0.67	24.90	0.38
LGB06c, sph, p.31	R	Sp2	b.d.l.	30.17	73.79	5.53	77.44	418.94	59.37	58.24	183.70	10.19	4237.26	b.d.l.	0.89	36.14	10.76	0.07	24.90	b.d.l.
LGB06c, sph, p.27	R	Sp2	b.d.l.	30.40	177.39	5.72	104.98	680.46	59.15	33.95	335.24	14.66	2856.84	b.d.l.	1.46	15.56	11.13	0.82	9.81	b.d.l.
LGB06c, sph, p.26	R	Sp2	b.d.l.	30.17	122.91	6.33	111.32	492.80	58.94	60.29	242.74	6.49	3164.53	b.d.l.	0.38	8.67	11.96	b.d.l.	9.80	b.d.l.
LGB04h, sph, p.44	D	Sp2	b.d.l.	32.56	160.19	7.10	99.21	363.64	59.45	111.61	115.17	9.49	4388.44	0.19	1.33	29.40	13.38	b.d.l.	36.02	0.27
LGB04h, sph, p.45	D	Sp2	1.88	32.53	110.60	6.72	113.15	421.69	59.45	147.13	153.96	8.27	3258.29	0.05	1.02	15.62	12.85	0.08	6.02	b.d.l.
LGB04h, sph, p.62	D	Sp2	b.d.l.	32.98	139.75	7.48	100.77	1023.19	58.22	405.07	138.38	15.62	4659.88	43.16	377.42	29.08	15.30	b.d.l.	19.00	b.d.l.
LGB06c, sph, p.28	D	Sp2	b.d.l.	30.63	201.68	6.80	112.57	566.78	58.11	131.53	195.61	15.63	4125.14	0.06	1.25	31.45	11.86	0.80	19.09	0.46
LGB06c, sph, p.29	D	Sp2	b.d.l.	29.83	103.39	6.60	113.09	565.01	58.11	174.28	208.04	10.80	3469.33	1.04	4.08	11.71	11.65	0.12	8.42	0.24
LGB04h, sph, p.43	D	Sp2	b.d.l.	32.71	120.34	7.39	110.93	523.48	57.90	188.87	206.55	12.57	3838.59	b.d.l.	0.37	3.03	11.50	b.d.l.	2.50	b.d.l.
LGB04h, sph, p.47	D	Sp2	b.d.l.	32.23	137.30	7.24	80.23	248.19	57.90	78.05	95.94	12.78	4657.82	b.d.l.	b.d.l.	4.39	10.84	b.d.l.	6.27	0.10
LGB04h, sph, p.54	D	Sp2	b.d.l.	33.28	147.75	7.22	82.28	186.59	57.90	73.67	58.95	11.15	4853.67	b.d.l.	b.d.l.	31.51	16.23	b.d.l.	27.51	b.d.l.
LGB04h, sph, p.46	D	Sp2	b.d.l.	32.42	130.06	8.39	120.67	603.26	56.49	219.52	246.75	10.63	3428.62	0.03	0.73	1.39	10.47	b.d.l.	0.93	b.d.l.
LGB04h, sph, p.48	D	Sp2	b.d.l.	32.40	145.09	8.34	86.01	274.75	56.49	120.80	74.83	7.65	4561.29	0.11	1.27	15.75	9.79	b.d.l.	13.60	0.10
LGB04h, sph, p.55	D	Sp2	b.d.l.	35.42	157.62	8.24	87.71	362.67	55.72	186.57	92.19	8.95	5272.03	1.55	26.28	20.00	15.37	b.d.l.	16.12	b.d.l.
n° of analyses	average		70.74	31.89	85.84	4.42	69.68	413.76	61.12	115.23	144.58	12.93	3397.28	14.09	30.93	22.90	17.62	0.25	17.34	0.32
62	min		1.88	28.79	9.92	1.12	10.53	73.52	55.72	0.60	18.88	3.46	1846.25	0.03	0.35	1.39	9.79	0.07	0.93	0.07
	max		343.21	35.42	296.28	8.39	151.57	1023.19	64.70	405.07	400.20	49.68	5329.22	396.74	377.42	156.76	36.32	0.82	87.79	1.34
	median		25.80	32.21	75.92	4.46	76.10	363.15	61.20	97.45	112.41	10.80	3254.08	0.53	4.18	15.68	17.49	0.12	11.20	0.24
	st.dev.		101.09	1.44	57.17	2.05	37.74	207.22	2.35	85.83	104.27	7.86	931.73	60.11	80.14	24.39	4.88	0.25	17.84	0.27

b.d.l. below detection limit

Table 6b. LA-ICP-MS analysis (ppm) of sphalerite from the Fonte Argentila area (FAR)

colour legend: L (Light Yellow) - Y (Yellow) - B (Brown) - R (Reddish Brown) (standard by EPMA Zn-content)

									standard										
Laser spots	colour	type	Al	S wt%	Mn	Fe wt%	Co	Cu	Zn wt%	Ga	Ge	Ag	Cd	In	Sn	Sb	Hg	Tl	Pb	Bi
FA17a, Sph, p.73	L	Sp1	b.d.l.	31.87	21.82	1.30	24.11	698.90	64.39	69.32	378.19	7.30	1067.25	0.08	0.90	13.00	31.75	b.d.l	3.83	0.13
FA17a, Sph, p.1	L	Sp1	b.d.l.	32.33	36.55	1.52	21.66	114.47	64.39	14.58	48.77	7.90	2720.22	0.18	1.39	10.29	36.68	b.d.l	5.49	b.d.l
FA17a, Sph, p.71	L	Sp1	b.d.l.	35.33	55.85	1.64	43.52	58.63	64.39	4.44	9.76	8.28	2384.62	10.10	9.71	16.88	49.75	b.d.l	10.69	b.d.l
FA17a, Sph, p.70	L	Sp1	b.d.l.	34.65	29.89	1.33	31.42	167.15	64.39	33.49	71.50	2.06	3206.33	20.52	0.66	4.00	46.49	b.d.l	5.33	0.26
FA17a, Sph, p.67	L	Sp1	b.d.l.	35.40	32.10	1.48	37.56	148.42	64.39	32.74	48.66	4.32	1277.46	4.39	26.29	7.85	42.78	b.d.l	4.55	b.d.l
FA17a, Sph, p.2	L	Sp1	b.d.l.	35.48	37.84	1.68	28.04	111.36	64.39	16.24	17.83	5.97	1228.91	24.93	26.93	5.89	44.69	b.d.l	4.87	b.d.l
FA17a, Sph, p.3	L	Sp1	b.d.l.	33.23	35.38	1.41	19.53	447.37	64.39	62.89	159.79	25.51	1453.60	7.46	20.60	76.02	47.14	b.d.l	15.59	b.d.l
FA17a, Sph, p.75	Y	Sp1	b.d.l.	34.08	60.45	1.92	17.25	50.30	64.39	1.76	4.36	6.20	3708.09	b.d.l	b.d.l	6.95	42.91	b.d.l	6.55	b.d.l
FA17a, Sph, p.76	Y	Sp1	b.d.l.	33.87	55.84	2.79	23.32	90.20	63.90	36.27	31.42	4.01	2010.33	b.d.l	0.40	5.03	29.92	b.d.l	3.77	b.d.l
FA17a, Sph, p.69	Y	Sp1	b.d.l.	35.98	59.09	2.75	45.98	421.57	63.90	71.22	191.39	4.72	1806.26	0.19	0.89	9.14	36.84	b.d.l	6.65	b.d.l
FA04, Sph, p.79	Y	Sp2	b.d.l.	34.73	25.24	2.29	50.58	307.21	62.03	5.20	41.47	77.27	2248.52	298.53	37.38	16.04	27.49	b.d.l	19.38	0.55
FA04, Sph, p.78	Y	Sp2	b.d.l.	34.96	33.88	3.05	42.23	760.66	62.03	42.11	93.54	246.78	3691.50	128.51	87.55	189.04	28.27	b.d.l	141.57	11.20
FA04, Sph, p.83	Y	Sp2	b.d.l.	30.72	35.89	3.24	21.17	122.55	62.03	19.90	26.26	15.28	3149.08	b.d.l	8.97	4.74	26.92	b.d.l	6.74	0.25
FA04, Sph, p.84	Y	Sp2	b.d.l.	30.63	32.30	3.28	22.08	184.75	62.03	53.04	49.89	34.66	3056.21	0.07	7.02	32.22	26.70	b.d.l	27.23	0.97
FA04, Sph, p.85	Y	Sp2	b.d.l.	30.83	35.89	3.45	21.91	83.57	62.03	18.93	23.91	14.74	3089.51	0.09	b.d.l	1.64	23.49	b.d.l	5.69	b.d.l
FA04, Sph, sp.4	Y	Sp2	b.d.l.	31.21	29.47	3.05	19.18	270.38	62.03	80.78	73.41	43.08	2676.19	0.14	16.73	13.98	25.89	b.d.l	14.15	0.56
FA17a, Sph, p.72	B	Sp2	b.d.l.	34.80	126.44	5.31	44.73	579.90	60.77	116.54	268.66	12.59	1996.91	b.d.l	0.63	11.67	22.87	b.d.l	7.50	b.d.l
FA17a, Sph, p.74	B	Sp2	b.d.l.	38.04	98.66	4.25	41.21	660.10	62.36	112.85	298.45	15.80	1905.49	0.09	1.97	16.64	21.23	b.d.l	13.91	0.14
FA17a, Sph, p.68	B	Sp2	b.d.l.	35.48	83.59	3.83	18.67	609.53	62.36	57.61	265.03	30.21	1000.88	0.93	41.41	37.09	33.33	b.d.l	24.60	b.d.l
FA04, Sph, p.77	B	Sp2	b.d.l.	33.48	194.66	3.61	46.53	494.79	62.03	6.02	59.32	90.53	4873.24	10.79	18.01	10.28	34.33	b.d.l	21.27	1.00
FA04, Sph, p.80	B	Sp2	b.d.l.	34.57	42.44	3.86	44.89	452.19	62.03	38.50	100.99	107.05	4437.39	95.15	25.27	54.85	25.34	b.d.l	43.99	23.61
FA04, Sph, p.81	B	Sp2	2.81	36.52	71.23	5.29	29.12	917.85	61.16	92.42	37.71	317.32	7589.09	64.63	155.87	174.06	21.55	b.d.l	190.75	5.36
FA04, Sph, p.82	B	Sp2	b.d.l.	30.23	44.17	3.50	39.57	630.62	62.03	68.33	199.04	263.03	5227.98	9.66	8.85	95.29	20.47	b.d.l	76.15	29.58
FA04, Sph, p.86	B	Sp2	b.d.l.	32.93	36.56	3.64	21.15	210.22	62.03	31.96	31.94	45.57	3098.29	0.15	1.48	3.58	23.92	b.d.l	35.42	0.19
FA04, Sph, p.1	B	Sp2	b.d.l.	31.28	40.80	3.98	60.89	380.72	62.03	56.27	162.45	102.91	3404.65	6.37	29.28	20.33	18.89	b.d.l	13.21	1.38
FA04, Sph, p.2	B	Sp2	b.d.l.	31.49	57.94	4.21	27.38	999.24	62.03	16.99	51.10	140.62	5900.66	846.50	86.43	90.21	16.63	b.d.l	98.31	13.16
FA04, Sph, p.3	B	Sp2	b.d.l.	31.44	63.13	4.58	33.37	251.74	62.03	13.40	10.47	179.55	6895.24	16.50	3.03	141.27	18.38	b.d.l	162.00	7.37
FA17a, sph-a.1	B	Sp2	b.d.l.	28.97	109.18	3.25	36.35	130.08	62.95	19.74	45.48	6.74	1703.98	0.09	b.d.l	13.32	18.97	b.d.l	17.77	b.d.l
FA17a, sph-a.2	R	Sp2	b.d.l.	29.93	181.33	7.51	58.31	510.98	58.21	192.32	197.38	7.54	2336.37	1.89	15.23	2.92	12.35	b.d.l	3.25	b.d.l
FA17a, sph-a.3	R	Sp2	b.d.l.	28.75	150.06	6.52	56.54	988.13	58.79	338.79	397.97	13.43	1599.59	0.15	4.49	b.d.l	10.83	b.d.l	b.d.l	b.d.l
FA17a, sph-a.4	R	Sp2	b.d.l.	27.08	119.36	5.51	56.12	829.42	59.30	204.95	378.60	10.86	1782.61	0.94	2.15	2.79	13.49	b.d.l	1.60	b.d.l
FA17a, sph-a.5	R	Sp2	b.d.l.	29.56	220.85	8.22	49.36	285.49	57.29	41.10	91.46	6.05	1884.98	b.d.l	b.d.l	1.61	8.73	b.d.l	1.17	b.d.l
FA17a, sph-a.6	R	Sp2	b.d.l.	28.71	157.42	6.52	37.83	348.91	58.79	18.40	153.12	9.98	1569.43	1.21	b.d.l	14.72	12.98	b.d.l	11.96	b.d.l
FA17a, sph-a.7	B	Sp2	b.d.l.	29.91	92.34	4.85	90.45	774.76	60.77	23.11	377.98	6.33	1732.04	b.d.l	b.d.l	6.16	12.18	b.d.l	0.82	b.d.l
FA17a, sph-a.8	W	Sp3	b.d.l.	29.07	18.29	0.68	9.52	66.48	65.54	23.81	13.51	3.28	1701.80	0.11	b.d.l	8.28	41.91	b.d.l	6.17	b.d.l
FA17a, sph-a.9	W	Sp3	b.d.l.	30.12	10.36	0.25	3.80	81.00	66.06	10.59	1.67	23.21	1665.43	1.69	8.80	67.04	40.47	b.d.l	33.25	b.d.l
FA17a, sph-a.10	W	Sp3	b.d.l.	31.09	14.67	0.44	9.91	25.49	65.16	13.63	1.34	3.59	1715.31	0.08	2.22	8.40	30.36	b.d.l	9.22	b.d.l
FA17a, sph-a.11	W	Sp3	7.04	29.74	18.95	1.01	35.88	201.16	64.15	9.24	96.26	9.01	1307.82	0.13	b.d.l	10.79	20.84	b.d.l	16.12	b.d.l
FA17a, sph-a.12	W	Sp3	b.d.l.	29.75	37.65	1.62	36.45	275.99	64.87	17.88	122.82	8.33	2051.91	0.26	1.32	19.69	21.08	b.d.l	20.91	b.d.l

Table 6b. LA-ICP-MS analysis (ppm) of sphalerite from the Fonte Argentila area (FAR) **(continue)**

n° of analyses																		
34	average	b.d.l	32.26	66.86	3.30	34.81	378.01	62.51	53.52	118.79	49.27	2721.93	47.05	21.03	32.20	27.41	b.d.l	28.72	5.98
	min	b.d.l	27.08	10.36	0.25	3.80	25.49	57.29	1.76	1.34	2.06	1000.88	0.07	0.40	1.61	8.73	b.d.l	0.82	0.13
	max	b.d.l	38.04	220.85	8.22	90.45	999.24	66.06	338.79	397.97	317.32	7589.09	846.50	155.87	189.04	49.75	b.d.l	190.75	29.58
	median	b.d.l	31.49	42.44	3.25	35.88	285.49	62.03	32.74	71.50	12.59	2051.91	1.21	8.85	12.34	25.89	b.d.l	12.58	0.99
	st.dev.	b.d.l	2.66	53.21	1.93	16.96	287.62	2.08	65.90	119.66	78.39	1578.65	154.53	33.39	47.32	11.22	b.d.l	45.27	9.12

b.d.l. below detection limit

Table 7. GGIMFis temperatures (°C) and sulphur fugacity (fS2) of generations of LGB and FAR sphalerites

		T °C	log10 (fS2)
Sp1 (LGB) *n*° 18	min	130	-20.64
	max	206	-15.90
	median	159	-18.38
	average	162	-18.26
	s.dev.	24	1.34
Sp2 (LGB) *n*° 25	min	150	-19.38
	max	218	-15.37
	median	180	-17.44
	average	181	-17.45
	s.dev.	19	1.00
Sp1-Sp2	total median	180	-17.55
	total average	173	-17.79
	s.dev	18	1.21
Sp1 (FAR) *n*° 8	min	110	-22.55
	max	230	-13.30
	median	171	-17.33
	average	171	-17.47
	s.dev.	37	2.85
Sp2 (FAR) *n*° 19	min	148	-20.18
	max	241	-13.37
	median	183	-17.29
	average	188	-16.73
	s.dev.	32	2.24
Sp1-Sp2	total median	178	-17.29
	total average	184	-16.95
	s.dev	34	2.40
Sp3 (FAR) n° 5	min	147	-18.97
	max	174	-15.76
	median	160	-18.4
	average	157	-17.6
	s.dev.	12	1.42

Table 8. EPMA analysis of galena from the Longobucco (LGB) and the Fonte Argentila area (FAR)

LGB

analysis spots	S	Sb	Pb	Total
LGB04h_B_gn1 Line 001	13.18	0.09	86.14	99.41
LGB04h_B_gn1 Line 002	11.51	b.d.l.	76.63	88.14
LGB04h_B_gn1 Line 003	13.43	0.03	85.81	99.27
LGB04h_B_gn1 Line 004	12.96	b.d.l.	84.41	97.37
LGB04h_B_gn1 Line 005	12.83	0.06	84.01	96.90
LGB04h_B_gn1 Line 006	12.84	0.05	85.85	98.74
LGB04h_B_gn1 Line 007	13.47	b.d.l.	87.09	100.56
LGB04h_B_gn1 Line 008	13.07	b.d.l.	86.08	99.15
min	11.51	0.03	76.63	88.14
max	13.47	0.09	87.09	100.56
average	12.91	0.06	84.50	97.44
median	13.02	0.05	85.83	98.94
st.dev.	0.62	0.02	3.33	3.93

FAR

analysis spots	S	Sb	Pb	Total
FA11c_L1 001	12.96	0.06	87.75	100.77
FA11c_L1 002	13.04	0.02	87.81	100.87
FA11c_L1 003	13.05	b.d.l.	86.14	99.19
FA11c_L1 004	13.11	0.04	87.65	100.80
FA11c_L1 005	13.16	0.06	86.63	99.85
FA11c_L1 006	13.26	b.d.l.	88.22	101.48
FA04_gn1 Line 001	12.31	b.d.l.	81.83	94.14
FA04_gn1 Line 002	13.36	b.d.l.	87.53	100.89
FA04_gn1 Line 003	13.51	b.d.l.	87.44	100.95
FA04_gn1 Line 004	13.09	b.d.l.	86.16	99.25
FA04_gn1 Line 005	13.32	b.d.l.	86.59	99.91
FA04_gn1 Line 006	13.20	b.d.l.	87.43	100.63
FA04_gn2 Line 001	13.51	b.d.l.	86.96	100.47
FA04_gn2 Line 002	13.51	b.d.l.	87.49	101.00
FA04_gn2 Line 003	13.24	b.d.l.	86.76	100.00
FA04_gn2 Line 004	13.09	b.d.l.	85.42	98.51
FA04_gn2 Line 005	13.19	b.d.l.	85.26	98.45
FA04_gn2 Line 006	13.41	b.d.l.	85.84	99.25
min	12.31	0.02	81.83	94.14
max	13.51	0.06	88.22	101.48
average	13.18	0.05	86.61	99.80
median	13.20	0.05	86.86	100.24
st.dev.	0.28	0.02	1.47	1.67

D.L.	S	Sb	Pb
average	0.02	0.02	0.08

b.d.l.	below detection limit

Table 9. SEM and EPMA analysis of pyrite from the Longobucco (LGB) and the Fonte Argentila area (FAR)

SEM analyses of pyrite in the Qz1 (LGB)

analysis spots	S wt%	Fe wt%	Cu wt%	As wt%	Ag wt%	Sn wt%	Au wt%	Total
LGB06a_py1	63.23	36.55	n.d.	0.22	n.d.	n.d.	n.d.	100.00
LGB06a_py2	63.15	36.60	n.d.	0.25	n.d.	n.d.	n.d.	100.00
LGB06a_py3	63.68	36.32	n.d.	0.17	n.d.	n.d.	n.d.	100.17
LGB06a_py4	63.35	36.49	n.d.	0.21	n.d.	n.d.	n.d.	100.05
LGB06b_py13	66.91	32.91	n.d.	0.17	n.d.	n.d.	n.d.	99.99
LGB06b_py14	67.06	32.94	n.d.	0.00	n.d.	n.d.	n.d.	100.00
LGB04b_py5	58.74	40.41	n.d.	0.85	n.d.	n.d.	n.d.	100.00
min	58.74	32.91		0.00				
max	67.06	40.41		0.85				
average	63.73	36.03		0.27				
median	63.35	36.49		0.21				
st.dev.	2.79	2.56		0.27				

EPMA analyses of pyrite in the Cal1 (LGB)

analysis spots	S wt%	Fe wt%	Cu wt%	As wt%	Ag wt%	Sn wt%	Au wt%	Total
LGB04h_Pyrite1	52.86	45.61	0.00	0.21	0.00	n.d.	n.d.	98.68
LGB04h_Pyrite2	52.64	46.44	0.00	0.17	0.01	n.d.	n.d.	99.26
LGB04h_Pyrite3	52.60	46.15	0.00	0.14	0.00	n.d.	n.d.	98.89
LGB04h_Pyrite4	50.36	44.73	0.01	0.10	0.00	n.d.	n.d.	95.20
LGB04h_Pyrite5	52.62	46.57	0.00	0.18	0.00	n.d.	n.d.	99.37
min	2.79	2.56	0.00	0.10				
max	63.35	46.57	0.01	0.27				
average	46.75	38.36	0.00	0.18				
median	52.62	45.61	0.00	0.18				
st.dev.	19.84	16.18	0.00	0.05				

EPMA analyses of pyrite in the Ccp (FAR)

analysis spots	S wt%	Fe wt%	Cu wt%	As wt%	Ag wt%	Sn wt%	Au wt%	Total
FA04_py.1	52.80	47.15	0.11	0.00	0.00	0.01	0.00	100.07
FA04_py.2	53.34	47.21	0.08	0.00	b.d.l.	0.00	b.d.l.	100.63
FA04_py.3	52.37	46.59	0.50	0.00	0.02	0.02	0.14	99.64
FA04_py.4	53.10	46.62	0.53	0.00	0.01	0.00	b.d.l.	100.26
FA04_py.5	53.42	46.90	0.04	b.d.l.	0.01	0.01	0.24	100.62
FA04_py.6	53.48	46.58	0.26	0.07	0.00	b.d.l.	0.00	100.39
FA04_py.7	53.31	46.89	0.38	b.d.l.	0.01	0.02	0.18	100.79
FA04_py.8	52.28	46.32	1.02	0.04	0.01	0.01	0.00	99.68
FA04_py.9	52.81	46.32	0.48	b.d.l.	0.02	b.d.l.	0.15	99.79
FA04_py.10	52.67	46.53	0.34	b.d.l.	0.02	0.00	b.d.l.	99.56
min	52.28	46.32	0.04	0.00	0.00	0.00	0.00	
max	53.48	47.21	1.02	0.07	0.02	0.02	0.24	
average	52.96	46.71	0.37	0.02	0.01	0.01	0.10	
median	52.96	46.61	0.36	0.00	0.01	0.01	0.14	
st.dev.	0.44	0.31	0.29	0.03	0.01	0.01	0.10	

D.L. (EPMA)	S	Fe	Cu	As	Ag	Sn	Au
average	0.01	0.01	0.02	0.01	0.01	0.01	0.07

b.d.l.	below detection limit
n.d.	not detected

Table 10. EPMA analysis of chalcopyrite from the Fonte Argentila area (FAR)

analysis spots	S	Fe	Cu	Zn	Ag	Sn	Total
FA04_Line ccp1 001	34.51	30.05	34.34	0.01	0.06	0.03	98.99
FA04_Line ccp1 002	34.62	29.99	34.61	b.d.l.	0.04	b.d.l.	99.26
FA04_Line ccp1 003	34.19	29.89	34.48	b.d.l.	0.04	0.03	98.63
FA04_Line ccp1 004	34.89	29.95	34.63	b.d.l.	0.03	0.03	99.52
FA04_Line ccp2 001	35.53	29.94	34.45	b.d.l.	0.03	b.d.l.	99.95
FA04_Line ccp2 002	35.00	29.16	33.92	0.14	0.05	0.01	98.28
FA04_Line ccp2 003	34.43	29.53	33.91	b.d.l.	0.04	0.01	97.92
FA04_Line ccp2 004	35.23	29.73	34.10	b.d.l.	0.04	b.d.l.	99.10
FA04_Line ccp2 005	35.17	29.42	33.74	0.01	0.04	b.d.l.	98.38
FA04_Line ccp2 006	33.00	29.51	33.91	b.d.l.	0.03	0.04	96.49
FA04_Line ccp3 001	34.73	30.02	34.57	b.d.l.	0.05	b.d.l.	99.37
FA04_Line ccp3 002	24.92	29.34	34.10	b.d.l.	0.03	0.75	89.14
FA04_Line ccp3 003	36.00	29.75	34.36	b.d.l.	0.03	0.18	100.32
FA04_Line ccp3 004	34.13	27.54	32.17	b.d.l.	0.05	0.12	94.02
FA04_Line ccp3 005	35.10	30.10	34.61	b.d.l.	0.06	b.d.l.	99.87
FA04_Line ccp3 006	35.12	30.21	34.50	b.d.l.	0.03	b.d.l.	99.86
FA04_Line ccp3 007	25.01	25.89	28.78	0.03	0.01	0.01	79.74
FA04_Line ccp3 008	35.01	30.03	34.22	b.d.l.	0.04	b.d.l.	99.30
FA04_Line ccp4 001	33.52	29.67	34.36	b.d.l.	0.01	0.06	97.62
FA04_Line ccp4 002	32.84	28.69	33.03	b.d.l.	0.04	0.04	94.64
FA04_Line ccp4 003	35.02	29.86	34.42	b.d.l.	0.03	0.05	99.38
FA04_Line ccp4 004	33.49	29.12	34.08	0.01	0.02	0.02	96.74
FA04_Line ccp4 005	35.69	29.85	34.46	b.d.l.	0.04	0.01	100.05
FA04_Line ccp4 006	35.05	29.72	34.48	b.d.l.	0.04	0.01	99.30
FA04_Line ccp4 007	35.23	29.73	34.40	b.d.l.	0.01	0.01	99.38
FA04_Line ccp4 008	34.88	28.63	32.36	b.d.l.	0.09	b.d.l.	95.96
FA04_Line ccp5 001	35.76	29.48	33.97	b.d.l.	0.05	b.d.l.	99.26
FA04_Line ccp5 002	35.00	29.66	34.20	b.d.l.	0.03	b.d.l.	98.89
FA04_Line ccp5 003	34.92	29.35	32.98	0.01	0.03	0.20	97.48
FA04_Line ccp5 004	35.43	29.55	34.32	0.04	0.02	0.22	99.58
FA04_Line ccp5 005	38.00	29.34	33.37	b.d.l.	0.03	0.15	100.89
FA04_Line ccp5 006	30.96	30.21	34.62	b.d.l.	0.04	b.d.l.	95.83
FA04_Line ccp5 007	39.05	29.30	33.51	b.d.l.	0.03	0.15	102.04
FA04_Line ccp5 008	35.40	29.64	34.13	b.d.l.	0.03	0.01	99.21

min	24.92	25.89	28.78	0.01	0.01	0.01	79.74
max	39.05	30.21	34.63	0.14	0.09	0.75	102.04
average	34.32	29.47	33.89	0.04	0.04	0.10	97.78
median	35.00	29.67	34.21	0.01	0.03	0.03	99.15
st.dev.	2.73	0.82	1.09	0.05	0.02	0.16	3.96

D.L.	S	Fe	Cu	Zn	Ag	Sn
average	0.01	0.01	0.02	0.01	0.01	0.01

b.d.l.	below detection limit

Table 11. LA-ICP-MS analysis (ppm) of chalcopyrite from the Fonte Argentila area (FAR) (standard by EPMA Fe-content)

			standard														
Laser spots	S wt%	Mn	Fe wt%	Co	Cu wt%	Zn	Ga	Ge	Ag	Cd	In	Sn	Sb	Au	Tl	Pb	Bi
FA04, Ccp, p.97	44.01	4.64	30.05	b.d.l.	34.53	194.99	b.d.l.	2.46	250.76	b.d.l.	2.73	19.97	11.03	b.d.l.	b.d.l.	12.44	1.12
FA04, Ccp, p.98	41.97	3.33	29.75	0.29	31.00	407.92	0.82	6.77	252.18	b.d.l.	199.94	1610.61	2.72	b.d.l.	b.d.l.	13.67	1.49
FA04, Ccp, p.99	40.31	n.d.	30.05	0.74	33.31	145.26	b.d.l.	b.d.l.	265.13	b.d.l.	10.72	57.37	29.38	1.51	0.29	177.91	2.25
FA04, Ccp, p.100	43.92	6.06	30.05	1.76	34.80	343.08	1.51	9.53	313.23	9.02	127.99	660.51	28.55	1.40	0.21	62.31	0.56
FA04, Ccp, p.5	37.23	6.17	30.05	b.d.l.	34.70	157.64	1.81	41.63	262.72	b.d.l.	1.81	39.03	4.62	0.27	b.d.l.	23.58	b.d.l.
FA04, Ccp, p.87	46.45	n.d.	30.05	b.d.l.	36.79	198.07	0.80	11.03	164.30	5.22	7.85	158.52	23.72	0.62	0.47	132.13	0.57
FA04, Ccp, p.88	44.61	9.14	30.05	b.d.l.	34.47	488.54	0.60	77.66	228.33	b.d.l.	5.21	195.41	20.39	0.89	0.45	276.35	0.18
FA04, Ccp, p.89	41.93	2.92	30.05	b.d.l.	35.42	358.89	0.94	6.41	255.82	3.46	67.69	264.10	5.66	b.d.l.	b.d.l.	10.18	b.d.l.
FA04, Ccp, p.90	38.88	41.10	30.05	0.66	31.54	6218.18	b.d.l.	3.71	279.06	36.09	6.79	101.81	186.69	1.48	4.38	4616.80	3.69
FA04, Ccp, p.6	51.15	4.68	30.05	b.d.l.	31.57	127.69	0.83	45.78	221.87	b.d.l.	10.77	260.09	26.51	0.67	0.91	199.82	0.31
FA04, Ccp, p.91	44.81	2.79	30.05	b.d.l.	35.75	218.38	b.d.l.	17.46	227.73	3.99	21.15	92.21	5.32	0.88	b.d.l.	9.59	0.39
FA04, Ccp, p.92	44.63	2.81	30.05	b.d.l.	34.88	228.31	0.98	92.14	298.83	3.97	6.81	292.23	7.01	b.d.l.	0.16	11.35	0.66
FA04, Ccp, p.93	46.21	2.42	30.05	b.d.l.	34.36	321.88	0.91	79.90	181.84	3.29	16.53	240.32	16.84	1.37	b.d.l.	96.93	0.89
FA04, Ccp, p.94	45.06	3.72	30.05	b.d.l.	34.41	292.72	0.66	1.98	200.24	4.77	94.55	629.91	6.88	1.16	b.d.l.	16.64	2.02
FA04, Ccp, p.95	47.56	3.75	30.05	b.d.l.	34.75	167.50	b.d.l.	68.85	187.16	b.d.l.	3.08	31.48	1.10	b.d.l.	b.d.l.	4.63	b.d.l.
FA04, Ccp, p.96	45.85	4.67	30.05	b.d.l.	34.08	462.66	b.d.l.	4.62	239.56	7.84	46.20	204.01	7.63	0.52	0.23	160.48	0.92
average	44.04	7.01	30.03	0.86	34.15	645.73	0.99	31.33	239.30	8.63	39.36	303.60	24.00	0.98	0.89	364.05	1.16
min	37.23	2.42	29.75	0.29	31.00	127.69	0.60	1.98	164.30	3.29	1.81	19.97	1.10	0.27	0.16	4.63	0.18
max	51.15	41.10	30.05	1.76	36.79	6218.18	1.81	92.14	313.23	36.09	199.94	1610.61	186.69	1.51	4.38	4616.80	3.69
median	44.62	4.19	30.05	0.70	34.50	260.51	0.87	11.03	245.16	4.77	10.75	199.71	9.33	0.89	0.37	42.94	0.89
st.dev.	3.41	9.97	0.08	0.63	1.57	1490.34	0.38	33.17	41.72	10.49	56.79	396.90	44.46	0.43	1.43	1137.26	0.99

b.d.l. below detection limit

Table 12a. EPMA analyses (wt%) of quartz from the Longobucco (LGB) area

legend: L (light quartz) - D (dark growth band)

analyses spots	type	Na	Al	Si	K	Ca	Ti
LGB06a-1La-qtzT1 Line 001	L	0.02	0.05	46.34	0.01	0.03	0.02
LGB06a-1La-qtzT1 Line 002	L	0.01	0.07	46.53	0.01	0.01	0.01
LGB06a-1La-qtzT1 Line 003	L	0.01	0.08	46.44	0.01	b.d.l.	0.01
LGB06a-1La-qtzT1 Line 004	D	0.03	0.27	46.18	0.09	0.02	0.02
LGB06a-1La-qtzT1 Line 005	D	0.04	0.17	45.84	0.04	0.04	b.d.l.
LGB06a-1La-qtzT1 Line 006	D	0.38	0.15	45.79	0.04	0.04	0.01
LGB06a-1La-qtzT1 Line 007	L	0.02	0.08	46.08	0.02	0.02	0.02
LGB06a-1La-qtzT1 Line 008	L	0.04	0.05	46.21	0.02	0.03	0.02
LGB06a-1La-qtzT1 Line 009	L	0.03	0.04	46.29	0.02	0.02	0.01
LGB06a-1La-qtzT1 Line 010	L	0.02	0.02	46.40	0.01	b.d.l.	0.01
LGB06a-1La-qtzT1 Line 011	L	0.01	0.02	46.25	0.01	0.01	0.02
LGB06a-1La-qtzT1 Line 012	L	0.04	0.03	46.46	0.02	0.01	0.01
LGB06a-1La-qtzT2 Line 001	D	0.01	0.18	46.14	0.03	0.05	0.02
LGB06a-1La-qtzT2 Line 002	D	0.05	0.16	45.60	0.05	0.05	0.01
LGB06a-1La-qtzT2 Line 003	L	0.07	0.04	46.29	0.05	0.05	0.01
LGB06a-1La-qtzT2 Line 004	L	0.02	0.05	46.26	0.01	0.01	0.01
LGB06a-1La-qtzT2 Line 005	L	0.02	0.07	46.36	0.02	0.02	0.02
LGB06a-1La-qtzT2 Line 006	L	0.03	0.08	46.52	0.02	0.01	0.02
LGB06a-1La-qtzT2 Line 007	L	0.07	0.07	46.09	0.03	0.08	0.02
LGB06a-1La-qtzT2 Line 008	L	0.03	0.02	46.60	0.02	0.01	0.02
LGB06a-1La-qtzT2 Line 009	L	0.05	0.02	45.72	0.05	0.02	0.01
LGB06a-1La-qtzT2 Line 010	L	0.03	0.01	46.42	0.01	0.01	0.01
LGB06a-1La-qtzT3 Line 001	D	0.03	0.23	44.51	0.02	0.03	0.02
LGB06a-1La-qtzT3 Line 002	D	b.d.l.	0.11	45.25	0.01	b.d.l.	0.02
LGB06a-1La-qtzT3 Line 003	D	0.03	0.21	44.93	0.06	0.03	0.01
LGB06a-1La-qtzT3 Line 004	D	0.02	0.06	45.23	0.01	0.01	0.01
LGB06a-1La-qtzT3 Line 005	D	0.02	0.13	44.87	0.01	0.02	0.01
LGB06a-1La-qtzT3 Line 006	D	0.02	0.15	45.33	0.04	0.02	0.01
LGB06a-1La-qtzT3 Line 007	D	0.04	0.30	45.73	0.03	0.06	0.01
LGB06a-1La-qtzT3 Line 008	L	0.04	0.30	45.66	0.02	0.03	0.01
LGB06a-1La-qtzT3 Line 009	L	0.06	0.05	46.67	0.02	0.02	0.02
LGB06a-1La-qtzT3 Line 010	L	0.03	0.39	45.52	0.01	0.02	0.02
LGB06a-1La-qtzT3 Line 011	L	0.01	0.07	46.39	0.01	0.02	0.01
LGB06a-1La-qtzT3 Line 012	L	0.01	0.02	46.65	0.01	b.d.l.	0.01
LGB06a-1La-qtzT3 Line 013	D	0.03	0.05	46.75	0.01	0.01	0.02
LGB06a-1La-qtzT3 Line 014	D	0.04	0.05	46.27	0.02	0.01	0.02
LGB06a-1La-qtzT3 Line 015	D	0.01	0.08	46.68	0.01	0.01	0.01
LGB06a-1La-qtzT3 Line 016	D	0.02	0.08	46.53	0.01	0.01	0.01
LGB06a-1La-qtzT3 Line 017	D	0.05	0.02	46.17	0.01	0.01	0.02
LGB06a-1La-qtzT3 Line 018	D	0.06	0.29	45.66	0.09	0.04	0.01
LGB06a-1La-qtzT3 Line 019	D	0.05	0.18	46.06	0.04	0.04	0.01
LGB06a-1La-qtzT3 Line 020	L	0.03	0.05	45.73	0.02	0.04	0.01

min	0.01	0.01	44.51	0.01	0.01	0.01
max	0.38	0.39	46.75	0.09	0.08	0.02
average	0.04	0.11	46.03	0.02	0.02	0.01
median	0.03	0.07	46.19	0.02	0.02	0.01
s.d.	0.06	0.09	0.54	0.02	0.02	0.00

	D.L.	Na	Al	Si	K	K	Ca
	average	0.009	0.006	0.013	0.004	0.006	0.007

b.d.l.	below detection limit

Table 12b. EPMA analyses (wt%) of quartz from the Fonte Argentila (LGB) area

legend: M (microcrystalline) - L (light quartz) - D (dark growth band)

analyses spots	type	Na	Mg	Al	Si	K	Ca	Ti
FA14a_qtz_L1 Line 001	M	0.02	b.d.l.	0.36	45.43	0.04	0.01	0.02
FA14a_qtz_L1 Line 002	M	0.02	b.d.l.	0.38	45.67	0.01	b.d.l.	0.01
FA14a_qtz_L1 Line 003	L	b.d.l.	b.d.l.	0.03	46.41	0.01	b.d.l.	0.02
FA14a_qtz_L1 Line 004	L	0.02	b.d.l.	0.04	46.10	0.01	0.02	0.02
FA14a_qtz_L1 Line 005	D	0.02	b.d.l.	0.34	45.72	0.01	0.03	0.01
FA14a_qtz_L1 Line 006	D	b.d.l.	b.d.l.	0.35	46.23	0.01	b.d.l.	0.02
FA14a_qtz_L1 Line 007	D	b.d.l.	b.d.l.	0.26	45.95	0.03	b.d.l.	0.02
FA14a_qtz_L1 Line 008	D	0.03	0.01	0.38	45.18	0.02	0.17	0.02
FA14a_qtz_L1 Line 009	L	0.02	b.d.l.	0.02	46.37	0.01	b.d.l.	0.02
FA14a_qtz_L1 Line 010	L	0.01	b.d.l.	0.02	46.69	0.01	0.01	0.02
FA14a_qtz_L1 Line 011	L	b.d.l.	b.d.l.	0.11	46.38	0.01	b.d.l.	0.01
FA14a_qtz_L1 Line 012	L	b.d.l.	b.d.l.	0.04	46.36	0.01	b.d.l.	0.02
FA14a_qtz_L2 Line 001	D	b.d.l.	b.d.l.	0.16	46.35	0.03	0.01	b.d.l.
FA14a_qtz_L2 Line 002	D	b.d.l.	0.01	0.27	45.98	0.03	b.d.l.	0.01
FA14a_qtz_L2 Line 003	D	0.04	b.d.l.	0.29	42.54	0.00	b.d.l.	0.03
FA14a_qtz_L2 Line 004	L	b.d.l.	b.d.l.	0.35	45.96	b.d.l.	b.d.l.	0.02
FA14a_qtz_L2 Line 005	L	b.d.l.	b.d.l.	0.38	45.96	0.02	0.04	0.02
FA14a_qtz_L2 Line 006	L	0.02	b.d.l.	0.03	45.64	0.02	0.05	0.01
FA14a_qtz_L2 Line 007	L	b.d.l.	b.d.l.	0.05	46.38	0.01	0.02	0.01
FA14a_qtz_L2 Line 008	L	b.d.l.	b.d.l.	0.03	46.46	b.d.l.	b.d.l.	b.d.l.
FA14a_qtz_L2 Line 009	D	0.02	0.01	0.73	43.72	0.09	0.05	0.01
FA14a_qtz_L2 Line 010	D	0.01	b.d.l.	0.07	46.03	0.02	0.02	0.02
FA14a_qtz_L2 Line 011	L	0.01	b.d.l.	0.05	46.46	b.d.l.	b.d.l.	b.d.l.
FA14a_qtz_L2 Line 012	L	0.07	b.d.l.	0.03	46.45	0.01	0.01	0.02
FA14a_qtz_L3 Line 001	M	0.01	0.01	0.35	45.88	0.03	0.03	0.02
FA14a_qtz_L3 Line 003	M	0.04	0.12	1.29	42.33	0.56	0.26	0.02
FA14a_qtz_L3 Line 004	M	0.02	0.02	0.53	45.41	0.10	0.02	0.02
FA14a_qtz_L3 Line 005	M	0.03	0.04	0.64	44.86	0.21	0.05	0.01
FA14a_qtz_L4 Line 001	M	0.03	b.d.l.	0.24	45.50	0.04	0.02	0.02
FA14a_qtz_L4 Line 002	M	0.03	0.01	0.40	44.64	0.08	0.05	0.01
FA14a_qtz_L4 Line 003	M	0.02	b.d.l.	0.26	45.56	0.03	0.02	0.01
FA14a_qtz_L4 Line 004	M	b.d.l.	b.d.l.	0.10	46.00	b.d.l.	0.01	0.03
FA14a_qtz_L4 Line 005	M	0.02	0.01	0.32	45.31	0.10	0.02	0.02
FA04_qz L1 Line 001	M	0.02	b.d.l.	0.42	43.90	0.04	0.01	0.03
FA04_qz L1 Line 002	M	0.01	b.d.l.	0.24	45.98	0.01	b.d.l.	0.01
FA04_qz L1 Line 003	M	0.04	b.d.l.	0.32	45.56	0.04	0.02	0.02
FA04_qz L1 Line 004	M	0.03	b.d.l.	0.37	45.76	0.05	0.01	0.02
FA04_qz L1 Line 005	M	0.03	0.01	0.41	45.70	0.03	b.d.l.	0.02
FA04_qz L1 Line 006	M	0.03	b.d.l.	0.44	45.49	0.07	0.05	0.01
FA04_qz L1 Line 007	M	0.03	b.d.l.	0.25	45.53	0.02	0.02	0.01
FA04_qz L1 Line 008	M	0.03	b.d.l.	0.33	46.72	0.06	0.05	0.02

min	0.01	0.01	0.02	42.33	0.00	0.01	0.01
max	0.07	0.12	1.29	46.72	0.56	0.26	0.03
average	0.02	0.02	0.28	45.62	0.05	0.04	0.02
median	0.02	0.01	0.29	45.88	0.03	0.02	0.02
s.d.	0.01	0.03	0.24	0.98	0.09	0.05	0.01

	D.L.	Na	Mg	Al	Si	K	K	Ca
	average	0.009	0.007	0.006	0.013	0.004	0.006	0.007

b.d.l.	below detection limit

Table 13. LA-ICP-MS analysis (ppm) of quarz (Qz2) from the Fonte Argentila area (FAR) and Mg-Li geothermometer data

		standard										
		Li	Na	Mg	Al	Si wt%	K	Ca	Ti	Cr	Fe	Ge	Mg-Li geothermometer (°C)
1	light quartz	15.20	99.00	15.40	700.00	46.70	171.00	406.00	0.04	0.51		2.31	128.99
2		14.77	19.20	15.00	306.00	46.70	5.00	416.00	0.05	1.33		1.37	128.95
3		26.50	63.00	55.00	181.00	46.70	17.00	407.00	0.17	0.90		1.22	117.86
4		40.30	42.00	8.30	784.00	46.70	23.30	332.00	0.07	1.01	0.30	2.29	156.11
5		14.50	82.00	20.00	343.00	46.70	13.50	580.00	0.04	0.97	1.20	2.27	124.12
6		16.00	52.00	25.00	431.00	46.70	22.40	364.00	0.04	1.24		1.81	122.19
7		5.77	160.00	105.00	133.50	46.70	10.90	530.00	0.15	0.98	1.10	0.96	87.66
8		7.47	60.00	21.00	112.40	46.70	15.60	388.00	0.06	1.27	0.18	1.03	113.34
9		2.88	63.00	4.40	111.20	46.70	4.90	418.00	0.02	0.68		0.64	122.54
10		3.57	163.00	21.00	131.00	46.70	18.70	493.00	0.13	0.87	1.60	0.91	102.76
11		4.41	20.20	6.80	80.10	46.70	5.40	311.00	0.03	0.80	1.10	1.30	122.40
12		29.60	93.00	29.00	872.00	46.70	154.00	710.00	0.06	1.08	5.20	1.89	129.52
13		14.90	72.60	3.80	446.00	46.70	39.00	670.00	0.05	0.79	0.50	2.22	152.26
max		40.30	163.00	105.00	872.00		171.00	710.00	0.17	1.33	5.20	2.31	156.11
min		2.88	19.20	3.80	80.10		4.90	311.00	0.02	0.51	0.18	0.64	87.66
median		14.77	63.00	20.00	306.00		17.00	416.00	0.05	0.97	1.10	1.37	122.54
average		15.07	76.08	25.36	356.25		38.52	463.46	0.07	0.96	1.40	1.56	123.75

		Li	Na	Mg	Al	Si wt%	K	Ca	Ti	Cr	Fe	Ge	
1	dark bands	122.00	326.00	52.90	4260.00	46.70	1390.00	890.00	0.20	0.45	6.30	6.67	142.99
2		117.00	267.00	28.50	2380.00	46.70	528.00	900.00	0.13	0.78	8.00	3.81	153.08
3		137.00	215.00	10.90	2600.00	46.70	410.00	521.00	0.13	0.92	0.60	6.34	174.12
4		135.00	159.00	81.00	3010.00	46.70	720.00	586.00	0.12	0.90	22.80	4.23	137.52
5		103.50	259.00	84.00	2660.00	46.70	850.00	920.00	0.12	0.62	24.30	4.58	132.55
6		68.70	92.00	41.00	1231.00	46.70	66.00	406.00	0.05	1.20	0.77	3.03	137.61
7		79.60	162.00	29.10	2120.00	46.70	508.00	760.00	0.08	0.67	9.40	4.89	145.93
8		70.20	170.00	123.00	4540.00	46.70	1510.00	810.00	0.10	0.73	17.50	3.92	120.43
9		37.80	116.00	14.20	1121.00	46.70	241.00	660.00	0.05	1.26	0.78	3.53	145.46
10		42.20	166.00	26.40	1850.00	46.70	474.00	566.00	0.08	0.95	0.30	3.50	136.82
11		23.70	185.00	38.00	1020.00	46.70	267.00	542.00	0.09	1.08	1.50	2.95	121.79
max		137.00	326.00	123.00	4540.00		1510.00	920.00	0.20	1.26	24.30	6.67	174.12
min		23.70	92.00	10.90	1020.00		66.00	406.00	0.05	0.45	0.30	2.95	120.43
median		79.60	170.00	38.00	2380.00		508.00	660.00	0.10	0.90	6.30	3.92	137.61
average		85.15	192.45	48.09	2435.64		633.09	687.36	0.10	0.87	8.39	4.31	140.76

Table 13. LA-ICP-MS analysis (ppm) of quarz (Qz2) from the Fonte Argentila area (FAR) and Mg-Li geothermometer data **(continue)**

		standard										
		Li	Na	Mg	Al	Si wt%	K	Ca	Ti	Cr	Fe	Ge	
1	microsrystalline qyartz	162.00	144.00	19.90	1990.00	46.70	245.00	613.00	0.09	0.59	5.70	3.71	165.71
2		241.00	207.00	12.50	2480.00	46.70	292.00	654.00	0.08	0.55	2.40	4.98	182.73
3		230.00	375.00	191.00	4850.00	46.70	2170.00	990.00	2.78	0.96	94.00	7.06	132.18
4		298.00	386.00	17.20	3820.00	46.70	661.00	1040.00	0.15	0.85	13.30	8.46	180.55
5		161.00	181.00	18.30	2490.00	46.70	301.00	684.00	0.07	0.78	11.60	5.37	167.19
6		141.50	153.40	13.80	2420.00	46.70	252.00	636.00	0.08	0.88	10.10	5.38	170.14
7		192.00	191.00	16.40	2350.00	46.70	330.00	740.00	0.09	0.83	8.80	5.12	172.73
8		199.00	212.00	18.50	2620.00	46.70	363.00	890.00	0.12	0.67	8.90	5.03	171.07
9		161.00	356.00	18.00	3890.00	46.70	1320.00	1180.00	0.16	0.71	2.10	7.80	167.51
10		364.00	258.00	4.30	3870.00	46.70	341.00	860.00	0.13	0.87	0.30	9.40	215.22
11		323.00	448.00	16.70	3710.00	46.70	800.00	1260.00	0.20	0.63	86.00	8.22	182.79
12		286.00	393.00	26.80	3660.00	46.70	932.00	1230.00	0.22	0.81	32.40	8.70	170.92
13		168.00	260.00	35.40	2540.00	46.70	488.00	1060.00	0.28	0.76	39.00	5.38	155.70
14		275.00	278.00	22.70	3550.00	46.70	685.00	1220.00	0.17	0.69	15.20	10.00	173.40
15		282.00	282.00	30.40	3640.00	46.70	690.00	1260.00	0.18	0.82	20.60	7.53	168.21
16		233.00	132.00	16.80	2800.00	46.70	208.00	640.00	0.08	0.91	6.20	3.58	176.07
17		262.00	303.00	19.40	3170.00	46.70	457.00	940.00	0.13	0.91	6.10	4.46	175.54
max		364.00	448.00	191.00	4850.00		2170.00	1260.00	2.78	0.96	94.00	10.00	215.22
min		141.50	132.00	4.30	1990.00		208.00	613.00	0.07	0.55	0.30	3.58	132.18
median		233.00	260.00	18.30	3170.00		457.00	940.00	0.13	0.81	10.10	5.38	171.07
average		234.03	268.20	29.30	3167.65		619.71	935.12	0.29	0.78	21.34	6.48	172.22

Table 14. EPMA analyses (wt%) of calcite from the Longobucco (LGB) and Fonte Argentila (FAR) areas

area	analyses spots	SiO2	FeO	MnO	MgO	*XMg*	CaO	Na2O	BaO	Al2O3	Total
LGB	LGB04h_B_cal	0.046	0.376	1.103	0.077	*0.001*	51.334	0.059	0.021	0.021	53.038
	LGB04h_B_cal.2	0.053	0.320	1.540	0.050	*0.001*	50.075	0.005	0.042	0.012	52.098
	LGB04h_B_cal.3	0.024	0.231	1.001	0.082	*0.002*	51.189	0.109	0.070	0.009	52.717
	LGB04h_B_cal.4	0.224	0.550	0.848	0.082	*0.002*	50.263	n.d.	0.062	0.156	52.187
	LGB04h_B_cal.5	0.042	0.165	1.066	0.037	*0.001*	50.965	0.179	0.065	0.011	52.531
	LGB04h_B_cal.6	0.026	0.322	1.139	0.102	*0.002*	50.128	0.119	0.066	n.d.	51.904
	LGB04h_B_cal.7	0.121	0.044	0.635	0.123	*0.002*	50.533	0.075	0.085	0.010	51.628
	LGB04h_B_cal.8	0.085	0.150	0.797	0.131	*0.003*	50.084	0.221	0.115	0.009	51.595
FAR	FA11d_line cal Line 001	0.019	0.197	1.216	0.296	*0.006*	53.165	0.043	0.047	0.007	54.996
	FA11d_line cal Line 002	0.157	0.143	0.862	0.185	*0.004*	48.218	n.d.	0.058	n.d.	49.627
	FA11d_line cal Line 003	n.d.	0.088	0.591	0.178	*0.003*	54.309	n.d.	0.047	n.d.	55.216
	FA11d_line cal Line 004	0.053	0.221	0.937	0.469	*0.009*	52.242	n.d.	0.207	0.017	54.155
	FA11d_line cal Line 005	0.292	0.276	1.376	0.168	*0.003*	51.880	0.005	0.167	0.028	54.195
	FA11d_line cal Line 006	0.017	0.167	0.937	0.227	*0.004*	55.453	0.015	0.034	n.d.	56.854
	min	0.017	0.044	0.591	0.037	*0.001*	48.218	0.005	0.021	0.007	49.627
	max	0.292	0.550	1.540	0.469	*0.009*	55.453	0.221	0.207	0.156	56.854
	average	0.089	0.232	1.003	0.158	*0.003*	51.417	0.083	0.078	0.028	53.053
	median	0.053	0.209	0.969	0.127	*0.003*	51.077	0.067	0.064	0.012	52.624
	s.d.	0.087	0.130	0.264	0.115	*0.002*	1.890	0.074	0.052	0.045	1.854

n.d.	not detected

Table 15a. LA-ICP-MS analyses (ppm) of calcite from the Longobucco area (LGB)

	standard																					
	Mg	Ca wt%	Mn wt%	Fe wt%	Sr	Y	Ba	La	Ce	Pr	Nd	Sm	Eu	Gd	Tb	Dy	Ho	Er	Tm	Yb	Lu	Th	U
LGB04h-1	21.48	39.38	0.61	0.01	47.45	76.30	0.28	26.05	68.40	9.38	39.70	14.32	4.30	15.43	2.50	13.40	2.30	5.34	0.62	3.28	0.43	0.00	0.00
LGB04h-2	900.00	39.06	0.67	0.17	72.50	118.30	5.31	61.30	128.60	16.39	66.60	20.38	8.20	23.42	3.86	21.14	3.60	8.23	0.92	4.89	0.64	0.54	0.01
LGB04h-3	598.00	39.10	0.72	0.12	65.60	119.10	5.44	38.80	88.70	11.59	47.70	16.05	6.60	19.50	3.55	20.27	3.50	8.06	0.89	5.02	0.61	0.02	0.00
LGB04h-4	15.93	39.89	0.10	0.01	37.94	25.44	0.72	4.18	11.16	1.53	6.20	2.31	0.50	3.03	0.74	5.05	0.93	2.42	0.28	1.55	0.19	0.00	0.00
LGB04h-5	58.60	39.60	0.38	0.02	37.80	15.45	1.60	4.01	9.63	1.31	5.49	2.20	0.61	2.57	0.49	2.97	0.53	1.24	0.15	0.88	0.11	0.00	0.00
LGB04h-6	31.30	39.72	0.26	0.01	45.61	18.07	1.83	6.13	13.94	1.86	7.57	2.94	0.79	3.50	0.63	3.49	0.58	1.25	0.14	0.78	0.09	0.00	0.00
LGB04h-7	225.30	38.96	0.86	0.16	83.00	96.50	0.74	21.98	47.20	6.00	23.04	8.15	3.51	11.29	2.43	15.61	2.75	6.75	0.75	4.04	0.49	0.00	0.00
LGB04h-8	168.30	38.87	0.79	0.31	85.20	310.20	2.35	34.14	98.20	15.25	71.70	31.45	11.29	44.95	8.37	48.80	8.22	18.00	1.70	7.53	0.79	0.00	0.00
LGB04h-9	291.00	39.01	0.73	0.23	74.20	250.00	1.91	190.00	418.00	52.50	224.00	62.00	16.40	63.50	9.50	46.00	7.29	15.66	1.67	8.07	0.90	0.06	0.09
LGB04h-10	198.30	38.50	1.22	0.24	52.76	160.50	1.60	42.20	87.50	11.10	45.20	13.82	7.93	17.91	3.57	22.53	4.32	11.73	1.48	9.07	1.20	0.05	0.00
LGB04h-11	146.90	38.86	0.85	0.27	67.10	204.30	1.74	50.20	119.70	16.20	70.00	24.00	7.77	30.60	5.72	33.90	6.10	15.62	1.88	9.85	1.17	0.01	0.01
LGB04h-12	108.80	39.16	0.65	0.17	69.30	249.30	3.81	104.40	246.00	33.40	134.50	41.90	13.23	49.30	8.20	44.70	7.22	15.16	1.40	6.11	0.68	0.01	0.01
LGB04hB-1	23.99	39.32	0.66	0.01	47.34	58.50	0.71	19.92	51.00	6.87	30.09	10.55	3.10	11.55	1.88	10.16	1.74	4.14	0.48	2.73	0.36	0.00	0.00
LGB04hB-2	933.00	39.01	0.75	0.14	77.40	132.70	3.92	36.19	84.00	11.05	47.00	16.02	6.43	20.44	3.83	21.91	3.79	9.02	1.03	5.82	0.74	0.02	0.00
LGB04hB-3	826.00	39.08	0.71	0.13	79.50	138.80	5.40	50.40	112.80	14.69	62.40	19.75	8.44	24.02	4.10	23.29	4.00	9.09	1.02	5.62	0.73	0.04	0.00
LGB04hB-4	9.09	39.89	0.10	0.00	23.67	50.50	0.84	4.46	12.84	1.80	7.61	3.05	0.62	4.09	1.09	8.39	1.85	5.87	0.97	6.72	0.92	0.00	0.00
LGB04hB-5	67.40	39.60	0.37	0.02	39.29	6.71	2.06	1.67	3.74	0.52	2.24	0.91	0.32	1.19	0.25	1.39	0.24	0.59	0.07	0.44	0.07	0.00	0.00
LGB04hB-6	33.78	39.73	0.25	0.01	44.27	11.75	2.89	3.80	8.29	1.09	4.61	1.87	0.58	2.23	0.39	2.31	0.40	0.88	0.10	0.53	0.07	0.00	0.00
LGB04hB-7	209.70	39.01	0.80	0.17	56.40	69.30	1.91	13.71	29.30	3.79	15.64	6.01	2.49	8.34	1.80	11.12	2.00	4.66	0.52	2.74	0.34	0.00	0.00
LGB04hB-8	317.00	38.96	0.74	0.26	80.80	195.00	1.35	21.47	59.10	9.09	43.30	18.43	6.67	26.44	5.00	29.22	4.98	11.07	1.15	4.95	0.55	0.00	0.00
LGB04hB-9	284.00	38.96	0.77	0.24	76.00	210.40	1.94	55.40	136.10	18.80	81.40	28.30	9.23	34.00	6.21	35.50	6.07	13.95	1.46	7.13	0.81	0.01	0.00
LGB04hB-10	186.70	38.69	1.07	0.21	56.00	205.30	1.88	71.30	147.10	18.40	73.40	21.68	11.96	26.41	5.11	31.83	6.13	16.54	2.21	14.27	1.92	0.03	0.00
LGB04hB-11	108.50	38.96	0.79	0.23	48.50	69.20	1.93	14.46	33.10	4.45	19.14	6.68	2.17	8.32	1.64	10.71	2.12	5.99	0.81	4.48	0.55	0.00	0.00
LGB04hB-12	117.60	39.07	0.69	0.22	76.70	294.30	3.70	130.30	297.90	39.20	162.40	50.60	16.36	58.30	9.51	50.80	8.05	16.51	1.47	5.95	0.63	0.01	0.00
max	933.00	39.89	1.22	0.31	85.20	310.20	5.44	190.00	418.00	52.50	224.00	62.00	16.40	63.50	9.51	50.80	8.22	18.00	2.21	14.27	1.92	0.54	0.09
min	9.09	38.50	0.10	0.00	23.67	6.71	0.28	1.67	3.74	0.52	2.24	0.91	0.32	1.19	0.25	1.39	0.24	0.59	0.07	0.44	0.07	0.00	0.00
average	245.03	39.18	0.65	0.14	60.18	128.58	2.33	41.94	96.35	12.76	53.79	17.64	6.23	21.26	3.76	21.44	3.70	8.66	0.97	5.10	0.62	0.03	0.01
median	157.60	39.06	0.71	0.17	61.00	118.70	1.91	30.10	76.20	10.22	44.25	15.17	6.52	18.71	3.56	20.71	3.55	8.15	0.94	4.99	0.62	0.00	0.00
s.d.	280.76	0.38	0.28	0.10	17.51	93.20	1.51	45.22	100.61	12.94	54.30	15.98	5.02	18.00	2.92	15.60	2.55	5.65	0.60	3.32	0.42	0.11	0.02

Table 15b. LA-ICP-MS analysis (ppm) of calcite from the Longobucco area (LGB)

PAAS Normalization by McLennan S. (2001)

	La	Ce	Pr	Nd	Sm	Eu	Gd	Tb	Dy	Y	Ho	Er	Tm	Yb	Lu
	30	64	7.1	26	4.5	0.88	3.8	0.64	3.5	22	0.8	2.3	0.33	2.2	0.32
	normalized														
LGB04h-1	0.87	1.07	1.32	1.53	3.18	4.89	4.06	3.91	3.83	3.47	2.88	2.32	1.87	1.49	1.35
LGB04h-2	2.04	2.01	2.31	2.56	4.53	9.32	6.16	6.03	6.04	5.38	4.50	3.58	2.78	2.22	1.99
LGB04h-3	1.29	1.39	1.63	1.83	3.57	7.50	5.13	5.55	5.79	5.41	4.38	3.50	2.69	2.28	1.90
LGB04h-4	0.14	0.17	0.22	0.24	0.51	0.57	0.80	1.16	1.44	1.16	1.16	1.05	0.85	0.71	0.58
LGB04h-5	0.13	0.15	0.18	0.21	0.49	0.69	0.68	0.77	0.85	0.70	0.66	0.54	0.46	0.40	0.34
LGB04h-6	0.20	0.22	0.26	0.29	0.65	0.90	0.92	0.98	1.00	0.82	0.73	0.55	0.42	0.36	0.29
LGB04h-7	0.73	0.74	0.85	0.89	1.81	3.99	2.97	3.80	4.46	4.39	3.44	2.93	2.28	1.84	1.53
LGB04h-8	1.14	1.53	2.15	2.76	6.99	12.83	11.83	13.08	13.94	14.10	10.28	7.83	5.16	3.42	2.47
LGB04h-9	6.33	6.53	7.39	8.62	13.78	18.64	16.71	14.84	13.14	11.36	9.11	6.81	5.06	3.67	2.80
LGB04h-10	1.41	1.37	1.56	1.74	3.07	9.01	4.71	5.57	6.44	7.30	5.40	5.10	4.49	4.12	3.74
LGB04h-11	1.67	1.87	2.28	2.69	5.33	8.83	8.05	8.94	9.69	9.29	7.63	6.79	5.68	4.48	3.66
LGB04h-12	3.48	3.84	4.70	5.17	9.31	15.03	12.97	12.81	12.77	11.33	9.03	6.59	4.25	2.78	2.11
LGB04hB-1	0.66	0.80	0.97	1.16	2.34	3.52	3.04	2.93	2.90	2.66	2.17	1.80	1.47	1.24	1.14
LGB04hB-2	1.21	1.31	1.56	1.81	3.56	7.31	5.38	5.98	6.26	6.03	4.73	3.92	3.13	2.65	2.31
LGB04hB-3	1.68	1.76	2.07	2.40	4.39	9.59	6.32	6.41	6.65	6.31	5.00	3.95	3.08	2.55	2.28
LGB04hB-4	0.15	0.20	0.25	0.29	0.68	0.70	1.08	1.71	2.40	2.30	2.31	2.55	2.94	3.05	2.87
LGB04hB-5	0.06	0.06	0.07	0.09	0.20	0.36	0.31	0.38	0.40	0.31	0.30	0.26	0.22	0.20	0.21
LGB04hB-6	0.13	0.13	0.15	0.18	0.42	0.66	0.59	0.62	0.66	0.53	0.50	0.38	0.31	0.24	0.23
LGB04hB-7	0.46	0.46	0.53	0.60	1.34	2.82	2.19	2.81	3.18	3.15	2.50	2.03	1.56	1.25	1.06
LGB04hB-8	0.72	0.92	1.28	1.67	4.10	7.58	6.96	7.81	8.35	8.86	6.23	4.81	3.48	2.25	1.72
LGB04hB-9	1.85	2.13	2.65	3.13	6.29	10.49	8.95	9.70	10.14	9.56	7.59	6.07	4.42	3.24	2.54
LGB04hB-10	2.38	2.30	2.59	2.82	4.82	13.59	6.95	7.98	9.09	9.33	7.66	7.19	6.69	6.49	5.99
LGB04hB-11	0.48	0.52	0.63	0.74	1.48	2.46	2.19	2.56	3.06	3.15	2.65	2.60	2.44	2.04	1.73
LGB04hB-12	4.34	4.65	5.52	6.25	11.24	18.59	15.34	14.86	14.51	13.38	10.06	7.18	4.45	2.70	1.96
max	6.33	6.53	7.39	8.62	13.78	18.64	16.71	14.86	14.51	14.10	10.28	7.83	6.69	6.49	5.99
min	0.06	0.06	0.07	0.09	0.20	0.36	0.31	0.38	0.40	0.31	0.30	0.26	0.22	0.20	0.21
average	1.40	1.51	1.80	2.07	3.92	7.08	5.60	5.88	6.12	5.84	4.62	3.76	2.92	2.32	1.95
median	1.00	1.19	1.44	1.70	3.37	7.40	4.92	5.56	5.92	5.40	4.44	3.54	2.86	2.27	1.93

Table 16a. EPMA analyses (wt%) of REE-F-carbonates from the Longobucco area (LGB)

analysis spot	Ca	Y	La	Ce	Pr	Nd	Sm	Gd	Dy	F	Cl	∑REE
LGB06a-1Lb-2-01	12.99	7.30	5.29	12.94	2.26	6.76	1.85	2.23	1.72	0.83	0.02	40.34
LGB06a-1Lb-2-02	13.36	7.51	4.90	11.63	2.00	6.14	1.70	2.13	1.48	0.71	0.06	37.50
LGB06a-1Lb-3-01	12.31	5.13	5.53	13.72	2.43	7.52	1.91	2.04	1.16	1.03	0.03	39.44
LGB06a-1Lb-3-02	13.14	5.85	6.29	14.87	2.54	7.85	1.88	2.07	1.28	1.26	0.03	42.64
LGB06a-1Lb-4-01	18.00	7.77	3.55	11.02	1.92	6.16	1.78	2.36	1.91	1.15	0.02	36.46
LGB06a-1Lb-5-01	12.25	5.88	5.47	13.25	2.30	7.19	1.85	2.05	1.38	0.78	0.03	39.36
LGB06a-1Lb-5-02	11.34	4.13	5.48	12.76	2.24	6.83	1.66	1.81	1.12	1.15	0.05	36.04
LGB06a-1Lb-5-03	29.97	0.90	1.48	3.64	0.57	1.83	0.47	0.46	0.49	0.74	0.03	9.83
LGB04b-1L-1-01	13.58	7.74	4.63	12.83	2.15	7.11	2.00	2.29	1.53	0.56	0.02	40.29
LGB04b-1L-1-02	41.63	0.22	0.20	0.75	0.11	0.46	0.12	0.13	0.39	0.48	b.d.l.	2.40
LGB04b-1L-1-03	13.76	8.89	4.47	12.31	2.17	6.85	1.94	2.50	1.68	0.81	0.02	40.81
LGB04b-1L-7	14.96	7.73	4.48	12.22	2.14	6.64	1.86	2.35	1.54	1.00	0.02	38.95
LGB04b-1L-9-01	21.91	4.93	3.47	8.85	1.56	5.22	1.52	2.04	1.18	0.92	0.01	28.77
LGB04b-1L-9-02	42.48	b.d.l.	b.d.l.	b.d.l.	0.03	b.d.l.	0.03	b.d.l.	0.48	0.04	b.d.l.	0.53
LGB04b-1L-9-03	22.81	4.34	3.14	8.91	1.61	5.14	1.51	1.87	1.20	0.89	0.01	27.72
LGB04b-1L-9-04	42.34	0.03	b.d.l.	0.03	b.d.l.	0.03	b.d.l.	b.d.l.	0.38	0.78	b.d.l.	0.47
LGB04b-1L-8-01	14.77	3.99	4.89	13.42	2.45	8.11	2.39	2.62	1.15	0.69	0.02	39.02
LGB04b-1L-8-02	22.28	2.35	3.81	10.31	1.94	6.52	1.77	2.06	0.83	0.45	0.02	29.59
LGB04b-1L-8-03	39.19	0.27	0.37	1.02	0.21	0.72	0.23	0.29	0.41	0.87	b.d.l.	3.52
LGB04b-1L-10-02	41.36	b.d.l.	b.d.l.	0.04	b.d.l.	b.d.l.	0.03	0.06	0.20	0.48	b.d.l.	0.32
LGB06a-1La-11-01	12.66	4.10	6.91	15.50	2.70	7.77	1.92	2.07	1.12	0.95	0.03	42.09
LGB06a-1La-11-02	12.58	3.65	7.10	15.74	2.71	8.03	2.02	2.08	0.97	0.86	0.03	42.31
LGB06a-1La-12-01	13.36	6.28	5.62	13.29	2.13	6.56	1.60	1.75	1.40	1.06	0.04	38.63
LGB06a-1La-13-01	15.06	3.47	7.51	13.82	2.27	6.07	1.22	1.14	0.77	1.00	0.04	36.27
LGB06a-1La-13-02	35.61	0.69	1.59	4.01	0.78	2.04	0.41	0.58	0.49	0.68	0.01	10.57
LGB06a-1La-13-03	13.19	3.16	7.94	15.41	2.42	6.86	1.30	1.32	0.73	0.90	0.04	39.13
LGB06a-1La-14-01	12.23	3.06	9.06	16.88	2.82	7.10	1.28	1.32	0.70	1.20	0.04	42.20
LGB06a-1La-14-02	12.34	2.58	9.69	17.56	2.85	6.68	1.17	1.12	0.60	1.02	0.02	42.25
LGB06a-1La-14-03	13.79	2.13	9.00	16.48	2.81	7.13	1.24	1.32	0.61	1.07	0.02	40.72
LGB06a-1La-15-01	14.62	2.38	7.56	15.36	2.50	6.86	1.24	1.34	0.57	0.85	0.04	37.82
LGB06a-1La-15-02	40.52	0.05	0.48	1.00	0.17	0.50	0.13	0.14	0.26	1.22	0.02	2.74
LGB04h_B_Fcarb5.1	12.82	4.56	5.64	13.67	2.93	7.57	2.23	3.54	1.12	1.03	0.04	41.25
LGB04h_B_Fcarb5.2	14.86	5.02	4.50	11.72	2.50	6.85	2.15	3.39	1.18	0.95	0.03	37.32
LGB04h_B_Fcarb5.3	16.62	4.95	3.84	9.60	2.03	5.67	1.84	3.06	1.25	0.58	0.04	32.22
LGB04h_B_Fcarb6.1	28.19	0.71	3.01	6.60	1.51	3.64	1.02	1.60	0.38	0.57	0.02	18.47
LGB04h_B_Fcarb6.2	12.65	4.50	5.18	12.98	2.85	8.01	2.67	4.21	1.11	0.78	0.03	41.51
LGB04h_B_Fcarb6.3	33.59	0.43	1.65	3.70	0.81	2.14	0.59	0.97	0.50	0.90	0.01	10.79
LGB04h_B_Fcarb8.1	20.30	1.13	4.90	11.73	2.48	6.17	1.56	2.53	0.45	0.54	0.03	30.96
LGB04h_B_Fcarb11.1	12.14	1.63	6.93	14.69	3.15	7.98	2.20	3.37	0.51	0.96	0.02	40.47
LGB04h_B_Fcarb11.2	11.59	2.24	6.24	13.96	3.04	7.72	2.22	3.53	0.64	0.93	0.03	39.59
LGB04h_B_Fcarb11.3	12.80	1.69	6.60	14.44	3.18	7.86	2.15	3.40	0.52	0.72	0.03	39.85

min	11.34	0.03	0.20	0.03	0.03	0.03	0.03	0.06	0.20	0.04	0.01	0.32
max	42.48	8.89	9.69	17.56	3.18	8.11	2.67	4.21	1.91	1.26	0.06	42.64
average	20.14	3.68	4.96	10.82	2.03	5.80	1.47	1.93	0.91	0.84	0.03	30.27
median	14.62	3.65	5.04	12.80	2.26	6.76	1.68	2.05	0.83	0.87	0.03	37.82
s.d.	10.65	2.52	2.39	5.13	0.89	2.42	0.71	1.03	0.46	0.25	0.01	14.72

D.L.	Ca	Y	La	Ce	Pr	Nd	Sm	Gd	Dy	F	Cl
average	0.009	0.036	0.033	0.032	0.033	0.031	0.032	0.031	0.029	0.030	0.004

b.d.l. below detection limit

Table 16b. REEs EPMA analyses (ppm) of REE-F-carbonates normalized to PAAS

PAAS Normalization by McLennan S. (2001)

La	Ce	Pr	Nd	Sm	Gd	Dy	Y
30	64	7.1	26	4.5	3.8	3.5	22
normalized							
8720	4053	40068	6640	32132	33986	22880	2684
8087	3642	35515	6026	29580	32531	19745	2762
9128	4295	43103	7381	33333	31076	15447	1888
10380	4657	45076	7709	32733	31606	17073	2151
5851	3451	34149	6043	30931	35969	25435	2858
9015	4150	40827	7061	32132	31209	18351	2163
9044	3997	39765	6708	28829	27638	14983	1517
2433	1139	10178	1793	8236	6952	6579	329
7637	4017	38247	6977	34835	34911	20441	2846
336	235	2006	455	2108	2027	5237	81
7370	3854	38550	6724	33784	38085	22416	3269
7384	3826	37943	6514	32432	35837	20557	2840
5724	2771	27623	5125	26426	31076	15796	1812
_	_	510	_	482	_	6352	_
5176	2789	28685	5050	26276	28432	16028	1595
_	11	_	32	_	_	5000	12
8059	4201	43559	7962	41592	39937	15331	1468
6287	3230	34452	6396	30781	31341	11072	866
618	319	3696	709	3955	4451	5425	99
_	12	_	_	467	926	2639	_
11392	4853	47960	7625	33484	31606	14867	1508
11716	4930	48112	7886	35135	31738	12871	1343
9269	4162	37791	6438	27928	26713	18699	2307
12391	4328	40372	5959	21171	17323	10214	1277
2616	1254	13793	2003	7060	8897	6496	252
13094	4825	42952	6733	22673	20101	9670	1161
14937	5284	50085	6969	22222	20101	9351	1123
15992	5498	50540	6556	20420	17059	8013	947
14852	5159	49933	7002	21622	20101	8135	782
12475	4810	44469	6733	21622	20497	7604	874
800	314	2981	493	2249	2108	3504	19
9297	4280	52058	7431	38889	53954	14867	1676
7426	3670	44469	6724	37387	51706	15679	1847
6329	3005	35970	5563	31982	46681	16609	1818
4965	2067	26864	3568	17718	24332	5111	262
8551	4063	50692	7861	46546	64137	14750	1653
2715	1157	14429	2104	10267	14762	6712	158
8087	3673	44014	6060	27177	38614	5963	417
11435	4598	56004	7835	38288	51441	6837	599
10295	4371	54031	7575	38589	53822	8551	825
10886	4522	56459	7718	37387	51838	6964	622

min	336	11	510	32	467	926	2639	12
max	15992	5498	56459	7962	46546	64137	25435	3269
average	8178	3387	36101	5696	25522	29372	12153	1352
median	8319	4007	40068	6640	29204	31209	11072	1343
s.d.	3938	1606	15758	2378	12431	15708	6074	926

Table 17a. LA-ICP-MS analysis (ppm) of fluorite from the Fonte Argentila area (FAR)

	Si	standard Ca wt%	La	Ce	Pr	Nd	Sm	Eu	Gd	Tb	Dy	Y	Ho	Er	Tm	Yb	Lu
1	510.00	55.52	3.70	5.23	1.15	8.40	6.40	4.29	15.60	2.39	11.80	189.00	2.03	3.29	0.28	1.21	0.13
2	1040.00	55.52	11.00	19.90	3.46	21.90	14.40	11.50	33.40	5.25	27.50	326.00	4.66	9.50	0.82	3.42	0.33
3	700.00	55.52	36.20	69.00	12.20	69.00	37.60	29.60	64.60	9.97	53.80	481.00	8.49	16.80	1.60	6.84	0.74
4	810.00	55.52	26.60	43.90	6.61	33.20	13.80	9.54	27.40	4.25	25.20	282.00	4.30	8.74	0.87	3.64	0.40
5	440.00	55.52	89.40	121.00	14.90	66.10	22.00	10.00	36.70	6.03	32.60	331.00	5.14	10.10	0.80	2.46	0.22
6	670.00	55.52	40.30	61.50	8.30	39.10	17.90	10.90	39.10	6.85	37.50	463.00	6.43	12.30	0.96	3.12	0.29
7	530.00	55.52	3.23	4.66	0.62	3.04	1.19	0.92	3.00	0.58	3.58	55.30	0.69	1.39	0.14	0.52	0.06
8	3260.00	55.52	21.70	32.70	5.25	27.30	13.50	10.90	26.30	4.34	22.90	230.00	3.81	8.14	0.80	3.48	0.39
9	1810.00	55.52	10.50	2.14	0.32	1.62	0.68	0.36	1.14	0.23	0.95	18.80	0.23	0.41	0.04	0.13	0.02
10	1230.00	55.52	7.90	6.50	1.35	10.00	6.61	4.71	17.00	2.36	12.70	195.00	1.95	3.55	0.30	1.28	0.15
11	1500.00	55.52	1.99	4.16	0.83	7.10	5.04	3.90	14.30	2.15	11.70	186.00	1.81	3.62	0.31	1.36	0.15
12	1170.00	55.52	7.40	13.10	2.53	17.50	13.00	8.80	28.10	4.53	22.20	321.00	3.64	7.00	0.63	2.35	0.24
13	770.00	55.52	45.70	92.50	14.80	86.70	43.70	22.20	77.20	12.20	65.10	466.00	10.39	20.90	2.04	8.56	0.82
14	850.00	55.52	3.30	3.72	0.57	3.21	1.65	1.49	5.84	1.12	6.80	102.00	1.22	2.80	0.25	1.06	0.13
15	990.00	55.52	30.30	46.20	5.84	26.70	8.70	5.25	17.20	2.85	16.20	211.00	2.62	5.53	0.49	1.80	0.17
max	3260.00		89.40	121.00	14.90	86.70	43.70	29.60	77.20	12.20	65.10	481.00	10.39	20.90	2.04	8.56	0.82
min	440.00		1.99	2.14	0.32	1.62	0.68	0.36	1.14	0.23	0.95	18.80	0.23	0.41	0.04	0.13	0.02
average	1085.33		22.61	35.08	5.25	28.06	13.74	8.96	27.13	4.34	23.37	257.14	3.83	7.60	0.69	2.75	0.28
median	850.00		11.00	19.90	3.46	21.90	13.00	8.80	26.30	4.25	22.20	230.00	3.64	7.00	0.63	2.35	0.22
s.d.	710.78		23.65	36.94	5.17	26.67	12.63	7.97	21.38	3.38	18.08	143.69	2.88	5.76	0.55	2.31	0.23

Table 17b. LA-ICP-MS analysis (ppm) of fluorite from the Fonte Argentila area (FAR)

PAAS Normalization by McLennan S. (2001)

	La	Ce	Pr	Nd	Sm	Eu	Gd	Tb	Dy	Y	Ho	Er	Tm	Yb	Lu
	30	64	7.1	26	4.5	0.88	3.8	0.64	3.5	22	0.8	2.3	0.33	2.2	0.32
	normalized														
1	0.123	0.082	0.162	0.323	1.422	4.875	4.105	3.734	3.371	8.591	2.538	1.430	0.836	0.550	0.406
2	0.367	0.311	0.487	0.842	3.200	13.068	8.789	8.203	7.857	14.818	5.825	4.130	2.485	1.555	1.025
3	1.207	1.078	1.718	2.654	8.356	33.636	17.000	15.578	15.371	21.864	10.613	7.304	4.848	3.109	2.297
4	0.887	0.686	0.931	1.277	3.067	10.841	7.211	6.641	7.200	12.818	5.375	3.800	2.636	1.655	1.238
5	2.980	1.891	2.099	2.542	4.889	11.364	9.658	9.422	9.314	15.045	6.425	4.391	2.427	1.118	0.681
6	1.343	0.961	1.169	1.504	3.978	12.386	10.289	10.703	10.714	21.045	8.038	5.348	2.909	1.418	0.906
7	0.108	0.073	0.088	0.117	0.264	1.045	0.789	0.906	1.023	2.514	0.863	0.604	0.427	0.238	0.172
8	0.723	0.511	0.739	1.050	3.000	12.386	6.921	6.781	6.543	10.455	4.763	3.539	2.436	1.582	1.219
9	0.350	0.033	0.045	0.062	0.151	0.409	0.300	0.358	0.271	0.855	0.281	0.177	0.116	0.057	0.058
10	0.263	0.102	0.190	0.385	1.469	5.352	4.474	3.688	3.629	8.864	2.438	1.543	0.903	0.582	0.472
11	0.066	0.065	0.117	0.273	1.120	4.432	3.763	3.359	3.343	8.455	2.263	1.574	0.939	0.618	0.463
12	0.247	0.205	0.356	0.673	2.889	10.000	7.395	7.078	6.343	14.591	4.550	3.043	1.909	1.068	0.756
13	1.523	1.445	2.085	3.335	9.711	25.227	20.316	19.063	18.600	21.182	12.988	9.087	6.182	3.891	2.575
14	0.110	0.058	0.080	0.123	0.367	1.693	1.537	1.750	1.943	4.636	1.525	1.217	0.745	0.482	0.413
15	1.010	0.722	0.823	1.027	1.933	5.966	4.526	4.453	4.629	9.591	3.275	2.404	1.479	0.818	0.534
max	2.98	1.89	2.10	3.33	9.71	33.64	20.32	19.06	18.60	21.86	12.99	9.09	6.18	3.89	2.58
min	0.07	0.03	0.04	0.06	0.15	0.41	0.30	0.36	0.27	0.85	0.28	0.18	0.12	0.06	0.06
average	0.75	0.55	0.74	1.08	3.05	10.18	7.14	6.78	6.68	11.69	4.78	3.31	2.09	1.25	0.88
median	0.37	0.31	0.49	0.84	2.89	10.00	6.92	6.64	6.34	10.45	4.55	3.04	1.91	1.07	0.68

Table 18. Fluorite fluid inclusions microthermometry data

Sample	Mineral species	FIA	No. of FIs	FIs type	Homogeniza-tion mode	Th range (°C)	mean Th (°C)	Tmi range (°C)	mean Tmi (°C)	Salinity range (wt% NaCl eq.)	mean salinity (wt% NaCl eq.)
FA11-Flr-E	Fluorite (euhedral crystal - core)	1	23	cluster	L+V --> L	76.3 to 100.3	88.6	-1.2 to 1.7	0.8	0 to 2.1	1.4
		2	5	PS trails	L+V --> L	76.8 to 83.6	80.5	-18.3 to -14.4	-16.6	18.2 to 21.2	19.9
		3	3	PS trail	L+V --> L	n.d.	n.d.	-4.7 to -4.5	-4.6	7.2 to 7.5	7.4
FA14-Flr-F	Fluorite (euhedral crystal - rim)	1	5	P cluster	L+V --> L	97.5 to 114.6	105.6	0.5	0.5	n.d.	n.d.
		2	5	PS trails L	L+V --> L	88	88	-2.7 to -1.5	-1.9	2.6 to 4.5	3.2
		3	8	trail // crystal edge	L+V --> L	77.5 to 85.5	83.3	2.9 to 4.7	3.8	n.d.	n.d.
FA14-Flr-E	Fluorite (brecciated crystal)	1	4	cluster	L+V --> L	78.0 to 83.6	81	-0.3 to 0	-0.2	0 to 0.5	0.3
		2	9	clusters	L+V --> L	72.2 to 83.2	78.3	-6.0 to -3.3	-4.9	5.5 to 9.1	7.7
		3	5	trail	L+V --> L	n.d.	n.d.	-15.2 to -9.0	-12.3	12.8 to 18.8	16.1

Table 19. Quartz-2 fluid inclusions microthermometry data

Sample	Mineral species	FIA	No. of FIs	FIs type	Homogenization mode	Th range (°C)	mean Th (°C)	Tmi range (°C)	mean Tmi (°C)	Salinity range (wt% NaCl eq.)	mean salinity (wt% NaCl eq.)
FA14-qz2	quartz. second generation (euhedral zoned crystal)	1a	20	cluster (core)	L+V --> L	136.4 to 146.8	140.9	-2.9 to -1.3	-1.9	2.3 to 4.8	3.2
		1b	6	cluster (core)	L+V --> L	127.7 to 131.8	129.8	-1.6 to -1.5	-1.6	2.6 to 2.8	2.7
		2a	9	trail (growth band)	L+V --> L	124.9 to 137.7	133	-1.8 to -0.6	-1.1	1.1 to 3.1	1.8
		2b	8	trail	L+V --> L	124.8 to 138	131.7	n.d.	n.d.	n.d.	n.d.
		3a	19	cluster	L+V --> L	125.0 to 149.8	137.8	-3.0 to -0.7	-1.9	1.2 to 5.0	3.1
		3b	19	cluster	L+V --> L	135.6 to 161.9	145.9	-3.7 to -2.1	-2.9	3.6 to 6.1	4.8
		4a	16	trail (growth band)	L+V --> L	126.3 to 136.4	132.8	-3.3 to -0.7	-2.1	1.2 to 5.5	3.6
		4b	8	trail (growth band)	L+V --> L	137.8 to 143.5	141.1	-1.9 to -0.8	-1.4	1.4 to 3.3	2.3
		4c	13	trail (growth band)	L+V --> L	129.6 to 140.5	136.4	-3.5 to -1.8	-2.7	3.1 to 5.8	4.4
		4d	12	trail (growth band)	L+V --> L	140.7 to 163.8	148.8	-3.6 to -2.0	-2.8	3.4 to 5.9	4.7
		5	9	trail (growth band)	L+V --> L	112.7 to 129.4	122.8	-2.0 to -0.3	-0.9	0.5 to 3.4	1.6
		6	16	trail (growth band)	L+V --> L	111.6 to 140.7	129.9	n.d.	n.d.	n.d.	n.d.
		7	8	cluster (rim)	L+V --> L	141.7 to 152.7	145.4	n.d.	n.d.	n.d.	n.d.